

High-Resolution Photoelectron Imaging of Cryogenically- Cooled Anions

By

Guo-Zhu Zhu

A dissertation submitted in partial satisfaction of the

requirements for the degree of

Doctor of Philosophy

in Chemistry

of the

Department of Chemistry

of

Brown University

Providence, RI

May 2019

© Copyright 2019 by Guo-Zhu Zhu

This dissertation by Guo-Zhu Zhu is accepted in its present form
by the Department of Chemistry
as satisfying the
dissertation requirement for the degree of Doctor of Philosophy.

Date _____

Lai-Sheng Wang, Advisor

Recommended to the Graduate Council

Date _____

Gerald J. Diebold, Reader

Date _____

Christoph G. Rose-Petruck, Reader

Approved by the Graduate Council

Date _____

Andrew G. Campbell
Dean of the Graduate School

Curriculum Vitae

Education

Ph.D. in Chemistry, Brown University Providence, RI	2013.09 – 2019.05
B.S. in Chemistry, Wuhan University Wuhan, China	2009.09 – 2013.06

Publications

1. **G. Z. Zhu**, C. H. Qian, and L. S. Wang. Tautomer-Specific Resonant Photoelectron Imaging of Deprotonated Cytosine Anions. *Angew. Chem. Int. Ed.* (2019). DOI: 10.1002/anie.201903444.
2. **G. Z. Zhu**, C. H. Qian, and L. S. Wang. Dipole-Bound Excited States and Resonant Photoelectron Imaging of Phenoxide and Thiophenoxide Anions. *J. Chem. Phys.* **149**, 164301 (2018). (**Editor's Pick**)
3. **G. Z. Zhu**, Y. Liu, Y. Hashikawa, Q. F. Zhang, Y. Murata, and L. S. Wang. Probing the Interaction between the Encapsulated Water Molecule and the Fullerene Cages in $\text{H}_2\text{O}@C_{60}^-$ and $\text{H}_2\text{O}@C_{59}\text{N}^-$. *Chem. Sci.* **9**, 5666–5671 (2018).
4. **G. Z. Zhu**, Y. Hashikawa, Y. Liu, Q. F. Zhang, L. F. Cheung, Y. Murata, and L. S. Wang. High-Resolution Photoelectron Imaging of Cryogenically-Cooled $C_{59}\text{N}^-$ and $(C_{59}\text{N})_2^{2-}$ Azafullerene Anions. *J. Phys. Chem. Lett.* **8**, 6220–6225 (2017).
5. **G. Z. Zhu**, Y. Liu, and L. S. Wang. Observation of Excited Quadrupole-Bound States in Cold Anions. *Phys. Rev. Lett.* **119**, 023002 (2017).
6. **G. Z. Zhu***, D. L. Huang*, and L. S. Wang. Conformation-Selective Resonant Photoelectron Imaging from Dipole-Bound States of Cold 3-Hydroxyphenoxide. *J. Chem. Phys.* **147**, 013910 (2017). (*These authors contribute equally.)
7. D. L. Huang*, **G. Z. Zhu***, Y. Liu, and L. S. Wang. Photodetachment Spectroscopy and Resonant Photoelectron Imaging of Cryogenically-Cooled Deprotonated 2-Hydroxypyrimidine Anions. *J. Mol. Spectrosc.* **332**, 86–93 (2017). (*These authors contribute equally.)
8. **G. Z. Zhu** and L. S. Wang. Communication: Vibrationally-Resolved Photoelectron Spectroscopy of the Tetracyanoquinodimethane (TCNQ) Anion and Accurate Determination of the Electron Affinity of TCNQ. *J. Chem. Phys.* **143**, 221102 (2015).
9. D. L. Huang, H. T. Liu, C. G. Ning, **G. Z. Zhu**, and L. S. Wang. Probing the Vibrational Spectroscopy of the Deprotonated Thymine Radical by Photodetachment and State-Selective Autodetachment Photoelectron Spectroscopy via Dipole-Bound States. *Chem. Sci.* **6**, 3129–3138 (2015).
10. D. L. Huang, **G. Z. Zhu**, and L. S. Wang. Communication: Observation of Dipole-Bound State and High-Resolution Photoelectron Imaging of Cold Acetate Anions. *J. Chem. Phys.* **142**, 091103 (2015).

Contributed Presentations

1. 256th ACS National Meeting. Aug. 19-23, 2018. Boston, MA. (Poster)
2. Gordon Research Conferences & Seminars. Vibrational Spectroscopy. Jul. 28 – Aug. 03, 2018. University of New England, Biddeford, ME. (Poster)
3. Gordon Research Conferences & Seminars. Molecular Interactions and Dynamics. Jul. 07–13, 2018. Stonehill College, Easton, MA. (Poster)
4. 20th Annual Northeast Student Chemistry Research Conference. Apr. 15, 2018. Northeastern University, Boston, MA. (Poster & 2-min elevator talk)
5. 2018 Conference on Cold and Controlled Molecules and Ions (CCMI). Mar. 25–29, 2018. University of Georgia, Athens, GA. (Poster)
6. Gordon Research Conferences & Seminars. Photoionization and Photodetachment. Feb. 17–23, 2018. Galveston, TX. (Poster & Talk)
7. IMNI 10th Anniversary Celebration and Poster Session. Sep. 29, 2017. Brown University, Providence, RI. (Poster)
8. 254th ACS National Meeting: Gaseous Ion Chemistry and Surface Reactions. Aug. 20–24, 2017. Washington, DC. (Talk)
9. Gordon Research Conferences & Seminars. Gaseous ions: structures, energetics & reactions. Feb. 11–17, 2017. Ventura, CA. (Poster)
10. 71st International Symposium on Molecular Spectroscopy. Mini-symposium: Spectroscopy in Traps. Jun. 20–24, 2016. University of Illinois at Champaign-Urbana, IL. (Talk)
11. 70th International Symposium on Molecular Spectroscopy. Jun. 22–26, 2015. University of Illinois at Champaign-Urbana, IL. (Talk)

Teaching Experiences

- Teaching Assistant, Chem 0330L Equilibrium, Rate and Structure Lab, Brown University 2014 (Fall), 2017 (Fall)
- Teaching Assistant, Chem 0350L Organic Chemistry Lab, Brown University 2014-2018 (Spring), 2016-2017 (Summer)
- Teaching Assistant, Chem 0360L Organic Chemistry Lab, Brown University 2016 (Fall)

To my mom

Acknowledgements

It has been five years and nine months since I came to Brown University to pursue my Ph.D. in August 2013. At the beginning, I would have never thought what I would experience and what my Ph.D. life would be. Only until now when it is almost done can I say that it has been really a period of learning and personal growth with about 65% ordinary time, 10% happiness, 5% excitement, 10% frustration, 5% anxiety and 5% fun. I would like to express my sincere gratitude to the wonderful people who have been part of my Ph. D. life.

First and foremost, I would like to thank my advisor, Prof. Lai-Sheng Wang, for giving me the opportunity to join the group in the first year when I knew nothing about spectroscopy. Everything would not be possible without his sterling guidance in doing experiments, troubleshooting instrumental problems, giving presentations, writing research papers, and more impressively, critical thinking about science. I have remembered the exciting moments when we discussed research and new results. I am also very grateful to have the opportunities to explore interesting ideas without restrictions from funding agency.

I would like to thank the Wang group. Many thanks to Daoling Huang, for teaching me to do experiments and grab the basic knowledge about the apparatus when I joined the group. Thanks to Chenhui Qian and Yuerou Zhang, the next masters of AP2, for taking up the torch and going for it. Thanks to Hongtao Liu, for offering timely suggestions when we had problem with the coldhead. Special thanks to Yuan Liu. He worked closely with me in the lab for a while and turned to do theory later. His theoretical supports were extraordinary. The discussions with him were always insightful

and enjoyable. Also, thanks to Ling Fung Cheung for his help in theoretical supports and relaxing lunch time. Thanks to Tian Jian for the encouraging discussions and suggestions all the time. Thanks to Joseph Czekner for being the long-lasting lab mate and super nice help in experiments. Thanks to Qianfan Zhang for synthesizing chemicals for my experiments. Thanks to Tengeng Chen, George Kocheril, Weijia Chen, Bin Bai and Hui Bai for many interesting talks and discussions.

I would like to thank Chen Fang, for his supportive syntheses of many compounds for my experiments, though most of the results were not striking. I want to thank our collaborators, Prof. Yasujiro Murata and Yoshifumi Hashikawa, for providing the fullerene samples, which turned out to have very interesting results. Thanks to Kenneth Talbot and Randy Goulet in the machine shop for making experiments easier with the tremendous supports. Thanks to Robert Wilson, Allen Sylvia, and Eric Friedfeld for continuing help with purchasing and shipping. Thanks to Al Tente for the electronic support and Rose Barreira for coordinating stuffs and arranging many letters.

Also, thanks to Prof. Gerald Diebold and Prof. Christoph Rose-Petruck for being my committee members and taking time to participate in ORP and final defenses. Special thanks to Prof. Gerald Diebold and Prof. Brenda Rubenstein for timely help of writing letters for me in a busy winter period.

I would also like to thank my friends. I was very grateful to Second Wang for being three-year roommate and for the countless fun walks in the nights of summer and in the mornings of winter. Thanks to Annan Wang, Bo Sheng and Gengqi Wang for sharing the happy time in the first year.

Last but not least, I want to thank my mom, dad and sister. Although they have no idea what I have been doing in the US for almost six years, they believe that I am going for something good. Of course, I would like to give my LAST thanks to the lovely Jasmine. Life has been becoming more colorful since I met with her.

April 2019

Table of Contents

Curriculum Vitae	iv
Acknowledgements	vii
Table of Contents	x
List of Tables	xiii
List of Figures	xv
Abstract	xvii
Chapter 1 Introduction	1
1.1 A brief history of anion photoelectron spectroscopy	4
1.2 The development of electrospray photoelectron spectroscopy in the Wang group	8
1.2.1 Coupling electrospray ionization with photoelectron spectroscopy	8
1.2.2 Incorporating the cryogenic ion trap into ESI-PES.....	11
1.2.3 High-resolution photoelectron imaging system	13
1.3 Multipole-bound states of anions	15
1.3.1 Dipole-bound state	16
1.3.2 Quadrupole-bound state	19
1.4 Experimental approaches to study multipole-bound states	20
1.4.1 Photodetachment spectroscopy	20
1.4.2 Resonant photoelectron spectroscopy via vibrational autodetachment of DBS	22
Chapter 2 Experimental methods	26
2.1 ESI source – Preparation of anions	27
2.2 Cryogenic Paul trap – Accumulation and cooling of anions.....	30
2.3 TOF-MS – Mass analyzing and selecting of anions	32
2.4 High-resolution photoelectron imaging system	34
2.5 Data processing.....	36
2.6 Timing sequences.....	36
Chapter 3 Accurate determination of the electron affinity of TCNQ	38
3.1 Introduction.....	39
3.2 Experimental methods	41
3.3 Results and discussion	41

3.4 Conclusions.....	45
3.5 Supporting information.....	47
Chapter 4 High-resolution photoelectron imaging of $C_{59}N^-$	48
4.1 Introduction.....	48
4.2 Experimental methods	50
4.3 Results and discussion	50
4.4 Conclusion	57
4.5 Supporting information.....	58
Chapter 5 Probing the intramolecular interactions in $H_2O@C_{60}^-$ and $H_2O@C_{59}N^-$	60
5.1 Introduction.....	60
5.2 Experimental methods	63
5.3 Results and discussion	63
5.3.1 The photoelectron images and spectra at 354.7 nm	63
5.2.2 The photoelectron images and spectra near detachment thresholds	65
5.2.3 The opposite shifts of the EAs: An electrostatic model.....	69
5.4 Conclusions.....	71
Chapter 6 Dipole-bound excited states and resonant photoelectron imaging of $C_6H_5O^-$ and $C_6H_5S^-$	72
6.1 Introduction.....	73
6.2 Experimental methods	75
6.3 Results.....	75
6.3.1 Non-resonant photoelectron spectra of $C_6H_5O^-$	75
6.3.2 Photodetachment spectrum of $C_6H_5O^-$	76
6.3.3 Resonant photoelectron spectra of $C_6H_5O^-$	80
6.3.4 Dipole-bound excited state and photodetachment spectrum of $C_6H_5S^-$	81
6.3.5 Resonant photoelectron images and spectra of $C_6H_5S^-$	84
6.4 Discussion.....	87
6.4.1 Non-resonant photoelectron spectra of $C_6H_5O^-$	87
6.4.2 Photodetachment spectra of $C_6H_5O^-$ and $C_6H_5S^-$	88
6.4.3 Resonant PES of $C_6H_5O^-$ via vibrational autodetachment from the DBS	91
6.4.4 Intramolecular inelastic rescattering in autodetachment from DBS of $C_6H_5O^-$	94
6.4.5 Resonant PES of $C_6H_5S^-$	96
6.4.6 Near-threshold resonances of $C_6H_5S^-$	97
6.4.7 Photoelectron angular distributions	98
6.4.8 Fundamental vibrational information resolved for C_6H_5O and C_6H_5S	100

6.5 Conclusions.....	102
6.6 Supporting information.....	103
Chapter 7 Tautomer-specific resonant photoelectron imaging of deprotonated cytosine anions	108
7.1 Introduction.....	108
7.2 Experimental methods	111
7.3 Results and discussion	111
7.4 Conclusions.....	118
7.5. Supporting information.....	119
Chapter 8 Observation of excited quadrupole-bound states in NC(C₆H₄)O⁻	127
8.1 Introduction.....	127
8.2 Experimental methods	128
8.3 Results and discussion	128
8.4 Conclusions.....	138
8.5 Supporting information.....	139
Bibliography	145
Abbreviations	168

List of Tables

Chapter 2 Experimental methods.....	26
Table 2.1. Preparations of solutions for ESI.....	29
Table 2.2. Pump configurations and pressures for TOF-MS vacuum chambers.....	32
Chapter 3 Accurate determination of the electron affinity of TCNQ	38
Table 3.1. Assignments of the observed vibrational peaks in the photoelectron spectrum of TCNQ ⁻	42
Table 3.2. Theoretical vibrational frequencies of neutral TCNQ.....	47
Chapter 4 High-resolution photoelectron imaging of C₅₉N⁻	48
Table 4.1. Assignments of observed vibrational peaks from the photoelectron spectra of C ₅₉ N ⁻	53
Table 4.2. Calculated harmonic frequencies for C ₅₉ N.....	59
Chapter 5 Probing the intramolecular interactions in H₂O@C₆₀⁻ and H₂O@C₅₉N⁻	60
Table 5.1. Observed vibrational peaks for H ₂ O@C ₆₀ ⁻ and H ₂ O@C ₅₉ N ⁻	67
Chapter 6 Dipole-bound excited states and resonant photoelectron imaging of C₆H₅O⁻ and C₆H₅S⁻	72
Table 6.1. Summary of the observed vibrational peaks from the photoelectron spectra of C ₆ H ₅ O ⁻	77
Table 6.2. Assignments of the observed resonances in the photodetachment spectrum of C ₆ H ₅ O ⁻	79
Table 6.3 Assignments of the observed resonances in the photodetachment spectrum of C ₆ H ₅ S ⁻	84
Table 6.4. Summary of the observed vibrational peaks in the photoelectron spectra of C ₆ H ₅ S ⁻	86
Table 6.5. Summary for all the observed fundamental vibrational frequencies of C ₆ H ₅ O and C ₆ H ₅ S.....	101
Table 6.6. Theoretical harmonic frequencies of C ₆ H ₅ O (X ² B ₁) and C ₆ H ₅ S (X ² B ₁).....	103
Table 6.7. The vibrational displacements and frequencies for selected fundamental modes of C ₆ H ₅ O (X ² B ₁ and A ² B ₂) and C ₆ H ₅ S (X ² B ₁).....	104
Chapter 7 Tautomer-specific resonant photoelectron imaging of deprotonated cytosine anions	108
Table 7.1. The optimized structures and relative energies of seven deprotonated cytosine anions.....	124
Table 7.2. The harmonic frequencies of six deprotonated cytosine radicals.....	125
Table 7.3. The summary of the observed peaks in the photodetachment spectrum.....	126
Table 7.4. Assignments of the observed vibrational peaks from the photoelectron spectra of [Cy-H] ⁻	126

Chapter 8 Observation of excited quadrupole-bound states in NC(C₆H₄)O⁻	127
Table 8.1. Assignments of the observed vibrational peaks from the photoelectron spectra of 4CP ⁻	140
Table 8.2. Assignments of observed QBS resonances in photodetachment spectrum of 4CP ⁻	141
Table 8.3. Experimental vibrational frequencies of 4CP, in comparison to theoretical harmonic frequencies.	142

List of Figures

Chapter 1 Introduction.....	1
Figure 1.1. Schematic diagram describing the principle of anion PES.	2
Figure 1.2. Schematic description of the electrospray ionization process.....	9
Figure 1.3. Schematic view of the first-generation ESI-PES apparatus.	10
Figure 1.4. Schematic view of velocity-map imaging.	14
Figure 1.5. Schematic view for the principle of photodetachment spectroscopy.	22
Figure 1.6. Principle of resonant PES via vibrational autodetachment of DBS of anion.	25
Chapter 2 Experimental methods.....	26
Figure 2.1. Schematics of the third-generation ESI-PES apparatus.	26
Figure 2.2. Schematics of the ESI source chamber	28
Figure 2.3. The assembly of the ion extraction electrodes.	33
Figure 2.4. Schematics of mass gate assembly.....	34
Figure 2.5. Schematics of the high-resolution photoelectron imaging system.	35
Figure 2.6. Timing sequences for the experiment.	37
Chapter 3 Accurate determination of the electron affinity of TCNQ	38
Figure 3.1. The molecular structure of TCNQ.	39
Figure 3.2. The photoelectron image and spectrum of TCNQ ⁻ at 354.7 nm.	41
Figure 3.3. Displacements for the three observed vibrational modes of TCNQ.	43
Figure 3.4. Schematic energy levels for TCNQ ⁻ and TCNQ.	44
Figure 3.5. Two-photon photoelectron spectrum of TCNQ ⁻ at 400.0 nm (3.100 eV).....	45
Chapter 4 High-resolution photoelectron imaging of C₅₉N⁻	48
Figure 4.1. The photoelectron image and spectrum of C ₅₉ N ⁻ and (C ₅₉ N) ₂ ²⁻ at 354.7 nm.	50
Figure 4.2. Photoelectron images and spectra of C ₅₉ N ⁻ at six different wavelengths	52
Figure 4.3. Differences of the total electron density ($\Delta\rho$) between anions and neutrals	56
Figure 4.4. The ν_{10} and ν_{15} vibrational modes of C ₅₉ N.....	58
Figure 4.5. Three different views of the HOMO of C ₅₉ N ⁻	58
Chapter 5 Probing the intramolecular interactions in H₂O@C₆₀⁻ and H₂O@C₅₉N⁻	60
Figure 5.1. Photoelectron images and spectra of fullerene anions at 354.7 nm	64
Figure 5.2. Comparisons of the photoelectron spectra of fullerene anions.	65
Figure 5.3. Photoelectron images and spectra of H ₂ O@C ₆₀ ⁻ and H ₂ O@C ₅₉ N ⁻	66
Figure 5.4. The electrostatic potential maps for the HOMO of fullerene anions.	69
Chapter 6 Dipole-bound excited states and resonant photoelectron imaging of C₆H₅O⁻ and C₆H₅S⁻	72
Figure 6.1. Non-resonant photoelectron spectra of C ₆ H ₅ O ⁻ at 480.60 nm and 354.7 nm.	76
Figure 6.2. The photodetachment spectrum of C ₆ H ₅ O ⁻	78
Figure 6.3. Resonant photoelectron images and spectra of C ₆ H ₅ O ⁻	80
Figure 6.4. Resonant photoelectron images and spectra of C ₆ H ₅ O ⁻ at three wavelengths	81
Figure 6.5. Photodetachment spectrum of C ₆ H ₅ S ⁻	82

Figure 6.6. Resonant photoelectron images and spectra of $C_6H_5S^-$ at twelve wavelengths. ...	85
Figure 6.7. Photoelectron images and spectra of $C_6H_5S^-$ at 503.55 nm and 501.84 nm.	86
Figure 6.8. Schematic energy level diagram for autodetachment from the DBS vibrational levels of $C_6H_5O^-$ to the neutral final states of C_6H_5O	90
Figure 6.9. Schematic energy level diagram for autodetachment from the DBS vibrational levels of $C_6H_5S^-$ to the neutral final states of C_6H_5S	91
Figure 6.10. Non-resonant images and spectra of $C_6H_5S^-$ at five different wavelengths.	105
Figure 6.11. Comparison of the non-resonant PE spectrum at 480.60 nm (Fig. 6.1) with the photodetachment spectrum (Fig. 6.2) for $C_6H_5O^-$	106
Figure 6.12. Comparison of the non-resonant photoelectron spectrum at 492.10 nm (Fig. 6.10) with the photodetachment spectrum (Fig. 6.5) for $C_6H_5S^-$	107
Figure 6.13. The HOMO orbitals of $C_6H_5O^-$ and $C_6H_5S^-$	107
Chapter 7 Tautomer-specific resonant photoelectron imaging of deprotonated cytosine anions	108
Figure 7.1. The top seven tautomers of deprotonated cytosine anions in the gas phase.	110
Figure 7.2. Non-resonant photoelectron images and spectra of $[Cy-H]^-$ at 354.7nm.....	111
Figure 7.3. The photodetachment spectrum of $[Cy-H]^-$	114
Figure 7.4. Photoelectron images and spectra of deprotonated cytosine anions	116
Figure 7.5. The top six tautomers of neutral cytosine in different conditions.	119
Figure 7.6. Possible deprotonation from the nitrogen sites of the six most stable neutral cytosines in aqueous solution.	120
Figure 7.7. Comparisons of the major vibrational progression in photoelectron spectrum at 354.7 nm to the Franck-Condon simulations of six higher energy tautomeric $[Cy-H]^-$ anions.....	121
Figure 7.8. Vibrational displacements and frequencies for the observed fundamental modes of the three deprotonated cytosine radicals.....	122
Figure 7.9. A schematic energy level diagram of deprotonated cytosine anions.	123
Chapter 8 Observation of excited quadrupole-bound states in $NC(C_6H_4)O^-$	127
Figure 8.1. Non-resonant photoelectron images and spectra of $4CP^-$ at different laser wavelengths.	129
Figure 8.2. Photodetachment spectrum of $4CP^-$	130
Figure 8.3. Resonant photoelectron images and spectra of $4CP^-$ at six different detachment wavelengths.	132
Figure 8.4. Resonant photoelectron images and spectra of $4CP^-$ at eleven different detachment wavelengths.....	133
Figure 8.5. A schematic energy level diagram for autodetachment from the QBS vibrational levels of $4CP^-$ to the neutral final states of $4CP$	139
Figure 8.6. Comparison of the non-resonant photoelectron spectrum at 385.57 nm with the photodetachment spectrum.	143
Figure 8.7. The calculated vibrational normal modes for neutral $4CP$ and their frequencies	144

Abstract of
High-Resolution Photoelectron Imaging of Cryogenically-Cooled Anions

by

Guo-Zhu Zhu

Ph.D., Brown University

May 2019

Photoelectron spectroscopy (PES) is a powerful technique to investigate the electronic structure and chemical bonding of gaseous anions and the corresponding neutrals upon electron detachment. The Wang lab first introduced electrospray ionization (ESI) to spectroscopy by developing a magnetic-bottle PES apparatus with an ESI ion source to study multiply-charged anions. The development of the third-generation ESI-PES apparatus at Brown by coupling a cryogenically-controlled Paul trap with high-resolution PE imaging has enabled accurate vibrational and electronic information to be obtained for singly charged anions produced by ESI and the neutral radicals. Here, the thesis work has focused on both non-resonant and resonant PES of cryogenically-cooled anions.

PES is usually done non-resonantly at the fixed laser wavelength. The first research project is to accurately measure the electron affinity (EA) of tetracyanoquinodimethane (TCNQ), an important organic electron acceptor, to be 3.383 ± 0.001 eV, which was erroneously reported in the literatures. High-resolution PES studies on fullerene-related anions, including $C_{59}N^-$, $H_2O@C_{60}^-$ and $H_2O@C_{59}N^-$, have yielded accurate EAs and vibrational structures for the corresponding neutral fullerenes. The

weak intramolecular interactions between the encapsulated water molecule and the cage anions in $\text{H}_2\text{O}@\text{C}_{60}^-$ and $\text{H}_2\text{O}@\text{C}_{59}\text{N}^-$ have also been probed.

Anions with dipolar neutral cores can have dipole-bound excited states (DBSs) just below the electron detachment threshold. Optical excitations to vibrational levels of DBS will induce vibrational autodetachment. DBSs of cryogenically-cooled phenoxide and thiophenoxide anions have been observed below the detachment thresholds. Vibrational autodetachments from the DBS levels in the resonant PES result in highly non-Franck-Condon photoelectron spectra, which have shown to be an effective method to obtain vibrational information of dipolar neutral radicals. In addition, DBSs of tautomeric deprotonated cytosine anions have been investigated, yielding tautomer-specific information in the resonant PES.

Molecule with vanishing dipole moment but large quadrupole moment can weakly bind an electron to form the quadrupole-bound anion. The first observation of excited quadrupole-bound state in the 4-cyanophenoxide anion, which shows similar autodetachment properties as DBS, will be discussed.

Chapter 1 Introduction

Negative ions, or anions, are atoms, molecules or clusters possessing net negative charges. The attention on gaseous anions was first drawn by Wildt in 1939 when he proposed the absorption of H^- to be the main source of solar opacity in the region of red and infrared wavelengths.¹ Since then, anions have been found to play important roles in a wide range of fields, such as ionic liquids,² anion- π interactions in supramolecular systems,³ radiation damage of DNA in biological environments,⁴ formation of atmospheric aerosols,⁵ the interstellar medium in astronomical environment⁶ and Titan's upper atmosphere as well as other planetary surroundings.⁶

One of the most powerful tools to study gaseous anions is photoelectron spectroscopy (PES), as schematically shown in Fig. 1.1. Briefly, a beam of mass-selected anions (M^-) is intersected with a laser beam. When the laser photon energy ($h\nu$) exceeds the binding energy (BE) of the electron in the anion, photoelectrons (e^-) can be ejected with various kinetic energies (KEs) depending on the resulting final neutral states (M). Since the energy applied to the system must be conserved, BE of the electrons can be readily determined as:

$$\text{BE} = h\nu - \text{KE},$$

where the photon energy $h\nu$ is known and the photoelectron KE is measured experimentally. The electron BE is usually used to plot the photoelectron spectrum as BE is independent on the laser photon energy used in the experiment. The intensities of the peaks in the spectrum follow the Franck-Condon principle,⁹ which means that the intensity of a vibronic transition is proportional to the square of the overlap integral

between the respective vibrational wavefunctions of the two electronic states involved in the transition.

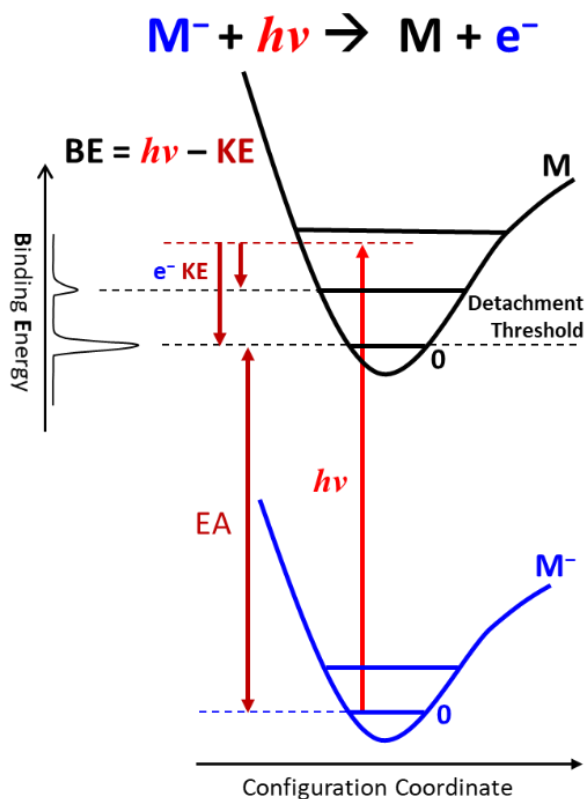


Figure 1.1. Schematic diagram describing the principle of anion PES.

PES can yield rich information about the anions and the corresponding neutrals. Directly, we can readily determine the electron affinity (EA) of the underlying neutral,⁹ i.e., detachment threshold of the anion, from the lowest-binding-energy peak in the spectrum, which represents the 0-0 detachment transition from the ground vibrational state of the anion to the ground vibrational state of the neutral (Fig. 1.1). Under high energy resolution, both vibrational and electronic information of the neutral can be obtained. Anion PES has been extensively utilized to probe the electronic structure of inorganic complexes,¹⁰ chemical bonding and structures of clusters,^{11,12} stepwise

solvation of anions to bulk limits,¹³ transition-state dynamics of bimolecular reactions^{12,14} and so on.

For my thesis work, anion PES, which was developed to the high-resolution photoelectron imaging apparatus¹⁵ in the Wang group (Chapter 2), has been applied to accurately determine the EA and vibrational structures of tetracyanoquinodimethane (Chapter 3), which is an important organic electron acceptor, and fullerene-related molecules, including $C_{59}N$ (Chapter 4), $H_2O@C_{60}$ and $H_2O@C_{59}N$ (Chapter 5). The intramolecular interactions between water molecules and the fullerene cage anions have been probed. In addition, I have studied the exotic excited states of various anions, such as the dipole-bound states of $C_6H_5O^-$ and $C_6H_5S^-$ (Chapter 6), deprotonated cytosine anions (Chapter 7) and quadrupole-bound states of $NC(C_6H_4)O^-$ (Chapter 8). It is found that dipole-bound states of deprotonated cytosine anions can be used to obtain the tautomer-specific information (Chapter 7).

The first chapter is organized as follows. In Section 1.1, a brief history of anion PES, which has spanned more than half a century, will be introduced. Section 1.2 will describe the instrumental developments in the Wang group, involving the combination of PES with electrospray ionization, cryogenic Paul trap and high-resolution photoelectron imaging. The historical studies of multipole-bound states, including dipole-bound state and quadrupole-bound state, will be discussed in Section 1.3. Lastly, Section 1.4 will discuss two experimental methods, photodetachment spectroscopy and resonant PES via vibrational autodetachment that we have developed to study multipole-bound states.

1.1 A brief history of anion photoelectron spectroscopy

PES is built on the photoelectric effect, which was first observed by Hertz in 1887¹⁶ and understood by Einstein in 1905.¹⁷ Fifty years later, Siegbahn and coworkers¹⁸ first developed the X-ray PES (XPS), which used X-ray photons to eject core electrons from atoms for chemical analyses of solids. In the early 1960s, Vilesov et al.¹⁹ and Turner et al.²⁰ independently utilized vacuum ultraviolet radiations, possessing much lower photon energies than X-ray, to study gaseous neutral molecules, which is well known as UPS. Several years later, Hall and coworkers reported the first anion PES experiment on He^- and measured the EA of an excited helium atom.²¹ In their experiment, continuous-wave (cw) argon ion monochromatic laser was used to photodetach He^- produced by a continuous ion source, while the resulting photoelectrons were detected by a hemispherical electron analyzer. And the technique of anion PES was quickly extended to study diatomic anions,^{22,23} alkali-metal anions,²⁴ small molecular anions,²⁵ negative cluster ions,²⁶ and transient species²⁷ by the groups of Hall, Lineberger, Ellison, Bowen, etc.

With the development of pulsed ion sources in the 1980s,^{28,29} the Johnson group reported the first pulsed PES experiment on anions of O^- , O_2^- and O_4^- in 1986.³⁰ The mass-selected anions prepared by electron impact ionization of a pulsed supersonic jet was photodetached by a pulsed Nd:YAG laser with the photoelectrons analyzed by a field-free time-of-flight (TOF) electron energy analyzer. Soon after, Smalley et al.^{31,32} and Ganteför et al.^{33,34} studied the metal and semiconductor cluster anions prepared from a pulsed supersonic beam coupled to a laser vaporization set-up. An excimer laser (6.4 eV) was used in photodetachment for the first time,^{31,32} allowing the investigations of the

valence states of metallic and semiconductor clusters possessing high BEs. A magnetic bottle TOF system^{34,35} was developed to detect the photoelectron with high efficiency. The Smalley's set-up³⁵ has been further developed by the Wang group³⁶ to study the chemical bonding and structures of metallic,^{36,37} oxides,^{38,39} carbides^{40,41} and boron-related clusters.^{11,42} The pulsed experiments have allowed the investigation of a variety of anionic species prepared by pulsed ion sources and enabled the utilization of pulsed laser with shorter wavelength for photodetachment. For example, the ninth harmonic of a Nd:YAG laser at 118.2 nm (10.488 eV) was reported recently by the Wang group⁴³ to study the superhalogen anions, which have detachment thresholds about 7 eV.

One of the major concerns of anion PES is the energy resolution of the photoelectron KE. The early cw experiments used the hemispherical electron analyzer could achieve a KE resolution of 5-8 meV for molecular anions.²⁷ The field-free and magnetic bottle TOF analyzer were mainly used in the pulsed experiments. The resolution that the field-free TOF could achieve was 5-8 meV with a lower collection efficiency.⁴⁴ The magnetic bottle system showed a good collection efficiency but suffered from severe Doppler broadening effect, yielding a KE resolution as good as 6 meV.⁴⁵

A more recently developed technique to improve the photoelectron energy resolution is velocity-map imaging (VMI). The technique was based on the ion imaging method originally used in the photodissociation experiment by Chandler and Houston in 1987.⁴⁶ The low resolution and distortion of the imaging was highly improved when Eppink and Parker developed the VMI in 1997.⁴⁷ It was introduced to photoelectron imaging of anions by Bordas et al.⁴⁸ and Sanov et al.⁴⁹ in the early 2000s. It was found that VMI was suitable for the detection of slow and fast photoelectrons simultaneously.⁵⁰

Impressive experimental accuracy of 0.06 meV (0.5 cm^{-1}) has been achieved very recently for the EA measurement of the Nb atom by the Ning group.⁵¹

Besides the instrumental development to achieve better performances of anion PES, a different spectroscopy, anion zero electron kinetic energy (ZEKE),⁵² was also developed to improve the resolution. ZEKE experiments were originally built to study neutral molecules by Müller-Dethlefs and Schlag.^{53,54} In ZEKE, a tunable pulsed laser is scanned across the detachment threshold, and the photoelectrons with nearly zero kinetic energies are selectively detected, yielding a very high energy resolution. The Neumark group adapted ZEKE to study anions and achieved an energy resolution as high as 1 cm^{-1} for atomic anions and $8\text{-}10 \text{ cm}^{-1}$ for molecular anions due to the rotational broadening.^{52,55,56} However, due to the experimental difficulties⁵² that near-zero energy photoelectrons are quite sensitive to stray electric and magnetic fields and requirement of s-wave detachment based on Wigner threshold law,⁵⁷ the high-resolution anion ZEKE were limited to a small fractions of anions, such as the anionic clusters⁵⁸ and anion-neutral complexes.⁵⁹

To overcome the issues of anion ZEKE, the VMI and anion ZEKE techniques were combined as slow photoelectron velocity-map imaging (SEVI) by the Neumark group.^{12,52} Simply, a tunable laser at several fixed wavelengths is used to photodetach the anion near the threshold of each detachment transition. The resulting slow photoelectrons are analyzed by VMI at low extraction voltages to achieve high resolutions. A series of high-resolution images obtained at various wavelengths are combined to yield the photoelectron spectrum with sub-meV energy resolution. Based on various VMI systems, the Neumark group achieved a resolution of 1.5 cm^{-1} for photodetachment of Cl^- ,⁵² while

the high-resolution imaging system in the Wang group (Section 1.2.3) recently obtained a 1.2 cm^{-1} resolution for near threshold electrons detached from Bi^- .⁶⁰ The best resolution was reported by the Ning group to be just 1 cm^{-1} for Nb^- .⁵¹ The developments of SEVI and high-resolution imaging techniques have achieved very impressive energy resolutions for atomic anions. However, the energy resolutions of molecular anions or anionic clusters are not as good as those in atomic anions due to the substantial internal energy of the anions even at room temperature, which can cause vibrational hot bands and rotational broadening for the spectrum. Therefore, it would be critical to cool down the anions to achieve a better resolution for molecular or cluster anions.

In 2005, the Wang group reported the first anion PES experiment for cold anions,⁶¹ which were cooled down via collisions with a buffer gas in a cryogenic Paul trap (Section 1.2.2).⁶² Vibrational hot bands were completely eliminated in the spectrum of C_{60}^- .⁶³ Very recently, the Neumark incorporated a cryogenic octupole ion trap into SEVI to develop cryo-SEVI⁶⁴ and achieved a resolution of $2\text{-}3 \text{ cm}^{-1}$ for deprotonated anthracene anions.⁶⁵ A similar combination of cryogenic ion trap with high-resolution imaging system has been developed in several groups, including the von Issendorff,⁶⁶ Ning⁶⁷ and Garand.⁶⁸

After more than fifty years of development of anion PES since 1967, the combination of high-resolution imaging system in detecting slow electrons based on SEVI and cryogenic ion trap to cool down the anions has been proven to be a huge success for excellent performance and extensive applicability. With the high-resolution photoelectron detection and preparation of cold anions, the anion PES has been widely applied to study weakly bound excited states of anions,¹⁵ structures of large polycyclic

aromatic hydrocarbons,^{12,69} anionic clusters^{12,66,67} and transient species in bimolecular reactions.¹²

1.2 The development of electrospray photoelectron spectroscopy in the Wang group

The Wang group have pioneered the study of solution anions in the gas phase by electrospray ionization and PES since 1998. The first-generation ESI-PES allowed the first spectroscopic studies of multiply-charged anions from solution samples (Section 1.2.1). Later, they introduced the cryogenic Paul trap to cool down anions using a closed cycle helium refrigerator for the first time (Section 1.2.2). The vibrational hot band was completely eliminated, and the spectra were much better resolved. Very recently, a multi-lens high-resolution photoelectron imaging system has been developed in the third-generation apparatus, showing an energy resolution as good as 1.2 cm^{-1} (Section 1.2.3). The coupling of the cryogenic Paul trap and high-resolution imaging has allowed the study of exotic excited states of anions, including dipole-bound states and quadrupole-bound states, which have very low electron binding energies as small as 20 cm^{-1} . More details are described as follow.

1.2.1 Coupling electrospray ionization with photoelectron spectroscopy

Electrospray ionization (ESI) is a soft ionization method, allowing ions prepared in the solution phase to be isolated into the gas phase.⁷⁰ As schematically shown in Fig. 1.2, the sample solution is loaded into the syringe of which the capillary tip is applied with a high voltage (several kV). The large charged droplets sprayed out in the electrospray process then enter into the heated desolvation capillary. With the removal of solvent molecules, the Coulomb repulsions between the ions in the droplets cause the

large droplets breaking up into small droplets, eventually forming isolated ions or solvated ionic clusters in the gas phase.

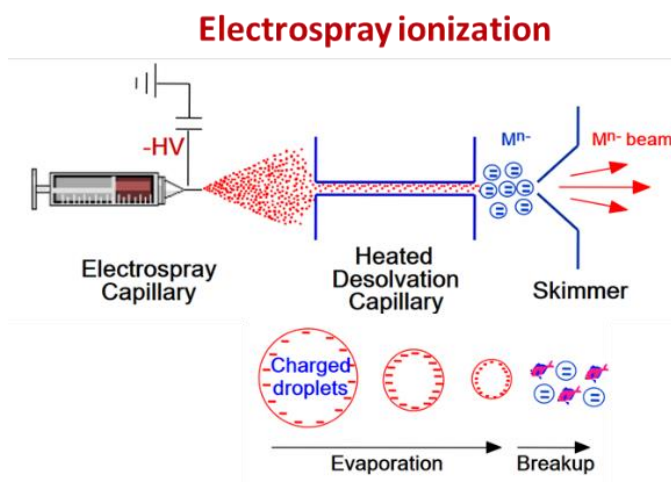


Figure 1.2. Schematic description of the electrospray ionization process.

The original idea of the method could date back to 1968 when Dole et al. tried to electrospray a solution of polystyrene molecules to generate a beam of macromolecules or macroions.⁷¹ Fifteen years later, Fenn fully developed ESI into a soft ionization method for biological molecules, that eventually won him a Nobel Prize in 2002.^{72,73} They even suggested that ESI might be useful to produce ions for various spectroscopic studies in the original report.⁷²

The application of ESI as ion source for spectroscopic studies was first developed by the Wang group in 1998.^{74,75} They successfully coupled the ESI with anion PES in their first-generation ESI-PES apparatus,⁷⁶ as presented in Fig. 1.3. Basically, the anions produced from the ESI were guided into a room-temperature Paul trap. After accumulation of 0.1 s, the ions were pulsed out into the extraction zone of a TOF mass spectrometer at a repetition rate of 10 Hz. The mass-selected anions were intersected by a

pulse laser for photodetachment. The magnetic-bottle electron analyzer was used to collect the photoelectrons with an energy resolution of about 2% ($\Delta KE/KE$).

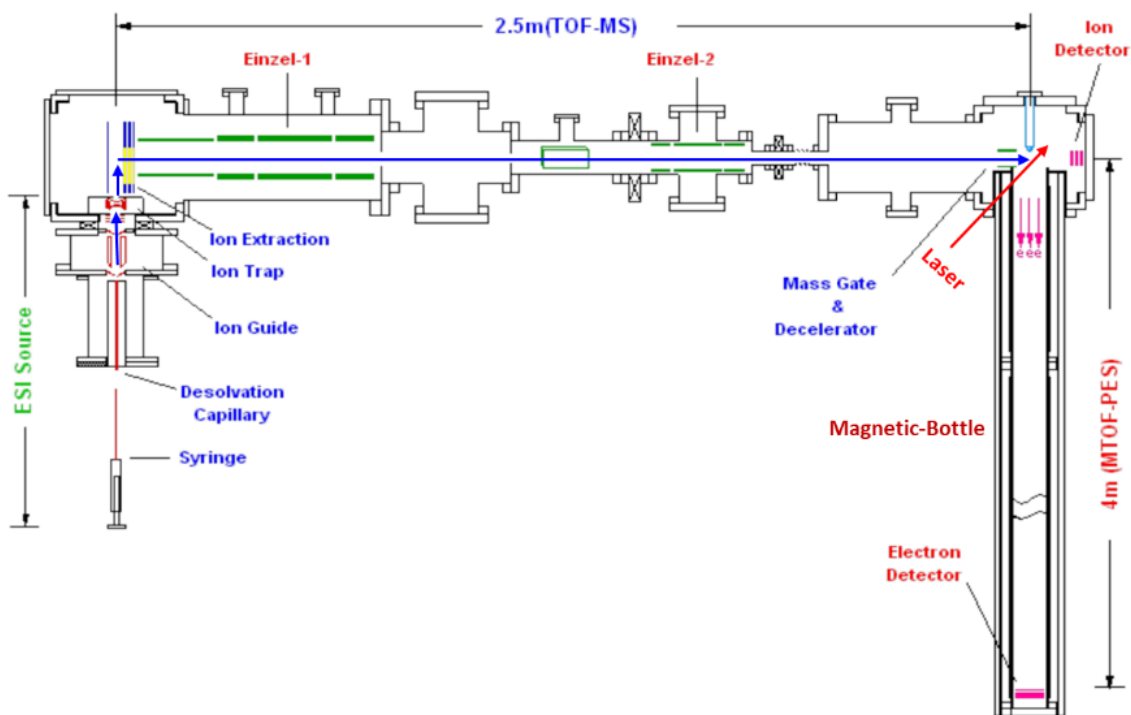


Figure 1.3. Schematic view of the first-generation ESI-PES apparatus. The blue arrows indicate the trajectory of the ion beam produced by ESI. Reproduced from [L. S. Wang, C. F. Ding, X. B. Wang, and S. E. Barlow, Photodetachment photoelectron spectroscopy of multiply charged anions using electrospray ionization. *Rev. Sci. Instrum.* **70**, 1957 (1999).], with the permission of AIP Publishing.

The combination enabled the spectroscopic study of multiply charged anions (MCAs) and the first direct observation of the repulsive Coulomb barrier,^{74,75} which is due to the short-range attraction by the nuclei and long-range repulsion from the negatively charged residual ion when an electron is detached from MCAs. MCAs with negative electron binding energies were even observed.⁷⁷ In addition, the stepwise solvations of various inorganic anions and the electronic structures of a number of inorganic clusters and coordination complexes were studied by anion PES with the

convenient preparation of the corresponding anions in the gas phase.^{10,78} The introduction of ESI to anion PES has been proven to be a general and powerful technique to study the solution phase species and chemistry in the gas phase.

Besides, ESI has been used to produce deprotonated protein chromophores for time-resolved PES studies by the Fielding group.⁷⁹ It has also been used to prepare protonated peptides or larger biomolecules for studies of various vibrational spectroscopies by the groups of Rizzo,⁸⁰ Johnson⁸¹ and Garand.⁸²

1.2.2 Incorporating the cryogenic ion trap into ESI-PES

Most of the species studied by the first-generation ESI-PES were MCAs, large molecular anions, anionic complexes and clusters, which could carry considerable internal energies at room temperature. As a result, rotational broadening and vibrational hot bands, which are due to photodetachment from rotationally and vibrationally excited anions, can cause the congestion of the spectra, limiting the spectral resolution and accuracy. Also, the temperature-dependent information from different conformations of molecules or isomers of weakly bound complexes and clusters may be easily averaged out when the ions are hot. Therefore, it is critical to cool down and control the temperatures of ions in order to improve the power of anion PES.

A number of methods, such as supersonic expansion,⁸³ helium nanodroplet^{84,85} and argon tagging,^{86,87} have been used to prepare cold molecules and ions. However, none of the methods could control the temperature precisely and be compatible with PES. A suitable cooling method with temperature tuning capability would be cryogenic ion cooling in a trap, which was first demonstrated by Gerlich and coworkers using a 22-pole trap.^{88,89} They successfully cooled down molecular ions to cryogenic temperature via

collisions with helium buffer gas in a radio-frequency (rf) 22-pole ion trap, which was attached to a helium refrigerator. The thermalized collision processes, which removed the thermal energy of the ions confined in the trap, could be well controlled by tuning the temperature of the attached cold head and the pressure of the loading buffer gas. Due to the flat trapping potential of the 22-pole trap minimizing the rf heating, it showed an excellent cooling capability for ions, which was subsequently applied to numerous studies in ion-molecule reactions and molecular ions spectroscopy.^{80,90-92} However, the flatness of the potential also caused deficient axial confinement of the ions, making it unsuitable for the ESI-PES experiments running at a low-repetition rate of 10 Hz.⁶²

In the late 2004, the Wang group first developed the temperature-controlled (10 – 350 K) 3D Paul trap for the second-generation ESI-PES apparatus.⁶² The Paul trap, with good axial and radial confinements of ions, was demonstrated to be quite suitable to extract ions for subsequent TOF mass analyses. And the anions were cooled by collision with buffer gas of 0.1 – 1 mTorr He/H₂ (4/1) for temperatures below 70 K or N₂ for temperatures above 70 K. The cooling effect on the ions was substantial. When the temperature decreased from 300 K to 70 K, the photoelectron spectra of both small anion ClO₂⁻ and large anion C₆₀⁻ showed better resolved peaks and complete elimination of vibrational hot bands, which usually cause the spectral congestions and inaccurate measurement of EA. Additionally, the temperature-dependent experiments of monocarboxylate anions CH₃CH₂nCO₂⁻ (n = 0-8) observed the weak C-H ... O hydrogen bonding for alkanes and conformational changes from linear to cyclic geometries.⁶¹

While the original set-up of cryogenic Paul trap built at Pacific Northwest National Laboratory has continued to show interesting observations,^{83,94} the Wang group has developed a new cold ion trap equipped with pulsed buffer gas and a more powerful cold head in the third-generation apparatus when moved to Brown University.¹⁵ When running experiment around 4.5 K, the ion temperature in the new trap has been determined to be 30 – 35 K from simulations of rotational profiles in the photodetachment spectra of several anions.⁹⁵⁻⁹⁷

Furthermore, a similar 3D quadrupole ion trap has recently been developed in the Garand group for anion SEVI experiment of polycyclic aromatic hydrocarbons.^{68,69} The powerfulness of cryogenic Paul trap has also been adapted by several groups to study cold ions and ionic clusters by vibrational or UV-UV spectroscopy.^{81,82,98-101}

1.2.3 High-resolution photoelectron imaging system

As the anions were cooled down to low temperature without hot bands, the performance of the second-generation ESI-PES was mainly limited by the low resolution of the photoelectron KE analyzer. The magnetic-bottle electron analyzer was used in the second-generation apparatus. It had an electron energy resolution of 2% ($\Delta KE/KE$),⁶² which severely limited the benefits from cold anions. Very recently, the Wang group incorporated the high-resolution imaging system in the third-generation equipment.¹⁵

The particle imaging technique¹⁰² was initially inspired from Solomon et al.¹⁰³ who attempted to visualize the photodissociation products in 1969 and from Yates et al.¹⁰⁴ who imaged the ion desorptions from electron stimulations on surfaces in 1974. In 1987, Chandler and Houston⁴⁶ first developed the ion imaging technique and obtained a two-dimensional image for the photodissociation products of CH_3I , showing both spatial

and angular distributions. The imaging technique was soon applied to study more photodissociations^{105,106} and bimolecular reactions.¹⁰⁷ However, the images suffered considerable distortions and low resolution. The big improvement came in 1997 when Eppink and Parker⁴⁷ developed velocity-map imaging (VMI) by using a simple three-plate electrostatic design (Fig. 1.4) with open electrodes instead of conventional grid electrodes. Due to the curved electric fields in VMI, particles with same initial velocity vectors but different initial spatial positions can be mapped onto the same point on the detector (Fig. 1. 4), greatly enhancing the energy resolution. Since then, it has been widely used in various experiments, such as photodissociation^{108,109} and reaction dynamics.^{110,111} In the early 2000s, Bordas et al.⁴⁸ and Sanov et al.⁴⁹ introduced VMI to PES experiments of cluster anions and yielded nice photoelectron images, which were previously obtained by Helm et al.¹¹² for multiphoton ionization of xenon atom with regular imaging technique. Both KE and angular distributions of photoelectrons could be obtained.¹¹³ And it was found that both slow and fast photoelectrons could be observed.⁵⁰ The ability to detect low-energy electrons and angular distributions makes VMI a popular method for high-resolution PES of anions. And SEVI developed by the Neumark group^{12,52} has achieved a high resolution of 1.5 cm^{-1} .

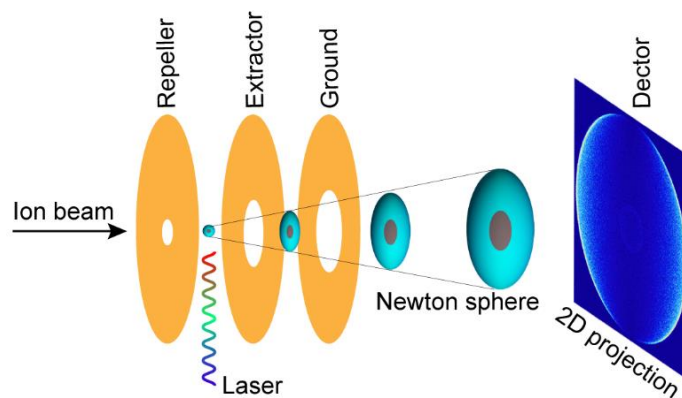


Figure 1.4. Schematic view of velocity-map imaging.

The initial VMI system in the Wang group was constructed based on the three-plate VMI from Eppink and Parker.⁴⁷ And it was used to image the intramolecular Coulomb repulsions of various MCAs produced by ESI, showing strong anisotropies in the photoelectron angular distributions.^{114,115} To study the anionic clusters with higher resolution, a multi-lens high-resolution VMI system was built in 2013.⁶⁰ The new VMI system could achieve energy resolution of 1.2 cm^{-1} for slow electrons while maintaining good resolution ($\Delta KE/KE \sim 0.53 \%$) for high KE electrons. The high-resolution photoelectron imaging system was then combined with the ESI-PES in the third-generation apparatus.¹⁵

The third-generation ESI-PES apparatus, equipped with the cryogenic Paul trap and high-resolution photoelectron imaging, was able to yield the most accurate EA of C_{60} measured to date as $2.6835 (6) \text{ eV}$.¹¹⁶ It has allowed the study of weakly bound states of anions, including both dipole-bound^{12,95,117-122} and quadrupole-bound excited states.⁹⁷

1.3 Multipole-bound states of anions

Electrons in neutrals and cations can experience net Coulomb attractions as $-ne^2/r$ ($n = 1$ for a neutral and 2 for a singly charged cation.) at large r distance, which gives rise to a series of bound electronic states.¹²³ In contrast, the excess electron in anion (singly-charged) has no net Coulomb attraction in the asymptotic regions. Instead, the electron experiences a long-range attractive potential with the neutral core expressed as:

$$V(r) = -\mu e \cos\theta/r^2 - eQ \cdot (3\mathbf{r}\mathbf{r} - r^2\mathbf{1})/3r^5 - \alpha \cdot \mathbf{r}\mathbf{r} e^2/2r^6,$$

where r is the distance between the electron and the molecule, θ is the angle between the molecule's dipole vector and the electron's position vector \mathbf{r} , μ is the electric dipole

moment. Q is the quadrupole tensor of the molecule and $\mathbf{1}$ is the unit tensor. α is the polarizability tensor of the molecule.¹²³ When the charge-dipole potential is dominating, the anion can be viewed as a dipole-bound anion, which can support dipole-bound state. Similarly, quadrupole-bound state and polarization (or correlation)-bound state can exist for anions of which the corresponding interactions are dominant.¹²³⁻¹²⁵

1.3.1 Dipole-bound state

When a neutral molecule possesses a large dipole moment ($\mu > \approx 2.5$ D), it can bind an excess electron by the long-range charge-dipole attraction scaled as $1/r^2$ with a BE on the order of a few to few hundreds meV.¹¹⁴⁻¹¹⁶ The resulting anion can support a dipole-bound state (DBS) with a diffuse orbital, which is analogous to Rydberg state in a neutral atom or molecule. This makes it an excellent many-body system to study quantum halo states¹²⁶ and electron-molecule interactions, such as vibronic coupling¹²⁷ and low-energy electron rescattering.¹²¹ DBS has also been proposed as the “doorway” to the formation of stable valence-bound anions,¹²⁸⁻¹³⁰ especially for those formed in the reductive DNA damage process by low-energy electrons attachment¹³¹ and those in the interstellar medium under astronomical environments.^{6,132,133}

In 1947, Fermi and Teller¹³⁴ first predicted a minimum dipole moment of 1.625 D (or $0.639 ea_0$, where e is the charge of the electron and a_0 is the Bohr radius) for a point dipole to bind an electron when studying the capture of negative mesotrons in matter. Interestingly, only one sentence, “*In the special case of mesotron capture by the hydrogen atom, it is found that when the mesotron approaches the nucleus to a distance of 0.639 Bohr radii, the binding energy of the electron becomes zero.*”, was described in the whole paper about the critical value without any derivation or interpretation. In 1950,

Wightman¹³⁵ obtained the same value by solving the Schrödinger equation describing the motion of a single electron in the presence of a charge-dipole potential. In the 1966-1967, several theoretical groups¹³⁶⁻¹³⁹ derived a similar value of minimum dipole moment for point or finite dipole to bind an electron, seemingly unaware of the earlier work. Later in 1976, Turner¹⁴⁰ wrote an interesting article detailing the history of earlier theoretical studies about the minimum dipole moment for electron binding and the numerical solution found in Fermi's notebook.

In the early 1970s, Crawford and Garrett¹⁴¹⁻¹⁴⁴ extended the calculations to include the effects of rotation, moment of inertia and dipole length on the minimum dipole moment to bind an electron and increased the value up to 2.0 D. A more practical estimate of 2.5 D was later suggested from extensive experimental observations.^{124,145,146} Later on, several groups,¹⁴⁷⁻¹⁵⁹ mainly including Adamowicz, Gutowski, Jordan, Simon, Skurski and Sommerfeld, used or developed various theoretical methods to study the electron binding energies in the dipole-bound anions of molecules and clusters, and to investigate the electronic structure as well as dispersion contributions in the electron-molecule interactions in DBS.

In addition, molecules with even larger dipole moments may possess more than one bound DBS. Early studies of a fixed dipolar system concluded that 9.64 D is required for the second DBS.^{160,161} Considering the rotational effects, Garrett predicted a critical dipole moment of 4.5 D for the second DBS.^{162,163} Very recently, the Wang group¹⁶⁴ attempted to search for a second DBS for deprotonated 2-hydroxypyrimidine anion, which has a calculated dipolar neutral core of 6.2 D. Although a large binding energy of

598 cm^{-1} was observed for ground DBS, no evidence of a second DBS was indicated below the detachment threshold. So far, higher DBS has not been observed yet.

Experimentally, the dipole-bound electron was first suggested by Wong and Schulz in 1974.¹⁶⁵ In their low-energy electron scattering experiment, the sharp structure near the threshold of excited state of CO (1.38 D) was attributed to dipole-dominated resonances. However, the small dipole moment was not able to bind the electron from theoretical perspectives. The direct evidence for DBS came from photodetachment experiments by Brauman and coworkers,^{166,167} who attributed the observed sharp resonances in the photodetachment cross section of enolate anions to dipole-supported excited states. Subsequently, Lineberger and coworkers carried out high-resolution photodetachment spectroscopy for a series of anions and observed rotational autodetachments via short-lived DBSs.¹⁶⁸⁻¹⁷²

Besides the studies of excited DBS, the other major experimental studies are about ground state dipole-bound anions (DBAs).¹⁴⁶ which were formed by Rydberg electron transfer (RET)^{173,174} or electron attachment to dipolar molecules or clusters. RET has been widely used by groups of Compton,^{124,129,175,176} Schermann,^{129,145,146,177} Bowen¹⁷⁸⁻¹⁸⁰ and Dunning^{181,182} to produce a variety of DBAs, which could be detached by electric field. Several DBAs of solvated clusters were prepared by free-electron attachment¹⁸³⁻¹⁸⁵ and studied by PES.^{178-180,183-185} In addition, Johnson et al.¹⁸⁶ reported the preparation for CH_3CN^- DBA by photodissociation of $\Gamma \cdot \text{CH}_3\text{CN}$ ion-molecule complex. Neumark et al. conducted time-resolved PES for anionic complexes of $\Gamma \cdot \text{CH}_3\text{NO}_2$ ¹⁸⁷ and $\Gamma \cdot \text{adenine}$.¹⁸⁸ They found the DBAs of CH_3NO_2 and adenine were

produced by electron transfer from Γ^- and showed the transition from DBAs to valence-bound anions.

Very recently, the Wang group first reported the resonant PES via vibrational autodetachment from DBS of $\text{C}_6\text{H}_5\text{O}^-$.¹¹⁷ The ground DBS of $\text{C}_6\text{H}_5\text{O}^-$ was found to be 97 cm^{-1} below the detachment threshold. The small binding energy of the DBS confirmed the weakly-bound nature and its fragility, which was able to be probed because of the preparation of cold $\text{C}_6\text{H}_5\text{O}^-$ anions in the cryogenic Paul trap and high-resolution photoelectron imaging analyzer equipped in the third-generation ESI-PES.¹⁵ More interestingly, mode-specific autodetachment from eight vibrational levels of the DBS was observed, yielding highly non-Franck-Condon resonant photoelectron spectra, due to the $\Delta v = -1$ vibrational propensity rule.^{189,190} Subsequently, more anions were found to support excited DBS below the anion photodetachment threshold^{95, 118-122,164} and the resonant PES obtained from vibrational autodetachment via DBS has resolved abundant vibrational features, especially for the low-frequency and Franck-Condon-inactive vibrational modes as well as conformation-selective information. In addition, the groups of Mabbs¹⁹¹ and Heaven^{192,193} have reported vibrational autodetachments from DBS resonances of diatomic anions.

1.3.2 Quadrupole-bound state

With vanishing dipole moments, but strong quadrupole moments, neutral molecules can form quadrupole-bound anions, in which the long-range charge-quadrupole attractive potential ($\sim 1/r^3$) dominates.^{123,124,194,195} Jordan and Liebman first suggested the rhombic $(\text{BeO})_2^-$ cluster as a quadrupole-bound anion.¹⁹⁶ This cluster and the similar $(\text{MgO})_2^-$ cluster studied by PES¹⁹⁷ have relatively high electron binding

energies and should probably be considered as valence-bound anions.¹²³ In addition, the rhombic alkali-halide dimers, such as $(\text{KCl})_2^-$ and $(\text{NaCl})_2^-$, and a series of complex organic molecules with vanishing dipole moments but large quadrupole moments have also been proposed to form quadrupole-bound anions.¹⁹⁸⁻²⁰⁰ Experimental studies of electron binding to quadrupolar molecules have been scarce. The CS_2^- anion was first observed via RET and was suggested to be a possible quadrupole-bound anion.^{201,202} The formamide dimer and the *para*-dinitrobenzene anions formed via RET were also suggested to be quadrupole-bound anions.^{203,204} A more conclusive example of a quadrupole-bound anion was from RET to the *trans*-succinonitrile.^{205,206} A valence-bound anion with a non-polar core may possess excited quadrupole-bound state (QBS) just below the electron detachment threshold, if the neutral core possesses a large quadrupole moment. However, such an excited QBS was not observed until 2017 when we reported the first observation of excited QBS,⁹⁷ which will be presented in Chapter 8.

1.4 Experimental approaches to study multipole-bound states

A significant part of this thesis concerns the studies of DBS and QBS of anions (Chapter 6-8). We have used two experimental approaches, photodetachment spectroscopy and resonant PES via vibrational autodetachment of DBS or QBS, which will be briefly described here.

1.4.1 Photodetachment spectroscopy

Photodetachment spectroscopy (PDS) is a method to study the photon energy dependences of photodetachment cross sections of anions. Photodetachment experiment was first done by Branscomb and coworkers^{207,208} for H^- and D^- using conventional

tungsten lamp as the light source. With the development of tunable dye laser in the late 1960s,^{209,210} Lineberger and Woodward²¹¹ applied it to photodetachment of the sulfur anion and obtained a very accurate EA for the sulfur atom. Later, the photodetachment experiment on the dipolar enolate anion done by Brauman and coworkers led to the first observation of resonances due to an excited DBS.^{166,167} Recently, PDS has been largely used to search for DBS or QBS resonances^{95,117-122,164,191-193} and accurately measure detachment thresholds of anions.^{212,213}

In our experiments, we have used PDS to search for DBS and QBS resonances, as schematically shown in Fig.1.5. If the anion (M^-) has a dipolar neutral core ($\mu > \approx 2.5$ D), it can support a DBS (M^-*_{DBS}) below the detachment threshold with a small binding energy of 1-100 meV. A tunable dye laser is used to scan across the detachment threshold of M^- while monitoring the photoelectron yield. When the laser wavelengths match with the DBS resonances, the corresponding electron yield is spiked as a sharp peak in the photodetachment spectrum. While the peak below the threshold is the ground vibrational level of the DBS due to resonant two-photon detachment, the peaks above the detachment threshold are excited vibrational levels of the DBS, which undergo vibrational autodetachment. The gradually increasing cross section of the baseline above the threshold is from regular non-resonant detachment process.

resonances in the photodetachment experiments of alkali atomic anions,²¹⁴ followed with sodium halide negative ions²¹⁵ and C_2^- .²¹⁶ The rotational autodetachments were also observed for a series of dipole-bound anions by high-resolution PDS.¹⁶⁸⁻¹⁷² No spectroscopic study of vibrational autodetachment was reported until 1985 when Lineberger and coworkers reported the infrared spectrum of NH^- .²¹⁷ The extra electron was ejected via autodetachment after excitation to ro-vibrational levels of NH^- . Later, vibrational autodetachment was applied to study the DBS of the enolate anion by PDS.²¹⁸ In 1996, Johnson et al.¹⁸⁶ reported the photon energy-dependent photoelectron spectra of CH_3CN^- , which showed non-Franck-Condon features due to a broad shape resonance. The resonant PES at the photon energy near the vibrationally-resolved shape resonances of O_2^- also resulted in the spectrum with non-Franck-Condon distribution, different from the non-resonant spectrum.²¹⁹ In addition, in the resonant PES of the p-benzoquinone anion²²⁰ and Au_2^- ,²²¹ significant non-Franck-Condon behaviors were observed due to autodetachments from shape and Feshbach resonances.

The pure vibrational autodetachment from DBS was first done for $C_6H_5O^-$ in 2013 by the Wang group using resonant PES.¹¹⁷ The vibrational autodetachments from DBS, involving a vibronic coupling with the breakdown of the Born-Oppenheimer approximation, are governed by the $\Delta v = -1$ propensity rule under harmonic approximation developed by Simon et al.,^{190,222} which was laid on Berry's theory¹⁸⁹ for autoionization in neutral molecules. More examples^{118-122,164} showed that the resulting resonant photoelectron spectra were highly non-Franck-Condon, giving rise to vibrational features involving low-frequency and Franck-Condon-inactive vibrational modes. The

resonant PES via vibrational autodetachment of DBS has been demonstrated as a very powerful tool to obtain vibrational information for dipolar neutrals.

The principle of resonant PES via vibrational autodetachment of DBS is schematically described in Fig. 1.6. It involves two processes. The first is resonant excitation, which has a high cross section, from the anion ground state to the DBS vibrational levels in the detachment continuum. Then autodetachment occurs from the DBS level to the neutral level. Briefly, when the photon energy is fixed at one of the DBS resonances above threshold found by PDS, vibronic coupling of the DBS electron and the vibrational modes can induce vibrational autodetachment. The autodetachment follows the $\Delta v = -1$ propensity rule under harmonic approximation,^{189,190,222} indicating that one quantum of vibrational energy is transferred to the DBS electron. The resulting neutral peak shows a higher intensity in comparison to the peak in the non-resonant spectrum due to the large cross section of the resonant excitation process. The resonant spectrum is also highly non-Franck-Condon with specific peaks enhanced from autodetachment. By comparing the relative peak intensities in the non-resonant and resonant spectra, we can deduce which peak is enhanced. Based on the $\Delta v = -1$ rule and excitation energies, the DBS vibrational levels of the anions can be assigned. Because the diffuse dipole-bound electron has little effect on the structure of neutral core, the geometries of the DBS and the corresponding neutral state are almost identical,^{95,117-122,164} which also means that the vibrational frequencies of DBS are the same as those in the neutral states. Therefore, the vibrational frequencies of neutral molecules can be obtained from the assignments of DBS vibrational levels.

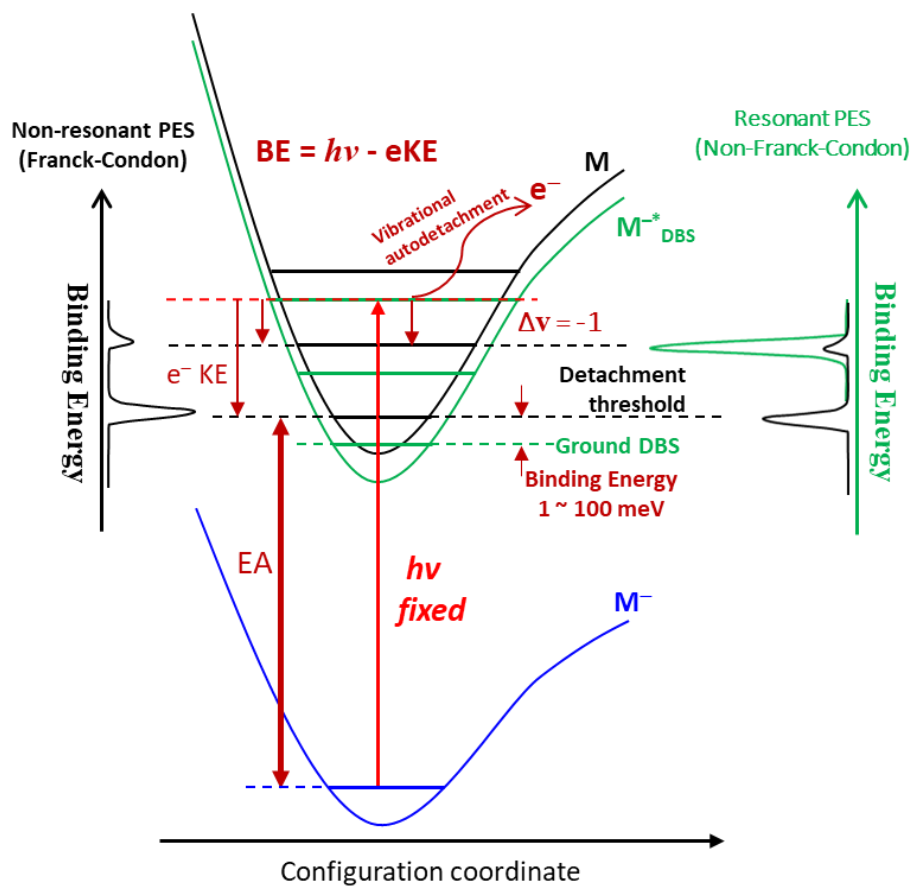


Figure 1.6. Principle of resonant PES via vibrational autodetachment of DBS of anion.

Chapter 2 Experimental methods

All experiments were carried out using the third-generation ESI-PES apparatus,¹⁵ as schematically shown in Fig. 2.1. It mainly consists of four parts, including an ESI source, a cryogenic Paul trap, a TOF mass spectrometer and a high-resolution photoelectron imaging analyzer, which has been partially or fully described previously in the Ph. D. dissertations of Dr. Phuong Diem Dau (January 2014)²²³ and Dr. Daoling Huang (May 2016).²²⁴ This chapter will discuss each component for experimental processes, from anion preparations (Section 2.1), ion cooling (Section 2.2) and mass analyzing (Section 2.3) to the photoelectron image taking (Section 2.4) and data processing (Section 2.5) as well as timing sequences (Section 2.6). The overall operation procedure is described here.

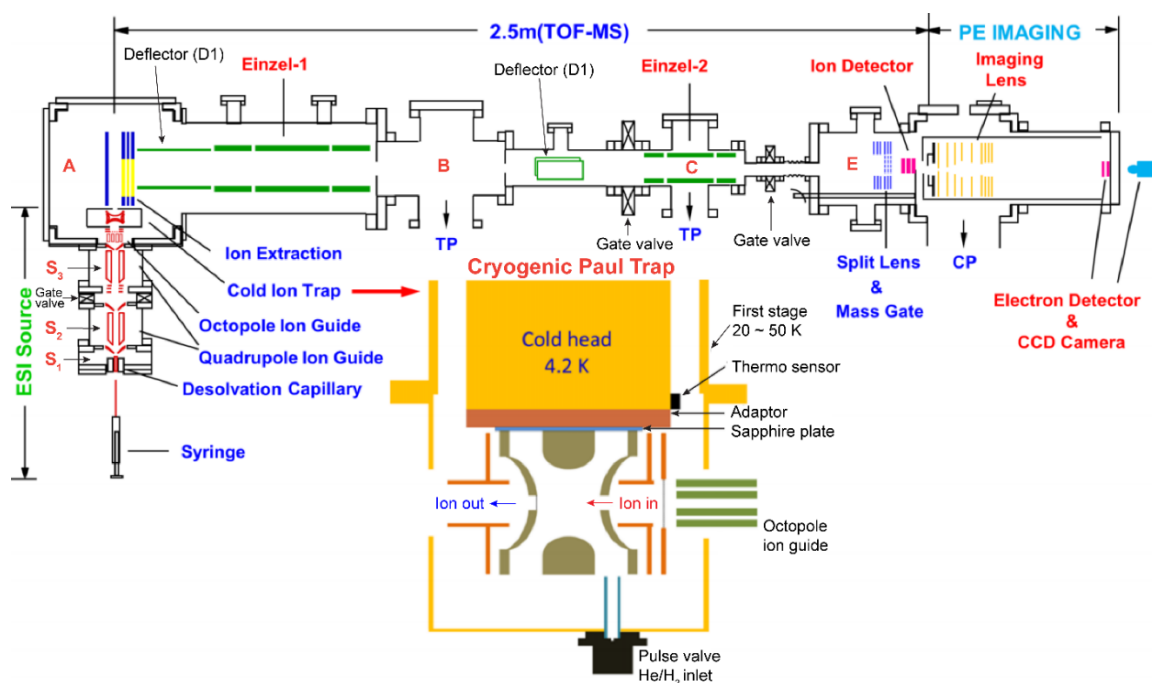


Figure 2.1. Schematics of the third-generation ESI-PES apparatus. TP, turbomolecular pump; CP, cryopump. Reproduced from [L. S. Wang, Perspective: Electrospray photoelectron spectroscopy: From multiply-charged anions to ultracold anions. *J. Chem. Phys.* **143**, 040901 (2015).], with the permission of AIP Publishing.

Briefly, anions were produced by electrospray of ~1 mM sample solutions. Two radio-frequency quadrupole and one octopole ion guides directed anions from the ESI source into a cryogenically-cooled Paul trap operated at 4.5 K. After being accumulated for 0.1 s and thermally cooled via collisions with 1 mTorr He/H₂ (4/1 in volume) buffer gas, anions were pulsed out at a 10 Hz repetition rate into the extraction zone of a TOF mass spectrometer. The desired anions were selected by a mass gate and photodetached in the interaction zone of the imaging lens by a Nd:YAG laser or a tunable dye laser. Photoelectrons were focused by a set of imaging lenses and projected onto a pair of 75-mm diameter micro-channel plates (MCPs) coupled to a phosphor screen, which were finally captured by a charge-coupled device (CCD) camera. The images were inverse-Abel transformed and reconstructed using the BASEX²²⁵ and pBasex²²⁶ programs, which were found to give similar results. The photoelectron spectra were based on BASEX, whereas the images are based on pBasex because it gives higher quality images. The photoelectron spectra were calibrated with the known spectra of Au⁻ at different photon energies. The electron kinetic energy (KE) resolution achieved was 3.8 cm⁻¹ for electrons with 55 cm⁻¹ KE and about 1.5% ($\Delta KE/KE$) for KE above 1 eV.

2.1 ESI source – Preparation of anions

The details of ESI source chamber is schematically presented in Fig. 2.2. It consists of three differentially pumped vacuum regions, S₁, S₂ and S₃. S₁ is pumped down to 470 mTorr by a mechanical pump (Edwards, E2M275). S₂ has a base pressure of around 30 mTorr, which is pumped by a blower pump (Stokes Vacuum 310.401) with the mechanical pump (Edwards, E2M80) as a backing pump. A turbomolecular pump

(Edwards, nEXT 300D), backed by a scroll pump (Edwards, XDS 35i), is used for vacuum region S_3 yielding a pressure of around 1.0×10^{-6} torr.

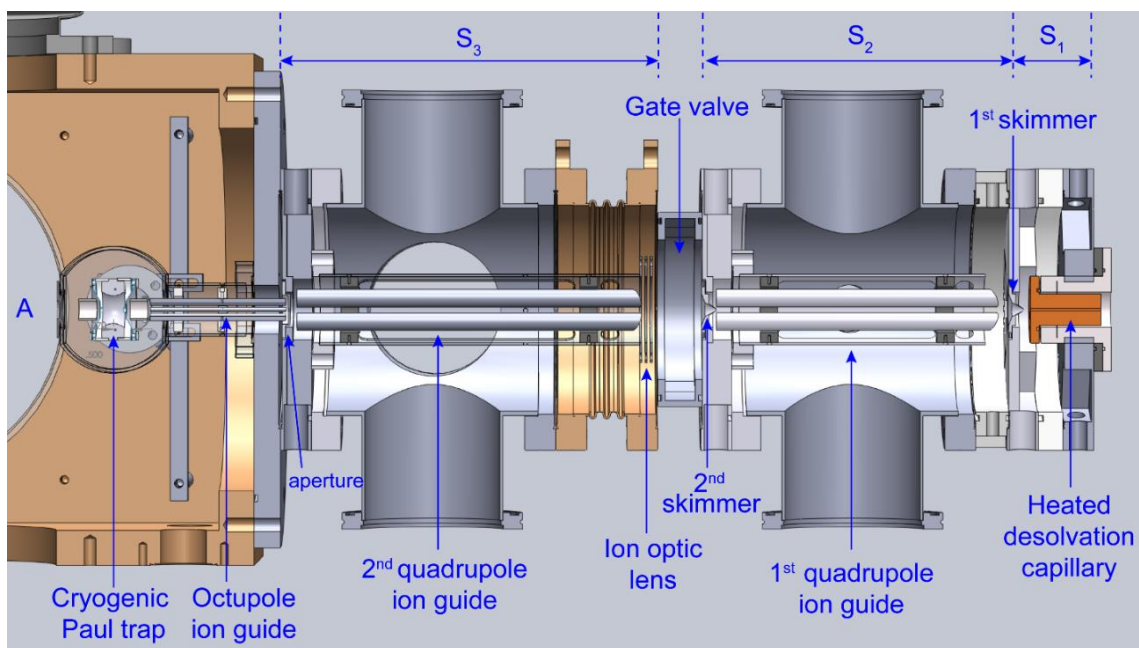


Figure 2.2. Schematics of the ESI source chamber. $S_1 - S_3$ are three vacuum regions.

All the anions studied in Chapters 3-8 were produced by electrospray (Section 1.2.1 in Chapter 1) of ~ 1 mM various solutions, which were made by dissolving the corresponding compounds into solvents with additive compounds, as listed in Table 2.1. Fullerene-related Compounds $[(C_{59}N)_2, H_2O@C_{60}$ and $(H_2O@C_{59}N)_2]$ ²²⁷ and tetrakis(dimethylamino)ethylene (TDAE)^{228,229} were synthesized, other compounds were commercially purchased. The additives of NaI and TDAE were added as reducing agents, while NaOH was used for deprotonation.

The prepared solutions are loaded into 2.5 mL syringe (Hamilton 1002LTN Syringe), which was placed on a microprocessor-controlled syringe pump (World Precision Instrument SP100i) for solution delivery. A fused silica needle with an outer diameter (O.D.) of 0.2 mm is connected to the end of the stainless-steel needle as spray

capillary. A biased negative voltage of 1.6 kV ~ 5.0 kV is applied to the capillary to generate the negatively charged droplets, which entered into a heated desolvation capillary (Fig. 2.2) acting as the interface between atmosphere and vacuum region.

Table 2.1. Preparations of solutions for ESI.

Chapter	Anions	Compounds	Solvents	Additive compounds
3	TCNQ ⁻	TCNQ ^b	CH ₃ CN	NaI
4,5	C ₅₉ N ⁻ , H ₂ O@C ₆₀ ⁻ and H ₂ O@C ₅₉ N ⁻	(C ₅₉ N) ₂ , H ₂ O@C ₆₀ and (H ₂ O@C ₅₉ N) ₂	ODCB ^c /CH ₃ CN (1/3 in volume)	TDAE ^d
6	C ₆ H ₅ O ⁻ , C ₆ H ₅ S ⁻	Phenol, thiophenol	CH ₃ OH/H ₂ O (9/1 in volume)	NaOH
7	[Cy-H] ^{-a}	cytosine	CH ₃ OH/H ₂ O (9/1 in volume)	NaOH
8	NC(C ₆ H ₄)O ⁻	NC(C ₆ H ₄)OH	CH ₃ OH/H ₂ O (9/1 in volume)	NaOH

^a[Cy-H]⁻ indicates the deprotonated cytosine anion. ^bTCNQ is tetracyanoquinodimethane. ^cODCB is o-dichlorobenzene. ^dTDAE is tetrakis(dimethylamino)ethylene.

The desolvation capillary is a stainless-steel tube, with an interior diameter of 0.8 cm, tightly inserted into a copper block (3.7 cm long and 3.4 cm O.D.), which is heated by a heater inserted through a drilled hole (3.1 cm long, 0.7 cm diameter) and mounted to the flange with insulation. The temperature of the capillary is measured by a thermal couple and tuned around 60 °C by the voltage output from a transformer. With the removal of solvents by the heated desolvation capillary, the charged droplets break up and form the isolated anions in the gas phase.

After the capillary, the first skimmer with a negative voltage of 5 – 20 V applied is mounted on the flange to separate the vacuum regions S₁ and S₂. In vacuum region S₂, a rf-only quadrupole ion guide (QID) is used to transmit ions with a transmission rate as high as 90% at low vacuum. The QID consists of four stainless steel electrodes (10 cm long, 2.5 cm diameter) of which the entrance end is cut by 45° to adjust to the skimmer. The power supply is centered at 1.0 MHz for ions with m/z around 70 – 2500.

A second skimmer with biased negative voltages of 0 – 5 V and a gate valve are placed to define the vacuum region S₃. A set of three-plate ion optic lens is followed to guide ions exiting from the first QID into the second QID due to the large thickness (around 3 cm) of the gate valve. The middle plate of the ion optic lens is applied with a +70 V biased voltage and the other two plates are grounded. To guide the ions through, a second QID (23 cm long, 2.5 cm diameter), of which the power supply is constructed based on previous designs.^{230,231}

After the second QID, ions enter through an aperture (3 mm diameter) into the octopole ion guide (8 cm long, 0.3 cm diameter) with 1.0 MHz rf frequency applied, which guides the ions into the cryogenic Paul trap more effectively with a flatter potential than QID.

2.2 Cryogenic Paul trap – Accumulation and cooling of anions

The cryogenic Paul trap is placed in vacuum region A, which is mainly pumped by the big magnetically levitated turbomolecular pump (Edwards, STP-A2203C) to a base pressure of $\sim 1.0 \times 10^{-7}$ torr and running pressure of $\sim 1.0 \times 10^{-6}$ torr.

As shown in the inset of Fig. 2.1, the ion trap consists of a hyperbolic ring electrode and two end cap electrodes for ion entrance and exit. During the operation, voltages of two end caps are kept at ground potential and only the ring electrode is applied with a rf potential to trap ions. The rf frequency is fixed at 1.0 MHz and the rf voltage is optimized for specific mass range. The rf voltage is off for a period of about 100 μ s for loading ions from the octopole ion guide. One grid electrode with varied

voltages (+ 30 V to + 70 V) and a tube lens (+ 10 V to + 60 V) are added in front of entrance end cap to assist ion loading.

With a repetition rate of 10 Hz running experiment, the loaded ions are accumulated in the trap for 0.1 s. Then, the entrance end cap is pulsed to around -70 V with the exit end cap simultaneously pulsed by + 30 V to extract ions out. A tube lens after the exit end cap is applied with a voltage about + 1 V to aid ions unloading and focusing into the extraction area of mass analyzer.

The Paul trap is cooled by a two-stage closed cycle helium coldhead (Sumitomo, RDK-415D2B) accompanied with a compressor (Sumitomo, F-70 L). The first stage can achieve a temperature of 20 – 50 K. The temperature of the second stage is achieved around 4.2 K. The Paul trap is attached to the second stage of the cold head via an extension and an adapter made of oxygen-free high purity copper. A 1 mm thick sapphire plate is inserted between the ion trap and the adapter for electrical insulation. To achieve better thermal conductivity, a 0.1 mm thick indium foil is placed between these junctions. In addition, the trap is enclosed in a gold-coated copper cylinder attached to the first stage of the coldhead to achieve better thermal shielding. A silicon diode thermal sensor is wrapped around the adapter to measure the temperature of the coldhead and send feedback to a temperature controller (LakeShore, 336 temperature controller). The temperature can be tuned at the range of 4.6 – 350 K. All the experiments were done at the lowest temperature around 4.6 K. The buffer gas is a mixture of 1 mbar He/H₂ (4:1 volume ratio), which is inlet into the trap by a pulsed valve (Parker Instrumentation, 060-0001-900).

2.3 TOF-MS – Mass analyzing and selecting of anions

TOF-MS is a method to determine ions mass-to-charge (m/z) ratio by measuring the different times of flights for ions possessing the same kinetic energy. As shown in Fig. 2.1, our set-up is a 2.5 m long flight tube, spanning over four differentially pumped vacuum regions A, B, C and E, which consists of an ion extraction zone, two deflectors, two sets of Einzel lens, a split lens, a mass gate and a MCP detector. The pumping configurations and pressures are listed in Table 2.2.

Table 2.2. Pump configurations and pressures for TOF-MS vacuum chambers. The unit of pressure is torr.

Region	A	B	C	E
Pump	Edwards, STP-A2203C	Edwards, nEXT 300 D or 400 T	Pfeiffer, TPU 180H	CTI-cryogenics, Cryo-torr 8 cryopump with 8200 compressor
Backing pump	Edwards, XDS 35i		Pfeiffer, MVP 070-3 diaphragm pump	
Base pressure	$\sim 1.0 \times 10^{-7}$	$\sim 1.5 \times 10^{-8}$	$\sim 1.0 \times 10^{-8}$	$\sim 7.0 \times 10^{-9}$
Running pressure	$\sim 1.0 \times 10^{-6}$	$\sim 8.0 \times 10^{-7}$	$\sim 4.0 \times 10^{-7}$	$\sim 1.5 \times 10^{-8}$

After thermal cooling and accumulation, ions are extracted and focused by a tube lens into the extraction zone of TOF-MS. As presented in Fig. 2.3, the ion extraction zone consists of a stack of electrode plates. Entering in the zone through the region of plate 3, ions are accelerated with the same kinetic energies by a pulsed voltage of -1.25 kV distributed over the whole stack. As the length of the flight tube is constant, ions with different m/z ratios can have different time of flights (t). The relation can be expressed as $m/z = c * t^2$, where c is a constant related with the length of the flight tube and the voltage supply. It can be easily determined by the known m/z ratio and time of flights of atomic anions of Γ^- and Au^- .

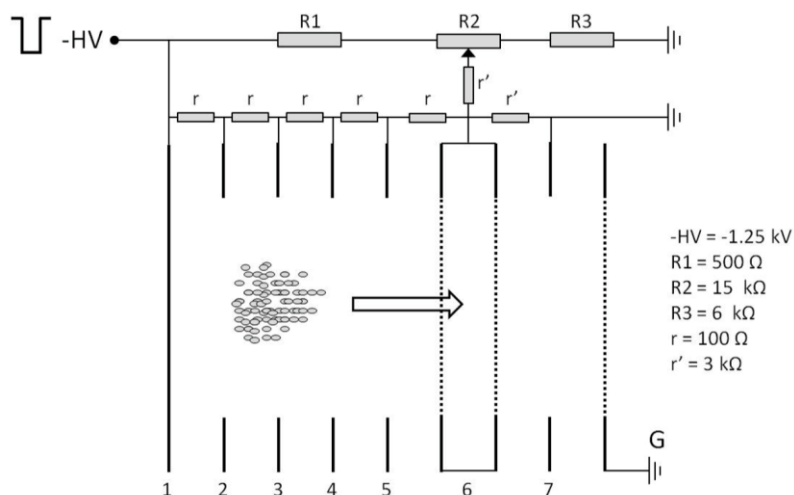


Figure 2.3. The assembly of the ion extraction electrodes.

After the extraction zone, the ion trajectory is aligned by a horizontal deflector (D1) and a vertical deflector (D2). The voltages are usually optimized between -10 V and $+10$ V to correct the trajectory to detector and achieve optimal ion signal. Two sets of Einzel lens made by three isolated copper cylinders are used to refocus the ion beam onto the detector. The middle electrodes of EL1 and EL2 are set at -511 V and -360 V, respectively, while two end electrodes are at ground potential.

The ion beam is refocused by a split lens ($0.3 - 0.5$ kV) into a mass gate, which can filter out undesired anions. The mass gate contains three grid electrodes (Fig. 2.4). The two end grid electrodes are grounded, while the middle one is applied by a pulsed voltage of -1.3 kV. When the desired anion arrives at the first grid, the second grid will be pulsed to ground for a short time ($0.5 - 1.2$ μ s) for the selected anion to pass through. The high voltage of -1.3 kV is then applied back to the second grid to block the rest of unwanted anions. The timing and the width of the pulse is based on the time of flight and the width of the mass signal of the desired anion. Anions are detected by a pair of MCP at the voltage of -2.5 kV.

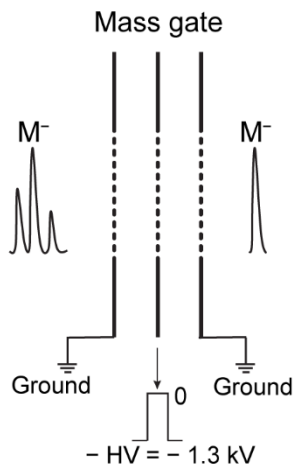


Figure 2.4. Schematics of mass gate assembly.

2.4 High-resolution photoelectron imaging system

The desired anions are intersected with the pulsed Nd:YAG (Continuum, SLII-20) or tunable nanosecond pulsed dye laser ($\Delta\lambda \sim 0.0015$ nm, Cobra-Stretch, Sirah CSTR-G-30) for photodetachment in the interaction zone of the image lens (Fig. 2.5). The photoelectron imaging system contains multiple electrodes based on the three-plate VMI system.⁴⁷ L_R represents the repeller electrode. L_1 and L_2 are the extractor electrodes, while L_3 is the ground electrode. Extra plates L_{12} and L_{23} are added as guarding electrodes between $L_1 - L_2$ and $L_2 - L_3$, respectively, to prevent fringe field penetration due to the relative large distances. After L_3 , three more shielding plates are added at ground potential to achieve optimal focusing. All the electrodes, made of oxygen-free copper with gold coated, have a thickness of 0.8 mm and outer diameter of 106 mm.

In experiments, voltage on L_R , named V_R , was set at low extraction voltage of -300 V to detect slow electrons with high resolution. V_R was also applied with a voltage of -1000 V or -1100 V to capture the fast photoelectrons, such as the electron detached

from vibrational ground DBS. The voltages of V_1 (~ 480 V) and V_2 (~ 160 V) were optimized to achieve an optimal focusing and resolution.

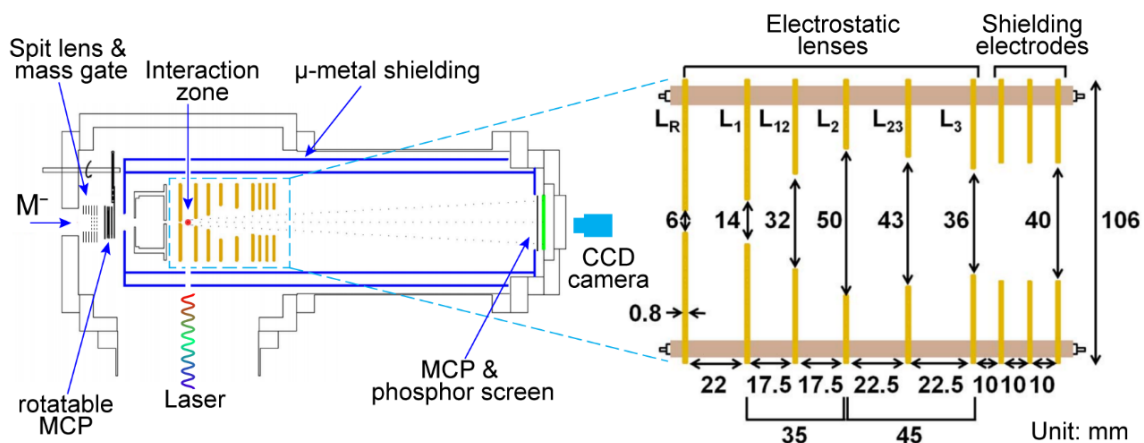


Figure 2.5. Schematics of the high-resolution photoelectron imaging system. Reproduced from [Iker León, Zheng Yang, Hong-Tao Liu, and L. S. Wang, The design and construction of a high-resolution velocity-map imaging apparatus for photoelectron spectroscopy studies of size-selected clusters *Rev. Sci. Instrum.* **85**, 083106 (2014).], with the permission of AIP Publishing.

After photodetachment, photoelectrons travel through the image system and impinge on the position-sensitive detector, which consists of a set of 75 mm diameter MCP detector coupled to a phosphor screen (Photonis USA, Inc.). The images are captured by a CCD camera (Uniq Vision Inc., Model UP930CL, 1024×1024 pixels). The imaging detector is about 1 m away from the interaction zone. The image lens and the entire electron flight path are enclosed by two concentric cylinders of μ -metal shielding with a thickness of 0.51 mm and diameters of 14.1 cm and 17.7 cm, respectively. Two holes are drilled on the μ -metal shielding below and above the interaction zone to allow detachment lasers travel through.

2.5 Data processing

The photoelectron image is two-dimensional (2D) projection of the three-dimensional (3D) photoelectron Newton sphere (Fig. 1.4), containing both the energy and angular information of photoelectrons, which has a cylindrical symmetry with the axis defined by the laser polarization direction. To reconstruct the initial distribution, an inverse-Abel transformation was carried out by both BASEX²²⁸ and pBasex²²⁹ programs, which yielded similar results. Due to a 2% distortion of our image, all the raw photoelectron images were circularized with a factor of 0.981 before the transformation. Assuming the interaction zone is a point source, the photoelectron KE is proportional to the radius (r) of the photoelectron image, which can be expressed as $KE = a*r^2$. In experiments, the interaction zone is not a perfect point, an additional term [$b*r$] was added in the expression as $KE = a*r^2 + b*r$ for extra effects. Constants a and b , depending on the geometry of the imaging system and the repeller voltage V_R , were determined by the known spectra of Au^- or I^- at different photon energies.

2.6 Timing sequences

The high-resolution photoelectron imaging experiments are operated at a repetition rate of 10 Hz, following the timing sequences as shown in Fig. 2.6. The timing is generated by four digital delay generators (Stanford Research Systems, DG 535).

Briefly, T_0 is the starting pulse of a whole experimental cycle. The anions produced by ESI are continuously loaded into the cryogenic Paul trap with a trapping time of 100 ms (T_1). After a short delay of 2 μ s (T_2) for the damping of the rf voltage applied to the trap, two end caps of the trap are applied with pulsed voltages (10 μ s of

pulse width) to unload anions. A delaying period (T_3), which indicates the time of flight of anions to the extraction region of TOF-MS, is carefully tuned before the high negative voltage pulse (-1.25 kV, 20 μ s) is applied to the extraction stacks. T_4 is the time of flight of desired anions from extraction region to the mass gate. It can be monitored on the oscilloscope (Tektronix, TDS 3032C). The pulse width of the mass gate is optimized between 0.5 to 1.2 μ s. The time of firing the laser is reference to repeller with a delaying period T_5 , which is the time of flight of the selected anion from the repeller to the photodetachment zone in the image lens. The width of Q-switch is 10 μ s. A pulsed voltage with width of 0.8 μ s (T_7) is applied to the MCP detecting photoelectrons about 0.5 μ s (T_6) prior the laser Q-switch. The CCD camera is started 100 μ s (T_8) after the starting pulse with a width of 50 μ s (T_9).

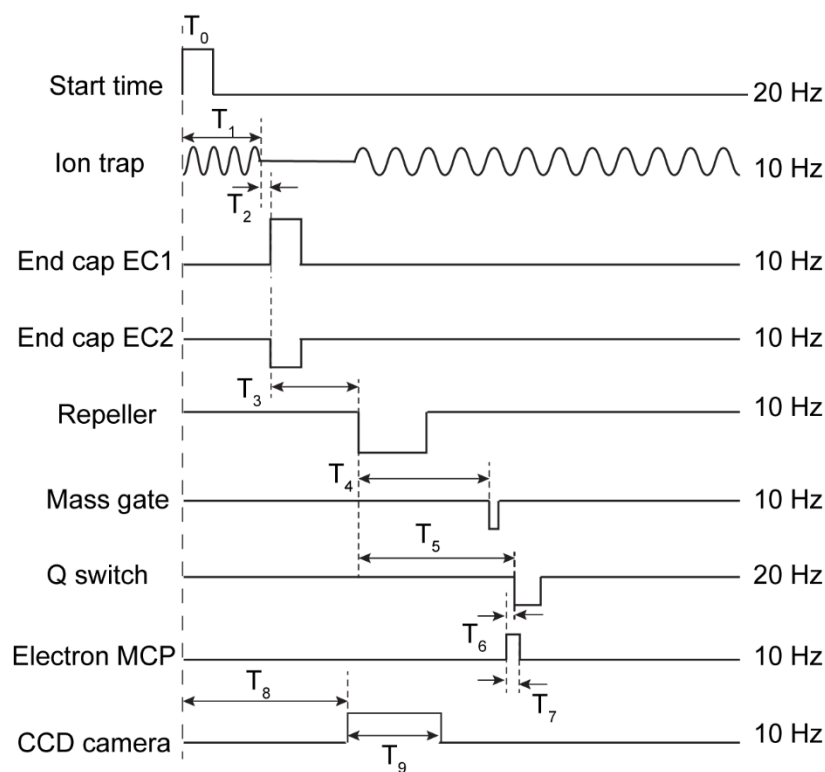


Figure 2.6. Timing sequences for the high-resolution photoelectron imaging experiments.

Chapter 3 Accurate determination of the electron affinity of

TCNQ*

This chapter²³² will discuss the first experiment I did independently for my thesis work. It was to measure the electron affinity (EA) of tetracyanoquinodimethane (TCNQ), which was erroneously reported in the literatures.

TCNQ is widely used as an electron acceptor to form highly conducting organic charge-transfer solids. Surprisingly, the electron affinity of TCNQ is not well known and has never been directly measured. Here we report vibrationally-resolved PES of the TCNQ⁻ anion produced using electrospray and cooled in a cryogenic ion trap. Photoelectron spectrum taken at 354.7 nm represents the detachment transition from the ground vibrational state of TCNQ⁻ to that of neutral TCNQ with a short vibrational progression. The EA of TCNQ is measured accurately to be 3.383 ± 0.001 eV ($27,289 \pm 8$ cm⁻¹), compared to the 2.8 ± 0.1 eV value known in the literature and measured previously using collisional ionization technique. In addition, six vibrational peaks are observed in the photoelectron spectrum, yielding vibrational frequencies for three totally symmetric modes of TCNQ. Two-photon PES via a bound electronic excited state of TCNQ⁻ at 3.100 eV yields a broad low kinetic energy peak due to fast internal conversion to vibrationally excited levels of the anion ground electronic state. The high EA measured for TCNQ underlies its ability as a good electron acceptor.

* The content of this chapter is reproduced or adapted from [G. Z. Zhu, and L. S. Wang, Communication: Vibrationally resolved photoelectron spectroscopy of the tetracyanoquinodimethane (TCNQ) anion and accurate determination of the electron affinity of TCNQ. *J. Chem. Phys.* **143**, 221102 (2015).], with the permission of AIP Publishing.

3.1 Introduction

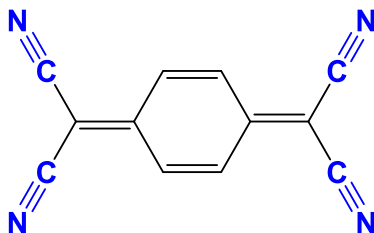


Figure 3.1. The molecular structure of TCNQ.

TCNQ (Fig. 3.1) is one of the best electron acceptors to form charge-transfer conducting organic solids.²³³⁻²³⁶ The electronic and structural properties of TCNQ and its anion (TCNQ⁻) have been studied quite extensively both experimentally and theoretically.²³⁷⁻²⁵¹ TCNQ possesses a high EA due to the presence of the highly electron-withdrawing CN groups (Fig. 3.1). The EA of TCNQ was first measured as 2.8 ± 0.1 eV by Compton and co-workers using collisional ionization between Cs and TCNQ to form $\text{Cs}^+ + \text{TCNQ}^-$.²³⁷ A later study by Compton and Cooper refined the EA of TCNQ to be $2.8 + 0.05/-0.3$ eV,²³⁸ but the EA value has been usually cited in the literature as 2.8 ± 0.1 eV for TCNQ. Brauman and co-workers measured the photodetachment spectrum of TCNQ⁻ in an ion cyclotron resonance mass spectrometer in the wavelength range of 350–1060 nm.²³⁹ They observed two resonant bands: a low-energy broad resonance between 600 and 1000 nm (2.1 to 1.2 eV) and another resonance between 360 and 470 nm (3.4 to 2.6 eV). These two resonances, corresponding to transitions to two electronic excited states of TCNQ⁻, were found to be very similar to electronic absorption spectrum of TCNQ⁻ in solution.²⁴⁰ However, no EA was measured from the photodetachment spectrum. More recently, Verlet and co-workers examined the ultrafast relaxation dynamics of the first excited state of gaseous TCNQ⁻ and also reported the photoelectron spectrum of TCNQ⁻ at a photon energy of 3.1 eV.²⁴² Two bands were observed in their

photoelectron spectrum, a narrower band centered at a photoelectron kinetic energy of 0.2 eV and a broad band centered at a kinetic energy of 2 eV. The narrower band was interpreted to be due to a one-photon detachment (resonant absorption followed by autodetachment to the ground state of neutral TCNQ), yielding an EA of 2.9 eV, which was considered to be in good agreement with the previous value of 2.8 ± 0.1 eV.

The EA of TCNQ has been calculated in several theoretical studies. Ortiz and co-workers obtained an EA of 2.74 eV using an electron propagator method.²⁴⁵ Skurski and Gutowski gave a range of EA between 2.76 and 2.95 eV at the configuration interaction (CI/PM3) level.²⁴⁷ These computed EAs were considered to be in good agreement with the available experimental EA of 2.8 ± 0.1 eV. More recently, Milian et al.²⁵⁰ computed the EA of TCNQ using the higher-level couple-cluster method [CCSD(T)] and obtained an EA of 3.22 eV, which was overestimated by 0.4 eV relative to the 2.8 eV experimental value. However, the authors showed that the same theoretical method tended to underestimate the EAs by 0.1 to 0.2 eV for similar compounds. This discrepancy made the authors skeptical about the previously measured EA for TCNQ and prompted them to call for additional measurement. Very recently, Nakashima et al. computed an EA of 3.31 eV for TCNQ using the symmetry adapted cluster configuration interaction method.²⁵¹

Here, we report vibrationally-resolved PES of TCNQ⁻ using photoelectron imaging at 354.7 nm. The 354.7 nm photoelectron spectrum represented detachment transition from the ground state of TCNQ⁻ to that of neutral TCNQ with a short vibrational progression consisting of seven resolved vibrational peaks. The EA of TCNQ was measured directly and accurately to be 3.383 ± 0.001 eV from the 0-0 vibrational transition. In addition, vibrational frequencies for three totally symmetric vibrational

modes were obtained for TCNQ, ν_1 (114 cm⁻¹), ν_2 (331 cm⁻¹), and ν_4 (709 cm⁻¹). A photoelectron spectrum was also obtained at 3.100 eV, in resonance with the second excited state of TCNQ⁻, as a result of two-photon detachment, following fast internal conversion.

3.2 Experimental methods

The experiment was done using our third-generation ESI-PES apparatus.¹⁵ The TCNQ⁻ anions were produced by electrospray of a 1 mM solution of TCNQ dissolved in acetonitrile and spiked with a small amount of NaI. More experimental details are provided in Chapter 2.

3.3 Results and discussion

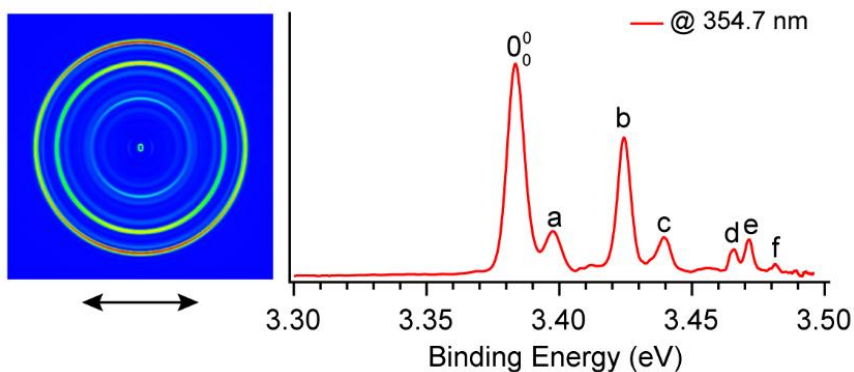


Figure 3.2. The photoelectron image and spectrum of TCNQ⁻ at 354.7 nm. The arrow below the image indicates the polarization direction of the laser.

Figure 3.2 shows a photoelectron image and spectrum of TCNQ⁻ at 354.7 nm. The spectrum was obtained by summing up several images to enhance the signal-to-noise ratios. This spectrum represents detachment transitions from the ground electronic and vibrational state of TCNQ⁻ to the ground electronic state of neutral TCNQ. The binding

energies of the seven observed peaks are given in Table 3.1, along with their assignments. The peaks correspond to the vibrational levels of neutral TCNQ. The short vibrational progression suggests that there is little geometry change between the anion and neutral TCNQ. The first and most intense peak at 27,289 cm⁻¹ (3.383 eV) corresponds to the 0-0 transition and defines accurately the EA of TCNQ. We note that the most recently computed EAs for TCNQ, 3.22 eV by Milian et al.²⁵⁰ and 3.31 eV by Nakashima et al.,²⁵¹ are in good agreement with the current measurement.

Table 3.1. Assignments of the observed vibrational peaks in the photoelectron spectrum of TCNQ⁻. The measured binding energies (BEs), shifts relative to the neutral vibrational ground state (0-0) are compared with the computed vibrational frequencies (ν_{theo}) of TCNQ.

Observed peaks	BE (cm ⁻¹) ^a	Shift (cm ⁻¹)	ν_{theo} (cm ⁻¹) ^b	Assignment
0-0	27,289(8)	0		
<i>a</i>	27,403(8)	114	118 (ν_1)	ν_1
<i>b</i>	27,620(8)	331	334 (ν_2)	ν_2
<i>c</i>	27,739(8)	450		$\nu_2 + \nu_1$
<i>d</i>	27,952(9)	663		$2\nu_2$
<i>e</i>	27,998(9)	709	725 (ν_4)	ν_4
<i>f</i>	28,079(10)	790		$2\nu_2 + \nu_1$

^aThe number in the parenthesis represents the uncertainty in the last digits.

^bSee the Table 3.2 in Section 3.5 for the full list of the computed vibrational frequencies and Fig. 3.3 for the normal modes of the observed frequencies.

To help assign the vibrational peaks, we computed the vibrational frequencies of TCNQ using density functional theory at the B3LYP/6-31+G(d,p) level using the Gaussian 09 package.²⁵² Since both TCNQ and its anion are planar with D_{2h} symmetry, only totally symmetric modes are allowed. Peak *a* represents a vibrational spacing of 114 cm⁻¹ (Table 3.1) which is in good agreement with the calculated frequency of vibrational mode ν_1 (118 cm⁻¹) involving the in-plane bending of four -CN groups (Fig. 3.3). Peak *b* represents the mode with the strongest Franck-Condon factors and the vibrational spacing of 331 cm⁻¹ (Table 3.1) agrees well with the calculated frequency of the in-plane

stretching mode ν_2 (334 cm^{-1} , Fig. 3.3). As shown in Table 3.1, peak *d* represents the first overtone of the ν_2 mode, whereas peaks *c* and *f* are combination modes of ν_2 and ν_1 . Peak *e* with a spacing of 709 cm^{-1} from the vibrational ground state is in good agreement with the computed frequency of the ν_4 mode (725 cm^{-1}), which involves the ring breathing vibration. The normal modes of the three observed vibrational frequencies are shown in Fig. 3.3.

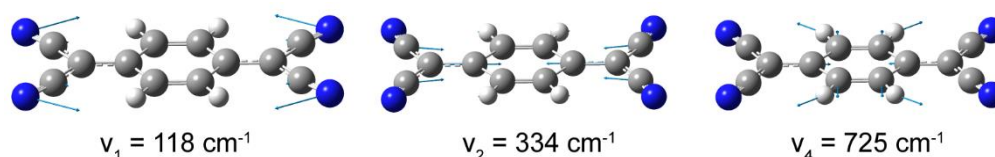


Figure 3.3. Displacements for the three observed vibrational modes of TCNQ. All the modes have symmetry of A_g (Table 3.2). The computed harmonic frequencies are also shown.

The highest occupied molecular orbital (HOMO) of TCNQ is a π orbital of b_{3u} symmetry. The lowest unoccupied molecular orbital (LUMO), where the extra electron resides in TCNQ⁻, is an antibonding π^* orbital of b_{2g} symmetry. The LUMO+1 orbital is also of b_{3u} symmetry. The ground state of TCNQ⁻ is ${}^2B_{2g}$ with an electron configuration of $3b_{3u}{}^23b_{2g}{}^14b_{3u}{}^0$. The photoelectron image shown in Fig. 3.2 exhibited a perpendicular distribution indicating an $s + d$ character, in agreement with detachment of a π electron from the π^* $3b_{2g}$ orbital. The first electronic excited state ($1{}^2B_{3u}$) of TCNQ⁻, observed between 600 to 1000 nm (2.1 to 1.2 eV),²³⁹ corresponds to excitation of an electron from the HOMO to the LUMO with an electron configuration of $3b_{3u}{}^13b_{2g}{}^24b_{3u}{}^0$, whereas the second excited state ($2{}^2B_{3u}$), observed between 360 and 470 nm (3.4 to 2.6 eV), corresponds to excitation of the electron in the LUMO to LUMO+1 with an electron configuration of $3b_{3u}{}^23b_{2g}{}^04b_{3u}{}^1$. Our measured EA of TCNQ indicates that the two

excited states of TCNQ⁻ are both bound states, as schematically shown in Fig. 3.4. Thus, a single photon absorption to the second excited state (2^2B_{3u}) of TCNQ⁻ would be impossible to induce electron detachment, as reported by Verlet and co-workers at a photon energy of 3.1 eV.²⁴²

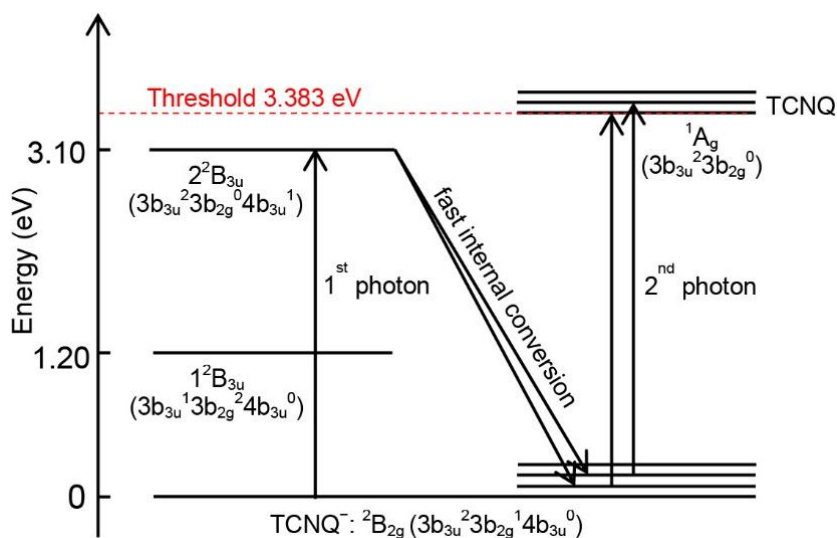


Figure 3.4. Schematic energy levels for TCNQ⁻ and TCNQ. It shows the resonant excitation using a 400.0 nm (3.100 eV) photon to the 2^2B_{3u} excited state of TCNQ⁻, followed by fast internal conversion to the vibrational levels of the TCNQ⁻ ground electronic state, as well as the detachment by a second photon off the vibrationally excited TCNQ⁻ to yield the spectrum in Fig. 3.5.

We have recently observed a bound excited state for AuS⁻ and observed vibrational level-dependent photoelectron spectra via resonant two-photon detachment.²⁵³ We tried to carry out a similar experiment using a photon energy of 3.100 eV (400.0 nm), which is in resonance with the 2^2B_{3u} excited state of TCNQ⁻. Resonant two-photon detachment should yield a photoelectron spectrum similar to Fig. 3.2, but at a much higher electron kinetic energy (~ 2.8 eV). However, we observed a spectrum with a very low electron kinetic energy centered at around 0.2 eV, as shown in Fig. 3.5. This observation suggests that the 2^2B_{3u} excited state of TCNQ⁻ must have a very short lifetime and undergoes fast internal conversion to the ground electronic state of TCNQ⁻,

producing highly vibrationally excited states. The second photon then detaches an electron from the highly vibrationally excited TCNQ⁻ in its ground electronic state, giving rise to the broad low kinetic energy band shown in Fig. 3.5. Since our detachment laser pulse had a pulse length of a few nanoseconds, the lifetime of the 2^2B_{3u} excited state must be much shorter than a few nanoseconds. We note that the spectrum in Fig. 3.5 is similar to the 0.2 eV KE band observed by Verlet and co-workers.²⁴² The broad band centered at a KE of 2 eV observed in their spectrum was likely due to resonant two-photon detachment, because of the short laser pulse used in their experiment.

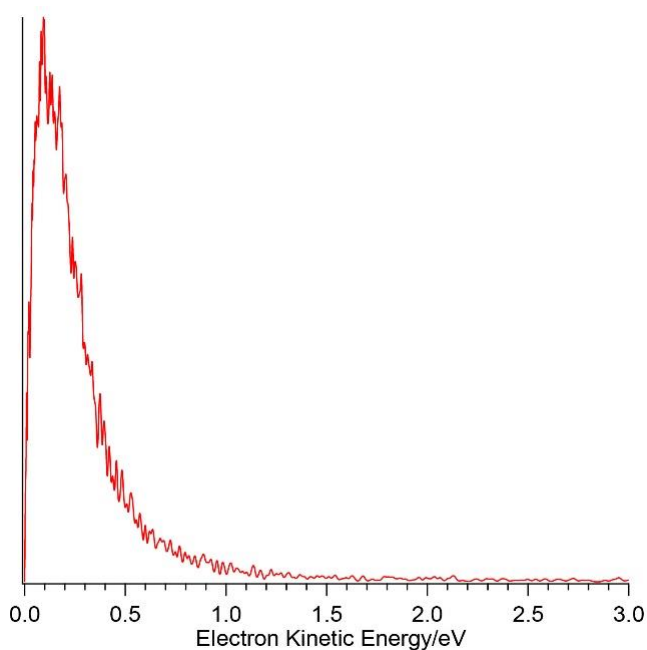


Figure 3.5. Two-photon photoelectron spectrum of TCNQ⁻ at 400.0 nm (3.100 eV). See Fig. 3.4 for the excitation processes.

3.4 Conclusions

In conclusion, we have obtained the first vibrationally-resolved photoelectron spectrum of TCNQ⁻ at 354.7 nm that allowed us to accurately measure the electron affinity of TCNQ to be 3.383 ± 0.001 eV. Additionally, three totally symmetric

vibrational modes were observed with frequencies of 114, 331, and 709 cm⁻¹ for the ν_1 , ν_2 , and ν_4 modes, respectively. The current EA value indicates that the isolated TCNQ⁻ anion possesses two bound electronic excited states (Fig. 3.4). Resonant excitation to the second excited state suggested a very short lifetime and fast internal conversion to the vibrational levels of the ground electronic state of TCNQ⁻. The current measurement uncovered an extremely high EA for TCNQ, which is comparable to that of the F atom (3.401 eV),²⁵⁴ and underlies its capacity as an excellent electron acceptor.

3.5 Supporting information

Table 3.2. Theoretical vibrational frequencies of neutral TCNQ. The harmonic frequencies were calculated using the B3LYP/6-31+G(d,p) method. The observed frequencies for the modes ν_1 , ν_2 , and ν_4 are given for comparison.

Symmetry	Mode	Theoretical (cm ⁻¹)	Experimental (cm ⁻¹)	Peak	Symmetry	Mode	Theoretical (cm ⁻¹)	
A _g	ν_1	118	114	a	A _u	ν_{28}	50	
	ν_2	334	331	b		ν_{29}	400	
	ν_3	607				ν_{30}	470	
	ν_4	725	709	e		ν_{31}	1014	
	ν_5	973				B _{1u}	ν_{32}	140
	ν_6	1233					ν_{33}	558
	ν_7	1493					ν_{34}	608
	ν_8	1673					ν_{35}	987
	ν_9	2327					ν_{36}	1005
	ν_{10}	3223					ν_{37}	1430
B _{1g}	ν_{11}	116			ν_{38}		1583	
	ν_{12}	446			ν_{39}		2329	
	ν_{13}	814			ν_{40}		3209	
B _{2g}	ν_{14}	147			B _{2u}		ν_{41}	84
	ν_{15}	305				ν_{42}	287	
	ν_{16}	633				ν_{43}	508	
	ν_{17}	764				ν_{44}	1137	
	ν_{18}	1013				ν_{45}	1230	
B _{3g}	ν_{19}	134			ν_{46}	1379		
	ν_{20}	374			ν_{47}	1594		
	ν_{21}	528			ν_{48}	2313		
	ν_{22}	622			ν_{49}	3222		
	ν_{23}	1206			B _{3u}	ν_{50}	47	
	ν_{24}	1341				ν_{51}	221	
	ν_{25}	1482				ν_{52}	482	
	ν_{26}	2313				ν_{53}	668	
	ν_{27}	3210				ν_{54}	872	

Chapter 4 High-resolution photoelectron imaging of $C_{59}N^{\dagger}$

This chapter²⁵⁵ will discuss photoelectron imaging study of cryogenically-cooled $C_{59}N^-$ produced from electrospray ionization. High-resolution photoelectron spectra are obtained for $C_{59}N^-$ for the first time, allowing seven vibrational frequencies of the $C_{59}N$ azafullerene to be measured. The electron affinity of $C_{59}N$ is determined accurately to be 3.0150 ± 0.0007 eV. The observed vibrational features are understood based on the calculated frequencies and compared with those of C_{60} and $C_{59}HN$. The photoelectron image of $(C_{59}N)_2^{2-}$, which has the same mass/charge ratio as $C_{59}N^-$, is also observed, allowing the second electron affinity of the $(C_{59}N)_2$ azafullerene dimer to be measured as 1.20 ± 0.05 eV. The intramolecular Coulomb repulsion of the $(C_{59}N)_2^{2-}$ dianion is estimated to be 1.96 eV and is investigated theoretically using the electron density difference between $(C_{59}N)_2^{2-}$ and $(C_{59}N)_2$.

4.1 Introduction

Azafullerene ($C_{59}N$), with one carbon atom in C_{60} substituted by a nitrogen atom, has received particular attention due to its unique electronic and chemical properties.^{256,257} The N-substitution results in a n -type doping, adding one electron to the close-shell π system of C_{60} .^{259,260} The extra unpaired electron is mainly localized on the C atom that is closest to the N atom in the [6,6] closed structure and exhibits sp^3 character.²⁶⁰⁻²⁶⁵ Hence, $C_{59}N$ is a reactive radical and can easily dimerize.^{256,257,262-265} The $C_{59}N^+$ cation is isoelectronic to C_{60} and was first observed as a gaseous species.²⁶⁶ The

[†] The content of this chapter is reproduced with permission from [G. Z. Zhu, Y. Hashikawa, Y. Liu, Q. F. Zhang, L. F. Cheung, Y. Murata, and L. S. Wang, High-resolution photoelectron imaging of cryogenically-cooled $C_{59}N^-$ and $(C_{59}N)_2^{2-}$ azafullerene anions. *J. Phys. Chem. Lett.* **8**, 6220-6225 (2017)]. Copyright 2017 American Chemical Society.

first macroscopic synthesis of $C_{59}N$ was in its dimer form, $(C_{59}N)_2$,²⁶⁷ allowing its physical and chemical properties to be characterized by a variety of techniques.²⁶⁸⁻²⁸² Most interestingly, the azafullerene has promising applications in molecular electronics as the basis for single-molecule rectifiers,²⁸³⁻²⁸⁵ field-effect transistors,^{286,287} and electron donor-acceptor systems.²⁸⁸⁻²⁹⁰ However, the electron affinity (EA) of $C_{59}N$, one of its most fundamental electronic and thermodynamic properties, is still not known experimentally. Theoretical calculations suggested an EA for $C_{59}N$ to be around 2.70 eV,^{260,262} which is comparable to the EA of C_{60} accurately known to be 2.6835 eV.¹¹⁶ In a C_{60} - $C_{59}N$ dyad,²⁸⁸ a higher reduction potential was observed for $C_{59}N$ than C_{60} , indicating a higher EA for $C_{59}N$ than C_{60} .

In the current study, we present a high-resolution photoelectron imaging study of cryogenically-cooled $C_{59}N^-$ anions produced from an electrospray ionization source. Vibrationally-resolved photoelectron spectra at various photon energies have been obtained, allowing us to measure the EA of $C_{59}N$ accurately for the first time to be 3.0150 eV, which is 0.3315 eV higher than that of C_{60} . Seven vibrational frequencies are also obtained for $C_{59}N$, five of which are found to be similar to those observed in the high-resolution photoelectron spectra of C_{60}^- .¹¹⁶ Additionally, we have also obtained the photoelectron spectrum for the parent $(C_{59}N)_2^{2-}$ dimer dianion, which has the same mass/charge ratio as $C_{59}N^-$, yielding the second EA of $(C_{59}N)_2$ to be 1.20 eV. The intramolecular Coulomb repulsion in the dimer dianion is estimated to be 1.96 eV. The extra charges in the dianion are shown to be more localized at the two ends of the dimer due to the electron-electron repulsion.

4.2 Experimental methods

The experiment was carried out on our third-generation ESI-PES apparatus. The details were described in Chapter 2.

4.3 Results and discussion

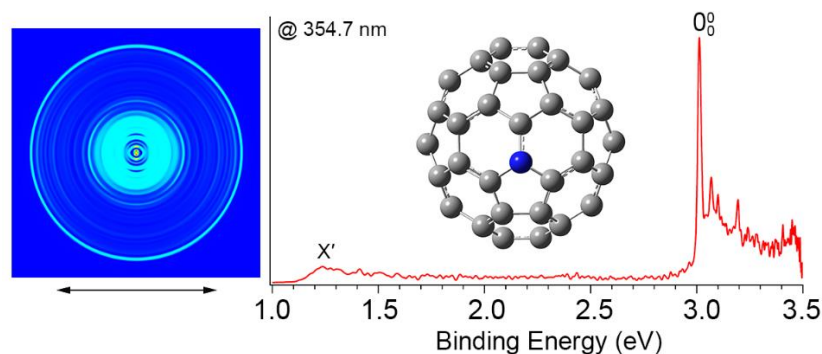


Figure 4.1. The photoelectron image and spectrum of $C_{59}N^-$ and $(C_{59}N)_2^{2-}$ at 354.7 nm. The inset shows the structure of $C_{59}N^-$. The weak peak X' represents detachment from $(C_{59}N)_2^{2-}$, while peak 0_0^0 denotes the detachment threshold of $C_{59}N^-$. The double arrow below the image indicates the direction of the laser polarization. Note the image corresponding to peak X' is cut off.

Figure 4.1 displays the photoelectron image and spectrum of the anion at $m/z = 722$ at a photon energy of 354.7 nm. The spectrum reveals two detachment regions, a weak and broad peak (X') at around 1.2 eV and a group of more intense peaks above 3 eV. This spectral pattern immediately suggests that the $m/z = 722$ mass signals contained both $C_{59}N^-$ and $(C_{59}N)_2^{2-}$. The 1.2 eV peak should come from the dianion, which is expected to have low binding energies due to the strong intramolecular Coulomb repulsion.²⁹¹ This low binding energy is comparable to that for a similar dianion, $[C_{60}OC_{60}]^{2-}$, which has an electron binding energy of 1.02 eV.²⁹² The strong peaks above 3.0 eV, which display some resemblances to the 354.7 nm spectrum of C_{60}^- ,¹¹⁶ should come from $C_{59}N^-$, representing transitions from the ground vibrational level of the anion

to vibrational levels of the electronic ground state of neutral $C_{59}N$. The first intense peak labeled 0_0^0 defines the EA of $C_{59}N$, which is more accurately measured to be 3.0150 ± 0.0007 eV in Fig. 4.2a to be discussed below. It should be noted that because of the existence of the repulsive Coulomb barrier no low-energy electrons are allowed for detachment from the $(C_{59}N)_2^{2-}$ dianion,²⁹¹ i.e., the spectral region for $C_{59}N^-$ above 3 eV should contain no contributions from higher binding energy detachment transitions from the dianion.

To better resolve the vibrational peaks for $C_{59}N$, we took high-resolution photoelectron images at six different wavelengths near the detachment threshold, as shown in Fig. 4.2. Photoelectron imaging allows low-energy electrons to be detected, significantly improving the spectral resolution for near-threshold detachment transitions.^{52,60} At 409.80 nm in Fig. 4.2a, peak 0_0^0 corresponds to an electron kinetic energy of 84 cm^{-1} and a line width (FWHM) of 12 cm^{-1} , yielding the most accurate value for the EA of $C_{59}N$ as 3.0150 ± 0.0007 eV. As reported previously,⁹⁶⁻⁹⁷ anions in our cryogenic Paul trap have a rotational temperature of ~ 30 K. Thus, the near-threshold peak width should mainly come from rotational broadening. Because of the *p*-wave detachment character, the cross section for the near-threshold detachment was quite low, as can be seen from the relatively poor signal/noise ratios in Fig. 4.2a. The EA of $C_{59}N$ is 0.3315 eV higher than that of C_{60} at 2.6835 eV.¹⁶⁶

By tuning the photon energies above threshold systematically, we were able to resolve seven additional vibrational peaks, labeled from A to G, up to a binding energy of 3.15 eV, as shown in Fig. 4.2b-f. The observed peaks, their binding energies, the shifts from peak 0_0^0 (i.e. the measured fundamental vibrational frequencies of $C_{59}N$) are

summarized in Table 4.1 and compared with our computed frequencies for $C_{59}N$ (see Table 4.2 in Section 4.5 for all the 174 calculated frequencies), as well as those of C_{60} and $C_{59}HN$.

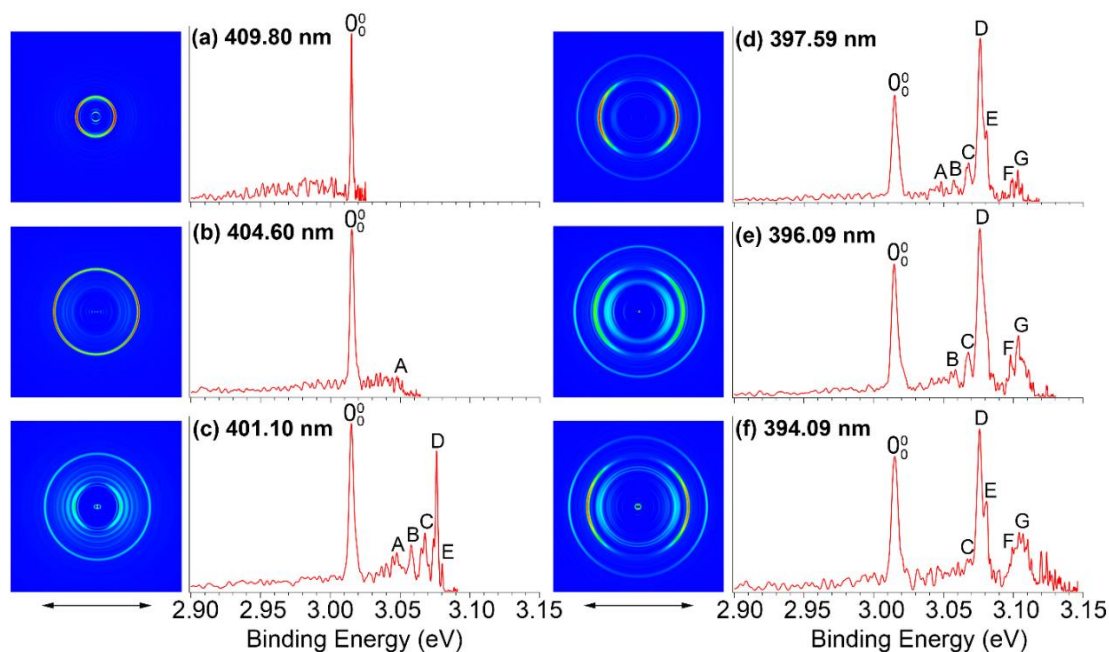


Figure 4.2. Photoelectron images and spectra of $C_{59}N^-$ at six different wavelengths. The double arrow below the images indicates the directions of the laser polarization.

Because of the structural similarities between $C_{59}N$ and C_{60} or $C_{59}HN$, we expect that they should share similar vibrational properties. Indeed, peaks A, B, and E-G, with shifts of 260, 341, 528, 674, and 713 cm^{-1} , are in good agreements with the vibrational frequencies of C_{60} obtained from our previous study of the cold C_{60}^- anion,¹¹⁶ as well as those from inelastic neutron scattering of solid C_{60} .²⁹³ The significant vibrational activities observed in the high-resolution photoelectron imaging of cold C_{60}^- were due to the Jahn-Teller effect in C_{60}^- (${}^2T_{1u}$), which does not have the I_h symmetry of neutral C_{60} . On the other hand, the substitution of a C by a N atom in C_{60} lowers the symmetry of $C_{59}N$ to C_s .²⁶³ Since neutral $C_{59}N$ and $C_{59}N^-$ both have C_s symmetry, all vibrational

Table 4.1. Assignments of observed vibrational peaks from the photoelectron spectra of $C_{59}N^-$. Their binding energies (BE) are given.^a

Peak	BE (eV)	Shift (cm ⁻¹)	Vibrational frequencies (cm ⁻¹)			
			C_{60}^- ^b	Solid C_{60} ^c	$C_{59}HN$ ^d	Theo. $C_{59}N$ ^e
0_0^0	3.0150(7)	0				
A	3.0473(12)	260	262	262, H _g (1) 268, H _g (1)	261.5 271	ν_1 (258) ν_2 (262) ν_3 (268)
B	3.0573(10)	341	348	340, T _{2u} (1) 353, G _u (1)		ν_4 (337) ν_5 (342) ν_6 (350)
C	3.0673(10)	421		431, H _g (2)	424 427	ν_{10} (418)
D	3.0760(7)	492		494, A _g (1)	492	ν_{15} (498)
E	3.0805(10)	528	531	526, T _{1u} (1) 534, H _u (2)	523 529 531	ν_{17} (524) ν_{18} (532) ν_{19} (535)
F	3.0986(7)	674	670	668, H _u (3)		ν_{26} (675) ν_{27} (678)
G	3.1035(7)	713	717	709, H _g (3) 713, T _{2u} (2)		ν_{30} (718) ν_{31} (720)

^aTheir relative shifts to peak 0_0^0 are compared with the vibrational frequencies of C_{60} and $C_{59}HN$, as well as our calculated frequencies for $C_{59}N$.

^bRef. 116: 16 vibrational frequencies of C_{60} were measured by high-resolution PE imaging of cold C_{60}^- .

^cRef. 293: Vibrational frequencies of C_{60} were measured by inelastic neutron scattering of solid C_{60} .

^dRef. 294, Vibrational frequencies of $C_{59}HN$ were measured by IR and Raman spectroscopy.

^eThe vibrational frequencies of $C_{59}N$ were calculated with at the B3LYP/Def2SVP level (see Table 4.2).

modes with A' symmetry are allowed in the photodetachment. We computed the vibrational frequencies of neutral $C_{59}N$ at the B3LYP/Def2SVP level and found 89 A' and 85 A'' modes, as given in Table 4.2 in Section 4.5. Because there is no vibrational degeneracy for the C_s $C_{59}N$, many vibrational modes have close frequencies, making unique assignments of the observed vibrational features for $C_{59}N$ challenging.

Comparing the experimental frequencies with the computed frequencies, we found that peaks A, B, and E can each be assigned to three possible A' modes with close frequencies, while peaks F and G can each be assigned to two possible A' modes, as shown in Table 4.1. Only peaks C and D, with shifts of 421 and 492 cm⁻¹, can be possibly

assigned uniquely to vibrational mode ν_{10} (418 cm^{-1}) and mode ν_{15} (498 cm^{-1}), respectively. The ν_{10} mode involves strong stretching of the N atom, while the mode ν_{15} is a totally symmetric breathing mode, as shown in Fig. 4.4. Note that peak D is the most intense vibrational feature in Figs. 4.2d-f. Similarly, one vibrational peak with frequency of 531 cm^{-1} in the photoelectron spectra of C_{60}^- was observed to be dominant at lower photon energies. This non-Franck-Condon and photon-energy-dependent vibrational intensities were interpreted previously as being due to a strong Hertzberg-Teller coupling in C_{60}^- .¹⁶⁶ The dominant intensity of peak D in Fig. 4.2 may be due to similar vibronic coupling effects in $C_{59}N^-$. The vibrational frequencies of $C_{59}HN$ have been measured by IR and Raman spectroscopy in the form of thin solid films.²⁹⁴ A number of the vibrational frequencies of $C_{59}N$ obtained in the current study are similar to those measured for $C_{59}HN$, as shown in Table 4.1.

The photoelectron images in Fig. 4.2 all exhibit distinct *p*-wave character with the photoelectron angular distributions parallel to the direction of the laser polarization, indicating that photodetachment of $C_{59}N^-$ is from an *s*-type orbital. This observation is consistent with the partial localization of the HOMO on the N atom and the nearby C atom, which shows *sp*³ character (Fig. 4.5).²⁶⁰⁻²⁶⁵

Even though the closed-shell $(C_{59}N)_2$ dimer was the parent azafullerene used to prepare the ESI solution and it was known to be stable in solution,^{256,257} the weak intensity of peak X' compared to peak 0_0^0 in Fig. 4.1 suggested that the majority of the $(C_{59}N)_2$ dimer was dissociated to the monomer either during the reduction by TDAE or in the ESI source. Assuming that $(C_{59}N)_2^{2-}$ and $C_{59}N^-$ have similar detachment cross sections at 354.7 nm, we estimated that the $(C_{59}N)_2^{2-}$ intensity was only ~5% of that for

$C_{59}N^-$ in the $m/z = 722$ mass peak. The low binding energy peak X' in Fig. 4.1 represents the detachment transition from $(C_{59}N)_2^{2-}$ to $(C_{59}N)_2^-$, yielding the second EA of $(C_{59}N)_2$ to be 1.20(5) eV. The first EA of $(C_{59}N)_2$ was calculated to be 2.85 eV, 0.15 eV higher than the calculated EA of $C_{59}N$ (2.70 eV).²⁶² If we assume the same error in the calculated EAs for the monomer and the dimer, we estimated the first EA of $(C_{59}N)_2$ to be ~3.16 eV. The difference between the first and second EA of $(C_{59}N)_2$ can be viewed as the intramolecular Coulomb repulsion between the two extra charges in $(C_{59}N)_2^{2-}$, which is estimated as 1.96 eV. In fact, the difference between the electron binding energies of $C_{59}N^-$ and $(C_{59}N)_2^{2-}$ (1.82 eV) gives a similar intramolecular Coulomb repulsion. The intramolecular electron-electron repulsion in the fullerene dianions, C_n^{2-} ($n = 70, 76, 78, 84$) were estimated to be in the range of 2.745 – 2.37 eV, with smaller values for the larger fullerenes.^{295,296} The even smaller value of 1.96 eV in $(C_{59}N)_2^{2-}$ is consistent with its larger molecular size. The C–C bond between the two $C_{59}N$ units in the azafullerene dimer is known to be quite weak, estimated to be only 7 kcal/mol (0.3 eV) by a thermal homolysis study.²⁷⁸ The Coulomb repulsion between the two extra charges in the dianion is much larger than the C–C bond energy, indicating the $(C_{59}N)_2^{2-}$ dianion is metastable relative to the bond cleavage to form two $C_{59}N^-$ monoanions. This result is consistent with the weak intensity of the dianion in the mass spectrum.

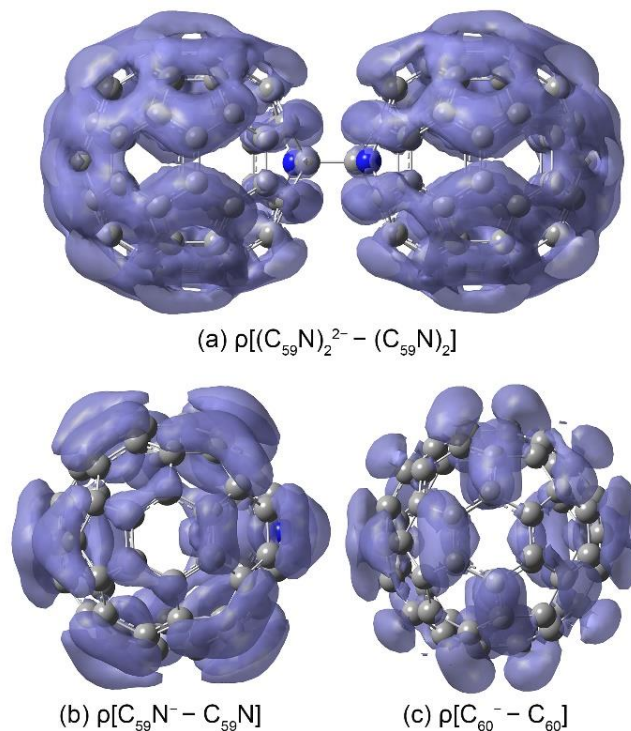


Figure 4.3. Differences of the total electron density ($\Delta\rho$) between anions and neutrals. (a) $(C_{59}N)_2^{2-}$ and $(C_{59}N)_2$, (b) $C_{59}N^-$ and $C_{59}N$, and (c) C_{60}^- and C_{60} . The calculations were done at the level of B3LYP/6-311++G(d,p).

To further understand the intramolecular Coulomb repulsion in $(C_{59}N)_2^{2-}$, we calculated the difference of the total electron density ($\Delta\rho$) between $(C_{59}N)_2^{2-}$ and $(C_{59}N)_2$ at the B3LYP/6-311++G(d,p) level using the Gaussian 09 package,²⁵² as shown in Fig. 4.3a. We used the optimized geometries under the same level of theory and basis sets for both the dianion and neutral. For comparison, we also computed the $\Delta\rho$ between $C_{59}N^-$ and $C_{59}N$ (Fig. 4.3b), as well as that between C_{60}^- and C_{60} (Fig. 4.3c). As shown in Fig. 4.3a, the extra electrons are delocalized over the surface of the azafullerene dimer with less densities near the N atoms but higher densities on the two ends. The uneven charge distribution is consistent with the expected Coulomb repulsion between the two extra electrons, and it is quite different from the localization of the HOMO on the N atoms in

neutral $(C_{59}N)_2$.^{260-262,268,269} In comparison, the extra electron in $C_{59}N^-$ is delocalized over the azafullerene surface with slightly more charge localized on the N atom (Fig. 4.3b), while the extra charge in C_{60}^- is evenly distributed over the fullerene surface (Fig. 4.3c).

4.4 Conclusion

In conclusion, we report the first high-resolution photoelectron imaging study of $C_{59}N^-$ and the first observation of the azafullerene dimer dianion $(C_{59}N)_2^{2-}$. The EA of $C_{59}N$ is measured accurately to be 3.0150(7) eV. Seven vibrational frequencies are also obtained for $C_{59}N$ and are assigned by comparing with calculated frequencies and those of C_{60} and $C_{59}HN$. Similar vibrational frequencies are observed for the three species, suggesting relatively small geometry changes upon substitution of one C by one N atom on the C_{60} cage. The photoelectron spectrum of the $(C_{59}N)_2^{2-}$ dimer dianion yielded a second EA for $(C_{59}N)_2$ to be 1.20(5) eV. The intramolecular Coulomb repulsion between the two extra charges in the dimer dianion was estimated to be 1.96 eV, much higher than the C–C bond linking the dimer, suggesting $(C_{59}N)_2^{2-}$ is metastable relative to dissociation to two $C_{59}N^-$, i.e., the $(C_{59}N)_2^{2-} \rightarrow 2C_{59}N^-$ reaction is exothermic. The intramolecular electron repulsion is investigated by the difference of the total electron density between $(C_{59}N)_2^{2-}$ and $(C_{59}N)_2$, revealing that the extra charges are pushed away from each other toward the two ends of the azafullerene dimer.

4.5 Supporting information

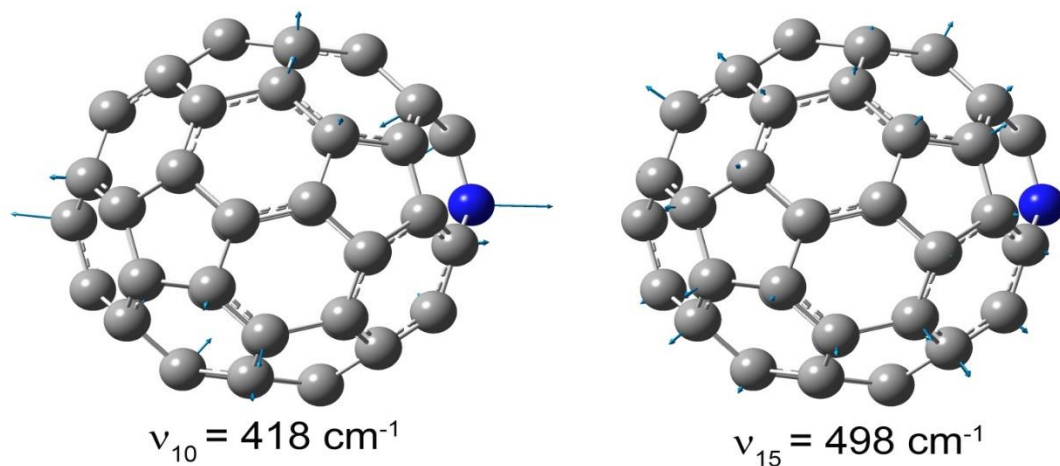


Figure 4.4. The ν_{10} and ν_{15} vibrational modes of $C_{59}N$.

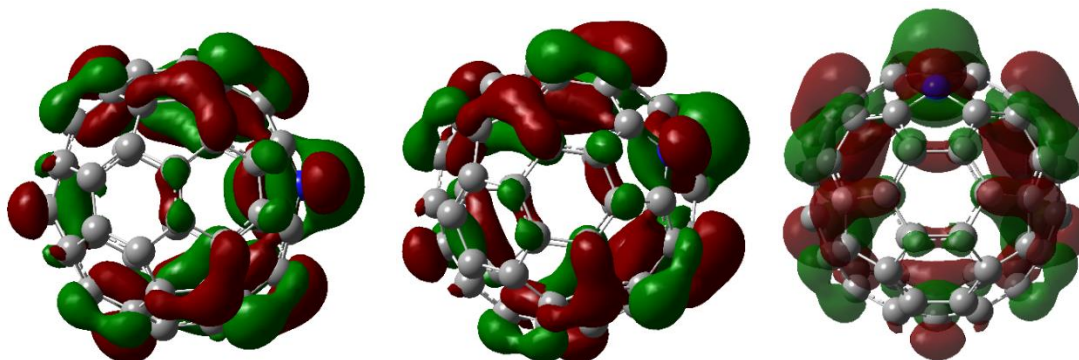


Figure 4.5. Three different views of the HOMO of $C_{59}N^-$. It shows the extra electron densities near the N atom.

Table 4.2. Calculated harmonic frequencies for C₅₉N. The calculations were done at the B3LYP/Def2SVP level of theory. The unit of frequency is cm⁻¹.

Mode	Freq.	Mode	Freq.	Mode	Freq.	Mode	Freq.
A' symmetry				A'' symmetry			
v ₁	258	v ₄₆	840	v ₉₀	261	v ₁₃₅	845
v ₂	262	v ₄₇	981	v ₉₁	265	v ₁₃₆	967
v ₃	268	v ₄₈	985	v ₉₂	346	v ₁₃₇	982
v ₄	337	v ₄₉	989	v ₉₃	352	v ₁₃₈	983
v ₅	342	v ₅₀	996	v ₉₄	355	v ₁₃₉	997
v ₆	350	v ₅₁	1107	v ₉₅	398	v ₁₄₀	1108
v ₇	356	v ₅₂	1115	v ₉₆	404	v ₁₄₁	1117
v ₈	406	v ₅₃	1122	v ₉₇	408	v ₁₄₂	1130
v ₉	407	v ₅₄	1132	v ₉₈	419	v ₁₄₃	1136
v ₁₀	418	v ₅₅	1140	v ₉₉	438	v ₁₄₄	1196
v ₁₁	431	v ₅₆	1207	v ₁₀₀	480	v ₁₄₅	1220
v ₁₂	435	v ₅₇	1216	v ₁₀₁	483	v ₁₄₆	1233
v ₁₃	477	v ₅₈	1223	v ₁₀₂	526	v ₁₄₇	1248
v ₁₄	482	v ₅₉	1231	v ₁₀₃	526	v ₁₄₈	1251
v ₁₅	498	v ₆₀	1239	v ₁₀₄	533	v ₁₄₉	1274
v ₁₆	506	v ₆₁	1257	v ₁₀₅	538	v ₁₅₀	1289
v ₁₇	524	v ₆₂	1281	v ₁₀₆	564	v ₁₅₁	1310
v ₁₈	532	v ₆₃	1291	v ₁₀₇	568	v ₁₅₂	1320
v ₁₉	535	v ₆₄	1295	v ₁₀₈	569	v ₁₅₃	1338
v ₂₀	563	v ₆₅	1315	v ₁₀₉	577	v ₁₅₄	1343
v ₂₁	567	v ₆₆	1341	v ₁₁₀	579	v ₁₅₅	1347
v ₂₂	576	v ₆₇	1343	v ₁₁₁	582	v ₁₅₆	1350
v ₂₃	579	v ₆₈	1350	v ₁₁₂	590	v ₁₅₇	1364
v ₂₄	587	v ₆₉	1355	v ₁₁₃	675	v ₁₅₈	1381
v ₂₅	592	v ₇₀	1378	v ₁₁₄	679	v ₁₅₉	1383
v ₂₆	675	v ₇₁	1384	v ₁₁₅	683	v ₁₆₀	1389
v ₂₇	678	v ₇₂	1397	v ₁₁₆	690	v ₁₆₁	1393
v ₂₈	684	v ₇₃	1415	v ₁₁₇	712	v ₁₆₂	1417
v ₂₉	699	v ₇₄	1430	v ₁₁₈	713	v ₁₆₃	1451
v ₃₀	718	v ₇₅	1456	v ₁₁₉	721	v ₁₆₄	1461
v ₃₁	720	v ₇₆	1463	v ₁₂₀	727	v ₁₆₅	1473
v ₃₂	724	v ₇₇	1472	v ₁₂₁	728	v ₁₆₆	1476
v ₃₃	724	v ₇₈	1473	v ₁₂₂	732	v ₁₆₇	1542
v ₃₄	729	v ₇₉	1478	v ₁₂₃	734	v ₁₆₈	1553
v ₃₅	735	v ₈₀	1505	v ₁₂₄	741	v ₁₆₉	1569
v ₃₆	743	v ₈₁	1531	v ₁₂₅	742	v ₁₇₀	1588
v ₃₇	748	v ₈₂	1543	v ₁₂₆	752	v ₁₇₁	1599
v ₃₈	751	v ₈₃	1558	v ₁₂₇	755	v ₁₇₂	1603
v ₃₉	751	v ₈₄	1571	v ₁₂₈	763	v ₁₇₃	1614
v ₄₀	764	v ₈₅	1585	v ₁₂₉	767	v ₁₇₄	1617
v ₄₁	768	v ₈₆	1606	v ₁₃₀	785		
v ₄₂	786	v ₈₇	1612	v ₁₃₁	792		
v ₄₃	789	v ₈₈	1616	v ₁₃₂	805		
v ₄₄	791	v ₈₉	1623	v ₁₃₃	807		
v ₄₅	810			v ₁₃₄	841		

Chapter 5 Probing the intramolecular interactions in

$\text{H}_2\text{O}@C_{60}^-$ and $\text{H}_2\text{O}@C_{59}\text{N}^-$ [‡]

This chapter²⁹⁷ will report a high-resolution photoelectron imaging study of cryogenically-cooled $\text{H}_2\text{O}@C_{60}^-$ and $\text{H}_2\text{O}@C_{59}\text{N}^-$ endohedral fullerene anions. The electron affinity (EA) of $\text{H}_2\text{O}@C_{60}$ is measured to be 2.6923 ± 0.0008 eV, which is 0.0088 eV higher than the EA of C_{60} , while the EA of $\text{H}_2\text{O}@C_{59}\text{N}$ is measured to be $3.0058 \text{ eV} \pm 0.0007 \text{ eV}$, which is 0.0092 eV *lower* than the EA of $C_{59}\text{N}$. The opposite shifts are found to be due to the different electrostatic interactions between the encapsulated water molecule and the fullerene cages in the two systems. There is a net Coulombic attraction between the guest and host in $\text{H}_2\text{O}@C_{60}^-$, but a repulsive interaction in $\text{H}_2\text{O}@C_{59}\text{N}^-$. We have also observed low-frequency features in the photoelectron spectra tentatively attributed to the hindered rotational excitations of the encapsulated H_2O molecule, providing further insights into the guest-host interactions in $\text{H}_2\text{O}@C_{60}^-$ and $\text{H}_2\text{O}@C_{59}\text{N}^-$.

5.1 Introduction

Endohedral fullerenes with encapsulated atoms, molecules or clusters have attracted wide interest due to their unique electronic, magnetic, and optical properties.²⁹⁸⁻³⁰⁰ Since the first observation of the endohedral fullerene $\text{La}@C_{60}$ in a mass spectrum in 1985,³⁰¹ a variety of such novel guest-host complexes containing noble gas atoms,^{302,303} the N atom and the N_2 molecule,^{304,305} metal atoms and metal clusters,^{300,306,307} have been

[‡] The content of this chapter is reproduced or adapted from Ref. 297, [G. Z. Zhu, Y. Liu, Y. Hashikawa, Q. F. Zhang, Y. Murata, and L. S. Wang, *Chem. Sci.* **9**, 5666-5671 (2018).], with permission from the Royal Society of Chemistry.

synthesized using the arc discharge or ion bombardment methods. These harsh production conditions were unable to make endofullerenes containing light molecules.³⁰⁸ A more rational synthetic approach, called molecular surgery on the fullerene surfaces,^{309,310} was successfully applied to the macroscopic synthesis of $\text{H}_2@\text{C}_{60}$,³¹¹ followed by the syntheses of $\text{H}_2\text{O}@\text{C}_{60}$,^{312,313} $\text{H}_2\text{O}@\text{C}_{59}\text{N}$,²²⁷ $\text{HF}@\text{C}_{60}$,³¹⁴ $(\text{H}_2\text{O})_2@\text{C}_{70}$,³¹⁵ and very recently even $(\text{H}_2\text{O}\cdot\text{HF})@\text{C}_{70}$.³¹⁶ The $\text{H}_2\text{O}@\text{C}_{60}$ and $\text{H}_2\text{O}@\text{C}_{59}\text{N}$ species are of special interest because the water molecule is isolated without hydrogen bonds. Many experimental and theoretical studies have been carried out to elucidate the novel properties of $\text{H}_2\text{O}@\text{C}_{60}$, such as its polarity,³¹⁷⁻³²³ quantum dynamics,³²⁴⁻³²⁹ magnetic,^{227,330} mechanical,³³¹ thermal³³² and electric properties^{322,323,333,334} as well as its chemical reactivity.^{321,335,336}

One of the most interesting questions about $\text{H}_2\text{O}@\text{C}_{60}$ concerned the nature of the guest-host interactions of the water molecule trapped in the C_{60} cage. No detectable difference was observed between the UV-Vis absorption spectra of the empty C_{60} and $\text{H}_2\text{O}@\text{C}_{60}$, suggesting that the water molecule has very weak interactions with the cage.³¹² This observation was further confirmed by studies of nuclear spin relaxation³³⁰ and electric conductance.³³⁴ However, theoretical calculations found strong dispersion interactions^{319,320,337-339} between the free rotating water molecule and C_{60} .^{312,320,324,339,340} The quantized rotational levels and the nuclear spin-isomerism of *ortho*- and *para*-water in $\text{H}_2\text{O}@\text{C}_{60}$ were studied by inelastic neutron scattering, far-infrared spectroscopy, and nuclear magnetic resonance.³²⁴⁻³²⁶ These studies revealed a splitting of the ground rotational state of *ortho*- H_2O and a symmetry-breaking of the C_{60} cage, indicating a quadrupolar interaction between H_2O and C_{60} .³²⁷⁻³²⁹ In addition, the dipole moment of

$\text{H}_2\text{O}@C_{60}$ was measured to be around 0.5 D,^{322,323} in good agreement with theoretical calculations.³¹⁷⁻³²¹ The significant reduction of the dipole moment of the encapsulated H_2O is a result of the strong shielding effect by the nonpolar C_{60} cage. A recent study reported that the rotation of the encapsulated water can be electrostatically perturbed by introducing polarized $C(C_{60})-X$ (X : heteroatom) bonds.³⁴¹

Unlike the extensive studies on $\text{H}_2\text{O}@C_{60}$, the $\text{H}_2\text{O}@C_{59}\text{N}$ endohedral azafullerene was only synthesized very recently in the dimer form, $(\text{H}_2\text{O}@C_{59}\text{N})_2$.²²⁷ The presence of the N atom breaks the symmetry of the fullerene and introduces a polar center. Theoretical calculations suggested an attractive electrostatic interaction between the O atom of H_2O and the N atom of $C_{59}\text{N}$.^{227,342,343} Comparison of the different guest-host interactions in $\text{H}_2\text{O}@C_{60}$ and $\text{H}_2\text{O}@C_{59}\text{N}$ would be very interesting. In particular, the electron affinity (EA) of the endohedral fullerenes can be a good probe of these guest-host interactions, because the extra electron in the C_{60}^- and $C_{59}\text{N}^-$ anions is expected to be sensitive to the encapsulated H_2O molecule.

Here, we present a high-resolution photoelectron imaging study of the $\text{H}_2\text{O}@C_{60}^-$ and $\text{H}_2\text{O}@C_{59}\text{N}^-$ anions cooled in a cryogenic ion trap. The EA of $\text{H}_2\text{O}@C_{60}$ is accurately measured to be 2.6923 ± 0.0008 eV, which is 0.0088 eV higher than the EA of C_{60} ,¹¹⁶ while the EA of $\text{H}_2\text{O}@C_{59}\text{N}$ is measured to be $3.0058 \text{ eV} \pm 0.0007$ eV, which is 0.0092 eV *lower* than the EA of $C_{59}\text{N}$.²⁵⁵ The opposite shifts suggest different guest-host interactions between the encapsulated water molecule and the fullerene cages, which are understood by an electrostatic model. A net Coulombic attraction between the water molecule and the HOMO electron in $\text{H}_2\text{O}@C_{60}^-$ is found to stabilize the anion and enhance the EA of $\text{H}_2\text{O}@C_{60}$ compared to C_{60} , while a repulsive interaction in

$\text{H}_2\text{O}@C_{59}\text{N}^-$ destabilizes the anion and decreases the EA of $\text{H}_2\text{O}@C_{59}\text{N}$ relative to $C_{59}\text{N}$. In addition, low-frequency features in the photoelectron spectra are observed and tentatively attributed to the hindered rotational excitations³²⁷⁻³²⁹ of the encapsulated H_2O molecule, providing further insights into the guest-host interactions in $\text{H}_2\text{O}@C_{60}^-$ and $\text{H}_2\text{O}@C_{59}\text{N}^-$.

5.2 Experimental methods

The experiments were done using our ESI-PES apparatus. The experimental details were provided in Chapter 2.

5.3 Results and discussion

5.3.1 The photoelectron images and spectra at 354.7 nm

Figure 5.1 shows the photoelectron images and spectra of $\text{H}_2\text{O}@C_{60}^-$ and $\text{H}_2\text{O}@C_{59}\text{N}^-$ at 354.7 nm. The first intense peak in each spectrum, labeled as 0_0^0 , represents the 0-0 transition from the anion to the neutral and defines the EAs for $\text{H}_2\text{O}@C_{60}$ and $\text{H}_2\text{O}@C_{59}\text{N}$, which are measured more accurately in the low photon energy spectra (*vide infra*). The peaks at higher binding energies represent transitions from the ground vibrational state of the anion to the excited vibrational levels of the neutral ground electronic state. They are better resolved in the high-resolution photoelectron images at lower photon energies near the detachment threshold to be discussed below. Fig. 5.1b also shows a weak peak (X') at ~ 1.2 eV, which is derived from the parent dimer dianion, $(\text{H}_2\text{O}@C_{59}\text{N})_2^{2-}$ with the same m/z as the monoanion. A similar dimer dianion was also observed in the 354.7 nm PE spectrum of $C_{59}\text{N}^-$

recently.²⁵⁵ The low binding energy for the dianion was due to the strong intramolecular Coulomb repulsion.^{15,75,291}

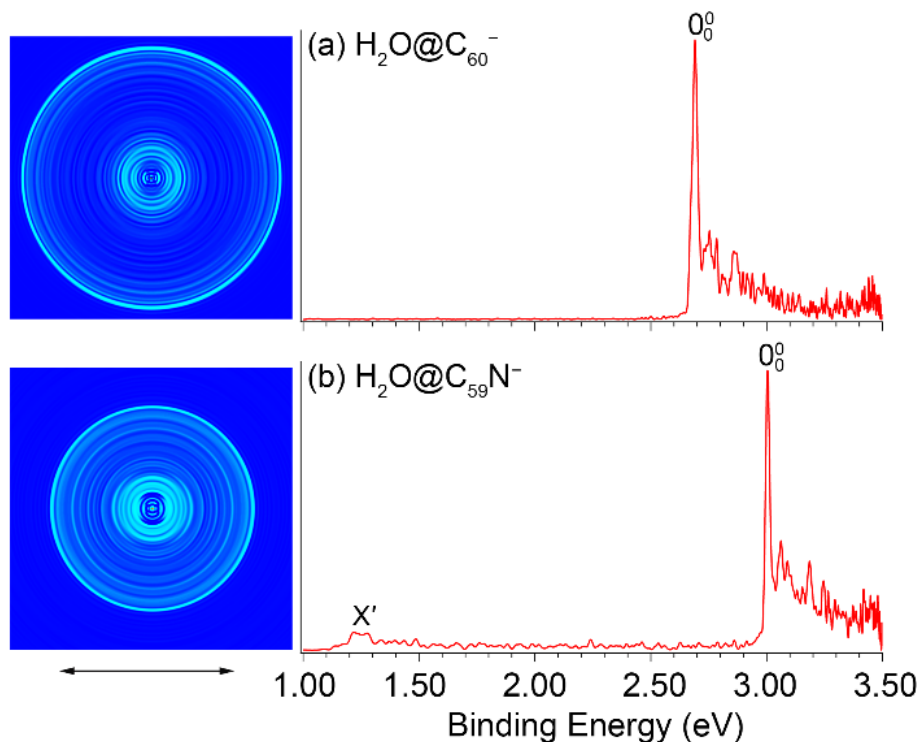


Figure 5.1. Photoelectron images and spectra of fullerene anions at 354.7 nm. (a) $\text{H}_2\text{O}@C_{60}^-$ and (b) $\text{H}_2\text{O}@C_{59}\text{N}^-$. The double arrow below the images indicates the direction of the laser polarization. Note the image corresponding to peak X' in (b) is cut off.

The 354.7 nm spectra of the endohedral fullerenes appear to be nearly identical to those of their corresponding parent fullerenes,^{116,255} as directly compared in Fig. 5.2. This observation suggests that indeed the encapsulated water molecule has little effect on the electronic and geometrical structures of the fullerene hosts. However, upon closer examination, a small spectral shift was revealed in each case, as shown in the expanded threshold region given in the respective inset of Fig. 5.2. Surprisingly, the two endohedral fullerenes exhibit opposite shifts. The electron binding energy of $\text{H}_2\text{O}@C_{60}^-$ was observed to be shifted slightly higher relative to that of C_{60}^- (Fig. 5.2a), whereas the

electron binding energy of $\text{H}_2\text{O}@C_{59}\text{N}^-$ was shifted slightly lower relative to that of $C_{59}\text{N}^-$. The opposite spectral shifts suggest subtle differences in the guest-host interactions of the encapsulated water molecule with the fullerene or azafullerene cages.

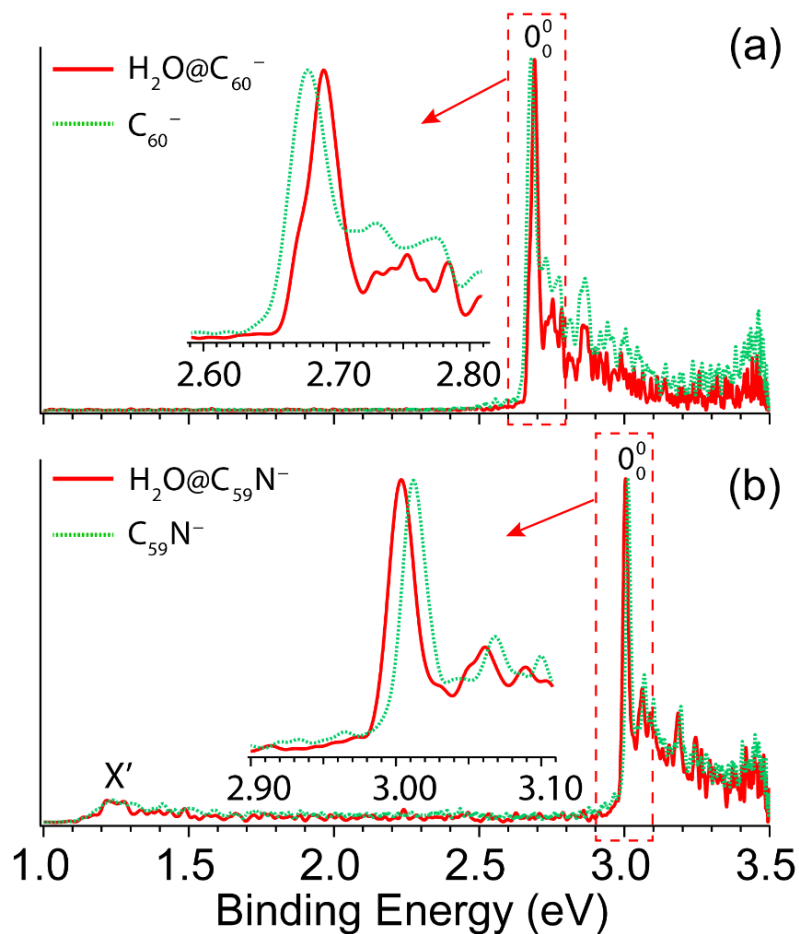


Figure 5.2. Comparisons of the photoelectron spectra of fullerene anions. (a) C_{60}^- and $\text{H}_2\text{O}@C_{60}^-$, (b) $C_{59}\text{N}^-$ and $\text{H}_2\text{O}@C_{59}\text{N}^-$ at 354.7 nm.

5.2.2 The photoelectron images and spectra near detachment thresholds

To measure the EAs more accurately and to resolve low-frequency vibrations, we measured PE images for $\text{H}_2\text{O}@C_{60}^-$ and $\text{H}_2\text{O}@C_{59}\text{N}^-$ at lower photon energies near the detachment thresholds, as shown in Fig. 5.3. We found that the detachment cross sections for the endohedral fullerenes were weaker than those of the corresponding empty fullerenes,^{116,255} in particular near the detachment thresholds. The spectra shown in Fig.

5.3 were averaged from 300,000 to 500,000 laser shots. At 456.60 nm (Fig. 5.3a), the 0_0^0 peak with a linewidth of 38 cm^{-1} at an electron kinetic energy of 186 cm^{-1} defines the most accurate value for the EA of $\text{H}_2\text{O}@C_{60}$ as $2.6923 \pm 0.0008\text{ eV}$, which is 0.0088 eV higher than the EA of C_{60} .¹¹⁶ The detachment cross section at this wavelength for $\text{H}_2\text{O}@C_{60}^-$ was particularly poor. The features below the 0_0^0 peak in Fig. 5.3a were partly due to background noise and partly due to hot band transitions, which were amplified relative to the 0_0^0 transition. At 411.12 nm (Fig. 5.3d), the 0_0^0 peak with an electron kinetic energy of 80 cm^{-1} and linewidth of 15 cm^{-1} yields the most accurate EA for $\text{H}_2\text{O}@C_{59}\text{N}$ to be $3.0058\text{ eV} \pm 0.0007\text{ eV}$, which is 0.0092 eV lower than the EA of $C_{59}\text{N}$.²⁵⁵

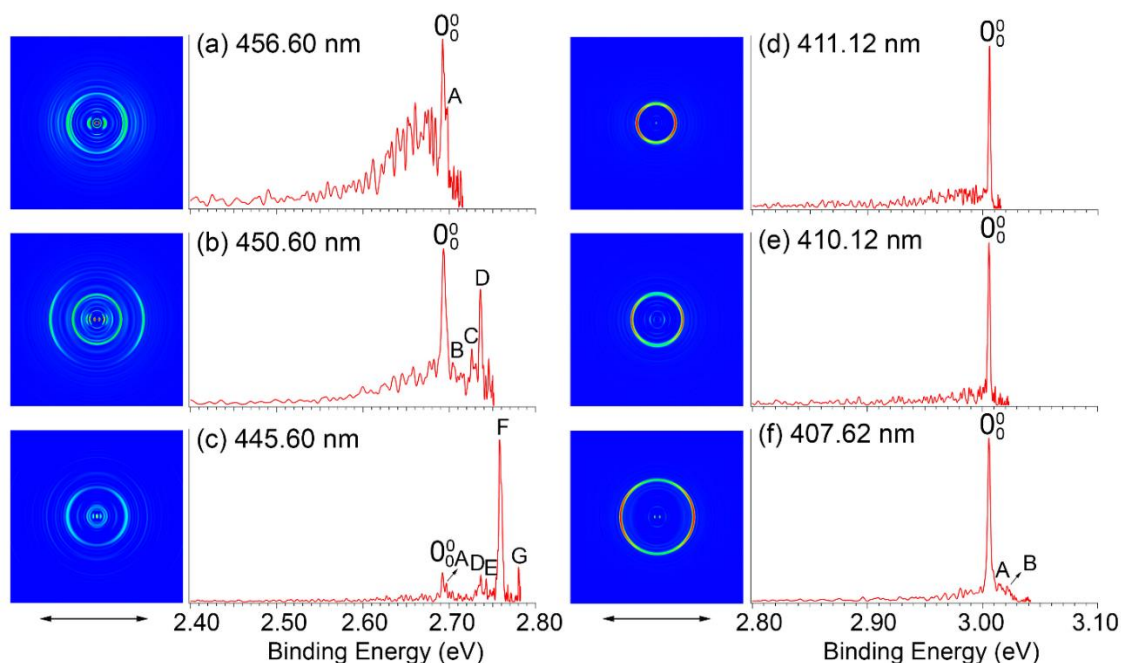


Figure 5.3. Photoelectron images and spectra of $\text{H}_2\text{O}@C_{60}^-$ and $\text{H}_2\text{O}@C_{59}\text{N}^-$ at various photon energies. $\text{H}_2\text{O}@C_{60}^-$: (a) 456.60 nm, (b) 450.60 nm and (c) 445.60 nm. $\text{H}_2\text{O}@C_{59}\text{N}^-$: (d) 411.12 nm, (e) 410.12 nm and (f) 407.62 nm. The double arrows below the images indicate the direction of the laser polarization.

In addition to the near-threshold spectra, two more spectra were taken to resolve low-frequency vibrational features for H₂O@C₆₀ and H₂O@C₅₉N, as shown in Figs. 5.3b-c and Figs. 5.3e-f, respectively. There are two types of vibrations for the endohedral fullerenes, one involving the fullerene cage and the other involving the encapsulated water molecules including the hindered rotations. The latter should be particularly sensitive to the guest-host interactions in the endohedral fullerenes. Figs. 5.3a-c resolve seven vibrational peaks, labeled as A-G for H₂O@C₆₀, while Fig. 5.3f resolve two peaks, A and B for H₂O@C₅₉N. The relative intensities of the low frequency peaks (A, B) are quite weak for both species, but they seem to be reproducible. The binding energies and shifts to the 0₀⁰ peak for all the vibrational features are summarized in Table 5.1.

Table 5.1. Observed vibrational peaks for H₂O@C₆₀⁻ and H₂O@C₅₉N⁻. Their binding energies (BE) measured from the photoelectron spectra in Fig. 5.3. Their shifts to peak 0₀⁰ are compared with the vibrational frequencies of C₆₀. The numbers in parentheses indicate the experimental uncertainties.

Anions	Peaks	BE (eV)	Shifts (cm ⁻¹)	Vib. Freq. (cm ⁻¹) ^a
C ₆₀ ⁻		2.6835(6) ^a		
H ₂ O@C ₆₀ ⁻	0 ₀ ⁰	2.6923(8)	0	
	A	2.6967(7)	35	
	B	2.7041(10)	95	
	C	2.7259(10)	271	262
	D	2.7361(7)	353	348
	E	2.7427(10)	406	
	F	2.7582(7)	531	531
G	2.7803(10)	710	717	
C ₅₉ N ⁻		3.0150(7) ^b		
H ₂ O@C ₅₉ N ⁻	0 ₀ ⁰	3.0058(7)	0	
	A	3.0151(12)	74	
	B	3.0217(12)	128	

^aRef. 116; ^bRef. 255.

Peaks C, D, F, G with shifts of 271, 353, 531, and 710 cm⁻¹, are similar to those observed in the photoelectron spectra of C₆₀⁻ and they should correspond to vibrational modes involving the C₆₀ cage.¹¹⁶ The strong and highly non-Franck-Condon peak F

observed in the 445.60 nm spectrum (Fig. 5.3c) is also observed for C_{60}^- , which was attributed to strong Hertzberg-Teller coupling.¹¹⁶ The weak peak E with a shift of 406 cm^{-1} corresponds to a $H_u(1)$ vibrational mode of C_{60} also observed by inelastic neutron scattering.²⁹³ These observations suggest that the H_2O molecule has little effect on the geometrical and electronic structure of the C_{60} host. Additionally, two weak peaks A and B with small shifts of 35 and 95 cm^{-1} , corresponding to very low-frequency transitions, are also tentatively identified. The lowest vibrational frequency of C_{60} is 260 cm^{-1} .^{116,255} Hence, these features should correspond to the hindered rotational excitations of the encapsulated water molecule, as revealed by the rigorous full-dimensional quantum calculations of the coupled translation-rotation excitations of the encapsulated water molecule. The observation of hindered rotational transitions indicates weak interactions between the encapsulated water molecule and the fullerene cages. The relatively high frequencies observed for the hindered rotational transitions in $\text{H}_2\text{O}@C_{59}\text{N}$ suggest stronger guest-host interactions in this system.

The photoelectron images of $\text{H}_2\text{O}@C_{60}^-$ and $\text{H}_2\text{O}@C_{59}\text{N}^-$ in Fig. 5.3 all exhibit distinct p -wave character with the photoelectron angular distributions parallel to the direction of the laser polarization, similar to those for C_{60}^- and $C_{59}\text{N}^-$.^{116,255} These observations indicate that the encapsulated water molecule does not affect the s -like HOMO of the fullerene cages. The p -wave nature of the outgoing electron is partly responsible for the low detachment cross sections near threshold according to the Wigner threshold law.⁵⁷

5.2.3 The opposite shifts of the EAs: An electrostatic model

The opposite shifts of the EAs of $\text{H}_2\text{O}@C_{60}$ and $\text{H}_2\text{O}@C_{59}\text{N}$ relative to their corresponding empty cages are consistent with previous theoretical calculations.^{321,342} The different effects of the encapsulated water on the EAs can be glimpsed from the electrostatic potential maps of the HOMO of the fullerene anions, as presented in Fig. 5.4. The extra charge in the half-filled HOMO of C_{60}^- is evenly distributed on the surface (Fig. 5.4a). Even though the encapsulated water molecule was known to have no preferred directions,^{312,320,324,339,340} it breaks the symmetry and dynamically induces a slightly higher charge density on the cage surface, where the H atoms point to (Fig. 5.4b).

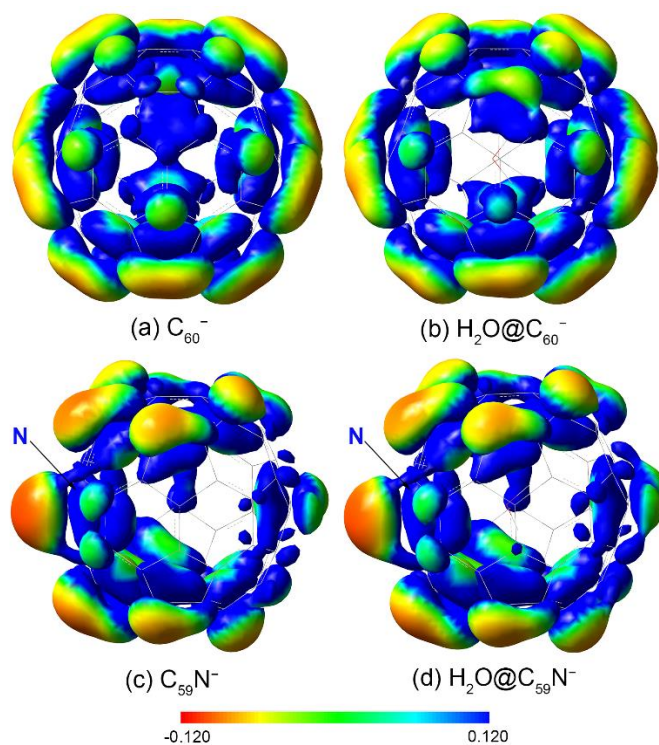


Figure 5.4. The electrostatic potential maps for the HOMO of fullerene anions. (a) C_{60}^- , (b) $\text{H}_2\text{O}@C_{60}^-$, (c) $C_{59}\text{N}^-$, (d) $\text{H}_2\text{O}@C_{59}\text{N}^-$. The calculation were done at B3LYP/6-311++G(d,p) level using the Gaussian 09 package.²⁵²

On the contrary, the HOMO of $C_{59}\text{N}^-$ is partially localized on the N atom and the C atoms around the N atom (Fig. 5.4c).²⁵⁵ The water molecule in $\text{H}_2\text{O}@C_{59}\text{N}^-$ has been

shown to adopt a global minimal structure with the O atom pointing to the N atom of the cage due to a weak N...O attractive interaction.^{342,343} Despite its orientation preference, the water encapsulation has relatively little effect on the HOMO of $C_{59}\text{N}^-$ (Fig. 5.4d). However, this orientation of the water molecule brings the electronegative O atom closer to the extra charge, inducing a repulsive interaction.

A simple electrostatic model is used to understand the interactions between the water molecule and the extra charge in the HOMO of the fullerene cages and to obtain insights about the observed different EA shifts in the two systems. In the model, partial charges on the water molecule are represented by point charges with $-2q$ located on the oxygen atom and $+q$ on each H atom, where q is obtained from a Mulliken population analysis of the total wavefunction of the water molecule. The Coulomb interaction can be expressed as:

$$V_{Coulomb} = - \sum_{i=1}^3 q_i \int d\vec{r} \frac{|\varphi_{HOMO}(\vec{r})|^2}{|\vec{r} - \vec{r}_i|}$$

where q_i and r_i represent the charge and position of each atom in the water molecule, $\varphi_{HOMO}(r)$ is the Kohn-Sham wavefunction of the HOMO of $\text{H}_2\text{O}@C_{60}^-$ and $\text{H}_2\text{O}@C_{59}\text{N}^-$ extracted from DFT calculations.³⁴⁴ The numerical integration is done with a fine grid converging to 1 meV accuracy. All the geometry optimization and electronic structure calculations were done using DFT at B3LYP/6-311++G(d,p) level of theory with the Gaussian 09 package.²⁵²

The Coulomb interaction in $\text{H}_2\text{O}@C_{60}^-$ was calculated to be -23 meV, indicating an attractive interaction between the encapsulated water molecule and the HOMO electron in $\text{H}_2\text{O}@C_{60}^-$. This weak attraction, which is in good agreement with previous

calculations,^{319,337-339} stabilizes the $\text{H}_2\text{O}@C_{60}^-$ anion and increases the EA of $\text{H}_2\text{O}@C_{60}$ relative to C_{60} . On the other hand, the simple electrostatic calculation on the $\text{H}_2\text{O}@C_{59}\text{N}^-$ anion yields a repulsive interaction of 64 meV. Hence, the water encapsulation destabilized the HOMO of the $C_{59}\text{N}^-$ anion, reducing the EA of $\text{H}_2\text{O}@C_{59}\text{N}$ relative to $C_{59}\text{N}$. This repulsive interaction is expected from the orientation of the H_2O molecule in $C_{59}\text{N}^-$ and its asymmetric electron density distribution (Fig. 5.4d). Even though the electrostatic model is rather crude, it correctly predicts the directions of the EA shifts in the two endohedral fullerenes. The interactions between the encapsulated water molecule and the fullerene cages are so weak that they were not detectable in the UV-Vis absorption spectra³¹² or the electrical conductance experiment.³³⁴

5.4 Conclusions

In conclusion, we report a high-resolution photoelectron imaging study of two endohedral fullerene anions, $\text{H}_2\text{O}@C_{60}^-$ and $\text{H}_2\text{O}@C_{59}\text{N}^-$. Accurate electron affinities are obtained for $\text{H}_2\text{O}@C_{60}$ (2.6923 ± 0.0008 eV) and $\text{H}_2\text{O}@C_{59}\text{N}$ (3.0058 ± 0.0007 eV) for the first time. The EA of $\text{H}_2\text{O}@C_{60}$ is found to be higher than that of C_{60} by 0.0088 eV, whereas the EA of $\text{H}_2\text{O}@C_{59}\text{N}$ is found to be lower than that of $C_{59}\text{N}$ by 0.0092 eV. These small EA shifts reflect the weak guest-host interactions in the endohedral fullerenes and the opposite shifts are understood using a simple electrostatic model between the encapsulated H_2O molecule and the HOMO of the fullerene anions. Low-frequency features due to the hindered rotational transitions of the encapsulated water molecule are also tentatively identified, providing further insight into the weak guest-host interactions in the two endohedral fullerenes.

Chapter 6 Dipole-bound excited states and resonant photoelectron imaging of $C_6H_5O^-$ and $C_6H_5S^-$ [§]

This chapter¹²² reports a photodetachment and resonant photoelectron-imaging studies of cryogenically cooled phenoxide ($C_6H_5O^-$) and thiophenoxide ($C_6H_5S^-$) anions. In a previous study¹¹⁷ a dipole-bound excited state was observed for $C_6H_5O^-$ at 97 cm^{-1} below the detachment threshold. Eight resonant photoelectron spectra were obtained via excitations to eight vibrational levels of the dipole-bound state (DBS) followed by autodetachment. Here we present a complete photodetachment spectrum of $C_6H_5O^-$ covering a spectral range $2,600\text{ cm}^{-1}$ above the detachment threshold and revealing nine additional vibrational resonances of the DBS. We also report the first observation of a dipole-bound excited state for $C_6H_5S^-$, 39 cm^{-1} below its detachment threshold of $18,982\text{ cm}^{-1}$. Photodetachment spectroscopy covering a spectral range $1,500\text{ cm}^{-1}$ above threshold reveals twelve vibrational resonances for the DBS of $C_6H_5S^-$. By tuning the detachment laser to the vibrational resonances in the DBS of $C_6H_5O^-$ and $C_6H_5S^-$, we obtain highly non-Franck-Condon resonant photoelectron spectra, as a result of mode-selectivity and the $\Delta v = -1$ propensity rule for vibrational autodetachment. Five new fundamental vibrational frequencies are obtained for the ground state of the C_6H_5O (X^2B_1) radical. Intramolecular inelastic scattering is observed in some of the resonant photoelectron spectra, leading to the excitation of the Franck-Condon-inactive lowest-frequency bending mode (ν_{20}) of C_6H_5O . The first excited state of C_6H_5O (A^2B_2) is observed to be 0.953 eV above the ground state. Twelve resonant photoelectron spectra

[§] The content of this chapter is reproduced from [G. Z. Zhu, C. H. Qian, and L. S. Wang, Dipole-bound excited states and resonant photoelectron imaging of phenoxide and thiophenoxide anions. *J. Chem. Phys.* **149**, 164301 (2018).], with the permission of AIP Publishing.

are obtained for $C_6H_5S^-$, allowing the measurements of seven fundamental vibrational frequencies of the C_6H_5S radical, whereas the non-resonant photoelectron spectrum only exhibits a single Franck-Condon active mode. The current study again demonstrates that the combination of photodetachment spectroscopy and resonant photoelectron spectroscopy is a powerful technique to obtain vibrational information about polar radical species.

6.1 Introduction

Due to the important role as the chromophore in aromatic amino acid tyrosine, which acts as the key catalysis in biological enzymes like photosystem II and the water oxidizing enzyme,³⁴⁵ the photochemistry of phenol has received considerable attentions.³⁴⁶⁻³⁴⁸ Extensive studies on the photodissociation of phenol, i.e., fission of the O-H bond to form H atom and the phenoxy radical (C_6H_5O), have shown the significance of the nonradiative decay pathway via the optically dark $^1\pi\sigma^*$ state for the protection from photochemical damage following UV absorptions.^{346,349-356} The photodissociation of thiophenol, the sulfur analogue of phenol, has also been widely investigated, revealing a similar $^1\pi\sigma^*$ -mediated pathway yielding the thiophenoxy radical (C_6H_5S).³⁵⁷⁻³⁶¹ As photodissociation products, C_6H_5O and C_6H_5S are also of great interest in many systems. For example, C_6H_5O is a crucial transient intermediate in the combustion and atmospheric chemistry of small aromatic molecules.³⁶²⁻³⁶⁵ As a part of the phenolic compounds, like vitamin E and resveratrol, C_6H_5O is also involved in the antioxidant and radical scavenging processes.³⁶⁶ Moreover, both C_6H_5O and C_6H_5S have been considered as the potential candidate molecules for the diffuse interstellar bands in astrophysics.^{367,368}

The electronic and vibrational properties of C_6H_5O and C_6H_5S have been extensively investigated both experimentally and theoretically.^{117,369-385} The electron affinities (EAs) of the C_6H_5O and C_6H_5S radicals were first estimated by photodetachment spectroscopy of the corresponding anions $C_6H_5O^-$ and $C_6H_5S^-$.³⁶⁹ An improved value for C_6H_5O was later measured by anion photoelectron spectroscopy (PES),³⁷⁰ which also yielded the excited state of C_6H_5O . Later, high-resolution PE spectra of $C_6H_5O^-$ and $C_6H_5S^-$ were obtained by slow electron velocity-map imaging (SEVI), which accurately determined the EAs of C_6H_5O and C_6H_5S to be 2.2538(8) eV and 2.3542(6) eV, respectively.³⁷¹ The electronically excited state of C_6H_5O was studied³⁷²⁻³⁷⁵ and the lowest electronic transition ($X^2B_2 \leftarrow A^2B_1$) was determined to be 0.9523(1) eV by cavity ringdown spectroscopy.³⁷⁵ The lowest excited state of C_6H_5S was also calculated³⁷⁶ and experimentally measured to be 0.3719(9) eV above the ground state.³⁷¹ In addition, the ground-state vibrational frequencies of C_6H_5O and C_6H_5S have been computed in several theoretical works³⁷⁶⁻³⁸⁰ and examined by various spectroscopies,^{370,371,381-385} such as anion PES,^{370,371} resonance Raman spectroscopy,³⁸¹⁻³⁸³ IR spectroscopy,³⁸⁴ and laser-induced fluorescence.³⁸⁵ Recently, we measured the vibrational frequencies of C_6H_5O by high-resolution resonant photoelectron imaging of cold $C_6H_5O^-$ from vibrational autodetachment via dipole-bound states (DBSs).¹¹⁷

In the current study, we report the complete photodetachment spectra of $C_6H_5O^-$ and $C_6H_5S^-$ and resonant photoelectron imaging. A DBS is observed for the first time for $C_6H_5S^-$, 39 cm^{-1} below its detachment threshold. In addition to the eight DBS vibrational resonances reported previously,¹¹⁷ nine new resonances are observed for $C_6H_5O^-$, whereas twelve vibrational resonances are observed for $C_6H_5S^-$. By setting the

detachment laser wavelengths to the DBS resonances for $C_6H_5O^-$ and $C_6H_5S^-$, we obtain resonant photoelectron images and spectra, which are highly non-Franck-Condon due to mode-selectivity¹¹⁷ and the $\Delta v = -1$ vibrational propensity rule.^{189,190} In total, five new fundamental vibrational frequencies are obtained for C_6H_5O and seven for C_6H_5S . Interestingly, intramolecular inelastic rescattering is observed in some resonant PE spectra of $C_6H_5O^-$, allowing the excitation of the Franck-Condon-inactive lowest-frequency bending mode ν_{20} of C_6H_5O to be observed. It is further shown that the photodetachment spectra for both $C_6H_5O^-$ and $C_6H_5S^-$ are in perfect agreement with the non-resonant PE spectra, vividly demonstrating the similar geometries between the neutral radicals and the dipole-bound anions, i.e. the weakly dipole-bound electron has little effect on the structure of the neutral core. Hence, the combination of photodetachment spectroscopy and resonant PES can be used to yield vibrational information for neutral polar radicals, rivaling IR spectroscopy.

6.2 Experimental methods

The experiments were done using our third-generation ESI-PES apparatus. The details were provided in Chapter 2.

6.3 Results

6.3.1 Non-resonant photoelectron spectra of $C_6H_5O^-$

Figure 6.1 shows the non-resonant photoelectron spectra of $C_6H_5O^-$ at 480.60 nm and 354.7 nm. At 480.60 nm, the first intense peak 0_0^0 represents the 0-0 transition from the anion to the neutral ($X^2B_1 \leftarrow X^1A_1$), giving an accurate EA of $18,173 \text{ cm}^{-1}$.^{117,371} Peaks A–D define a single vibrational progression of mode ν_{11} , as also observed previously.^{117,371} At the higher photon energy of 354.7 nm, transitions to the neutral

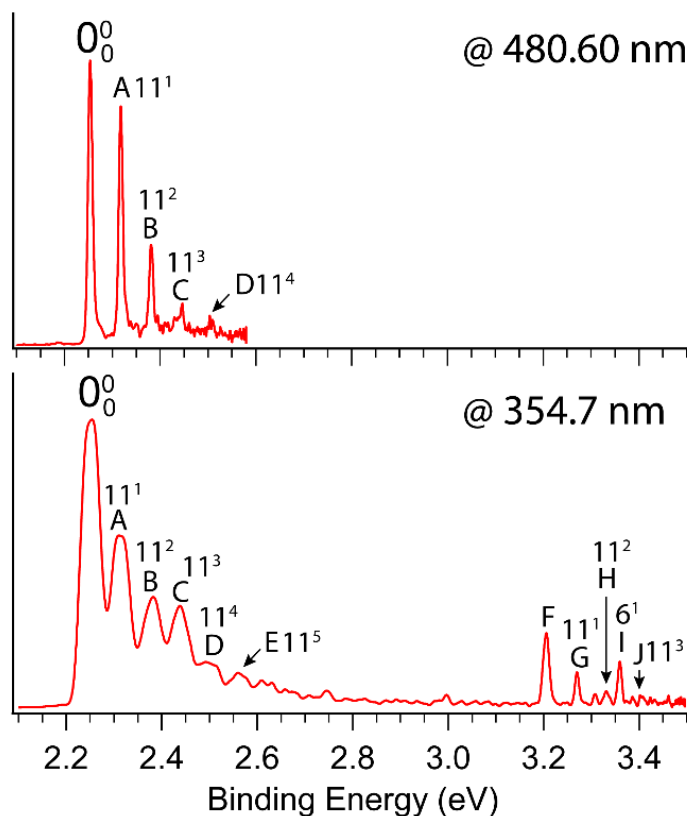


Figure 6.1. Non-resonant photoelectron spectra of $C_6H_5O^-$ at 480.60 nm and 354.7 nm.

excited state (A^2B_2) are also observed. The origin transition represented by peak F is measured to be 3.2056 ± 0.0020 eV, which lies $0.9524(20)$ eV above the ground state, consistent with the value determined by cavity ringdown spectroscopy.³⁷⁵ Peaks G–J represent vibrational excitations of the excited state. The electron binding energies of all the observed peaks A–J for the ground and excited states of C_6H_5O , their shifts from the origin of each state and assignments are summarized in Table 6.1, where other vibrational features from the resonant photoelectron spectra are also given (*vide infra*).

6.3.2 Photodetachment spectrum of $C_6H_5O^-$

The photodetachment spectrum of $C_6H_5O^-$ was measured by monitoring the total electron yield while scanning the dye laser wavelength at 0.1 nm/step across the

Table 6.1. Summary of the observed vibrational peaks from the photoelectron spectra of C₆H₅O⁻. Their binding energies (BE), shifts from the 0-0 transitions of the \tilde{X}^2B_1 and \tilde{A}^2B_2 states, assignments are given. The calculated frequencies at the B3LYP/6-311++G(d,p) level of theory are also given for the fundamental vibrational modes (see Table 6.6 in Section 6.6 for all modes).

Peak ^a	BE (eV) ^b	Shift (cm ⁻¹)	Assignment	Theor. Freq. (cm ⁻¹)
0₀⁰	2.2532(4)	0	\tilde{X}^2B_1	
A	2.3175(6)	519	11 ¹	531
B	2.3815(6)	1035	11 ²	
C	2.4460(6)	1555	11 ³	
D	2.5097(6)	2069	11 ⁴	
E	2.5740(20)	2587	11 ⁵	
a	2.2750(10)	176	20 ¹	184
b	2.2984(10)	365	14 ¹	375
c	2.3116(10)	471	19 ¹	474
d	2.3315(6)	632	18 ¹	642
e	2.3511(6)	790	10 ¹	804
f	2.3737(6)	972	9 ¹	983
g	2.3956(6)	1149	11 ¹ 18 ¹	
h	2.4044(6)	1220	11 ² 20 ¹	
i	2.4152(6)	1307	10 ¹ 11 ¹	
j	2.4298(10)	1425	10 ¹ 18 ¹	
k	2.4374(6)	1486	9 ¹ 11 ¹	
l	2.4602(6)	1670	11 ² 18 ¹	
m	2.4680(6)	1733	11 ³ 20 ¹	
n	2.4928(6)	1933	10 ¹ 11 ¹ 18 ¹	
o	2.5008(6)	1997	9 ¹ 11 ²	
F	3.2056(20)	0	\tilde{A}^2B_2	
G	3.2699(20)	519	11 ¹	524
H	3.3328(20)	1026	11 ²	
I	3.3594(20)	1240	6 ¹	1319
J	3.4029(20)	1591	11 ³	

^aPeaks in bold were reported previously in ref. 117. The peaks designated by lower case letters were observed in the resonant photoelectron spectra.

^bNumbers in parentheses indicate the experimental uncertainties in the last digit.

detachment threshold, as presented in Fig. 6.2. A smaller step size of 0.01 nm/step was used in separate scans near each observed resonance to determine a more accurate peak position. In the previous study,¹¹⁷ photodetachment spectra were only measured for the

ν_{11} progression without continuously scanning the dye laser. The arrow in Fig. 6.2 denotes the detachment threshold at $18,173\text{ cm}^{-1}$. Below threshold, the weak peak labeled as 0 represents the ground vibrational level of the DBS of $C_6H_5O^-$, which is due to resonant two-photon detachment.¹¹⁷ The binding energy of the DBS, defined as the energy difference between the neutral ground state and the ground state of the DBS, was determined to be $97 \pm 5\text{ cm}^{-1}$ previously.¹¹⁷ Above threshold, the continuous baseline indicates the cross section of the non-resonant detachment signal. The seventeen peaks,

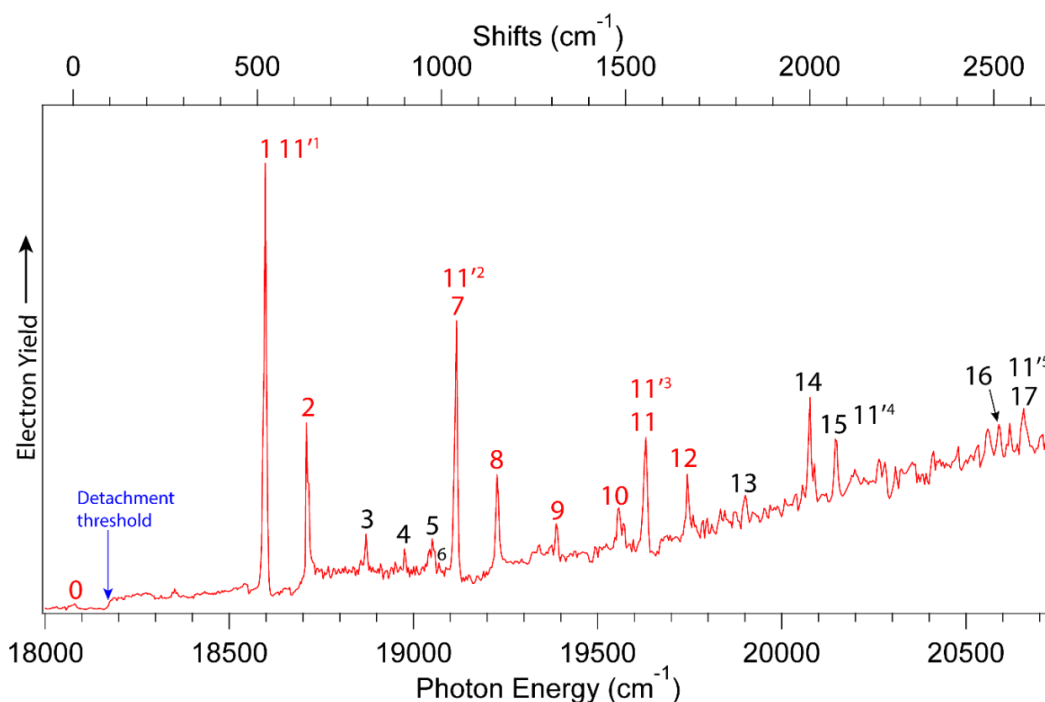


Figure 6.2. The photodetachment spectrum of $C_6H_5O^-$. It was done by measuring the total electron yield as a function of photon energy across the detachment threshold. The arrow at $18,173\text{ cm}^{-1}$ marks the detachment threshold. The peak 0 below threshold represents the vibrational ground state of the dipole-bound excited of $C_6H_5O^-$ and it is from resonant two-photon detachment, while peaks 1–17 are due to autodetachment from the DBS vibrational levels. The peaks labeled in red color were reported previously,¹¹⁷ and the peaks in black color are newly resolved. The assignments of peaks 1, 7, 11, 15, and 17 to the vibrational progression of mode ν_{11}' are also given.

labeled as 1–17, represent optical excitations to the vibrational levels of the DBS of $C_6H_5O^-$, followed by autodetachment. The peak numbers in red were reported

previously.¹¹⁷ The peaks labeled in black numbers are newly observed, because of the continuous scan of the detachment wave length and the broader spectral range covered in the current study (up to $\sim 2,600$ cm⁻¹ above threshold). The vibrational progression of mode ν_{11}' up to the fifth quantum (peak **17**) is observed in the current spectrum.

The photon energies, shifts from the ground vibrational level of the DBS, and the assignments of the observed vibrational resonances are given in Table 6.2. The assignments are all based on the resonant photoelectron spectra in Figs. 6.3 and 6.4 and the calculated vibrational frequencies presented in Table 6.6 in Section 6.6.

Table 6.2. Assignments of the observed resonances in the photodetachment spectrum of C₆H₅O⁻.

Peak ^a	Wavelength (nm)	Photon Energy (cm ⁻¹) ^b	Shift (cm ⁻¹)	Assignment
0	553.22	18076(5)		Ground state
1	537.78	18595(5)	519	11 ^{'1}
2	534.53	18708(5)	632	18 ^{'1}
3	529.93	18870(5)	794	10 ^{'1}
4	527.00	18975(5)	899	16 ^{'1}
5	524.86	19053(5)	977	9 ^{'1}
6	524.42	19069(5)	993	8 ^{'1}
7	523.22	19112(5)	1036	11 ^{'2}
8	520.17	19224(5)	1148	11 ^{'1} 18 ^{'1}
9	515.90	19384(5)	1308	10 ^{'1} 11 ^{'1}
10	511.05	19568(5)	1492	9 ^{'1} 11 ^{'1}
11	509.36	19632(5)	1556	11 ^{'3}
12	506.50	19743(5)	1667	11 ^{'2} 18 ^{'1}
13	502.47	19902(5)	1826	10 ^{'1} 11 ^{'2}
14	498.04	20079(5)	2003	9 ^{'1} 11 ^{'2} /10 ^{'1} 11 ^{'2} 20 ^{'1}
15	496.33	20148(5)	2072	11 ^{'4}
16	485.67	20590(5)	2514	9 ^{'1} 11 ^{'3} /10 ^{'1} 11 ^{'3} 20 ^{'1}
17	483.90	20665(5)	2589	11 ^{'5}

^aPeaks in bold were reported in ref. 117.

^bNumbers in parentheses indicate the experimental uncertainties in the last digit.

6.3.3 Resonant photoelectron spectra of $C_6H_5O^-$

By tuning the detachment laser to the newly observed peaks in Fig. 6.2, we obtain nine resonant PE spectra of $C_6H_5O^-$, as shown in Figs. 6.3 and 6.4. Resonant PE spectra corresponding to the peaks numbered in red were reported before.¹¹⁷ As discussed previously,^{97,117-121,164,386} two detachment pathways contributed to the resonant PE spectra: the non-resonant detachment process represented by the continuous signals in Fig. 6.2 and the resonantly-enhanced vibrational autodetachment via the DBS. Due to the mode selectivity^{97,117-121,164,386} and the $\Delta v = -1$ propensity rule^{189,190} in the autodetachment process, the resonantly-enhanced spectra in Figs. 6.3 and 6.4 are highly non-Franck-Condon in comparison to the non-resonant spectra in Fig. 6.1: one or more vibrational peaks are enhanced in the resonant photoelectron spectra.

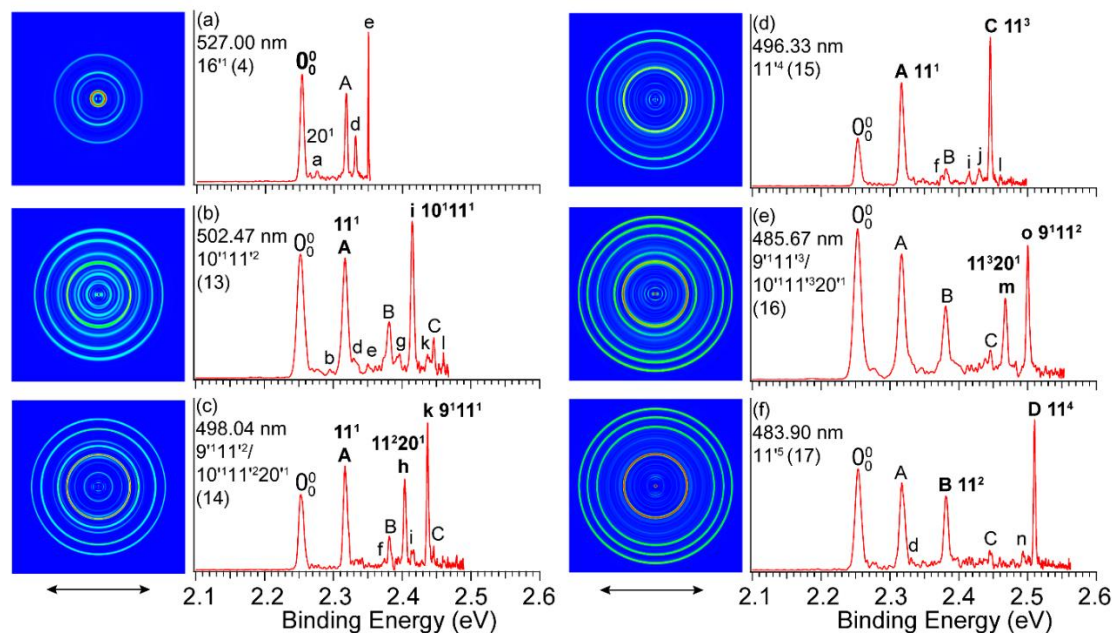


Figure 6.3. Resonant photoelectron images and spectra of $C_6H_5O^-$. The laser wavelengths are corresponding to the six resonances (in parentheses) in Fig. 6.2. The autodetachment-enhanced peaks are labeled in bold face. And the assigned vibrational levels of DBS are given. The double arrows below the images indicate the direction of the laser polarization.

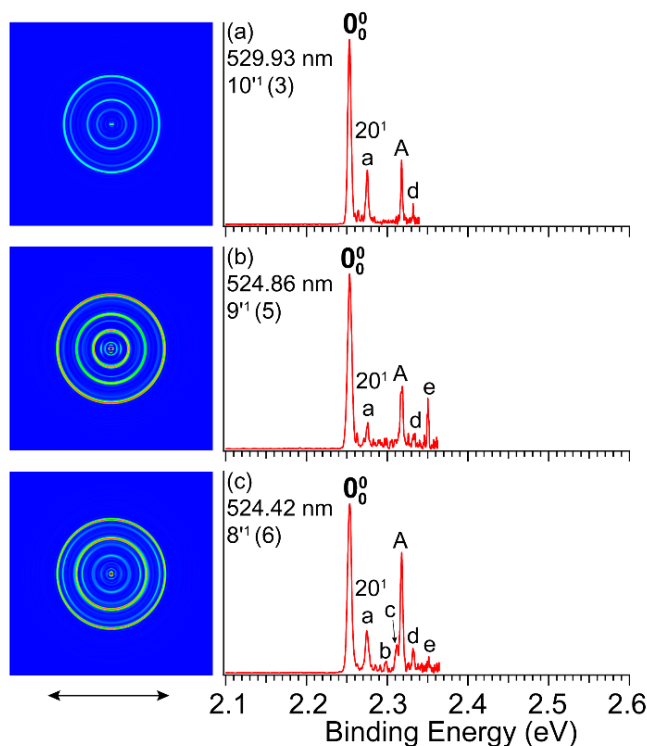


Figure 6.4. Resonant photoelectron images and spectra of $C_6H_5O^-$ at three different wavelengths. They are corresponding to peaks **3**, **5**, and **6** in Fig. 6.2. The first peak 0_0^0 labeled in bold face is enhanced due to autodetachments from fundamental vibrational levels of the DBS. The peak *a* assigned to the out-of-plane bending mode ν_{20} of C_6H_5O is observed to be due to the intramolecular inelastic rescattering effect.^{119,121,164} The double arrow below the images indicates the direction of the laser polarization.

Figures 6.3b, 6.3c, and 6.3e contain autodetachment from combinational and overlapping vibrational levels of the DBS of $C_6H_5O^-$, while Figs. 6.3a, 6.3d, 6.3f and Fig. 6.4 are due to autodetachment from a single vibrational level of the DBS. The assignments of the enhanced vibrational peaks are given in bold face in Figs. 6.3 and 6.4. All the additionally observed peaks (*a-o*), their binding energies, shifts relative to the 0_0^0 transition and the assignments are also given in Table 6.1.

6.3.4 Dipole-bound excited state and photodetachment spectrum of $C_6H_5S^-$

High-resolution photoelectron spectra of $C_6H_5S^-$ using SEVI were reported previously and the EA of C_6H_5S was measured to be $18,982(5) \text{ cm}^{-1}$.³⁷¹ For the ground

state transition, a single vibrational progression in the ν_{11} mode was observed with a frequency of 427 cm^{-1} without observable Franck-Condon activities in any other vibrational modes. We measured additional non-resonant PE spectra at several different laser wavelengths (Fig. 6.10 in Section 6.6). These spectra agree with the previous SEVI spectra. The near threshold spectrum (Fig. 6.10a) has a peak width of 1.5 meV mainly due to rotational broadening, yielding an EA of $2.3535(6)\text{ eV}$ ($18,982 \pm 5\text{ cm}^{-1}$).

To search for the DBS, we measured the photodetachment spectrum of $C_6H_5S^-$ from below the detachment threshold up to $\sim 1,500\text{ cm}^{-1}$ above threshold, as shown in Fig. 6.5. We indeed found a DBS for $C_6H_5S^-$, as revealed by the resonant peaks on top of the

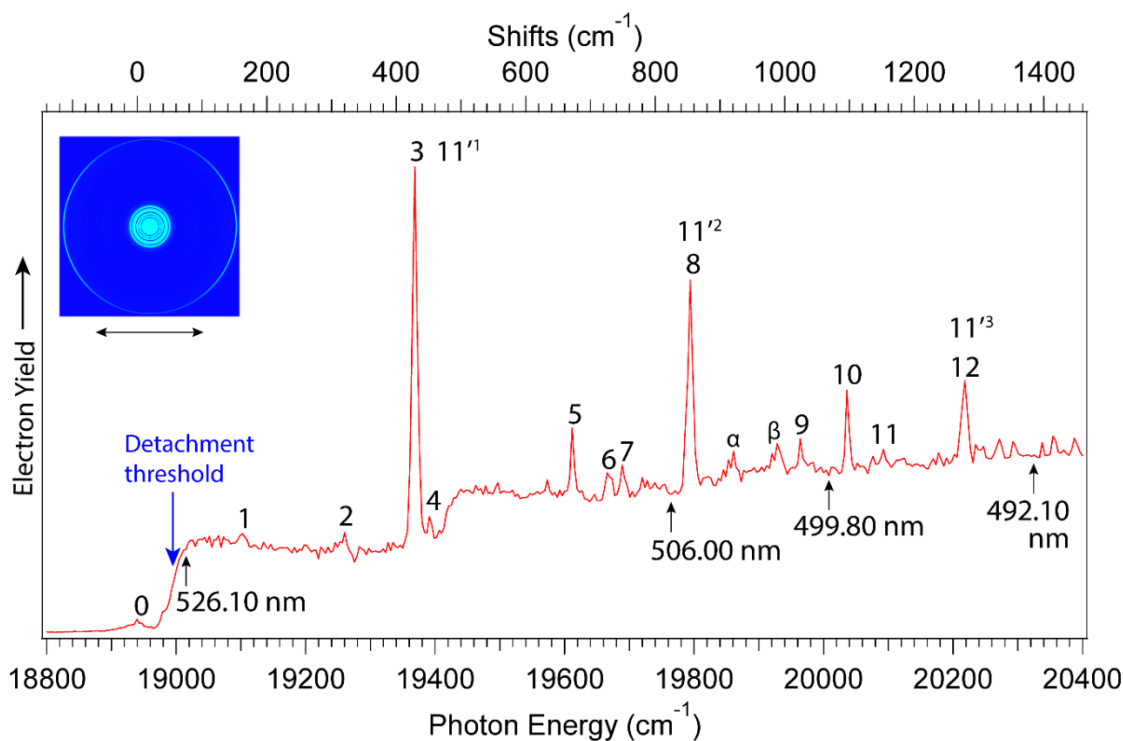


Figure 6.5. Photodetachment spectrum of $C_6H_5S^-$. It was done by measuring the total electron yield as a function of photon energy across the detachment threshold. The down-pointing arrow at $18,982\text{ cm}^{-1}$ marks the detachment threshold. The four up-pointing arrows pointing at the baseline indicate the detachment photon energies used in the non-resonant spectra presented in Fig. 6.10a–d. The peak 0 below threshold represents the vibrational ground state of the DBS of $C_6H_5S^-$. It is due to resonant two-photon detachment, corresponding to the outmost ring in the inset. The double arrow below the inset image indicates the direction of the laser polarization. The assignments of peaks **3**, **8**, and **12** to the vibrational progression of mode ν_{11}' are given.

continuous detachment signals (**1–12**). The down-pointing arrow indicates the detachment threshold at $18,982\text{ cm}^{-1}$. It is interesting to note that the non-resonant detachment cross section of $C_6H_5S^-$ seems to be significantly higher than that of $C_6H_5O^-$ (Fig. 6.2). The four up-pointing arrows indicate the wavelengths used to take the non-resonant photoelectron spectra in Fig. 6.10. The twelve peaks, labeled as **1–12**, correspond to resonant excitations to vibrational levels of the DBS of $C_6H_5S^-$ followed by autodetachment, while peaks α and β exhibit a strong threshold enhancement (see below).⁵⁷ The weak below-threshold peak **0** at an excitation energy of $18,943\text{ cm}^{-1}$ came from resonant two-photon detachment, as revealed by the PE image in the inset of Fig. 6.5. This peak is 39 cm^{-1} below the detachment threshold, defining the binding energy of the DBS. This value is smaller than the 97 cm^{-1} binding energy of the DBS in $C_6H_5O^-$, as expected from the smaller dipole moment of C_6H_5S (3.2 D, see Section 6.4.2 below) than that of C_6H_5O (4.1 D). The outmost ring in the inset of Fig. 6.5 is the resonant two-photon detachment signal from the DBS ground state and the p -wave character of the image is consistent with the s -like orbital of the DBS, as also observed in $C_6H_5O^-$ and other anions.^{117-120,164,386}

The photon energies, shifts from the ground vibrational level of the DBS and assignments of the vibrational resonances observed in Fig. 6.5 are given in Table 6.3. The assignments are all based on the resonant photoelectron spectra in Figs. 6.6 and the calculated vibrational frequencies presented in Table 6.6 in Section 6.6.

Table 6.3. Assignments of the observed resonances in the photodetachment spectrum of $C_6H_5S^-$.

Peak	Wavelength (nm)	Photon Energy (cm^{-1}) ^a	Shift (cm^{-1})	Assignment
0	527.90	18943(5)		Ground state
1	523.53	19101(5)	158	20¹
2	519.22	19260(5)	317	20²
3	516.33	19367(5)	424	11¹
4	515.68	19392(5)	449	19¹
5	509.91	19611(5)	668	18¹
6	508.51	19665(5)	722	10¹
7	507.92	19688(5)	745	11¹20²
8	505.25	19792(5)	849	11²
9	500.91	19964(5)	1021	8¹
10	499.10	20036(5)	1093	11¹18¹
11	497.72	20092(5)	1149	10¹11¹
12	494.64	20217(5)	1274	11³
α	503.55	19859(5)	916	Threshold enhancement
β	501.84	19927(5)	984	Threshold enhancement

^aNumbers in parentheses indicate the experimental uncertainties in the last digit.

6.3.5 Resonant photoelectron images and spectra of $C_6H_5S^-$

The resonant photoelectron images and spectra of $C_6H_5S^-$ are presented in Fig. 6.6. Similar to $C_6H_5O^-$, the resonant spectra, comprising of non-resonant detachment signals and resonant autodetachment signals, are highly non-Franck-Condon compared with the non-resonant spectra in Fig. 6.10 in Section 6.6 due to the mode selectivity and the $\Delta v = -1$ propensity rule. Except for the spectra in Figs. 6.6g, j and k, which involve autodetachment from combinational vibrational levels of the DBS, most of the resonant photoelectron spectra are from vibrational levels of single modes. The assignments of the enhanced vibrational peaks are given in bold face. As can be seen in Fig. 6.5, the non-resonant detachment cross sections of $C_6H_5S^-$ are relatively high. Hence, some of the resonant enhancement in the resonant spectra of $C_6H_5S^-$ are not as dramatic as those in $C_6H_5O^-$. The resonant spectra corresponding to peaks α and β in Fig. 6.5 are displayed in

Fig. 6.7 and there seem to be a strong threshold effect. All the observed peaks in the photoelectron spectra, their binding energies, shifts from the 0_0^0 transition and assignments are summarized in Table 6.4.

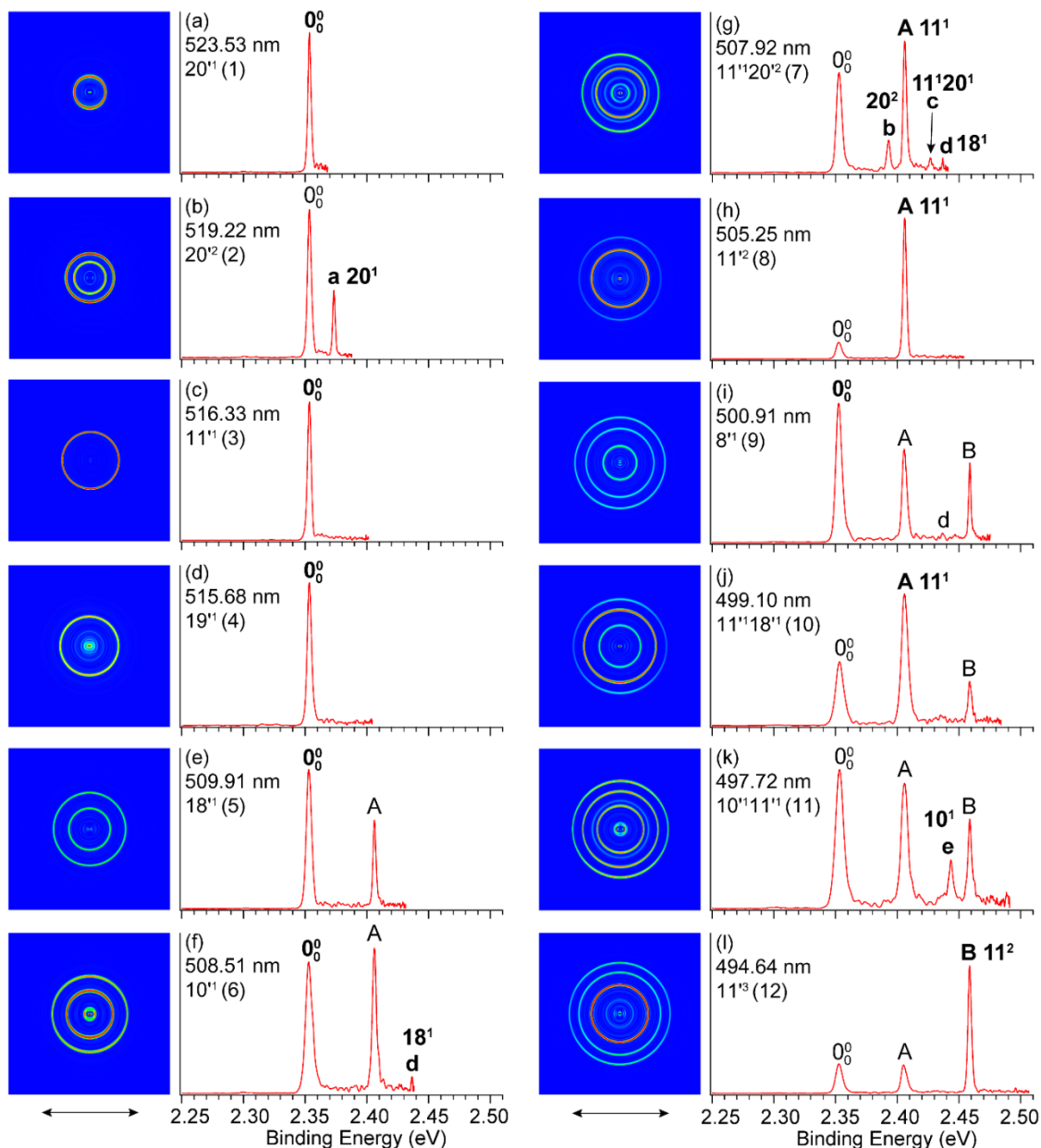


Figure 6.6. Resonant photoelectron images and spectra of $C_6H_5S^-$ at twelve wavelengths. They correspond to peaks 1-12 (in parentheses) in Fig. 6.5. The autodetachment-enhanced peaks are labeled in bold face. And the assigned vibrational levels of DBS are also given. The double arrows below the images indicate the direction of the laser polarization.

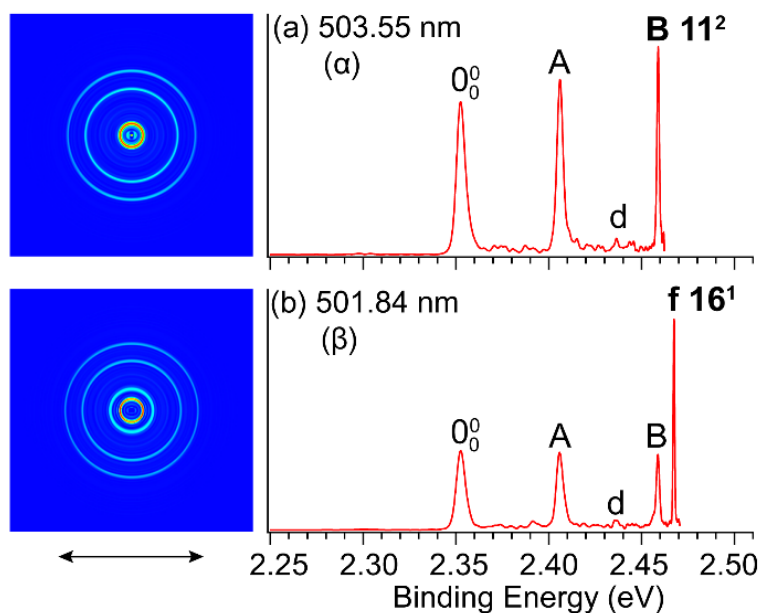


Figure 6.7. Photoelectron images and spectra of $C_6H_5S^-$ at 503.55 nm and 501.84 nm. They correspond to the peaks α and β in Fig. 6.5. The enhanced peaks B (11^2) and f (16^1) are due to threshold enhancement,⁵⁷ rather than the autodetachment enhancement via DBS. The double arrow below the images indicates the directions of the laser polarization.

Table 6.4. Summary of the observed vibrational peaks in the photoelectron spectra of $C_6H_5S^-$. Their binding energies (BE), shifts from the 0-0 transition, and assignments are given. The theoretical frequencies of the fundamental vibrational modes of C_6H_5S radical at the B3LYP/6-311++G(d,p) level of theory are also given (see Table 6.6 in Section 6.6 for a full list).

Peak	BE (eV) ^a	Shift (cm ⁻¹)	Assignment	Theo. freq. (cm ⁻¹)
0_0^0	2.3535(6)	0	Neutral ground state	
A	2.4058(6)	422	11^1	427
B	2.4587(6)	848	11^2	
C	2.5109(6)	1269	11^3	
a	2.3733(8)	160	20^1	161
b	2.3929(8)	318	20^2	
c	2.4274(10)	596	$11^1 20^1$	
d	2.4362(10)	667	18^1	683
e	2.4435(10)	726	10^1	730
f	2.4678(6)	922	16^1	937

^aNumbers in parentheses indicate the experimental uncertainties in the last digit.

6.4 Discussion

6.4.1 Non-resonant photoelectron spectra of $C_6H_5O^-$

The vibrational peaks shown in the non-resonant photoelectron spectra in Fig. 6.1 are governed by the Franck-Condon principle, i.e., only symmetry-allowed modes with significant Franck-Condon activities can be observed. To assist the spectral assignments of the numerous non-Franck-Condon vibrational modes observed in the resonant PE spectra, we calculated the harmonic frequencies of the ground electronic state of C_6H_5O (X^2B_1) and C_6H_5S (X^2B_1) at the B3LYP/6-311++G(d,p) level of theory with the Gaussian 09 package.²⁵² The frequencies of the excited state for C_6H_5O (A^2B_2) were calculated using the time-dependent density function theory at the same level. These computed frequencies are given in Table 6.6 in Section 6.6.

As reported previously,^{117,370,371} peaks A-E in Fig. 6.1 represent the vibrational progression of the most Franck-Condon-active mode ν_{11} with a measured frequency of 519 cm^{-1} , which involves an in-plane ring stretching (Table 6.7 in Section 6.6). At 354.7 nm, peaks F-J at higher binding energies represent the excited state of C_6H_5O (A^2B_2), which was observed in a previous low resolution photoelectron spectrum at 1.06(5) eV above the ground state.³⁷⁰ Peak F at 3.2056 eV is the 0_0^0 transition to the excited state, defining a more accurate excitation energy of 0.9524(20) eV above the ground state, in agreement with the value measured previously in the cavity ringdown experiment.³⁷⁵ Peaks F, G, H, and J represent the vibrational progression of the ring-stretching ν_{11} mode with a spacing of 519 cm^{-1} , the same as that of the ground state. Peak I is from a different vibrational mode with a frequency of $1,240\text{ cm}^{-1}$. Our calculation shows two A_1 modes ν_6 (1319 cm^{-1}) and ν_7 (1199 cm^{-1}) close to the 1240 cm^{-1} experimental frequency. Previous

high-level calculations reported scaled frequencies of 1201-1252 cm^{-1} for ν_6 and 1143-1154 cm^{-1} for ν_7 .³⁷⁴ Hence, we tentatively assign peak I to the fundamental mode ν_6 of the excited state of C_6H_5O (A^2B_2). This mode involves the C-O stretching, as shown in Table 6.7 in Section 6.6.

6.4.2 Photodetachment spectra of $C_6H_5O^-$ and $C_6H_5S^-$

The vibrational resonances in $C_6H_5O^-$ were first observed serendipitously using our room temperature ion trap.¹⁵ With the cryogenically-controlled ion trap, we examined these resonances more carefully and observed the mode-selectivity in the first resonant PE spectra via vibrational autodetachment.¹¹⁷ Eight DBS resonances including the progression of mode ν_{11}' up to the third quantum were probed then. The binding energy of the DBS was found to be 97 cm^{-1} , but the photodetachment spectrum was not continuously scanned. In the current work, the full photodetachment spectrum of $C_6H_5O^-$ is obtained up to $\sim 2,600$ cm^{-1} above the detachment threshold, as shown in Fig. 6.2. Apart from the previously reported DBS resonances labeled in red color, nine more vibrational resonances are observed and labeled in black color in the new photodetachment spectrum (Fig. 6.2). As shown previously,^{95,118-121,164,386} all the resonances display the asymmetric Fano line shapes as expected,³⁸⁷ due to the interference between the non-resonant direct detachment and the resonant autodetachment. The vibrational progression of mode ν_{11}' is observed up to the fifth quantum in Fig. 6.2. We found previously that the vibrational frequencies of the ν_{11}' mode in the DBS of $C_6H_5O^-$ was the same as the ν_{11} mode in neutral C_6H_5O within our experimental accuracy (the ' was used to designate the DBS vibrational modes), consistent with the fact that the highly diffuse dipole-bound electron has no effect on the structure of the molecular core. This is further verified by the perfect

match of the frequencies and relative intensities of almost all the vibrational peaks between the non-resonant photoelectron spectrum and the photodetachment spectrum (see Fig. 6.11 in Section 6.6).

We estimated the dipole moment of C_6H_5S to be 3.2 D at the B3LYP/6-311++G(d, p) level of theory. Hence, the $C_6H_5S^-$ anion should also be able to support a DBS, which is indicated by the vibrational resonances in the photodetachment spectrum in Fig. 6.5. With a smaller dipole moment compared to that of C_6H_5O (4.1 D),¹¹⁷ the binding energy for the DBS of $C_6H_5S^-$ is also expected to be smaller, as indicated by the peak 0 in Fig. 6.5, which is measured to be 39 cm^{-1} below the detachment threshold. This peak represents the ground vibrational level of the DBS, which is confirmed by the resonant two-photon detachment image (inset in Fig. 6.5). This is further verified by the similarity of the non-resonant photoelectron spectrum at 492.10 nm and the photodetachment spectrum of $C_6H_5S^-$, as shown in Fig. 6.12 in Section 6.6.

In addition, more vibrational peaks, which are absent in the non-resonant PE spectra, are observed in the photodetachment spectra (see Figs. 6.11 and 6.12 in Section 6.6). The relative intensities of the ν_{11} progression between the photodetachment spectra and the photoelectron spectra obey the Franck-Condon principle for both systems. However, the resonant excitations to the DBS allow some vibrational levels with low or negligible Franck-Condon factors in the photoelectron spectra to be observed in the photodetachment spectra. Therefore, richer and more accurate vibrational information for the C_6H_5O and C_6H_5S radicals can be obtained from the photodetachment spectra in Figs. 6.2 and 6.5, as well as the resonant photoelectron spectra. The assignments of the observed vibrational resonances given in Tables 6.2 and 6.3 are all based on the resonant

photoelectron spectra presented in Figs. 6.3, 6.4, 6.6, and 6.7 along with the calculated vibrational frequencies given in Table 6.6 in Section 6.6. The schematic energy level diagrams showing autodetachment from the vibrational levels of the DBS to the neutral states are presented in Figs. 6.8 and 6.9 for $C_6H_5O^-$ and $C_6H_5S^-$, respectively.

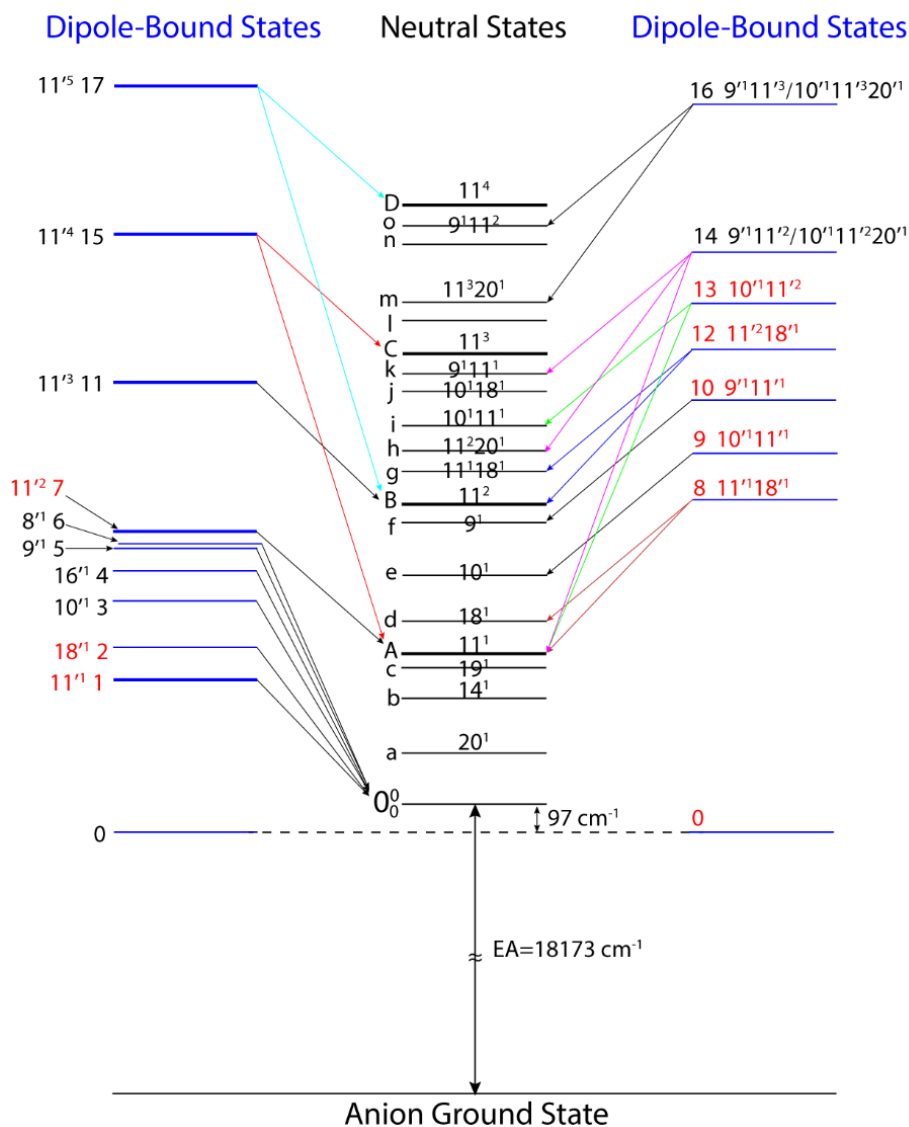


Figure 6.8. Schematic energy level diagram for autodetachment from the DBS vibrational levels of $C_6H_5O^-$ to the neutral final states of C_6H_5O . The single-mode vibrational levels of the DBS are given on the left with arrows indicating the autodetachment. The combinational and overlapping vibrational levels of the DBS are given on the right. The vibrational progressions of mode ν_{11} in the DBS and neutral states are highlighted in bold face. The detachment threshold ($18,173 \text{ cm}^{-1}$) and the DBS binding energy (97 cm^{-1}) of $C_6H_5O^-$ are also given. The peaks and assignments in red color were reported previously.¹¹⁷ The assignments of the final neutral states and the DBS levels are given in Tables 6.1 and 6.2, respectively.

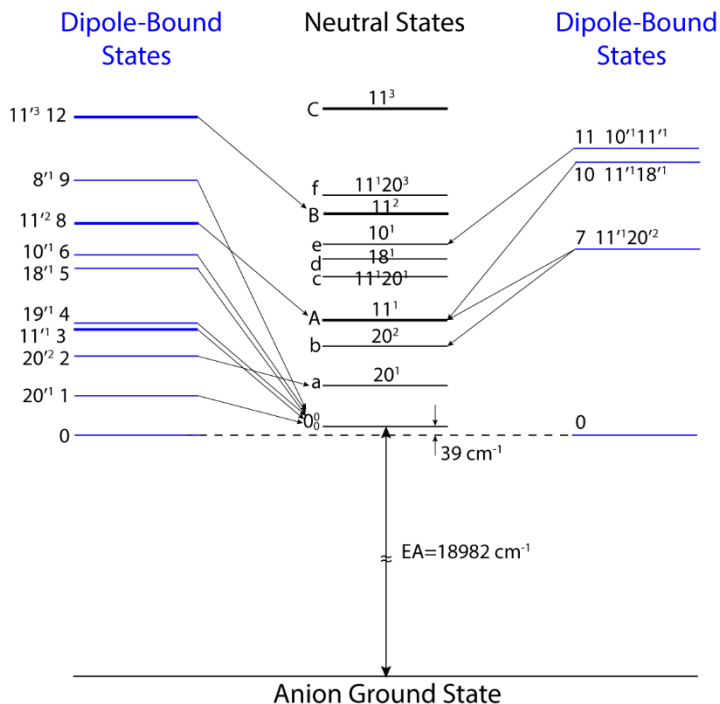


Figure 6.9. Schematic energy level diagram for autodetachment from the DBS vibrational levels of $C_6H_5S^-$ to the neutral final states of C_6H_5S . The single-mode vibrational levels of the DBS are given on the left with arrows indicating the autodetachment. The combinational vibrational levels of the DBS are given on the right. The vibrational progressions of mode ν_{11} in the DBS and neutral states are highlighted in bold face. The detachment threshold ($18,982\text{ cm}^{-1}$) and the DBS binding energy (39 cm^{-1}) of $C_6H_5S^-$ are also given. The assignments of the DBS levels and the final neutral states are given in Tables 6.3 and 6.4, respectively.

6.4.3 Resonant PES of $C_6H_5O^-$ via vibrational autodetachment from the DBS

As shown previously,^{117-121,164,386} autodetachment from the vibrational levels of the DBS to final neutral states exhibits mode selectivity and obeys the $\Delta v = -1$ propensity rule under the harmonic approximation.^{189,190} For autodetachment involving vibrational levels of a single mode (ν'_x), the n th vibrational level of this mode ($\nu'_x{}^n$) in the DBS autodetaches to the $(n-1)$ th level of the same mode in the neutral ($\nu_x{}^{n-1}$), in which one quantum of vibrational energy is coupled to the dipole-bound electron. For autodetachment from a combinational vibrational level ($\nu'_x{}^m\nu'_y{}^n\dots$) of the DBS, the final neutral level can be either $\nu_x{}^{m-1}\nu_y{}^n\dots$ or $\nu_x{}^m\nu_y{}^{n-1}\dots$ (mode selectivity), provided the

vibrational frequencies are all larger than the binding energy of the DBS. Hence, relative peak intensities of these final neutral vibrational levels will be enhanced in comparison to those in non-resonant photoelectron spectra, giving rise to highly non-Franck-Condon resonant photoelectron spectra. It has also been shown that certain modes in the combinational levels have stronger couplings with the dipole-bound electron.¹¹⁷

Tuning the detachment laser to the seventeen resonances in Fig. 6.2 will result in seventeen resonant photoelectron spectra for $C_6H_5O^-$. The resonant spectra obtained for peaks **1**, **2** and **7–12** were reported previously.¹¹⁷ As can be seen in Fig. 6.2, these resonances are relatively strong, which was why they were found previously without systematic wave length scans.^{15,117} The nine new resonant photoelectron spectra presented in Figs. 6.3 and 6.4 are discussed in detail here.

Figure 6.3a at 527.00 nm is from the weak resonant peak **4** (Fig. 6.2). As shown previously,¹¹⁷ peaks d and e are due to the 18^1 and 10^1 final vibrational states, which have negligible Franck-Condon factors (Fig. 6.1), but they are very intense in Fig. 6.3a mainly due to threshold enhancement,⁵⁷ in particular for peak e. The photon energy used in Fig. 6.3a agrees with the excitation to the 16^1 DBS level (Table 6.2), which should show an enhancement of the 0_0^0 transition relative to peak A (11^1). However, this enhancement is not very obvious, probably due to the fact that peak A also displays some threshold enhancement. Figs. 6.3d and f correspond to resonant excitations to 11^4 and 11^5 of the DBS, respectively, resulting in strong enhancement of 11^3 (C) and 11^4 (D), following the $\Delta v = -1$ propensity rule. However, peak A (11^1) is also significantly enhanced in Fig. 6.3d, as well as peak B (11^2) in Fig. 6.3f. These enhancements are surprising, which indicate $\Delta v = -3$ for the autodetachment, i.e., coupling of three quanta of the ν_{11}' mode to

the dipole-bound electron to induce autodetachment. These deviations from the $\Delta v = -1$ propensity rule are due to anharmonic effects at higher vibrational levels, which have been observed previously.^{118,121,164,386} It is interesting to note that $\Delta v = -2$ does not seem to occur for this mode. This vibrational level dependence of the anharmonic effects is not well understood and deserves further theoretical attention.

In Fig. 6.3b, peak A (11^1) is slightly enhanced and peak *i* (10^111^1) is greatly enhanced, suggesting that the resonant peak **13** corresponds to a combinational DBS level of 10^111^2 . However, it is surprising that the 11^2 final state, involving coupling of one quantum of the ν_{10}' mode, is not enhanced, whereas the slight enhancement of the 11^1 final state would require the coupling of one quantum of the ν_{11}' mode and one quantum of the ν_{10}' mode. We also observed previously that the ν_{10}' mode does not seem to couple to the dipole-bound electron in the resonant excitation to the 10^111^1 DBS level.¹¹⁷ In Fig. 6.3c, the enhancements of three peaks, A (11^1), *h* (11^220^1) and *k* (9^111^1), are due to autodetachment from two degenerate combinational DBS levels, 9^111^2 and $10^111^220^1$. The same case is observed in Fig. 6.3e, where the excitations to combinational vibrational levels of 9^111^3 and $10^111^320^1$ give the enhancement of peak *o* (9^111^2) and peak *m* (11^320^1), respectively. Only one peak getting enhanced in each combinational level indicates the selectivity of vibrational mode in the vibronic coupling induced autodetachment, meaning that mode ν_{11}' in 9^111^3 and mode ν_{10}' in $10^111^320^1$ are favored to couple with the dipole-bound electron, which cause the enhancement of peaks *o* and *m*, respectively.

In addition, numerous weak peaks *a*, *b*, *d*, *f*, *g*, *j*, *l* and *n* are also observed in Fig. 6.3. The assignments of peaks *a*, *b* and *j* are based on the comparison to the calculated

frequencies in Table 6.6 in Section 6.6. Peak *a* will be discussed below. The weak peak *b* with a shift of 365 cm^{-1} is assigned to the mode ν_{14} (calculated frequency 375 cm^{-1}), which is an out-of-plane bending mode as shown in Table 6.7 in Section 6.6. Peak *j* shifted by $1,425\text{ cm}^{-1}$ from peak 0_0^0 is assigned to a combinational vibrational level of $10^1 18^1$ with the frequencies measured to be 790 cm^{-1} for ν_{10} and 632 cm^{-1} for ν_{18} .¹¹⁷ The other peaks were reported previously.¹¹⁷ All the observed peaks, their binding energies, shifts and the assignments are summarized in Table 6.1. The observed vibrational resonances of the DBS and their autodetachment channels for $C_6H_5O^-$ are given schematically in Fig. 6.8.

6.4.4 Intramolecular inelastic rescattering in autodetachment from DBS of $C_6H_5O^-$

Figure 6.4 shows three resonant photoelectron spectra due to autodetachment from three fundamental vibrational levels, 10^1 , 9^1 , and 8^1 of the DBS of $C_6H_5O^-$. The 0_0^0 peak in all spectra is enhanced, as expected from the $\Delta v = -1$ propensity rule. Interestingly, peak *a* is also observed in these spectra with significant intensities. With a shift of 176 cm^{-1} from the 0_0^0 peak, peak *a* is assigned to the lowest-frequency bending mode ν_{20} of C_6H_5O (184 cm^{-1} calculated frequency, Table 6.7 in Section 6.6), which is Franck-Condon-forbidden and absent in the non-resonant photoelectron spectra.^{117,371} Excitation of this vibrational state in these resonant photoelectron spectra is attributed to intramolecular inelastic rescattering, which has been observed previously and usually results in excitations of low-frequency and Franck-Condon-forbidden vibrational modes.^{119,121,164} The idea is that the outgoing autodetached electron from the DBS can interact with the neutral core to cause excitations of the low-frequency vibrations. The rescattering process is similar to electron energy loss spectroscopy,^{388,389} in which

electrons with fixed kinetic energies cause vibrational excitations of surface adsorbates or gaseous molecules via electronic to vibrational energy transfers. In the current cases, autodetachment from vibrational levels $10'^1$ (794 cm^{-1}), $9'^1$ (977 cm^{-1}) and $8'^1$ (993 cm^{-1}) results in the outgoing photoelectrons with kinetic energies of 697 cm^{-1} , 880 cm^{-1} , and 896 cm^{-1} , respectively. Some of the outgoing electrons are rescattered inelastically by the neutral core and excite the ν_{20} vibrational mode. In fact, the photoelectron kinetic energies in these three cases are all higher than the calculated frequencies of several other bending modes, i.e., ν_{14} (375 cm^{-1}), ν_{30} (446 cm^{-1}), ν_{19} (474 cm^{-1}), ν_{29} (597 cm^{-1}) and ν_{18} (642 cm^{-1}). Some of these modes are indeed excited, such as peak *d* due to the ν_{18} mode or peak *b* (ν_{14}) and *c* (ν_{19}) in Fig. 6.4c (Table 6.1), but mode ν_{20} exhibits the strongest rescattering effect.

Vibronic coupling or Herzberg-Teller coupling has been invoked previously to explain observations of Franck-Condon-inactive vibrational modes or anomalous vibrational intensities in PES.^{116,390} While we cannot rule out the effects of vibronic coupling in the observation of the ν_{20} mode, the strong intensity observed in the resonant photoelectron spectra shown in Fig. 6.4 seems to be similar to the inelastic rescattering we observed previously,^{119,121,164} as well as that observed in electron-impact induced autodetachment³⁹¹ and that in rotationally-resolved photoelectron spectra of NH_3 .³⁹² It appears that the relative intensity of the rescattering depends on the outgoing electron kinetic energies and the relative contribution of the autodetached electrons. For example, no significant ν_{20} excitation was observed in any of the resonant spectra from autodetachment of the ν_{11}' (519 cm^{-1}) levels of the DBS (Figs. 6.3d and f and in ref. 117), resulting in an outgoing electron with a much smaller kinetic energy of 422 cm^{-1} .

Autodetachment from the $16'^1$ (899 cm^{-1}) level would yield an outgoing electron with a kinetic energy similar to those from $10'^1$, $9'^1$ or $8'^1$. However, the autodetachment contribution to the 0_0^0 transition is very small (Fig. 6.3a), consistent with the very weak ν_{20} excitation according to the rescattering model.

6.4.5 Resonant PES of $C_6H_5S^-$

Similar to the resonant photoelectron spectra of $C_6H_5O^-$, twelve resonant spectra are obtained for $C_6H_5S^-$ (Fig. 6.6), by tuning the detachment laser to the twelve resonances in Fig. 6.5. The non-resonant photoelectron spectra of $C_6H_5S^-$ are very simple, showing a progression of the ν_{11} mode only (Fig. 6.10 in Section 6.6).³⁷¹ The resonant spectra of $C_6H_5S^-$ are also quite simple, and some of the expected enhancements are not very prominent. Figs. 6.6a, c and d, corresponding to resonances **1**, **3** and **4** in Fig. 6.5, only show the single 0_0^0 peak, suggesting excitations to fundamental vibrational levels of $20'^1$, $11'^1$, and $19'^1$ of the DBS, respectively, following the $\Delta v = -1$ vibrational autodetachment propensity rule. Figs. 6.6e, f and i correspond to excitations to the $18'^1$, $10'^1$ and $8'^1$ DBS levels, respectively, according to the computed frequencies (Table 6.6 in Section 6.6). However, the enhancement of peak 0_0^0 relative to peak A in these resonant photoelectron spectra is not so obvious, probably because there may also be a slight near-threshold enhancement of peak A. In Figs. 6.6b, h and l, peaks *a* (20^1), A (11^1) and B (11^2) are greatly enhanced, respectively. These spectra correspond to excitations to the $20'^2$, $11'^2$, and $11'^3$ DBS levels, respectively, following straightforwardly the $\Delta v = -1$ propensity rule. The peak *a* in Fig. 6.6b with a shift of 160 cm^{-1} from the 0_0^0 peak is due to the lowest-frequency bending mode ν_{20} of C_6H_5S , which has a calculated frequency of 161 cm^{-1} (Tables 6.6 and 6.7 in Section 6.6).

The remaining resonant photoelectron spectra in Figs. 6.6g, j and k all involve autodetachment from combinational vibrational levels of the DBS of $C_6H_5S^-$. The enhancement of peak A (11^1) in Fig. 6.6j and peak *e* (10^1) in Fig. 6.6k are due to autodetachment from combinational levels of $11'^118'^1$ and $10'^111'^1$, respectively. Clearly, one vibrational mode is more favored to couple with the dipole-bound electron during autodetachment, i.e., mode ν_{18}' in $11'^118'^1$ and mode ν_{11}' in $10'^111'^1$, resulting in the significantly enhanced peak A (11^1) and peak *e* (10^1). Such mode-selectivity in the autodetachment processes involving combinational vibrational levels is observed previously,^{117-119,121,164,386} as well as above for $C_6H_5O^-$. Finally, Fig. 6.6g shows three enhanced peaks, *b* (20^2), A (11^1), and *c* (11^120^1), implying autodetachment from a combinational level of $11'^120'^2$. The autodetachment to peak *b* and *c* follows the $\Delta v = -1$ rule, but autodetachment to peak A (11^1) would involve $\Delta v = -2$ in the bending mode ν_{20}' . A weak peak *d* is also observed in Fig. 6.6g with a shift of 667 cm^{-1} from the 0_0^0 peak, consistent with the excitation of ν_{18} (computed frequency of 683 cm^{-1} , Table 6.6 in Section 6.6). Peak *d* is likely due to a threshold effect, which is in fact also observed near the threshold in Fig. 6.6f.

All the observed vibrational resonances of the DBS and their autodetachment channels for $C_6H_5S^-$ are schematically shown in Fig. 6.9.

6.4.6 Near-threshold resonances of $C_6H_5S^-$

Figure 6.7 shows the photoelectron spectra of $C_6H_5S^-$ taken at the photon energies corresponding to the weak resonant peaks α and β in Fig. 6.5. Peak B in Fig. 6.7a is the 11^2 vibrational level of C_6H_5S . The photon energy of peak α is 916 cm^{-1} above the ground state of the DBS, but 916 cm^{-1} does not correspond to any combinational levels of $\nu_{11}'^2$.

Hence, the enhanced 11^2 peak seems to be a near-threshold effect. Similarly, peak *f* in Fig. 6.7b also seems to be due to a near-threshold enhancement. Peak *f* is at 922 cm^{-1} relative to the 0_0^0 peak and corresponds to 16^1 (computed frequency of ν_{16} is 937 cm^{-1} , Table 6.6 in Section 6.6), which is not present in the non-resonant photoelectron spectra (Fig. 6.10 in Section 6.6). The photon energy of peak β is 984 cm^{-1} above the DBS ground state of $C_6H_5S^-$, but 984 cm^{-1} does not correspond to any combination level of ν_{16}^1 . According to the Wigner threshold law,⁵⁷ *s*-wave detachment channels from *p*-type orbitals should have significant intensities near the detachment threshold. As shown in Fig. 6.13 in Section 6.6, the HOMO of $C_6H_5S^-$ is a *p*-type delocalized π orbital. And the detachment from the HOMO results in an *s* + *d* angular distribution,³⁷¹ as also shown in the current non-resonant photoelectron spectra.

However, in the vicinity of the 11^1 detachment channel near $19,420\text{ cm}^{-1}$ (Fig. 6.5), a step was observed, also consistent with the expected threshold behavior for *s*-wave detachment, rather than a peak as observed in the case of peak α for the 11^2 detachment channel. Hence, the α peak was most likely due to vibronic coupling.^{116,390} The ν_{16} mode is an out-of-plane bending mode (Table 6.7 in Section 6.6) and should be Franck-Condon-inactive. Hence, the strong enhancement of the 16^1 peak corresponding to peak β is also most likely due to vibronic coupling.

6.4.7 Photoelectron angular distributions

For one-photon detachment with linearly polarized light, the photoelectron angular distribution (PAD) depends on the symmetry of the orbital where the electron is detached, and is governed by an anisotropy parameter β which varies between -1 and 2 .^{113,393} The π type HOMOs of $C_6H_5O^-$ and $C_6H_5S^-$ (Fig. 6.13 in Section 6.6) are similar

and are expected to give rise to PADs of $s + d$ characters, in agreement with the observed β values of $-0.6 \sim -0.3$ in the non-resonant photoelectron spectra.^{117,371} The resonant two-photon detachment from the ground vibrational level of a DBS always gives a distinct p -wave character,^{117-121,164,386} as presented in the inset of Fig. 6.5 for $C_6H_5S^-$, which indicates an s -type orbital for the DBS. However, autodetachment from the above-threshold resonances results in isotropic distributions.¹¹⁷ With contributions from both direct detachment and vibrational autodetachment via DBS, the enhanced peaks in the resonant photoelectron spectra can have various PADs depending on the relative ratio of the two detachment channels. For example, the weakly enhanced peak 0_0^0 in Figs. 6.3a and 6.4 from autodetachment of resonances **3–6** in Fig. 6.2 has a β value of $-0.5 \sim -0.2$, close to the value from direct detachment. On the other hand, peak 0_0^0 in Fig. 6.6c, peak A (11^1) in Fig. 6.6h, and peak B (11^2) in Fig. 6.6l, corresponding to strong resonances of **3**, **8**, and **12** in Fig. 6.5, respectively, possess β values of around 0.15. The images are almost isotropic due to the large contribution from the autodetachment channel.

However, the images of the enhanced peaks i (10^111^1), m (11^320^1), and o (9^111^2) in Fig. 6.3 for $C_6H_5O^-$ show clear p -wave distributions with β values of $0.5 \sim 0.8$. Similarly, the images of peaks a (20^1) and d (18^1) in Figs. 6.3a and 6.4 for $C_6H_5O^-$ also exhibit distinct p -wave distributions. Similar PADs are observed for peaks a (20^1), c (11^120^1) and d (18^1) with β values of $0.1 \sim 0.3$ in Fig. 6.6 for $C_6H_5S^-$. It turns out that these peaks all represent out-of-plane bending excitations of C_6H_5O and C_6H_5S (Table 6.7 in Section 6.6). It is understandable that the low-frequency bending modes play important roles in the PADs for electron ejections. Further studies of these PADs may

gain interesting insights into the vibronic coupling leading to autodetachment from the DBS.

6.4.8 Fundamental vibrational information resolved for C_6H_5O and C_6H_5S

The resemblances between the non-resonant photoelectron spectra and the photodetachment spectra (Figs. 6.11 and 6.12 in Section 6.6) suggest similar geometries of the neutral radicals and the dipole-bound anions, because the weakly dipole-bound electron has little effect on the structure of the neutral core. Since photodetachment spectroscopy has higher spectral resolution, it could be a powerful tool to resolve vibrational information for the neutral radicals with large dipole moment.^{95,117-121,164,386} Furthermore, the vibrational features with negligible Franck-Condon factors can be resolved in resonant photoelectron spectra via vibrational autodetachment from DBS. As summarized in Table 6.5, the combination of photodetachment spectroscopy and resonant photoelectron spectra yields five new fundamental vibrational modes for the ground state of the C_6H_5O radical and seven fundamental vibrational modes for the ground state of C_6H_5S . Two vibrational modes, ν_{11} and ν_6 , are also obtained for the excited state (A^2B_2) of C_6H_5O from the non-resonant spectrum at 354.7 nm (Fig. 6.1). The experimental frequencies for the ground states of the two radicals agree well with the theoretical frequencies calculated at both the B3LYP/6-311++G(d,p) level and the B3LYP/aug-cc-pVTZ (scaled by 0.9687 in ref. 371) level of theory. It is interesting to note that the frequencies calculated by the B3LYP/6-311++G(d,p) level have not been scaled. The good agreement with the experimental values suggest the suitability of using B3LYP/6-311++G(d,p) to calculate vibrational frequencies, in particular, the low frequencies of small organic molecules.

Table 6.5. Summary for all the observed fundamental vibrational frequencies of C₆H₅O and C₆H₅S. They are corresponding to the peaks observed from the photodetachment and photoelectron spectroscopy.

	State	Mode ^a	Observed freq. (cm ⁻¹) ^b	Observed peaks ^c	B3LYP/ 6-311++G(d,p)	B3LYP/aug-cc-pVTZ (scaled by 0.9687) ^d
C ₆ H ₅ O	\tilde{X}^2B_1	<i>v</i> ₂₀	176(8)	a	184	182
		<i>v</i> ₁₄	365(8)	b	375	369
		<i>v</i> ₁₉	471(8)	c	474	466
		<i>v</i>₁₁	519(6)/519(5)	A/1	531	515
		<i>v</i>₁₈	632(6)/632(5)	d/2	642	635
		<i>v</i>₁₀	790(6)/794(5)	e/3	804	782
		<i>v</i> ₁₆	899(5)	4	919	906
		<i>v</i>₉	977(5)	5	983	959
		<i>v</i> ₈	993(5)	6	1008	979
		\tilde{A}^2B_2	<i>v</i> ₁₁	519(15)	G	524
<i>v</i> ₆	1240(15)		I	1319	1201-1252 ^e	
C ₆ H ₅ S	\tilde{X}^2B_1	<i>v</i> ₂₀	160(6)/158(5)	a/1	161	156
		<i>v</i> ₁₁	422(6)/424(5)	A/3	427	414
		<i>v</i> ₁₉	449(5)	4	463	450
		<i>v</i> ₁₈	667(8)/668(5)	d/5	683	667
		<i>v</i> ₁₀	726(8)/722(5)	e/6	730	709
		<i>v</i> ₁₆	922(5)	f	937	923
		<i>v</i> ₈	1021(5)	9	1038	1009

^aThe modes in bold were reported in a previous study.¹¹⁷^bNumbers in parentheses indicate the experimental uncertainties in the last digit.^cPeaks in letter are observed in the photoelectron spectra and peaks in number are observed in the photodetachment spectra.^dThe reported fundamental frequencies and the calculated frequencies are from ref. 371.^eThe calculated frequencies for the C₆H₅O (\tilde{A}^2B_2) at various high level of theories are from ref. 374.

6.5 Conclusions

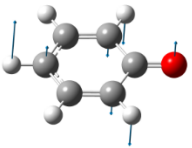
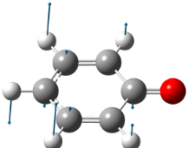
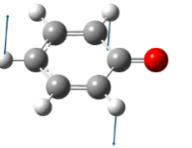
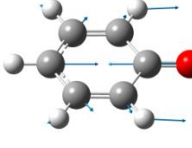
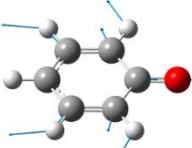
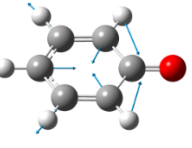
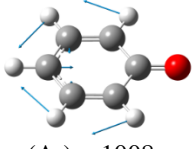
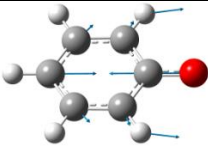
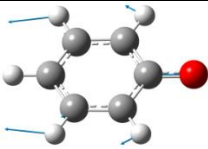
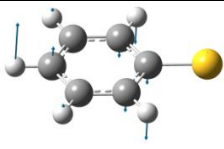
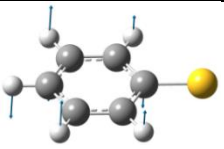
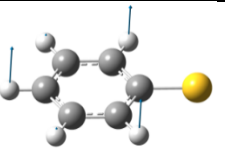
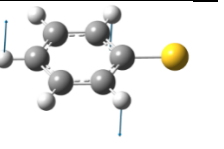
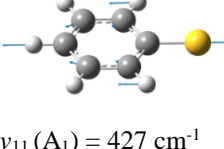
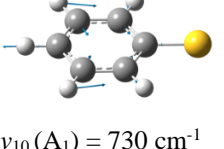
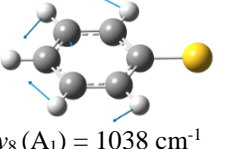
In conclusion, we report an investigation of the photodetachment spectroscopy and resonant photoelectron imaging of cryogenically-cooled $C_6H_5O^-$ and $C_6H_5S^-$ anions via vibrational levels of the dipole-bound states. Nine new DBS vibrational resonances are observed for $C_6H_5O^-$. The dipole-bound excited state is observed for the first time for $C_6H_5S^-$ with a binding energy of only 39 cm^{-1} . Twelve above-threshold vibrational resonances are observed for $C_6H_5S^-$. Resonant photoelectron images and spectra are obtained by tuning the detachment laser to the vibrational levels of the DBS. The observed vibrational features in both the photodetachment spectra and the resonant photoelectron spectra are assigned using the calculated frequencies and the $\Delta v = -1$ propensity rule for vibrational autodetachment from DBS. Five extra fundamental vibrational modes, including three low-frequency modes, are resolved for the ground state of C_6H_5O (X^2B_1). And two fundamental vibrational modes are also resolved for its excited state (A^2B_2). Intramolecular inelastic rescattering has been observed in the autodetachment process leading to the excitation of the lowest-frequency bending mode (ν_{20}) of C_6H_5O . Seven fundamental vibrational modes, including several low-frequency modes, are resolved for the ground state of C_6H_5S (X^2B_1), compared to the single ν_{11} vibrational progression observed in the non-resonant photoelectron spectra. The combination of photodetachment spectroscopy and resonant photoelectron imaging for cold anions is shown again to be a powerful method to obtain vibrational information of dipolar neutral radicals.

6.6 Supporting information

Table 6.6. Theoretical harmonic frequencies of C₆H₅O (X^2B_1) and C₆H₅S (X^2B_1). The calculations were done with density functional theory at the B3LYP/6-311++G(d,p) level. The harmonic frequencies of C₆H₅O (A^2B_2) are calculated with time-dependent density-functional theory at the same level.

Mode	Symmetry	C ₆ H ₅ O (cm ⁻¹)		C ₆ H ₅ S (cm ⁻¹)
		X^2B_1	A^2B_2	X^2B_1
v ₁	A ₁	3199	3208	3202
v ₂		3188	3199	3190
v ₃		3167	3168	3169
v ₄		1585	1624	1595
v ₅		1481	1461	1480
v ₆		1417	1319	1199
v ₇		1166	1199	1077
v ₈		1008	1045	1038
v ₉		983	989	1004
v ₁₀		804	834	730
v ₁₁		531	524	427
v ₁₂	A ₂	978	953	990
v ₁₃		797	807	844
v ₁₄		375	434	384
v ₁₅	B ₁	977	946	1007
v ₁₆		919	868	937
v ₁₇		787	731	764
v ₁₈		642	654	683
v ₁₉		474	512	463
v ₂₀		184	223	161
v ₂₁	B ₂	3196	3207	3199
v ₂₂		3174	3173	3178
v ₂₃		1544	1574	1576
v ₂₄		1442	1458	1458
v ₂₅		1338	1351	1341
v ₂₆		1275	1266	1302
v ₂₇		1165	1182	1179
v ₂₈		1089	1095	1095
v ₂₉		597	623	621
v ₃₀		446	378	299

Table 6.7. The vibrational displacements and frequencies for selected fundamental modes of C_6H_5O (X^2B_1 and A^2B_2) and C_6H_5S (X^2B_1). They were calculated at the B3LYP/6-311++G(d,p) level of theory.

C_6H_5O (X^2B_1)				
	$\nu_{20} (B_1) = 184 \text{ cm}^{-1}$	$\nu_{19} (B_1) = 474 \text{ cm}^{-1}$	$\nu_{18} (B_1) = 642 \text{ cm}^{-1}$	$\nu_{16} (B_1) = 919 \text{ cm}^{-1}$
				
	$\nu_{14} (A_2) = 375 \text{ cm}^{-1}$	$\nu_{11} (A_1) = 531 \text{ cm}^{-1}$	$\nu_{10} (A_1) = 804 \text{ cm}^{-1}$	$\nu_9 (A_1) = 983 \text{ cm}^{-1}$
				
	$\nu_8 (A_1) = 1008 \text{ cm}^{-1}$			
C_6H_5O (A^2B_2)				
	$\nu_{11} (A_1) = 524 \text{ cm}^{-1}$	$\nu_6 (A_1) = 1319 \text{ cm}^{-1}$		
C_6H_5S (X^2B_1)				
	$\nu_{20} (B_1) = 161 \text{ cm}^{-1}$	$\nu_{19} (B_1) = 161 \text{ cm}^{-1}$	$\nu_{18} (B_1) = 683 \text{ cm}^{-1}$	$\nu_{16} (B_1) = 937 \text{ cm}^{-1}$
				
	$\nu_{11} (A_1) = 427 \text{ cm}^{-1}$	$\nu_{10} (A_1) = 730 \text{ cm}^{-1}$	$\nu_8 (A_1) = 1038 \text{ cm}^{-1}$	

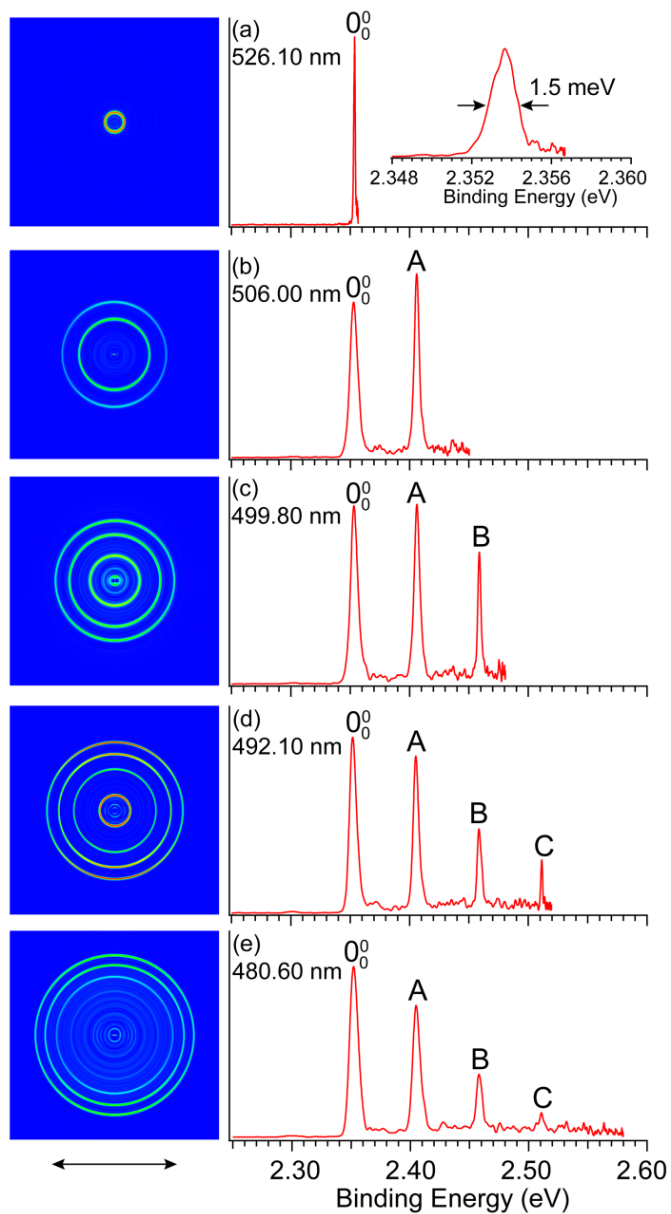


Figure 6.10. Non-resonant images and spectra of $C_6H_5S^-$ at five different wavelengths. The double arrow below the images indicates the direction of the laser polarization.

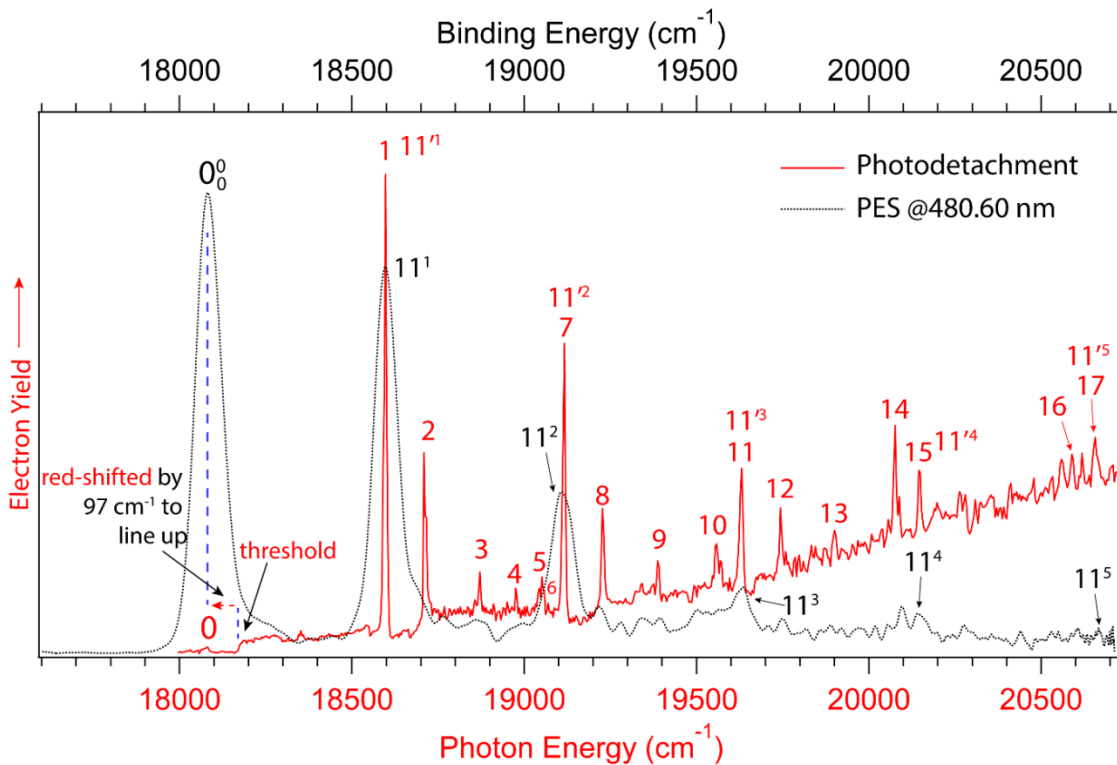


Figure 6.11. Comparison of the non-resonant photoelectron spectrum at 480.60 nm (Fig. 6.1) with the photodetachment spectrum (Fig. 6.2) for $C_6H_5O^-$. The photoelectron spectrum is red-shifted by 97 cm^{-1} to line up the peak 0_0^0 with peak 0 (the ground vibrational level of the neutral C_6H_5O and the DBS of $C_6H_5O^-$). The vibrational progression of mode ν_{11} agrees well with each other, indicating that the weakly bound electron in the DBS of $C_6H_5O^-$ has little effect on the neutral core C_6H_5O .

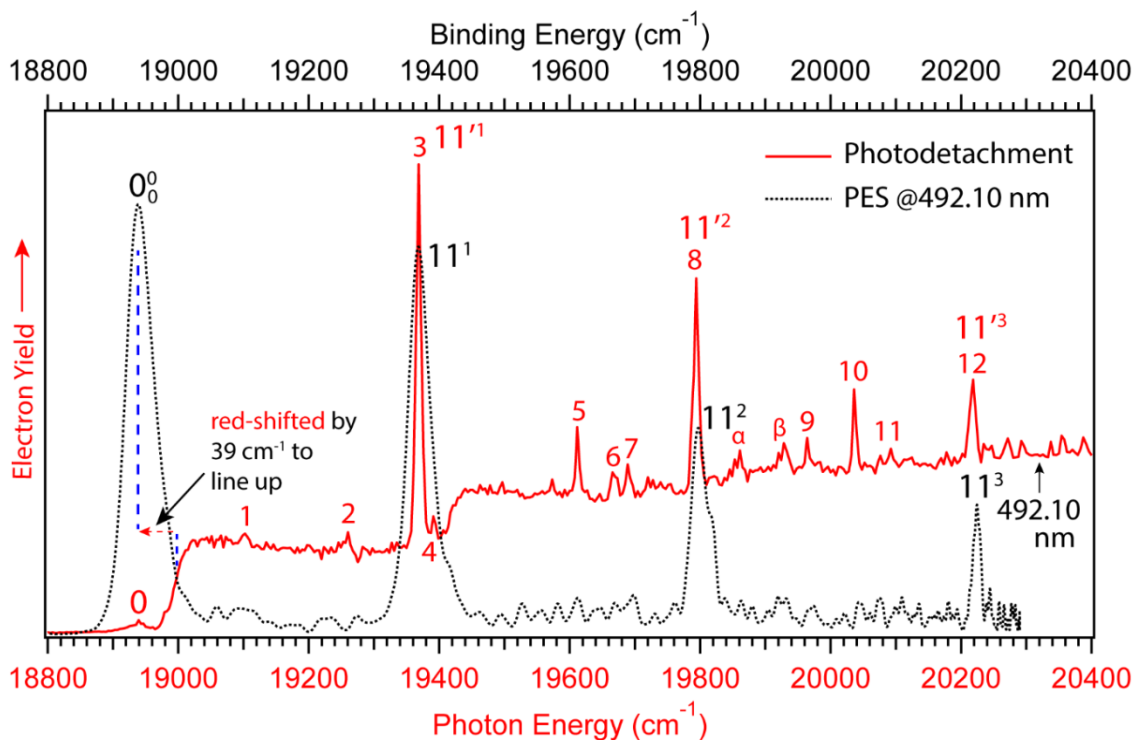


Figure 6.12. Comparison of the non-resonant photoelectron spectrum at 492.10 nm (Fig. 6.10) with the photodetachment spectrum (Fig. 6.5) for $C_6H_5S^-$. The photoelectron spectrum is red-shifted by 39 cm^{-1} to line up the peak 0_0^0 and peak 0 (the ground vibrational level of neutral C_6H_5S and the DBS of $C_6H_5S^-$). The vibrational progression of mode ν_{11} agrees well with each other, indicating the weakly bound nature of the DBS electron, which has little effect on the neutral C_6H_5S core.

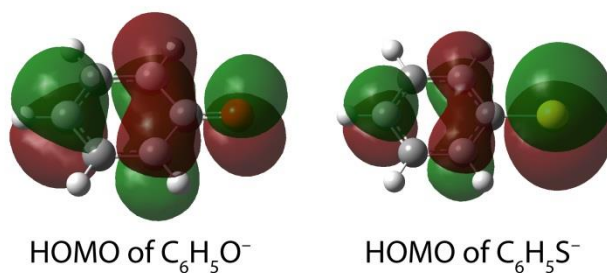


Figure 6.13. The HOMO orbitals of $C_6H_5O^-$ and $C_6H_5S^-$. The calculations were done at the B3LYP/6-311++G(d, p) level of theory.

Chapter 7 Tautomer-specific resonant photoelectron imaging of deprotonated cytosine anions**

This chapter³⁹⁴ will discuss one of applications of DBS, which is to obtain the tautomer-specific information for deprotonated cytosine anions.

Tautomers of the nucleobases play fundamental roles in spontaneous mutations of DNA. Tautomers of neutral cytosine have been studied in the gas phase, but much less are known about charged species. Here we report the observation and characterization of three tautomers of deprotonated cytosine anions, [trans-keto-amino-N3H-H8b] (**tKAN3H8b⁻**), [cis-keto-amino-N3H-H8a] (**cKAN3H8a⁻**) and [keto-amino-H] (**KAN1⁻**), produced by electrospray ionization. Excited dipole-bound states (DBSs) are uncovered for the three anions by photodetachment spectroscopy. Excitations to selected DBS vibrational levels of **cKAN3H8a⁻** and **tKAN3H8b⁻** yield tautomer-specific resonant photoelectron spectra. The current study provides further insight into tautomerism of cytosine and suggests a new method to study the tautomers of nucleobases using electrospray ionization and anion spectroscopy.

7.1 Introduction

As fundamental building blocks of DNA and RNA, nucleic acid bases are involved in the transmission and encoding of genetic information. Tautomerism is crucial to the structure and proper function of DNA because the formation of rare tautomers can cause mismatches in base pairing, resulting in spontaneous mutagenesis.^{395,396} The

** The content of this chapter is reproduced with permission from [G. Z. Zhu, C. H. Qian, and L. S. Wang, Tautomer-specific resonant photoelectron imaging of deprotonated cytosine anions. *Angew. Chem. Int. Ed.* (2019). DOI: 10.1002/anie.201903444.]. Copyright Wiley-VCH Verlag GmbH & Co. KGaA.

tautomers of cytosine, one of the pyrimidine bases, have been studied in different environments. Theoretical calculations have shown that the isolated neutral cytosine molecule can adopt six tautomers, as shown in Fig. 7.5 in Supporting Section 7.5, where their relative stabilities in aqueous solution³⁹⁷ and gas phase³⁹⁸ are also given. The canonical tautomer of keto-amino-N1H (**KAN1H**) predominantly exists under the physiological condition, and it is the tautomer that forms the Watson-Crick pair with guanine via hydrogen-bonding.³⁹⁵ The other rare tautomers have been observed by various spectroscopic techniques.³⁹⁹⁻⁴⁰⁵ The effect of water molecules on the structural dynamics and tautomerism of cytosine have also been investigated,^{406,407} showing that water can facilitate tautomerization from the canonical form to the rare tautomers by lowering the activation barriers of the prototropic process. The high stability of the keto-amino tautomers in solution derives from their large dipole moment.^{397,408} Early thermodynamic and kinetic studies showed that the major **KAN1H** and minor **KAN3H** forms (Fig. 7.5a in Supporting Section 7.5) are in equilibrium in aqueous solution.⁴⁰⁹ In addition, various tautomeric forms have also been studied for the radical anion and cation of cytosine, and the protonated cytosine.⁴¹⁰⁻⁴¹⁴

However, relatively little is known for the deprotonated cytosine anion ([Cy-H]⁻),⁴¹⁵⁻⁴¹⁷ despite their potential roles in DNA damage. The ionization of DNA bases by low-energy electrons is a crucial process for DNA damage after radiation.⁴¹⁸ Dissociative electron attachment experiment has shown that [Cy-H]⁻ is the most abundant anion fragment,⁴¹⁹ which can pair with guanine to form anionic complexes.⁴²⁰ The cytosine tautomers can be deprotonated at different sites to produce a plethora of negative ions (Fig. 7.6 in Supporting Section 7.5). Luo et al.⁴¹⁵ calculated the structures of five

different [Cy-H]⁻ anions deprotonated from the canonical **KAN1H** tautomer and computed the electron affinities (EAs) for the corresponding neutral [Cy-H] radicals. Considering the deprotonation from other rare tautomers and searching for 95 initial structures, Vázquez et al.⁴¹⁶ found that the six most stable [Cy-H]⁻ anions were, in the order of stability, **tKAN3H8b⁻** > **cKAN3H8a⁻** > **KAN1⁻** > **cEAOH8a⁻** > **cKAN1H8a⁻** > **tEAOH8a⁻** (Table 7.1 in Supporting Section 7.5).

For the current study, we recalculated the structures and relative energies of these six anions, as well as a seventh anion **tKAN1H8b⁻** (Fig. 7.1) from deprotonation of **KAN1H**. The computed EAs and dipole moments of their corresponding radicals are presented in Table 7.1. The three most stable [Cy-H]⁻ anions are similar to those by Vázquez et al.⁴¹⁶ It is interesting to note that the most stable anion **tKAN3H8b⁻** is not deprotonated from the canonical **KAN1H** cytosine (Fig. 7.6 in Supporting Section 7.5). Parsons et al.⁴¹⁷ reported a low-resolution photoelectron imaging study on the [Cy-H]⁻ anion produced by a pulsed discharge method. A congested broad band was observed and the spectrum was assigned to be from the **KAN1⁻** anion with a measured EA for the **KAN1** neutral radical as 3.037(15) eV, compared with the theoretical values of 3.00 eV by Lou et al.⁴¹⁵ and 3.37 eV by Vázquez et al.⁴¹⁶ However, no other tautomeric forms of the [Cy-H]⁻ anion have been disclosed.

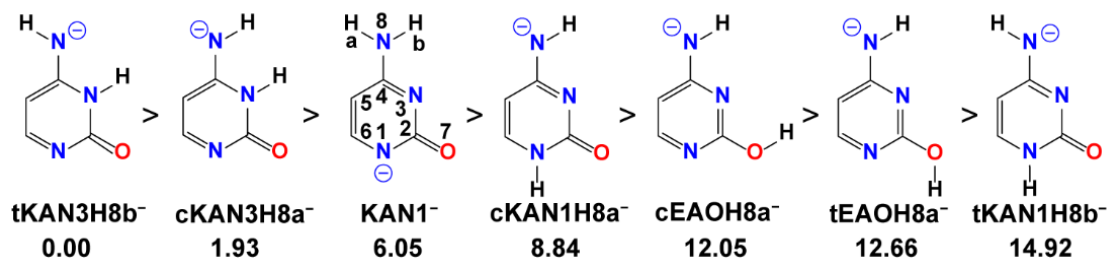


Figure 7.1. The seven most stable tautomers of deprotonated cytosine anions in the gas phase. The values below the structures show the calculated relative stabilities in kcal/mol.

Here we report a high-resolution photoelectron imaging and photodetachment spectroscopy study of [Cy-H]⁻. Three tautomeric deprotonated cytosine anions, **tKAN3H8b⁻**, **cKAN3H8a⁻** and **KAN1⁻**, have been observed. The photodetachment spectrum shows strong DBS resonances, due to autodetachment from vibrational levels of the excited DBSs of the **tKAN3H8b⁻** and **cKAN3H8a⁻** anions. Several weak resonant peaks are tentatively assigned to a third deprotonated anion **KAN1⁻**, which is expected to have weak ion abundance due to its low stability.

7.2 Experimental methods

The experiments were done using the third-generation ESI-PES apparatus. The details were described in the Chapter 2.

7.3 Results and discussion

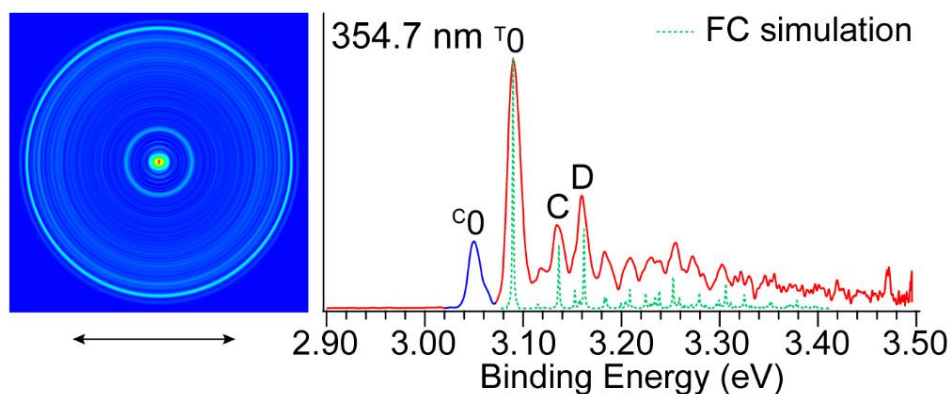


Figure 7.2. Non-resonant photoelectron image and spectrum of [Cy-H]⁻ at 354.7 nm. The peak (c0) is due to detachment from **cKAN3H8a⁻**, while the peaks above T0 are from **tKAN3H8b⁻**. The Franck-Condon (FC) simulation of **tKAN3H8b⁻** is presented as dot. The double arrow below the image shows the direction of the laser polarization.

Figure 7.2 shows the non-resonant photoelectron image and spectra of [Cy-H]⁻ at 354.7 nm. The complexity of the vibrational structures suggests possible presence of

different tautomeric anions. To assist the spectral assignments, we have done Franck-Condon simulations for all the seven low-lying anions using the FC-LabII program⁴²¹ and compared them with the spectrum. Figure 7.2 shows that the simulated spectrum of **tKAN3H8b⁻** is in good agreement with the spectral features at higher binding energies (above the peak ^T0), while the simulated spectra of the other anions are not (Fig. 7.7 in Supporting Section 7.5). This means that the peaks at higher binding energies are due to photodetachment from **tKAN3H8b⁻**, which is the most stable tautomeric anion according to our calculations (Table 7.1 in Supporting Section 7.5) and previous study by Vázquez et al.⁴¹⁶ The peak labeled ^T0 defines the EA of the neutral **tKAN3H8b** radical, which is more accurately measured to be 3.0870(5) eV in the near-threshold resonant photoelectron spectra (*vide infra*). The measured EA is in perfect agreement with our computed value for **tKAN3H8b**, which also represents the largest EA among the first seven tautomers (Table 7.1 in Supporting Section 7.5). Peaks C and D, with shifts of 373 cm⁻¹ and 575 cm⁻¹ from peak ^T0, represent the most Franck-Condon-active vibrational modes ^Tv₂₁ (376 cm⁻¹) and ^Tv₁₈ (583 cm⁻¹) of **tKAN3H8b** (Table 7.2 in Supporting Section 7.5), respectively. Both modes involve in-plane H-atom vibrations (Fig. 7.8b in Supporting Section 7.5). The peak labeled ^C0 at the lower binding energy should come from another tautomer, most likely the second most stable **cKAN3H8a⁻** species (*vide infra*). The EA of the **cKAN3H8a** radical defined by peak ^C0 is measured to be 3.0471(5) eV, which agrees well with our computed value (Table 7.1 in Supporting Section 7.5).

The **cKAN3H8a** and **tKAN3H8b** radicals are calculated to have dipole moments of 3.35 D and 5.55 D (Table 7.1 in Supporting Section 7.5), respectively, which are large enough to support excited DBSs for the corresponding anions. We conducted

photodetachment spectroscopy by monitoring the total electron yield while scanning the laser wavelength across the detachment thresholds, as shown in Fig. 7.3. The arrow (^CEA) at 24577 cm⁻¹ and the arrow (^TEA) at 24898 cm⁻¹ indicate the detachment thresholds of **cKAN3H8a⁻** and **tKAN3H8b⁻**, respectively, which are consistent with the measured EAs from the photoelectron spectra (Fig. 7.2 and 7.4). Around 24300 cm⁻¹, the peaks labeled ^C0' and ^T0' represent the ground vibrational levels of the DBSs of **cKAN3H8a⁻** and **tKAN3H8b⁻**, respectively. These peaks are below the respective detachment thresholds by 325 cm⁻¹ (^C0' below ^CEA) and 577 cm⁻¹ (^T0' below ^TEA), representing the binding energies of the DBSs of the two anions. The larger DBS binding energy for **tKAN3H8b⁻** is consistent with the larger dipole moment of the corresponding neutral **tKAN3H8b** radical. The below-threshold peaks ^C0' and ^T0' are due to resonant two-photon detachment. The resonant two-photon photoelectron image corresponding to peak ^T0' is shown in the inset of Fig. 7.3. The *p*-wave angular distribution of the two-photon signals is consistent with detachment from an *s*-type dipole-bound orbital of **tKAN3H8b⁻**, as observed previously.¹¹⁷⁻¹²² Above ^CEA, the peaks ^C1 to ^C3 correspond to vibrational levels of the DBS of **cKAN3H8a⁻**, as a result of vibrational autodetachment. The peaks ^T1 to ^T7 represent the DBS vibrational levels of **tKAN3H8b⁻**. The weaker peaks ^T1 and ^T2 below ^TEA are due to resonant two-photon detachment, while the strong peaks ^T3 to ^T7 are due to autodetachments from vibrational levels of the DBS of **tKAN3H8b⁻**.

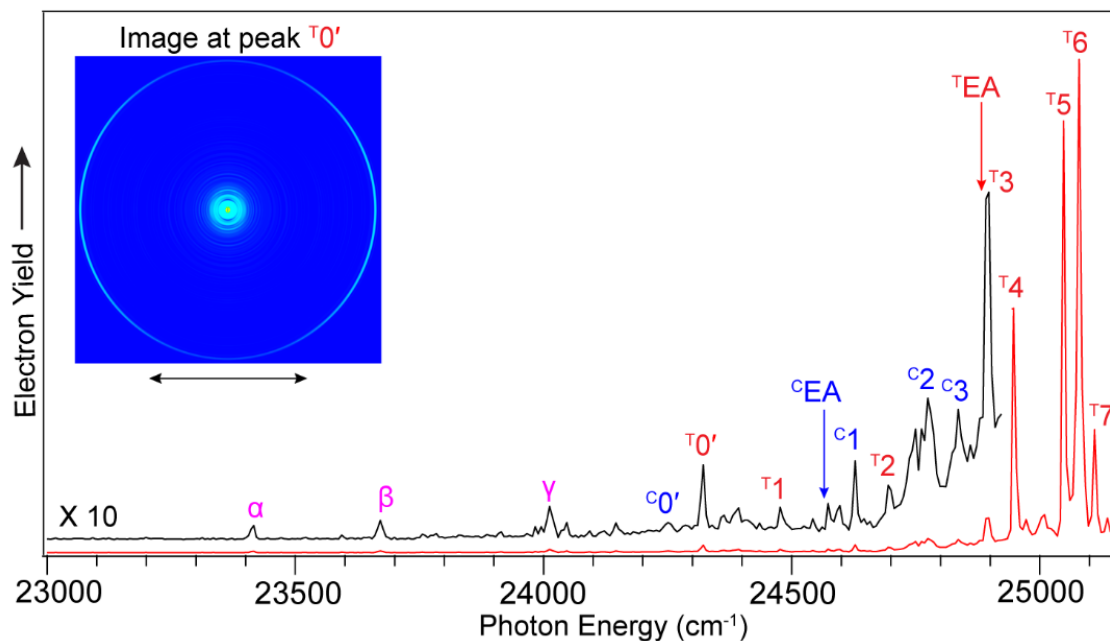


Figure 7.3. The photodetachment spectrum of [Cy-H]⁻. The spectrum was obtained by measuring the total electron yield as a function of photon energy across the detachment thresholds of **cKAN3H8a⁻** and **tKAN3H8b⁻**, indicated by the arrows below ^cEA and ^TEA, respectively. The curve below 24900 cm⁻¹ is expanded by 10 times. Peaks ^c0' and ^T0' represent the ground DBS vibrational levels of **cKAN3H8a⁻** and **tKAN3H8b⁻**, respectively. Peaks ^c1-^c3 are due to autodetachment from vibrational levels of the DBS of **cKAN3H8a⁻**, while peaks ^T1-^T7 are from **tKAN3H8b⁻**. Peaks α, β and γ at lower photon energies are assigned to DBS levels of **KAN1⁻**. The outmost ring in the inset shows the photoelectron image obtained with a photon energy corresponding to peak ^T0', due to resonant two-photon detachment. The double arrow below the image indicates the direction of the laser polarization.

At even lower photon energies in Fig. 7.3, three weak peaks, labeled as α, β and γ, are also observed, which are not from **cKAN3H8a⁻** or **tKAN3H8b⁻**. They could be from the DBS of the **KAN1⁻** anion, whose neutral core has a very large dipole moment of 7.79 D (Table 7.1 in Supporting Section 7.5). The energy shifts of peaks β and γ relative to peak α are 255 cm⁻¹ and 594 cm⁻¹, respectively. We also calculated the vibrational frequencies of all the other neutral radicals with dipole moments larger than 2.5 D (Table 7.2 in Supporting Section 7.5). The shifts of 255 cm⁻¹ and 594 cm⁻¹ are found to agree well with the fundamental vibrational modes ^{KA}v₂₈ (231 cm⁻¹) and ^{KA}v₂₂ (593 cm⁻¹) of **KAN1**, respectively (Fig. 7.8c in Supporting Section 7.5). This indicates the presence of

a third tautomer in the ion beam (Fig. 7.1). The intensity of the **KAN1⁻** anion is very weak, because of its relatively high energy, so that no clear spectral features are observed for this tautomer in the photoelectron spectra.

The photon-energy shifts from the respective ground vibrational levels of the DBS and assignments of the observed resonances are given in Table 7.3 in Supporting Section 7.5. The assignments of all the resonances are based on the calculated vibrational frequencies (Table 7.2 in Supporting Section 7.5) and vibrational autodetachments in the resonant photoelectron spectra (Figs. 7.4a-h), which yield tautomer-specific information. We have shown previously that vibrational frequencies in the DBS are the same as those in the neutral states,¹¹⁷⁻¹²² i.e., the diffuse dipole-bound electron has little effect on the neutral cores.

By tuning the detachment laser wavelengths to the above-threshold peaks (^C1-^C3 and ^T3-^T7), we have obtained eight high-resolution resonantly-enhanced photoelectron images and spectra (Figs. 7.4a-h). As discussed previously,¹¹⁷⁻¹²² two detachment channels contribute to the resonant photoelectron spectra: the non-resonant detachment represented by the baseline in Fig. 7.3 and the resonantly-enhanced vibrational autodetachment via the DBS resonances. Autodetachment from DBS vibrational levels generally follows the mode selectivity¹¹⁷ and $\Delta v = -1$ propensity rule,^{189,190} which result in highly non-Franck-Condon photoelectron spectra.

The resonant photoelectron spectra involving autodetachment from vibrational levels of the DBSs of **cKAN3H8a⁻** or **tKAN3H8b⁻** are essentially tautomer-specific because resonant excitations to the DBSs have much higher cross sections than the non-resonant photodetachment processes, which are not tautomer-specific. In comparison

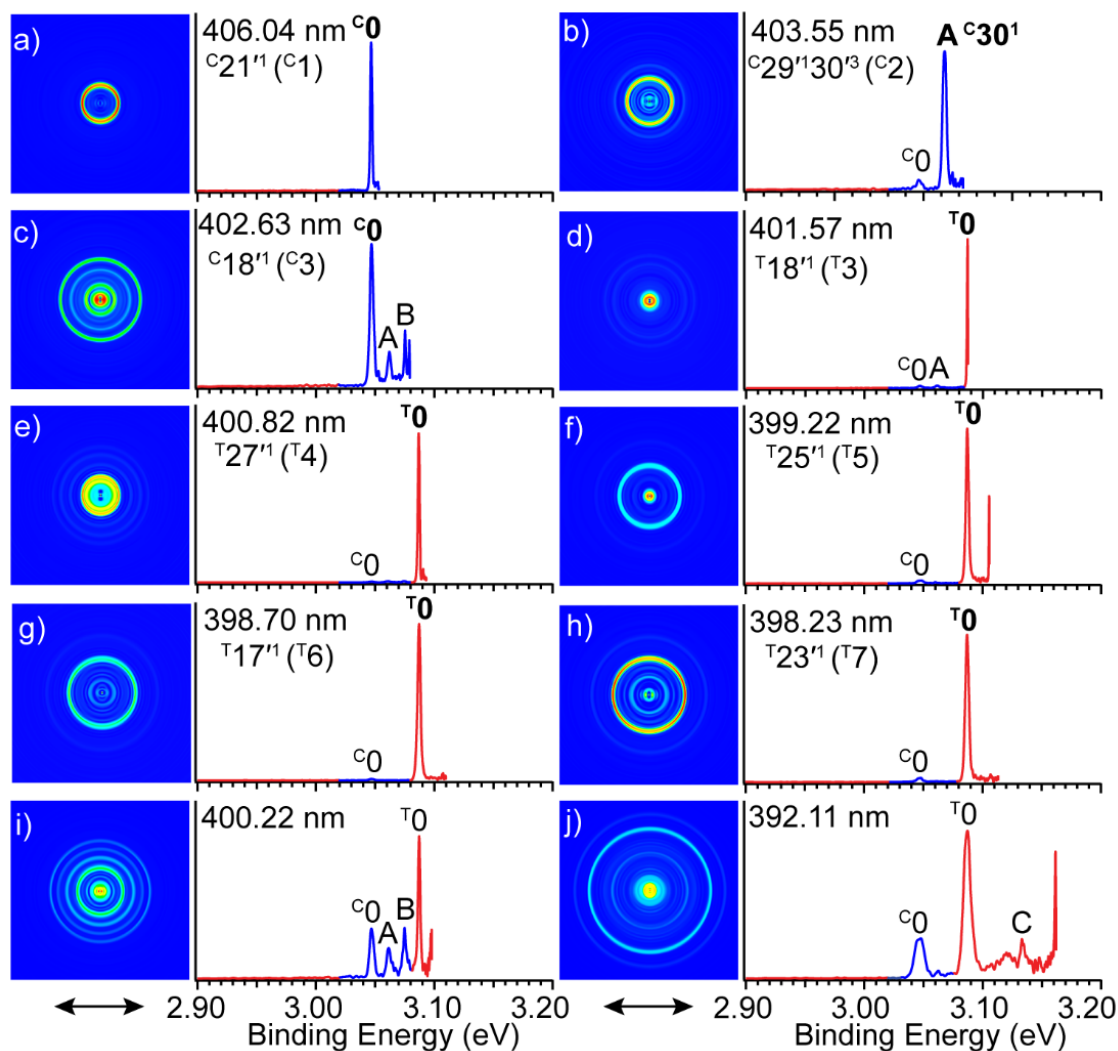


Figure 7.4. Photoelectron images and spectra of deprotonated cytosine anions. Tautomer-specific resonant spectra were taken at a) 406.04 nm, b) 403.55 nm, c) 402.63 nm, d) 401.57 nm, e) 400.82 nm, f) 399.22 nm, g) 398.70 nm and h) 398.23 nm and the non-resonant images/spectra were taken at i) 400.22 nm and j) 392.11 nm. a)-c) correspond to autodetachment from fundamental vibrational levels of the DBS of **cKAN3H8a⁻**, while d)-h) are from the DBS of **tKAN3H8b⁻**. The peak numbers in the parentheses correspond to the DBS resonances in Figure 7.3 and the assignments are also given. Peaks labeled in bold face indicate the enhanced final neutral vibrational levels due to vibrational autodetachment from the DBS. The double arrows below the images show the directions of the laser polarization.

with non-resonant spectra in Figs. 7.4i and 7.4j, resonant spectra in Figs. 7.4a and 7.4c showing spectral features from the **cKAN3H8a⁻** tautomer displays enhancement of peak **c₀**, which should be due to autodetachment from fundamental vibrational levels of the DBS of **cKAN3H8a⁻**, according to the $\Delta v = -1$ propensity rule. The photon energies used

in Figs. 7.4a and 7.4c, corresponding to the DBS resonances of ^C1 and ^C3 in Fig. 7.3, are 375 cm⁻¹ and 585 cm⁻¹ above the DBS ground vibrational level (^C0') of **cKAN3H8a**⁻, in good agreement with the calculated frequencies of the fundamental vibrational modes of ^Cv₂₁ (375 cm⁻¹) and ^Cv₁₈ (581 cm⁻¹) of **cKAN3H8a**, respectively (Table 7.2 and Fig. 7.8a in Supporting Section 7.5). Hence, the DBS resonances of ^C1 and ^C3 should be assigned to the ^C21¹ and ^C18¹ DBS vibrational levels of **cKAN3H8a**⁻. The good agreement of the frequencies of the neutral radical and the dipole-bound anions is consistent with the weakly-bound nature of the extra electron in the DBS, as shown previously.¹¹⁷⁻¹²² The greatly enhanced peak A (^C30¹) in Fig. 7.4b is due to excitation to the combinational DBS vibrational level of ^C29¹30³ of **cKAN3H8a**⁻ followed by the $\Delta v = -3$ vibrational autodetachment, indicating a breakdown of the $\Delta v = -1$ propensity rule due to anharmonic effects involving the low-frequency bending mode. Similarly, Figs. 7.4d-h all display strongly enhanced peak ^T0, due to resonant excitations to the DBS vibrational levels of ^T18¹, ^T27¹, ^T25¹, ^T17¹ and ^T23¹ of **tKAN3H8b**⁻, followed by $\Delta v = -1$ vibrational autodetachment. The tautomer-specificity of the resonant spectra is vividly revealed in these spectra, as can be seen by the almost negligible intensity of the ^C0 peak due to the **cKAN3H8a**⁻ tautomer. A schematic energy level diagram showing the autodetachment processes for the eight resonant photoelectron spectra is displayed in Fig. 7.9 in Supporting Section 7.5.

The photon energies and assignments of all the observed DBS resonances of the [Cy-H]⁻ anions are summarized in Table 7.3 in Supporting Section 7.5. The measured vibrational frequencies for neutral **cKAN3H8a** and **tKAN3H8b** radicals are compared with the calculated frequencies in Table 7.4 in Supporting Section 7.5.

The observed ion abundance suggests the order of stabilities for the three anions as **tKAN3H8b⁻** > **cKAN3H8a⁻** > **KAN1⁻**, consistent with the theoretical predictions for the deprotonated cytosine anions both from the current study (Table 7.1 in Supporting Section 7.5) and the previous calculation by Vázquez et al.⁴¹⁶ It is interesting to note that the three observed anions could all come from direct deprotonation from the **KAN3H** tautomer (Fig. 7.6 in Supporting Section 7.5), which is the second most stable tautomer in solution. The **tKAN3H8b⁻** and **cKAN3H8a⁻** anions can also come from direct deprotonation from the rare *trans*- and *cis*-keto-imino tautomers, respectively. Only the **KAN1⁻** anion can come from direct deprotonation of the most stable **KAN1H** canonical cytosine in solution. Direct deprotonation from the **KAN1H** canonical cytosine would also produce the **cKAN1H8a⁻** and **tKAN1H8b⁻** anions, which are higher energy species.

7.4 Conclusions

In summary, two tautomeric deprotonated cytosine anions, **tKAN3H8b⁻** and **cKAN3H8a⁻**, have been identified by high-resolution PEI, photodetachment spectroscopy, and resonant PEI. The EAs of **tKAN3H8b** and **cKAN3H8a** are measured accurately to be 3.0870(5) eV and 3.0471(5) eV, respectively. Excited dipole-bound states are observed for **tKAN3H8b⁻** and **cKAN3H8a⁻** and their vibrational ground states are found to be bound by 577 cm⁻¹ and 325 cm⁻¹ below the respective detachment thresholds. Tautomer-specific photoelectron spectra are obtained for **tKAN3H8b⁻** and **cKAN3H8a⁻** using resonant PEI via vibrational autodetachment from specific vibrational resonances of the DBSs. Photodetachment spectroscopy also revealed weak DBS resonances assigned to a third tautomer, **KAN1⁻**, which is relatively high in energy. The

ion abundances revealed in the relative intensities in the PEI and photodetachment spectra indicate the order of stabilities for the three anions as **tKAN3H8b⁻** > **cKAN3H8a⁻** > **KAN1⁻**. The current study suggests that photodetachment spectroscopy and resonant PEI, coupled with cryogenic ion cooling, are powerful techniques to investigate the structures and stabilities of the nucleic acid base anions and to obtain tautomer-specific spectroscopic information.

7.5. Supporting information

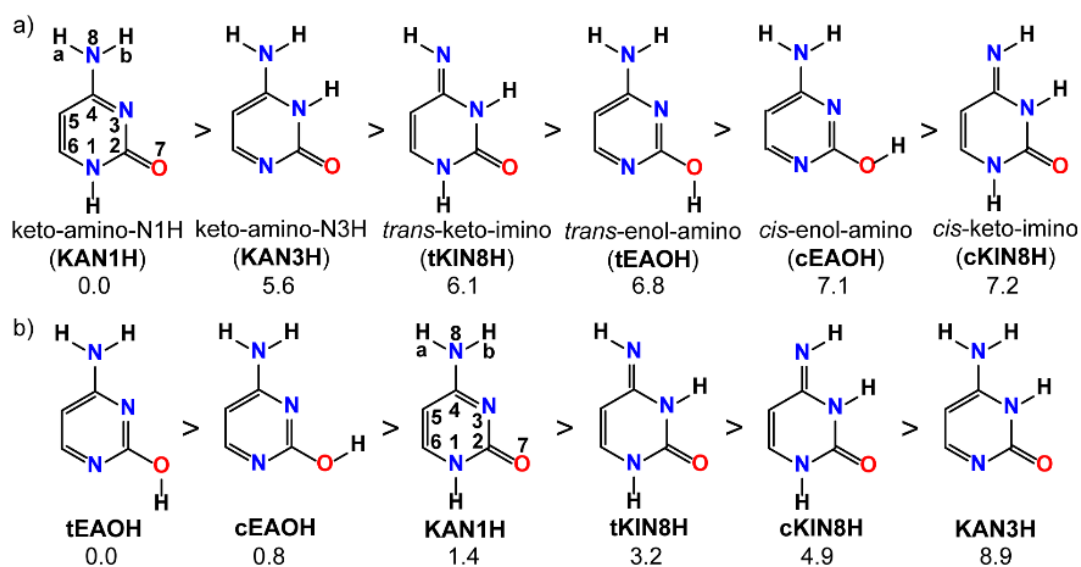


Figure 7.5. The top six tautomers of neutral cytosine in different conditions. (a) aqueous solution³⁹⁷ and (b) gas phase.³⁹⁸ The numbers below the structure shows the relative stabilities in kcal/mol.

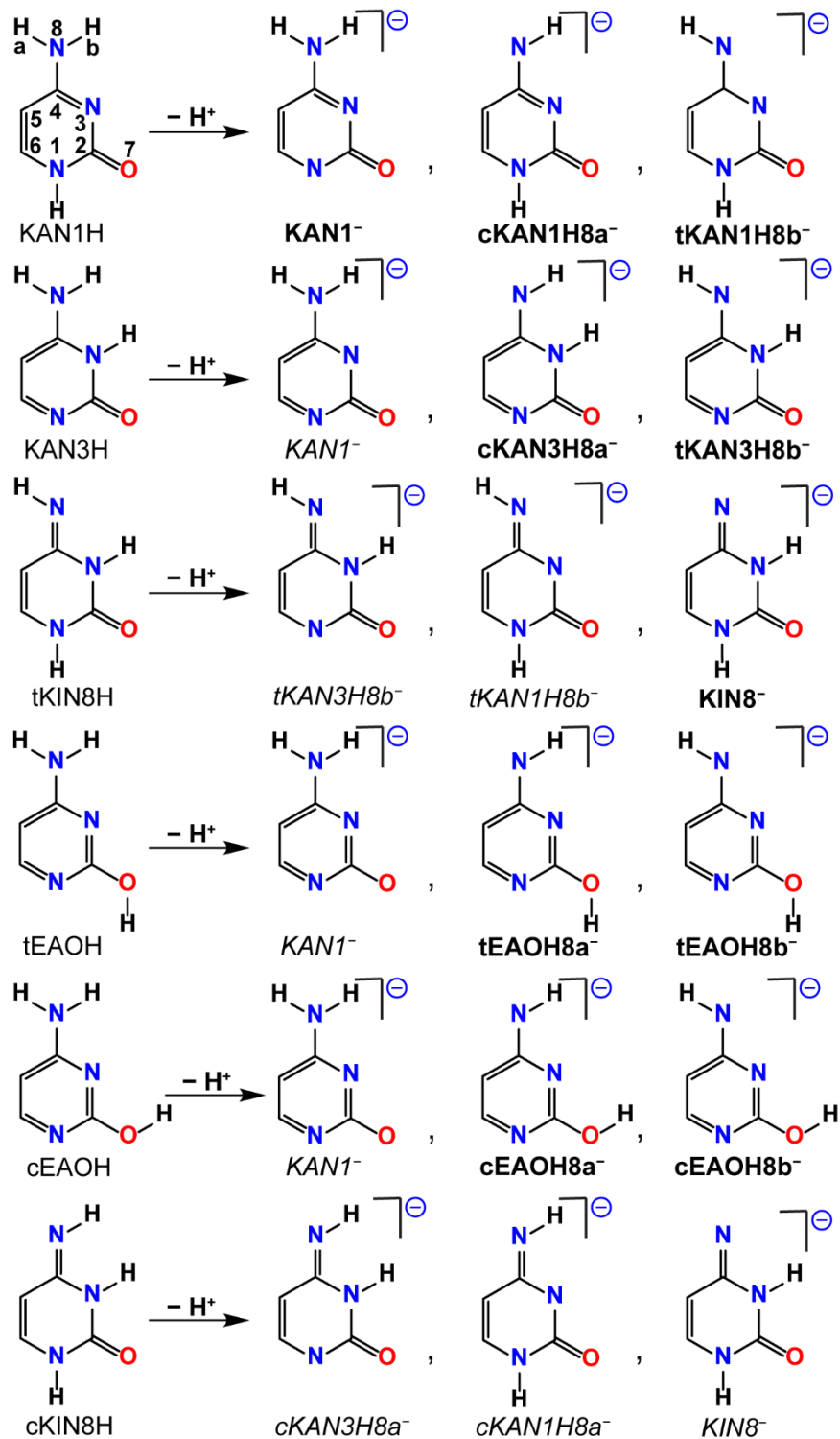


Figure 7.6. Possible deprotonation from the nitrogen sites of the six most stable neutral cytosines in aqueous solution. A total of ten unique anions can be obtained and named in **bold face**. Deprotonation from different tautomers can lead to the same anions and the repetitive anions are named in *italic face*.

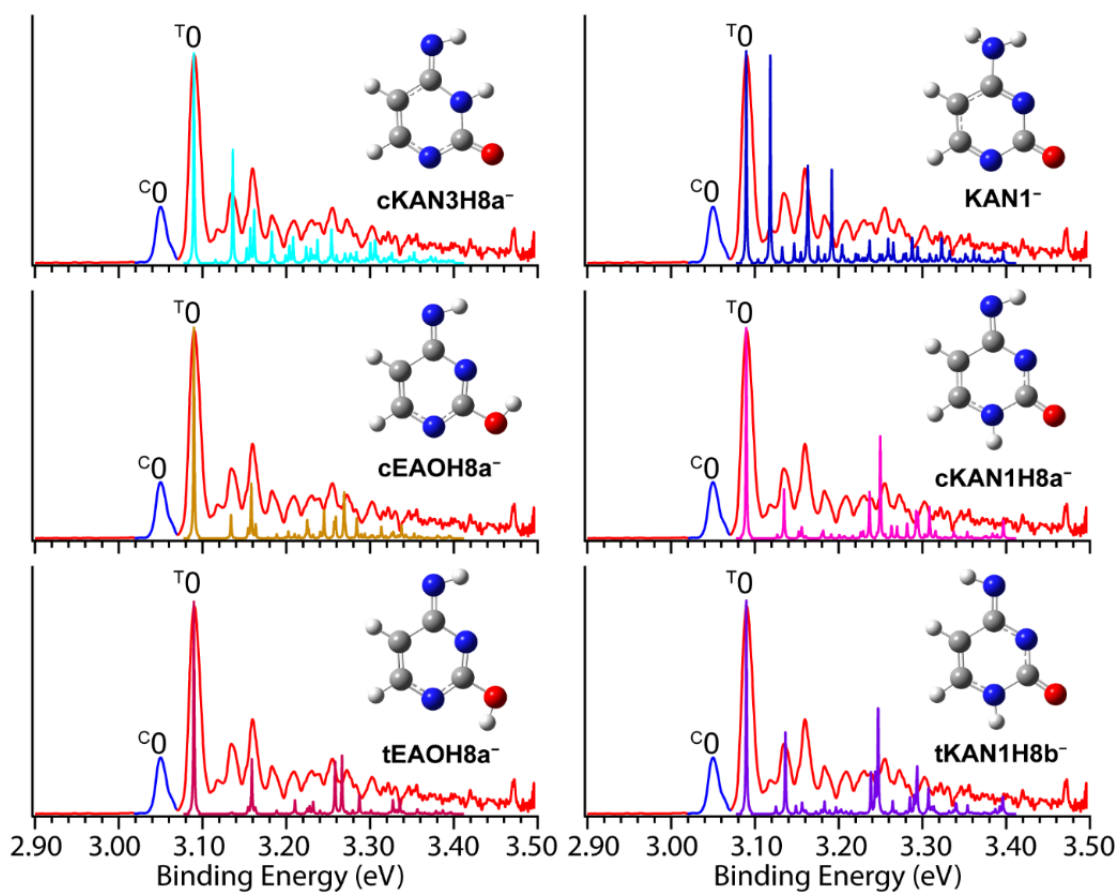


Figure 7.7. Comparisons of the major vibrational progression in photoelectron spectrum at 354.7 nm to the Franck-Condon simulations of six higher energy tautomeric [Cy-H]⁻ anions. The structures for the neutrals and anions of **cKAN1H8a⁻** and **tKAN1H8b⁻** were optimized at the B3LYP/6-31+G(d,p) level of theory, while those of other tautomeric forms were done at the B3LYP/6-311++G(d,p) level using the Gaussian 09 package.²⁵²

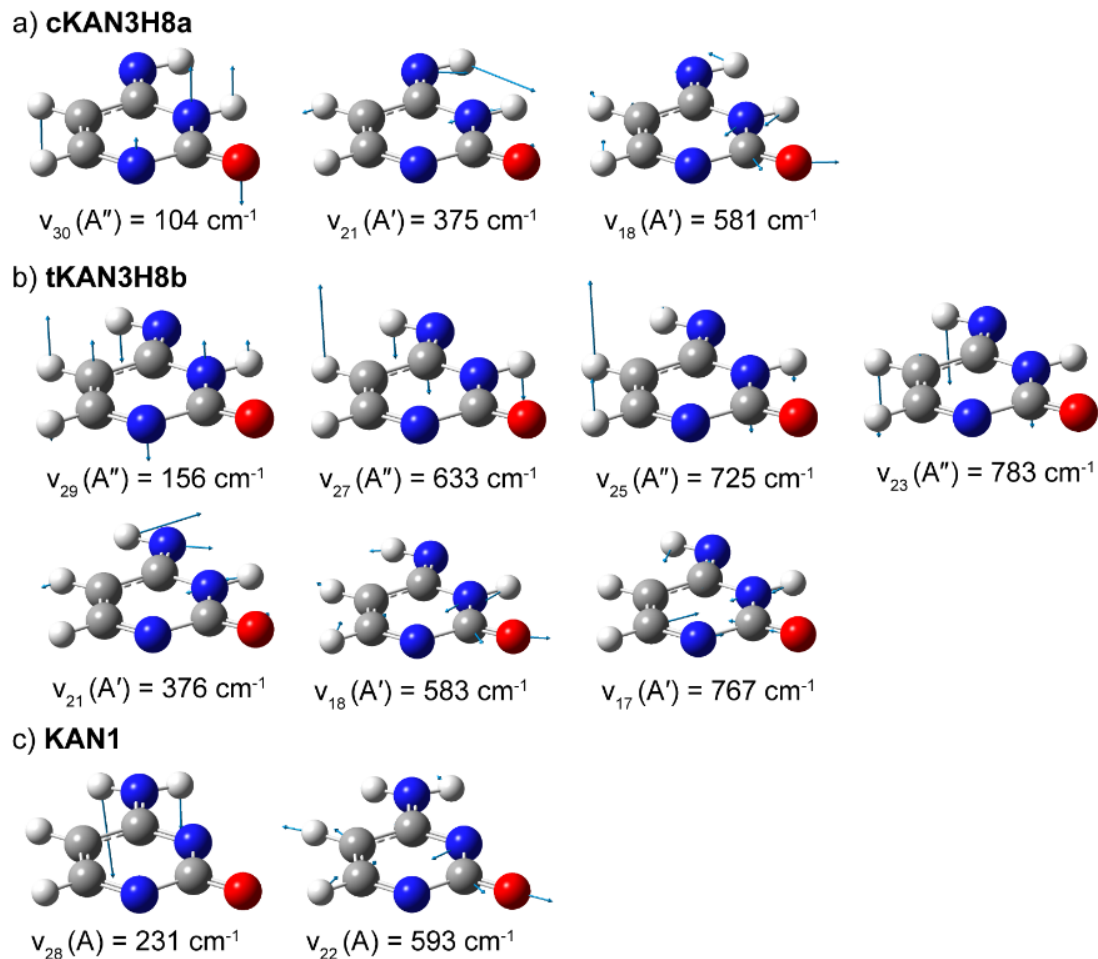


Figure 7.8. Vibrational displacements and frequencies for the observed fundamental modes of the three deprotonated cytosine radicals. a) **cKAN3H8a**, b) **tKAN3H8b** and c) **KAN1**, calculated at the B3LYP/6-311++G(d,p) level of theory. **cKAN3H8a** and **tKAN3H8b** have C_s symmetry, while **KAN1** has C_1 symmetry.

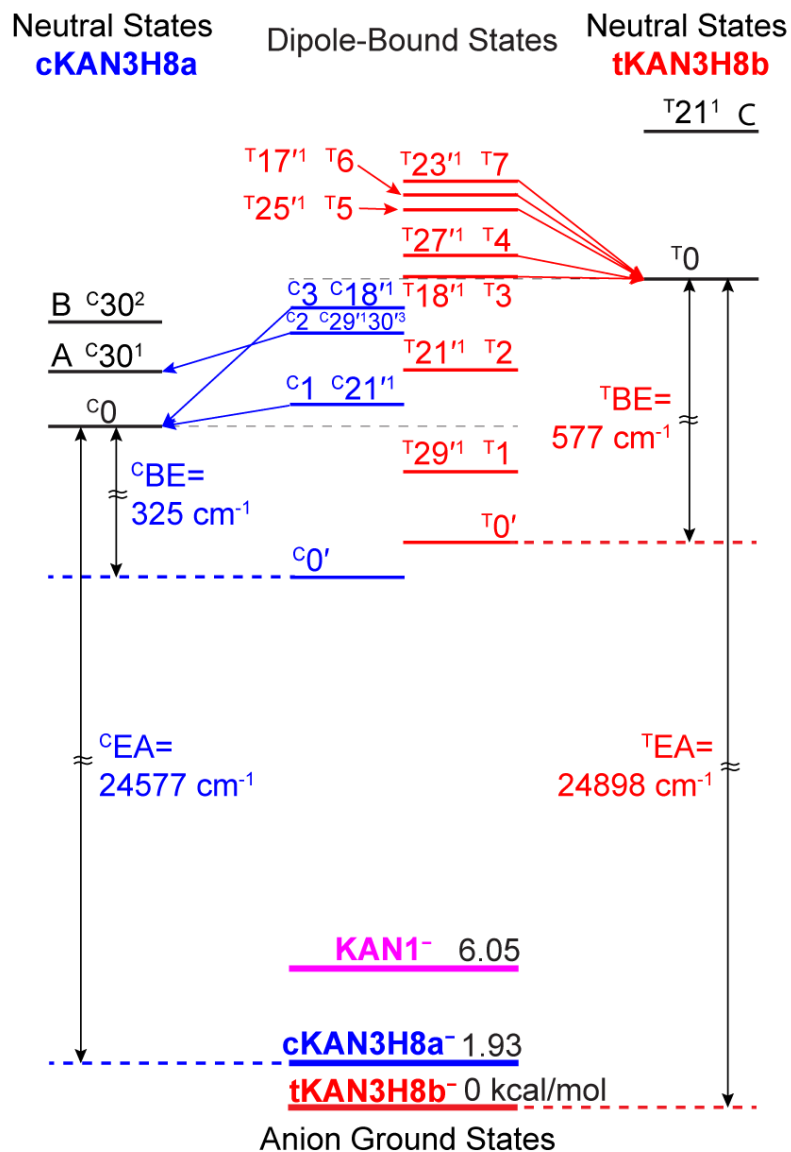
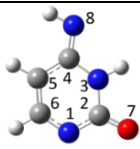
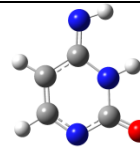
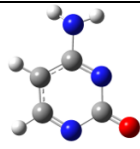
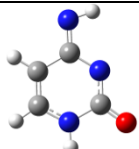


Figure 7.9. A schematic energy level diagram of deprotonated cytosine anions. The arrows represent autodetachments from the DBS vibrational levels of **cKAN3H8a⁻** and **tKAN3H8b⁻** to the respective neutral levels, corresponding to the eight resonant photoelectron spectra in Figures 3a-3h. The autodetachments from the DBS of **cKAN3H8a⁻** are given on the left, while those of **tKAN3H8b⁻** are presented on the right. The relative energies calculated for the three anions are presented in kcal/mol. The detachment thresholds of the **cKAN3H8a⁻** and **tKAN3H8b⁻** anions and the binding energies (BE) of the corresponding DBS are also given.

Table 7.1. The optimized structures and relative energies of seven deprotonated cytosine anions. Our calculations were done at the B3LYP/6-311++G(d,p) level of theory. The energies (ΔE) are relative to the most stable anion **tKAN3H8b⁻**. The electron affinity (EA) and dipole moment (μ) of the corresponding neutral radicals are calculated at the same level. The theoretical values of ΔE and EA from Luo et al.⁴¹⁵ and Vázquez et al.⁴¹⁶ are also compared. Luo et al.⁴¹⁵ used the B3LYP/DZP++ method for both ΔE and EA. Vázquez et al.⁴¹⁶ calculated the ΔE at the MP2/6-3111+G(2d,p) level of theory. The electron detachment energies of the anions were done at the P3//6-3111++G(2df,2p) level from MP2/6-3111+G(2d,p) optimized geometries.

					
		tKAN3H8b⁻	cKAN3H8a⁻	KAN1⁻	cKAN1H8a⁻
ΔE (kcal/mol)	Current work	0	1.93	6.05	8.84
	Luo et al. ⁴¹⁵			0.00	3.15
	Vázquez et al. ⁴¹⁶	0	1.9	3.0	8.0
EA (eV)	Current work	3.087	3.031	3.029	3.016
	Luo et al. ⁴¹⁵			3.00	2.96
	Vázquez et al. ⁴¹⁶	3.45	3.43	3.37	3.57
μ (D)	Current work	5.55	3.35	7.79	5.04

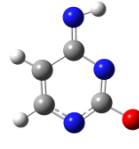
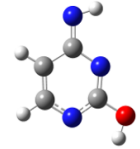
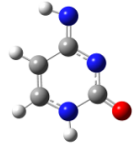
				
		cEAOH8a⁻	tEAOH8a⁻	tKAN1H8b⁻
ΔE (kcal/mol)	Current work	12.05	12.66	14.92
	Luo et al. ⁴¹⁵			8.78
	Vázquez et al. ⁴¹⁶	7.8	8.5	
EA (eV)	Current work	2.732	2.707	2.993
	Luo et al. ⁴¹⁵			2.94
	Vázquez et al. ⁴¹⁶	3.10	3.10	
μ (D)	Current work	5.55	3.35	7.79

Table 7.2. The harmonic frequencies of six deprotonated cytosine radicals. The calculations were done at the B3LYP/6-311++G(d,p) level of theory. The **KAN1** species has C₁ symmetry, while the other neutral radicals have C_s symmetry. The unit of frequency is cm⁻¹.

Modes	KAN1	Modes	cKAN3H8a	tKAN3H8b	cKAN1H8a	tKAN1H8b	tEAOH8a
v ₁ (A)	3725	v ₁ (A')	3589	3589	3601	3603	3792
v ₂ (A)	3595	v ₂ (A')	3454	3499	3420	3419	3429
v ₃ (A)	3189	v ₃ (A')	3231	3210	3246	3222	3227
v ₄ (A)	3139	v ₄ (A')	3142	3137	3203	3198	3167
v ₅ (A)	1650	v ₅ (A')	1745	1748	1758	1751	1593
v ₆ (A)	1600	v ₆ (A')	1532	1528	1627	1631	1533
v ₇ (A)	1536	v ₇ (A')	1510	1515	1543	1530	1469
v ₈ (A)	1440	v ₈ (A')	1443	1434	1452	1438	1426
v ₉ (A)	1378	v ₉ (A')	1404	1404	1394	1407	1360
v ₁₀ (A)	1366	v ₁₀ (A')	1374	1366	1281	1259	1344
v ₁₁ (A)	1282	v ₁₁ (A')	1324	1314	1238	1235	1255
v ₁₂ (A)	1246	v ₁₂ (A')	1190	1202	1180	1197	1214
v ₁₃ (A)	1109	v ₁₃ (A')	1147	1159	1117	1129	1148
v ₁₄ (A)	1078	v ₁₄ (A')	1080	1087	1101	1093	1093
v ₁₅ (A)	982	v ₁₅ (A')	994	999	962	966	1014
v ₁₆ (A)	977	v ₁₆ (A')	927	925	933	916	972
v ₁₇ (A)	910	v ₁₇ (A')	773	767	769	764	796
v ₁₈ (A)	820	v ₁₈ (A')	581	583	572	571	591
v ₁₉ (A)	750	v ₁₉ (A')	545	545	546	553	557
v ₂₀ (A)	747	v ₂₀ (A')	509	508	533	535	523
v ₂₁ (A)	645	v ₂₁ (A')	375	376	365	377	356
v ₂₂ (A)	593	v ₂₂ (A'')	986	977	969	959	990
v ₂₃ (A)	558	v ₂₃ (A'')	794	783	794	769	839
v ₂₄ (A)	526	v ₂₄ (A'')	789	741	775	759	775
v ₂₅ (A)	494	v ₂₅ (A'')	737	725	702	702	690
v ₂₆ (A)	369	v ₂₆ (A'')	641	649	625	620	647
v ₂₇ (A)	347	v ₂₇ (A'')	576	633	539	464	535
v ₂₈ (A)	231	v ₂₈ (A'')	382	376	392	374	430
v ₂₉ (A)	181	v ₂₉ (A'')	162	156	183	185	201
v ₃₀ (A)	114	v ₃₀ (A'')	104	102	102	85	167

Table 7.3. The summary of the observed peaks in the photodetachment spectrum. Their corresponding wavelengths, photon energies (hv), shifts from the ground DBS vibrational levels of **cKAN3H8a⁻**, **tKAN3H8b⁻** and **KANI⁻** are given. Theoretical frequencies are from Table 7.2.

Peak	Wavelength (nm)	hv (cm ⁻¹)	Shift (cm ⁻¹)	Assignment	Theo. Freq. (cm ⁻¹)
C0'	412.34	24252 (7)	(C)0	Ground DBS of cKAN3H8a⁻	
C ₁	406.06	24627(5)	(C)375	C ₂₁ ^{1l}	375
C ₂	403.55	24780(5)	(C)528	C ₂₉ ^{1l} 30 ³	
C ₃	402.63	24837(5)	(C)585	C ₁₈ ^{1l}	581
T0'	411.16	24321(5)	(T)0	Ground DBS of tKAN3H8b⁻	
T ₁	408.56	24476(5)	(T)155	T ₂₉ ^{1l}	156
T ₂	404.88	24699(5)	(T)378	T ₂₁ ^{1l}	376
T ₃	401.57	24902(5)	(T)581	T ₁₈ ^{1l}	583
T ₄	400.82	24949(5)	(T)628	T ₂₇ ^{1l}	633
T ₅	399.22	25049(5)	(T)728	T ₂₅ ^{1l}	725
T ₆	398.70	25082(5)	(T)761	T ₁₇ ^{1l}	767
T ₇	398.23	25111(5)	(T)790	T ₂₃ ^{1l}	783
DBS resonances of KANI⁻					
α	427.04	23417 (7)	(KA)0	Ground DBS of KANI⁻	
β	422.42	23672 (5)	(KA)255	K ^A ₂₈ ^{1l}	231
γ	416.47	24011(5)	(KA)594	K ^A ₂₂ ^{1l}	593

Table 7.4. Assignments of the observed vibrational peaks from the photoelectron spectra of [Cy-H]⁻. Their binding energies (BE), energy shifts from the vibrational origins of deprotonated neutral radicals, **cKAN3H8a** and **tKAN3H8b**, are given. Theoretical frequencies are from Table 7.2.

Peaks	BE (eV)	Shift to C ⁰ (cm ⁻¹)	Shift to T ⁰ (cm ⁻¹)	Assignment	Theo. Freq. (cm ⁻¹)
C ⁰	3.0471 (5)	0		Neutral ground state (cKAN3H8a)	
T ⁰	3.0870 (5)		0	Neutral ground state (tKAN3H8b)	
A	3.0619 (7)	119		C ₃₀ ¹	104
B	3.0752 (5)	227		C ₃₀ ²	
C	3.1332 (5)		373	T ₂₁ ¹	376
D	3.1583 (6)		575	T ₁₈ ¹	583

Chapter 8 Observation of excited quadrupole-bound states in

$\text{NC}(\text{C}_6\text{H}_4)\text{O}^{-\dagger\dagger}$

This chapter⁹⁷ will discuss the first observation of an excited quadrupole-bound state (QBS) in an anion. High-resolution photoelectron imaging of cryogenically-cooled 4-cyanophenoxide anions (4CP^-) yields an electron detachment threshold of 24927 cm^{-1} . Photodetachment spectrum reveals a resonant transition 20 cm^{-1} below the detachment threshold, which is attributed to an excited QBS of 4CP^- because neutral 4CP has a large quadrupole moment with a negligible dipole moment. The QBS is confirmed by observation of seventeen above-threshold resonances due to autodetachment from vibrational levels of the QBS.

8.1 Introduction

A dipolar molecule can bind an electron in a diffuse orbital, which is dominated by the long-range charge-dipole attractive potential scaled as $1/r^2$.¹²³⁻¹²⁵ Such dipole-bound states (DBSs) play important roles in electron-molecule interactions and considered to be the “doorway” to the formation of valence-bound anions. When a molecule has vanishing dipole moment, but large quadrupole moments, it can bind an extra electron by the long-range charge-quadrupole attractive potential ($\sim 1/r^3$), forming the quadrupole-bound anion (QBA).¹⁴⁶ The QBA at ground state has been observed by Rydberg electron transfer. However, excited quadrupole-bound state (QBS) of anion, which is optically excited from valence-bound state of anion, has not been observed.

^{††} The content of this chapter is reproduced or adapted with permission from [G. Z. Zhu, Y. Liu, and L. S. Wang, Observation of excited quadrupole-bound states in cold anions. *Phys. Rev. Lett.* **119**, 023002 (2017)]. Copyright 2017 American Physical Society.

More detailed introduction was described in the Chapter 1. Here we report the first observation of an excited QBS in the 4-cyanophenoxide anion (4CP^-) cryogenically-cooled in an ion trap. The neutral 4CP radical (see inset of Fig. 8.1) has a very small dipole moment of 0.3 D, which is insufficient to form a DBS. Its large quadrupole moment (traceless quadrupole moment: $Q_{xx} = 5.4$, $Q_{yy} = 15.1$, $Q_{zz} = -20.5 \text{ D}\cdot\text{\AA}$) suggests that it may be a good candidate to search for excited QBS.

8.2 Experimental methods

The experiments were done using our third-generation ESI-PES apparatus. The detailed descriptions were provided in the Chapter 2.

8.3 Results and discussion

Figure 8.1 shows the non-resonant PE images and spectra of 4CP^- at three photon energies. The first intense peak, labeled as 0_0^0 , denotes the detachment transition from the vibrational ground state of 4CP^- to that of neutral 4CP, representing the electron affinity of 4CP or the electron detachment threshold of 4CP^- . The spectrum in Fig. 8.1a, with a photon energy slightly above the detachment threshold, gives the best resolved 0_0^0 peak with a width of 11 cm^{-1} mainly due to rotational broadening, yielding an accurate electron affinity for 4CP as $24927 \pm 5 \text{ cm}^{-1}$. At higher photon energies, numerous vibrational peaks, labeled as A–J, are resolved for the ground electronic state of 4CP. The strongest vibrational peak B corresponds to the most Franck-Condon-active mode. To better resolve peak B, we tuned the detachment laser to be just above the binding energy of peak B at 393.57 nm, resolving an additional peak C. The intensity of peak B is

significantly enhanced due to the threshold effect. The electron binding energies of all the observed vibrational peaks, their shifts from peak 0_0^0 , and their assignments are summarized in Table 8.1 in Supporting Section 8.5.

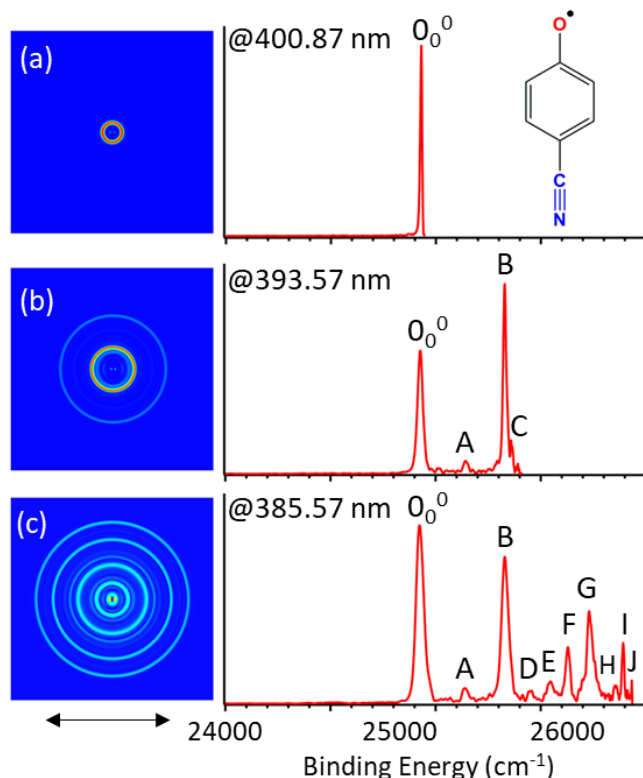


Figure 8.1. Non-resonant photoelectron images and spectra of 4CP^- at different laser wavelengths. (a) 400.87 nm, (b) 393.57 nm, and (c) 385.57 nm. The double arrow below the images indicates the direction of the laser polarization. The structure of neutral 4CP is shown in the inset of (a).

To search for possible QBSs, we measured the photodetachment spectrum of 4CP^- by monitoring the total electron yield while scanning the dye laser across the detachment threshold (Fig. 8.2). The arrow at 24927 cm^{-1} indicates the detachment threshold, consistent with the photoelectron spectra in Fig. 8.1. The three underneath-baseline arrows indicate the detachment wavelengths used in the non-resonant photoelectron images in Fig. 8.1.

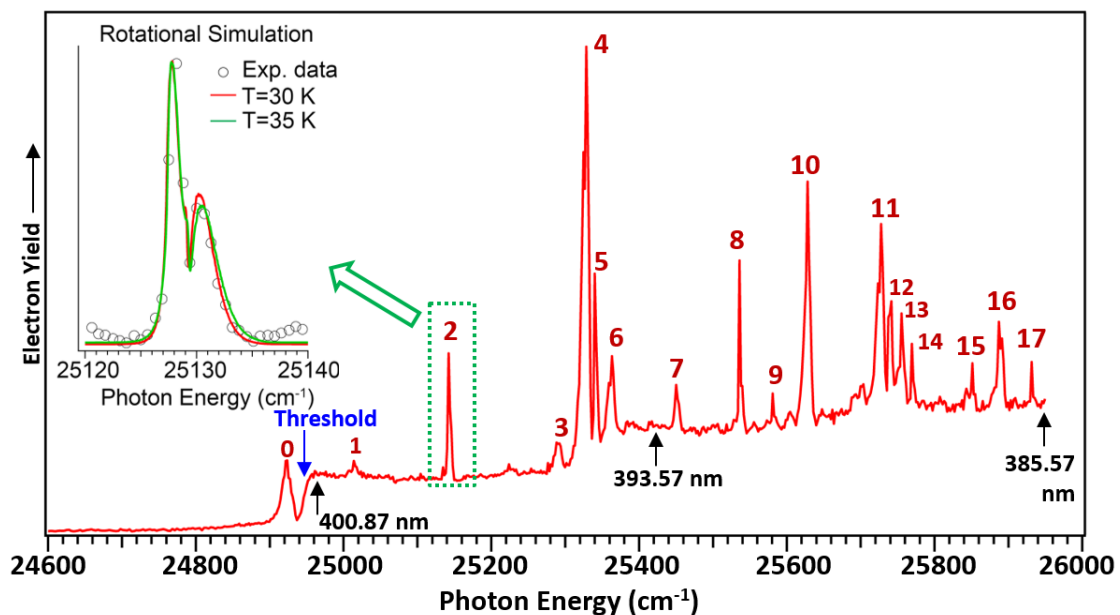


Figure 8.2. Photodetachment spectrum of 4CP^- . It was done by measuring the total electron yield as a function of photon energy across the detachment threshold. The blue arrow at 24927 cm^{-1} indicates the detachment threshold of 4CP^- . The three black arrows indicate the detachment photon energies used for the non-resonant photoelectron spectra in Fig. 8.1. The peaks 1–17 are due to autodetachment from QBS vibrational levels of 4CP^- ; while peak 0 below threshold represents the vibrational ground state of the QBS and is from resonant two-photon processes. The inset shows a high-resolution scan of peak 2, revealing the rotational profile, along with rotational simulations at two temperatures.

Below threshold, one broad peak, labeled as 0, is observed due to two-photon processes. Because 4CP^- cannot support DBSs, this below-threshold peak should be due to the vibrational ground state of the putative QBS, because no other peaks were observed below peak 0. This peak is 20 cm^{-1} below the detachment threshold, suggesting the weakly-bound nature of the electron in the QBS relative to the detachment continuum. The continuous signals above threshold represent non-resonant photodetachment signals. Seventeen above-threshold peaks are observed, due to autodetachment from excited vibrational levels of the QBS. The inset shows the simulation of the rotational profile for peak 2 at a high-resolution scan, yielding a rotational temperature of 30–35 K, consistent with previous estimates.^{95,96} See the Supporting Section 8.5 for details of the rotational

simulation. The top scale is relative to the vibrational ground state of the QBS. The corresponding photon energies, shifts from peak 0, and assignments of the QBS resonances in photodetachment spectrum are given in Table 8.2 in Supporting Section 8.5.

The local dipoles of the two polar centers ($-\text{CN}$ and $\text{C}-\text{O}$) in the neutral planar 4CP radical have opposite directions, resulting in a vanishing dipole moment of 0.3 D but a large quadrupole moment. Hence, the dominating potential that binds the electron in the excited state of 4CP^- should be between the quadrupole moment and the electron. This interaction is scaled as $1/r^3$, much weaker than the electron and dipole interaction in DBSs. The peak 0 observed in Fig. 8.2 gives rise to a small binding energy of 20 cm^{-1} for the QBS of 4CP^- . Thus, any vibrational excitation of the QBS would be above the detachment threshold and can lead to vibrationally-induced autodetachment via vibrational to electronic energy transfer or vibronic coupling. The electron in the excited QBS is expected to be in a highly diffuse orbital with little effect on the structure of the neutral core. This is confirmed by the similarity of the observed vibrational peaks in the photodetachment spectrum in Fig. 8.2 and those in the non-resonant photoelectron spectrum in Fig. 8.1c. A direct comparison is presented in Fig. 8.6 in Supporting Section 8.5, where the 385.57 nm photoelectron spectrum is overlaid onto the photodetachment spectrum in the same energy scale by lining up the peak 0_0^0 in the photoelectron spectrum and the peak 0 of the photodetachment spectrum. All the major vibrational peaks and their relative intensities agree with each other in the two spectra, except that the photodetachment spectrum has higher resolution. This resemblance provides strong evidence for the weakly bound nature of the excess electron in the QBS, which has little effect to the neutral core, just as that observed for DBSs.¹¹⁷⁻¹²⁰ Hence, the

photodetachment spectrum of the QBS can be used to yield more accurate vibrational information for the neutral radical.

By tuning the dye laser wavelength to the above-threshold peaks, we have obtained seventeen high-resolution resonantly-enhanced photoelectron images and spectra, as shown in Figs. 8.3 and 8.4. These resonant photoelectron spectra consist of contributions from two different detachment processes: i) non-resonant detachment represented by the baseline in Fig. 8.2 (such as the spectra in Fig. 8.1), and ii) the much stronger resonant autodetachment signal represented by the above-threshold peaks. The

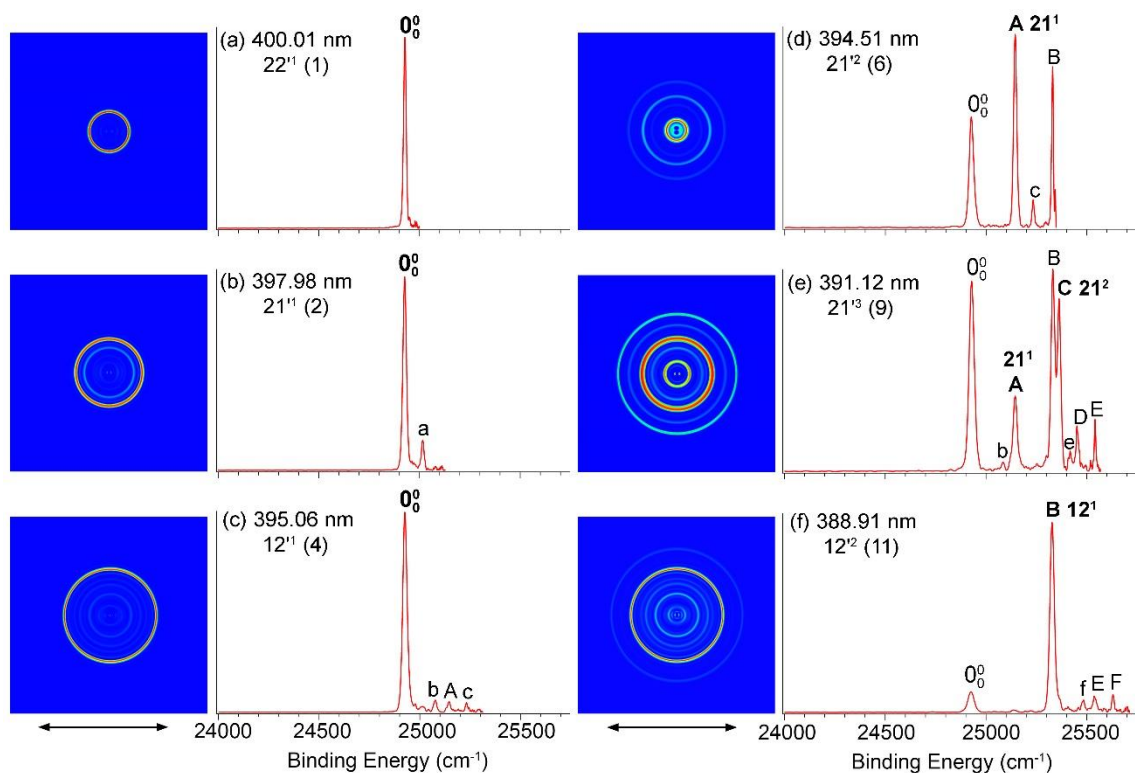


Figure 8.3. Resonant photoelectron images and spectra of 4CP^- at six different detachment wavelengths. They are corresponding to excitations to vibrational levels involving single vibrational modes of the QBS followed by autodetachment via vibronic coupling. The QBS vibrational levels and the peak number (in parentheses) used in Fig. 8.2 are given. The peaks labeled in bold face indicate the autodetachment-enhanced final neutral vibrational levels. The double arrows below the images represent the direction of the laser polarization.

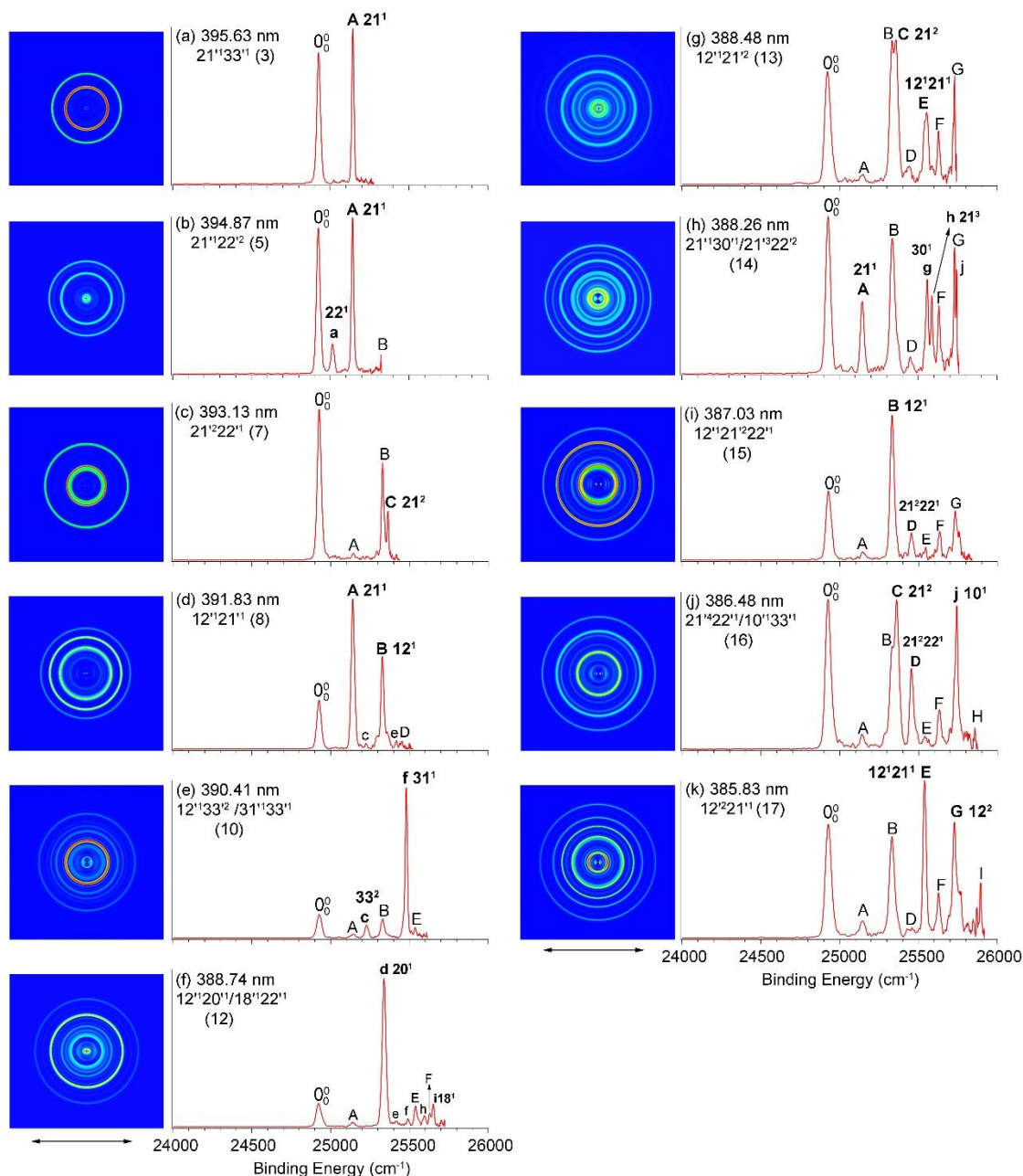


Figure 8.4. Resonant photoelectron images and spectra of 4CP^- at eleven different detachment wavelengths. They are involving autodetachment from combinational and overlapping vibrational levels of the quadrupole-bound state. The QBS vibrational levels and the peak number (in parentheses) used in Fig. 8.2. are given. The labels in bold face indicate the autodetachment-enhanced final neutral vibrational levels. The double arrows below the images indicate the direction of the laser polarization.

latter involves two steps, i.e., resonant excitation to a vibrational level of the QBS, followed by transfer of vibrational energies to the weakly-bound electron to induce

detachment. The vibrationally-induced autodetachment from DBSs generally obeys the $\Delta v = -1$ propensity rule under the harmonic-oscillator approximation^{189,190} and yields highly non-Franck-Condon PE spectra.¹¹⁷⁻¹²⁰ This propensity rule is expected to hold true for vibrational autodetachment from the QBS due to the even more weakly-bound nature of the QBS electron. The six spectra in Fig. 8.3 show autodetachment involving single vibrational modes of the QBS; while the eleven spectra in Fig. 8.4 represent excitations to combinational and overlapping vibrational levels of the QBS. The enhanced vibrational levels (in bold face), the detachment laser wavelengths, the assigned vibrational levels of the QBS, and the corresponding peak number (in parentheses) used in Fig. 8.2 are given in each spectrum. Ten new vibrational peaks, labeled as a–j, are observed in the resonant spectra and are also listed in Table 8.1 in Supporting Section 8.5.

To understand the vibrational peaks in Figs. 8.1 and 8.2, we calculated the vibrational frequencies of neutral 4CP at the B3LYP/6-311++G(d,p) level using the Gaussian 09 package.²⁵² The thirty-three normal modes are shown in Fig. 8.7 in Supporting Section 8.5. The calculated frequencies are unscaled and agree well with the observed frequencies for most vibrational modes. Because both 4CP^- and 4CP have C_{2v} symmetry, only modes with A_1 symmetry are allowed in principle. Peaks B and G form a vibrational progression for the most Franck-Condon-active mode ν_{12} (A_1), which is an in-plane N...O stretching mode (Fig. 8.7 in Section 8.5). The very weak peaks A and C correspond to a vibrational progression of the ν_{21} (B_1) mode, which is an out-of-plane bending mode (Fig. 8.7 in Section 8.5). The assignments of all the observed peaks are given in Table 8.1 (Section 8.5) by using the calculated vibrational frequencies and the resonant photoelectron spectra.

According to the $\Delta v = -1$ propensity rule for vibrationally-induced autodetachment, excitation to the n th vibrational level of a given mode ($v'_x{}^n$) of the QBS autodetaches to the $(n-1)$ th level of the same neutral mode ($v_x{}^{n-1}$) with one vibrational quantum transferred to the QBS electron. The corresponding $v_x{}^{n-1}$ vibrational peak will be enhanced significantly in comparison to that in the non-resonant photoelectron spectrum, giving rise to highly non-Franck-Condon resonant photoelectron spectra. Figures 8.3a-c show significant enhancement of peak 0_0^0 , indicating autodetachments from the fundamental vibrational level of different modes ($v'_x{}^1$) of the QBS. The photon energies used for the spectra in Figs. 8.3a-c correspond to excitations to vibrational levels 22^1 , 21^1 and 12^1 of the QBS, respectively. In Figs. 8.3d and 8.3f, peaks A and B, corresponding to vibrational level 21^1 and 12^1 of 4CP, respectively, are greatly enhanced in comparison to the intensity of peak 0_0^0 in the non-resonant photoelectron spectra. These are due to excitations to the QBS vibrational levels of 21^2 and 12^2 , followed by $\Delta v = -1$ autodetachment. Both peaks A (21^1) and C (21^2) in Fig. 8.3e are enhanced. The photon energy used for the spectrum in Fig. 8.3e corresponds to excitation to the 21^{13} vibrational level of the QBS. Hence, the enhancement of peak A is a result of transferring two vibrational quanta to the QBS electron (i.e. $\Delta v = -2$), which suggests a large anharmonicity in the v'_{21} (B_1) mode.¹⁸⁹ In addition, numerous weak peaks a-c, e, and f are also observed in Fig. 8.3. As given in Table 8.1 (Section 8.5), the shifts of peak a and b relative to peak 0_0^0 are 89 cm^{-1} and 155 cm^{-1} , respectively, which correspond to the two lowest frequency modes v_{22} (B_1 , 93 cm^{-1}) and v_{33} (B_2 , 157 cm^{-1}) of neutral 4CP (Table 8.2 in Section 8.5). Their appearances in the resonant photoelectron spectra are most likely

due to intramolecular electron rescattering, as observed previously.¹²¹ The assignments of peaks c (33^2), e (12^122^1), and f (31^1) are based on the calculated frequencies.

The remaining eleven resonant photoelectron spectra in Fig. 8.4 all involve excitations to combinational or overlapping vibrational levels of the QBS with more complicated autodetachment processes. For excitation to a combinational level, $v'_x{}^m v'_y{}^n \dots$, of the QBS, the final neutral level can be either $v_x{}^{m-1} v_y{}^n \dots$ or $v_x{}^m v_y{}^{n-1} \dots$, based on the $\Delta v = -1$ propensity rule under harmonic approximation^{189,190} and mode-selectivity.¹¹⁷ For example, the wavelength used in Fig. 8.4a probes the combinational level of $21'^1 33'^1$ of the QBS. The great enhancement of peak A (21^1) indicates the mode-selectivity during autodetachment, i.e., the in-plane scissoring mode v_{33}' (B_2) couples more strongly with the QBS electron than the v_{21}' (B_1) mode does. The enhancement of peak A (21^1) and B (12^1) in Fig. 8.4d suggest excitation to the combinational level of $12'^1 21'^1$ of the QBS. The higher intensity of peak A is due to the stronger coupling of the QBS electron with the in-plane stretching mode v_{12}' (A_1).

Figures 8.4b, c, g, and k all display cases involving transitions to combinational vibrational levels of the QBS, in which one vibrational mode is combined with an overtone of another mode. The spectra in Figs. 8.4c, g, and k all show autodetachment following the $\Delta v = -1$ rule. The enhancement of peak C (21^2) in Fig. 8.4c is due to autodetachment from combinational level of $21'^2 22'^1$ of the QBS with one quantum of mode v_{22}' coupled to the outgoing electron; while the enhancement of peak E ($12^1 21^1$) and G (12^2) in Fig. 8.4k are from autodetachment from the $12'^2 21'^1$ QBS level, involving the coupling of the QBS electron with one quantum of mode v_{12}' (A_1) and v_{21}' (B_1), respectively. The breakdown of the $\Delta v = -1$ propensity rule is observed in Fig. 8.4b.,

where peaks a (22^1) and A (21^1) are enhanced due to autodetachment from the $21'^122'^2$ of QBS level. To reach the 21^1 final state, two quanta of mode ν_{22}' (B_1) must be coupled to the outgoing electron during the autodetachment. The spectrum in Fig. 8.4i involves autodetachment from a combinational level of three vibrational modes of the QBS, $12'^121'^222'^1$. The enhancement of peak B (12^1) indicates breakdown of the $\Delta\nu = -1$ rule, while the enhancement of peak D (21^222^1) follows the $\Delta\nu = -1$ rule.

Even more complicated cases are those involving resonant excitations to overlapping vibrational levels of the QBS, as shown in Figs. 8.4e, f, h and j. In Fig. 8.4e, a new peak f (31^1) is observed, suggesting excitation to the $31'^133'^1$ QBS vibrational level with strong vibronic coupling involving the ν_{33}' (B_2) mode in the autodetachment. A weaker peak c (33^2), which is also enhanced, is due to autodetachment from the combinational level of $12'^133'^2$. Fig. 8.4f also shows two new enhanced peaks d (20^1) and i (18^1), implying two overlapping combinational levels, $12'^120'^1$ and $18'^122'^1$, respectively, with only one mode in each case strongly coupled with the outgoing electron. In Fig. 8.4h, the enhancement of peak A (21^1) and g (30^1) is due to autodetachment from the combinational level of $21'^130'^1$; while the new peak h (21^3) is due to autodetachment from the $21'^322'^2$ level in violation of the $\Delta\nu = -1$ rule. The enhancements of peak G and j are attributed to the threshold effect. Finally, the enhanced peak j (10^1) in Fig. 8.4j suggests excitation to the $10'^133'^1$ combinational level with the ν_{33}' (B_2) mode coupled to the QBS electron. The other two enhanced peaks C (21^2) and D (21^222^1) are due to autodetachment from the $21'^422'^1$ combinational level, with violation of the $\Delta\nu = -1$ rule in both autodetachment channels. It seems that there is a higher probability for the

breakdown of the $\Delta v = -1$ rule involving the ν_{21}' (B_1) and ν_{22}' (B_2) modes, suggesting strong anharmonicity in these modes.

Figure 8.5 shows schematically the seventeen vibrational levels of the QBS and their autodetachment channels to the neutral final states of 4CP. All the assignments for the observed vibrational resonances of the QBS are summarized in Table 8.2 in Section 8.5. The experimental vibrational frequencies for 4CP are compared with the calculated frequencies in Table 8.3 (Section 8.5).

8.4 Conclusions

In summary, we report the first observation of an excited quadrupole-bound state for cryogenically-cooled cyanophenoxide anions, whose neutral core possesses a vanishing dipole moment but a large quadrupole moment. The quadrupole-bound state is found to have a binding energy of 20 cm^{-1} relative to the detachment threshold. Seventeen excited vibrational levels of the QBS are observed as resonances in the photodetachment spectrum. The weakly-bound nature of the electron in the QBS is confirmed by the observation of the similarity of the non-resonant photoelectron spectra and the photodetachment spectrum and the $\Delta v = -1$ vibrational autodetachment propensity rule in the resonant photoelectron spectra.

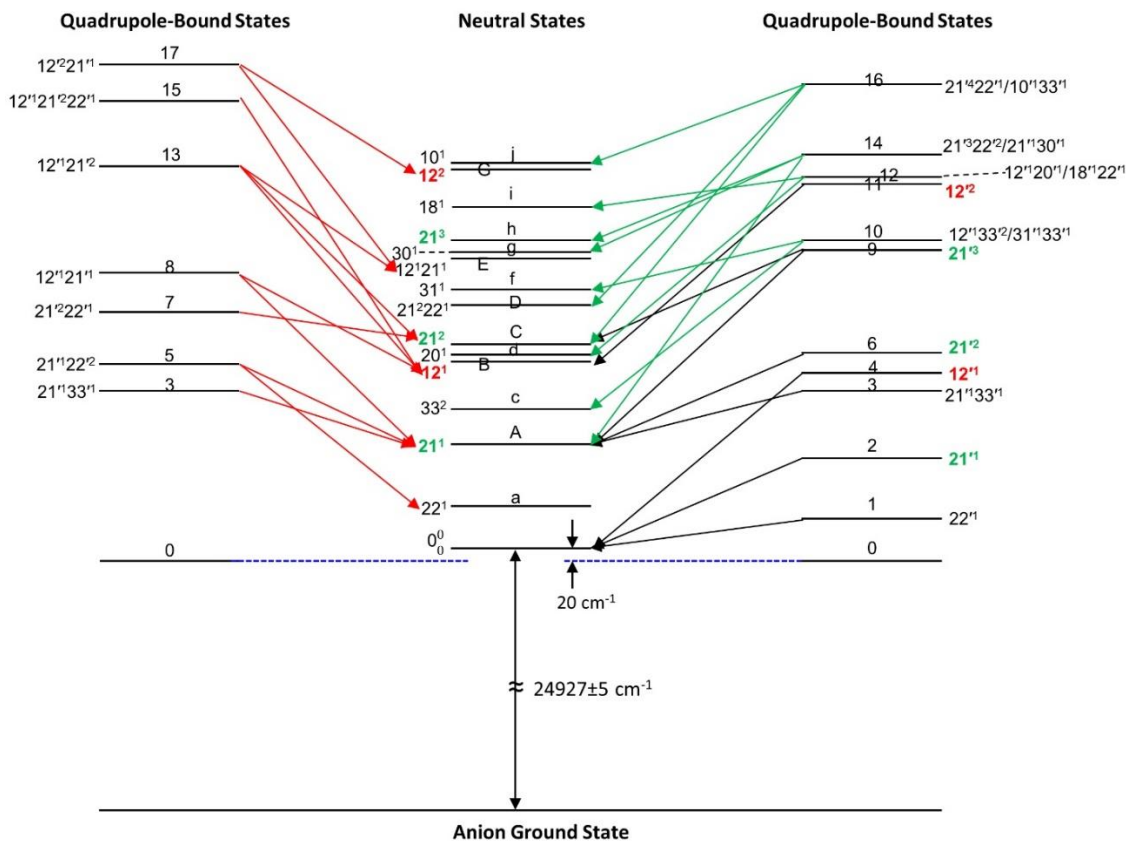


Figure 8.5. A schematic energy level diagram for autodetachment from the QBS vibrational levels of 4CP^- to the neutral final states of 4CP . The combinational vibrational levels of the QBS are given on the left with the red arrows denoting the autodetachment. Single-mode and overlapping vibrational levels of the QBS are given on the right with the black arrows indicating autodetachment from single-mode levels and the green arrows for autodetachment from the overlapping levels. The vibrational progressions for mode ν_{12} and ν_{21} are highlighted both in the neutral levels and the QBS levels (red and green, respectively). The detachment threshold (24927 cm^{-1}) and the QBS binding energy (20 cm^{-1}) of 4CP^- are also given. The QBS peak labels (numbers) and the peak labels from the photoelectron spectra (letters) are given. The assignments of the final neutral states and the QBS levels are given in Tables 8.1 and 8.2 in Supporting Section 8.5, respectively.

8.5 Supporting information

The high-resolution spectrum of peak 2, shown in inset of Fig. 8.2, resolves its rotational profile, which is simulated using the Pgoopher program⁴²² with the calculated rotational constants for 4CP^- ($a = 5637.36 \text{ MHz}$, $b = 1006.73 \text{ MHz}$, $c = 854.19 \text{ MHz}$) and 4CP ($a = 5470.65 \text{ MHz}$, $b = 1030.83 \text{ MHz}$, $c = 867.39 \text{ MHz}$). The simulation yields J_{max}

= 70 and $T_{\text{rot}} = 30\text{-}35$ K with a line width of 0.15 cm^{-1} . The obtained rotational temperature of $30\text{-}35$ K for the cryogenically cooled anion in the Paul trap is consistent with the values estimated previously for the uracil anion⁹⁵ and the acetate anion.⁹⁶

Table 8.1. Assignments of the observed vibrational peaks from the photoelectron spectra of 4CP^- . The binding energies (BE) and energy shifts from the vibrational origins of 4CP are given. Peaks A-J correspond to those observed in the non-resonant photoelectron spectra in Fig. 8.1, while peaks a-j are observed from the resonant photoelectron spectra in Figs. 8.3 and 8.4. The binding energies of peaks 0_0^0 , and A-J are measured more accurately from the resonant photoelectron spectra. Numbers in parentheses indicate the experimental uncertainties in the last digit.

Peak	BE (cm^{-1})	Shift (cm^{-1})	Assignment
0_0^0	24927(5)	0	Neutral Ground State
A	25145(5)	218	21^1
B	25331(5)	404	12^1
C	25362(5)	435	21^2
D	25451(5)	525	$21^2 22^1$
E	25541(5)	614	$12^1 21^1$
F	25630(5)	703	$11^1/12^1 33^2/31^1 33^1$
G	25731(5)	804	12^2
H	25853(5)	926	$12^1 21^2 22^1$
I	25891(5)	964	$10^1 33^1/21^4 22^1$
J	25933(5)	1006	$12^2 21^1$
a	25016(5)	89	22^1
b	25082(5)	155	33^1
c	25231(5)	304	33^2
d	25339(5)	412	20^1
e	25418(5)	491	$12^1 22^1$
f	25480(5)	553	31^1
g	25557(5)	630	30^1
h	25586(5)	659	21^3
i	25652(5)	725	18^1
j	25742(5)	815	10^1

Table 8.2. Assignments of observed QBS resonances in photodetachment spectrum of 4CP^- . Numbers in parentheses indicate the experimental uncertainties in the last digit.

Peak	Photon energy (cm^{-1})	Shift (cm^{-1})	Assignment
0	24907(5)	0	Ground state
1	24999(5)	92	$22'^1$
2	25127(5)	220	$21'^1$
3	25276(5)	369	$21'^133'^1$
4	25313(5)	406	$12'^1$
5	25325(5)	418	$21'^122'^2$
6	25348(5)	441	$21'^2$
7	25437(5)	530	$21'^222'^1$
8	25521(5)	614	$12'^121'^1$
9	25568(5)	661	$21'^3$
10	25614(5)	707	$12'^133'^2/31'^133'^1$
11	25713(5)	806	$12'^2$
12	25724(5)	817	$12'^120'^1/18'^122'^1$
13	25741(5)	834	$12'^121'^2$
14	25756(5)	849	$21'^322'^2/21'^130'^1$
15	25838(5)	931	$12'^121'^222'^1$
16	25875(5)	968	$21'^422'^1/10'^133'^1$
17	25918(5)	1011	$12'^221'^1$

Table 8.3. Experimental vibrational frequencies of 4CP, in comparison to theoretical harmonic frequencies. The calculations were done at the B3LYP/6-311++G(d,p) level of theory. The peaks from which the experimental vibrational frequencies are obtained are also given. The peaks 1–4, 10, 12, 14, 16, refer to the labels used in Fig. 8.2 and Table 8.2. The peaks labeled with letters refer to those used in the photoelectron spectra (Figs. 8.1, 8.3, and 8.4) and in Table 8.1.

Mode	Symmetry	Theoretical (cm^{-1})	Experimental (cm^{-1})	Peak
ν_1	A_1	3205		
ν_2		3187		
ν_3		2291		
ν_4		1590		
ν_5		1492		
ν_6		1429		
ν_7		1222		
ν_8		1156		
ν_9		988		
ν_{10}			803	819/815
ν_{11}		711	703	F
ν_{12}		413	406/404	4/B
ν_{13}	A_2	986		
ν_{14}		795		
ν_{15}		374		
ν_{16}	B_1	980		
ν_{17}		863		
ν_{18}		733	725/725	12/i
ν_{19}		553		
ν_{20}		435	412/412	12/d
ν_{21}		226	220/218	2/A
ν_{22}		93	92/89	1/a
ν_{23}		B_2	3203	
ν_{24}	3187			
ν_{25}	1491			
ν_{26}	1435			
ν_{27}	1293			
ν_{28}	1277			
ν_{29}	1114			
ν_{30}	638		629/630	14/g
ν_{31}	556		558/553	10/f
ν_{32}	441			
ν_{33}	157		149/155	3/b

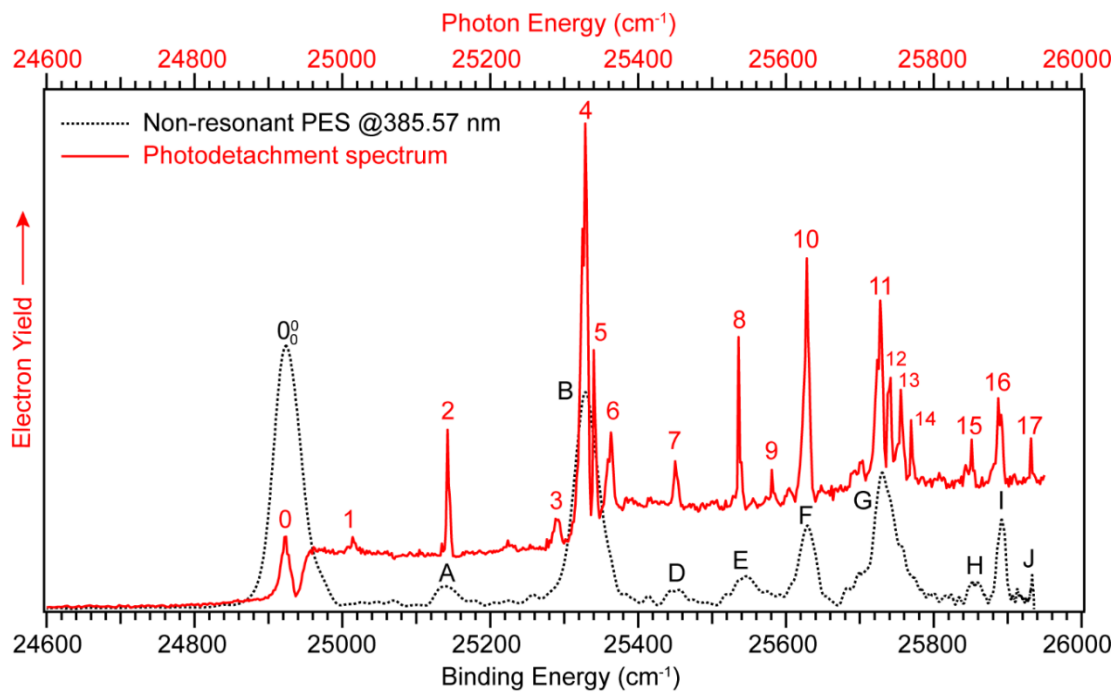


Figure 8.6. Comparison of the non-resonant photoelectron spectrum at 385.57 nm with the photodetachment spectrum. The photodetachment spectrum is blue-shifted by 20 cm^{-1} to line up the peak 0_0^0 and peak 0 (the ground vibrational level of the neutral and the QBS). All the peaks in the non-resonant photoelectron spectrum can be found in the corresponding photodetachment spectrum, suggesting the weakly bound nature of the excited QBS electron, which has little effect on neutral 4CP core.

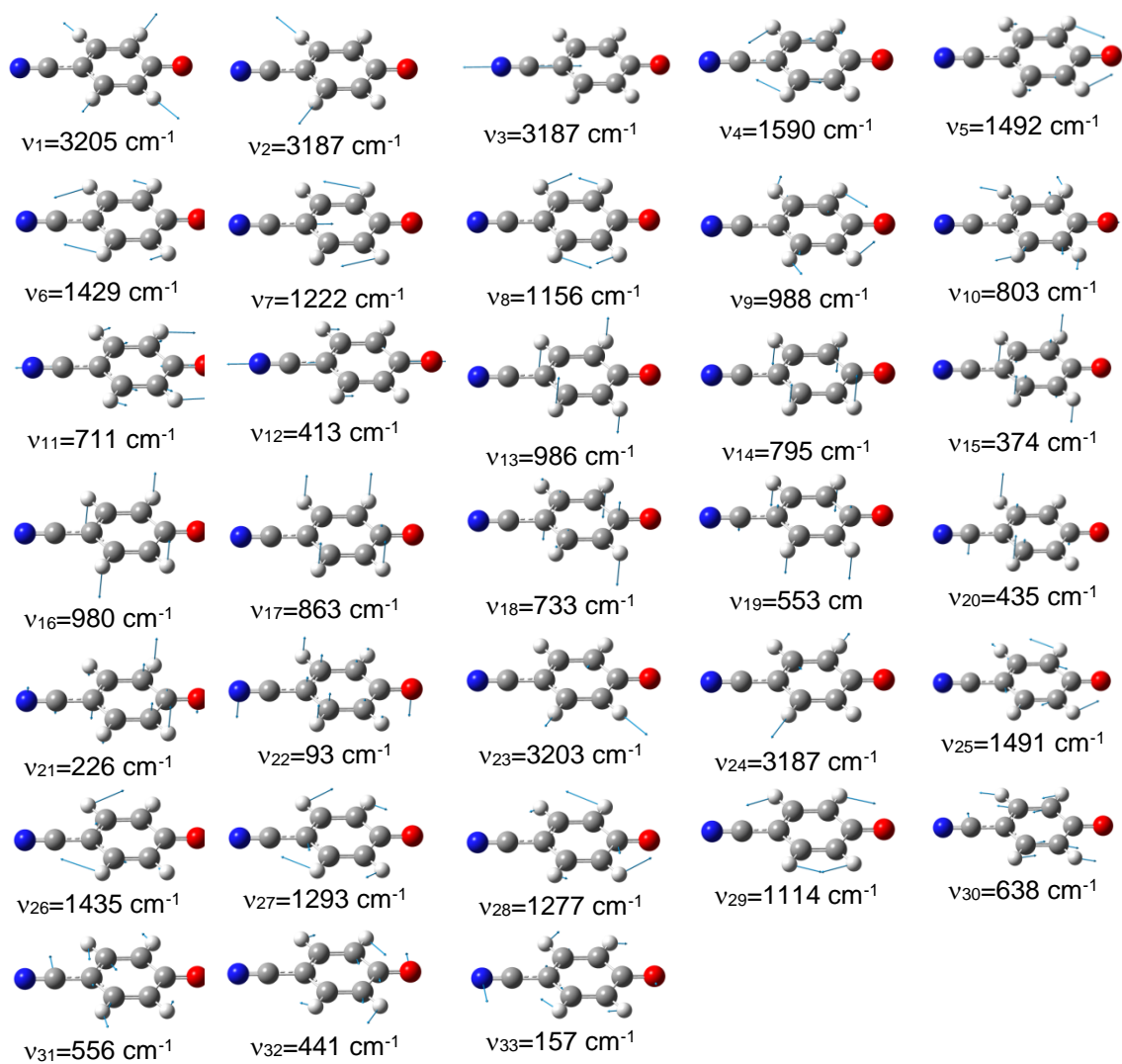


Figure 8.7. The calculated vibrational normal modes for neutral 4CP and their frequencies. The arrows indicate the displacement vectors.

Bibliography

1. R. Wildt, *Astrophys. J.* **89**, 295 (1939).
2. V. H. Paschoal, L. F. O. Faria, and M. C. C. Ribeiro, *Chem. Rev.* **117**, 7053 (2017).
3. B. L. Schottel, H. T. Chifotides, and K. R. Dunbar, *Chem. Soc. Rev.* **37**, 68 (2008).
4. A. Kumar, and M. D. Sevilla, *Chem. Rev.* **110**, 7002 (2010).
5. S. Schobesberger, et al. *Atoms. Chem. Phys.* **15**, 55 (2015).
6. R. C. Fortenberry, *J. Phys. Chem. A* **119**, 9941 (2015).
7. T. J. Millar, C. Walsh, and T. A. Field, *Chem. Rev.* **117**, 1765 (2017).
8. E. U. Condon, *Ameri. J. Phys.* **15**, 365 (1947).
9. J. C. Rienstra-Kiracofe, G. S. Tschumper, H. F. Schaefer III, S. Nandi, and G. B. Ellison, *Chem. Rev.* **102**, 231 (2002).
10. T. Waters, X. B. Wang, and L. S. Wang, *Coord. Chem. Rev.* **251**, 474-491 (2007)
11. W. L. Li, X. Chen, T. Jian, T. T. Chen, J. Li, and L. S. Wang, *Nat. Rev. Chem.* **1**, 0071 (2017).
12. M. L. Weichman, and D. M. Neumark, *Annu. Rev. Phys. Chem.* **69**, 101 (2018).
13. X. B. Wang, X. Yang, J. B. Nicholas, and L. S. Wang, *Science* **294**, 1322-1325 (2001).
14. R. E. Continetti, and H. Guo, *Chem. Soc. Rev.* **46**, 7650 (2017).
15. L. S. Wang, *J. Chem. Phys.* **143**, 040901 (2015).
16. H. Hertz, *Annalen der Physik* **267**, 983 (1887).
17. A. Einstein, *Annalen der Physik.* **17**, 132–148 (1905).
18. C. Nordling, E. Sokolowski, and K. Siegbahn, *Phys. Rev.* **105**, 1676 (1957).
19. F. I. Vilesov, B. L. Kurbatov, and A. N. Terenin, *Dokl. Akad. Nauk SSSR* **138**, 1329-1332 (1961).
20. D. W. Turner, and M. I. Al Jobory, *J. Chem. Phys.* **37**, 3007 (1962).
21. B. Brehm, M. A. Gusinow, and J. I. Hall, *Phys. Rev. Lett.* **19**, 737 (1967).

BIBLIOGRAPHY

22. M. W. Siegel, R. J. Celotta, J. L. Hall, J. Levine, and R. A. Bennett, *Phys. Rev. A* **6**, 607 (1972).
23. R. J. Celotta, R. A. Bennett, J. L. Hall, M. W. Siegel, and J. Levine, *Phys. Rev. A* **6**, 631 (1972)
24. A. Kasdan and W. C. Lineberger, *Phys. Rev. A* **10**, 1658 (1974).
25. J. M. Oakes, and G. B. Ellison, *J. Am. Chem. Soc.* **105**, 2969 (1983).
26. J. V. Coe, J. T. Snodgrass, C. B. Freidhoff, K. M. McHugh, and K. H. Bowen, *J. Chem. Phys.* **83**, 3169-3170 (1985).
27. K. M. Ervin, J. Ho, and W. C. Lineberger, *J. Chem. Phys.* **91**, 5974 (1989).
28. M. A. Johnson, M. L. Alexander, and W. C. Lineberger, *Chem. Phys. Lett.* **112**, 285 (1984).
29. L. S. Zheng, P. J. Brucat, C. L. Pettiette, S. Yang, and R.E. Smalley, *J. Chem. Phys.* **83**, 4273(1985).
30. L. A. Posey, M. J. Deluca, and M. A. Johnson, *Chem. Phys. Lett.* **131**, 170 (1986).
31. O. Cheshnovsky, P.J. Brucat, S. Yang, C. L. Pettiette, M. J. Craycraft, and R. E. Smalley, *Proc. Int. Symp. on the Physics and Chemistry of Small Clusters*, eds. P. Jena, S. Khanna, and B. Rao, NATO ASI Series (Plenum Press, New York, 1987).
32. O. Cheshnovsky, S. H. Yang, C. L. Pettiette, M. J. Craycraft, Y. Liu, and R. E. Smalley, *Chem. Phys. Lett.* **138**, 119 (1987).
33. G. Ganteför, K. H. Meiwes-Broer, and H. O. Lutz, *Phys. Rev. A* **37**, 2716 (1988).
34. G. Ganteför, M. Gausa, K. H. Meiwes-Broer, and H. O. Lutz, *Z. Phys. D* **9**, 253 (1988).
35. O. Cheshnovsky, S. H. Yang, C. L. Pettiette, M. J. Craycraft, and R. E. Smalley, *Rev. Sci. Instrum.* **58**, 2131 (1987).
36. L. S. Wang, H. S. Cheng, and J. Fan, *J. Chem. Phys.* **102**, 9480-9493 (1995).
37. L. F. Cui, and L. S. Wang, *Int. Rev. Phys. Chem.* **27**, 139-166 (2008).
38. L. S. Wang, H. Wu, S. R. Desai, and L. Lou, *Phys. Rev. B* **53**, 8028-8031 (1996).
39. H. Wu and L. S. Wang, *J. Chem. Phys.* **107**, 8221-8228 (1997).

BIBLIOGRAPHY

40. L. S. Wang, X. B. Wang, H. Wu, and H. C. Cheng, *J. Am. Chem. Soc.* **120**, 6556-6562 (1998).
41. L. S. Wang and X. Li, *J. Chem. Phys.* **112**, 3602-3608 (2000).
42. L. S. Wang, *Int. Rev. Phys. Chem.* **35**, 69-142 (2016).
43. J. Yang, X. B. Wang, X. P. Xing, and L. S. Wang, *J. Chem. Phys.* **128**, 201102 (2008).
44. A. Weaver, R. B. Metz, S. E. Bradforth, and D. M. Neumark, *J. Phys. Chem.* **92**, 5558 (1988).
45. H. Handschuh, G. Gantefor, and W. Eberhardt, *Rev. Sci. Instrum.* **66**, 3838 (1995)
46. D. W. Chandler, and P. L. Houston, *J. Chem. Phys.* **87**, 1445 (1987).
47. A. T. J. B. Eppink, and D. H. Parker, *Rev. Sci. Instrum.* **68**, 3477 (1997).
48. B. Baguenard, J. C. Pinaré, C. Bordas, and M. Broyer, *Phys. Rev. A* **63**, 023204 (2001).
49. E. Surber, and A. Sanov, *J. Chem. Phys.* **116**, 5921 (2002).
50. E. Surber, and A. Sanov, *Phys. Rev. Lett.* **90**, 093001 (2001).
51. Z. Luo, X. Chen, J. Li, and C. Ning, *Phys. Rev. A* **93**, 020501 (2016).
52. D. M. Neumark, *J. Phys. Chem. A* **112**, 13287–13301 (2008).
53. K. Müller-Dethlefs, M. Sander, and E. W. Schlag, *Chem. Phys. Lett.* **112**, 291 (1984).
54. K. Müller-Dethlefs, and E. W. Schlag, *Annu. Rev. Phys. Chem.* **42**, 109 (1991).
55. T. Kitsopoulos, I. Waller, J. Loeser, and D. Neumark, *Chem. Phys. Lett.* **159**, 4 (1989).
56. T. Lenzer, I. Yourshaw, M. R. Furlanetto, G. Reiser, and D. M. Neumark, *J. Chem. Phys.* **110**, 9578 (1999).
57. E. P. Wigner, *Phys. Rev.* **71**, 1002 (1948).
58. G. R. Burton, C. Xu, C. C. Arnold, and D. M. Neumark, *J. Chem. Phys.* **104**, 2757 (1996).
59. C. C. Arnold, D. M. Neumark, D. M. Cyr, and M. A. Johnson, *J. Phys. Chem.* **99**, 1633 (1995).
60. Iker León, Zheng Yang, Hong-Tao Liu, and L. S. Wang, *Rev. Sci. Instrum.* **85**, 083106 (2014).

BIBLIOGRAPHY

61. X. B. Wang, H. K. Woo, B. Kiran, and L. S. Wang, *Angew. Chem., Int. Ed.* **44**, 4968 (2005).
62. X. B. Wang, and L. S. Wang, *Rev. Sci. Instrum.* **79**, 073108 (2008).
63. X. B. Wang, H. K. Woo, and L. S. Wang, *J. Chem. Phys.* **123**, 051106 (2005).
64. C. Hock, J. B. Kim, M. L. Weichman, T. I. Yacovitch, and D. M. Neumark, *J. Chem. Phys.* **137**, 244201 (2012).
65. M. L. Weichman, J. A. DeVine, D. S. Levine, J. B. Kim, and D. M. Neumark, *Proc. Natl. Acad. Sci. U.S.A.* **113**, 1698 (2016).
66. C. Bartels, C. Hock, R. Kuhnen, and B. von Issendorff, *J. Phys. Chem. A* **118**, 8270 (2014).
67. H.-F. Li, Y.-X. Zhao, Z. Yuan, Q.-Y. Liu, Z.-Y. Li, X.-N. Li, C.-G. Ning, and S.-G. He, *J. Phys. Chem. Lett.* **8**, 605 (2017).
68. S. J. Kregel, G. K. Thurston, J. Zhou, and E. Garand, *J. Chem. Phys.* **147**, 094201 (2017).
69. S. J. Kregel, G. K. Thurston, and E. Garand, *J. Chem. Phys.* **148**, 234306 (2018).
70. J. B. Fenn, M. Mann, C. K. Meng, S. F. Wong, and C. M. Whitehouse, *Mass Spectrom. Rev.* **9**, 37 (1990).
71. M. Dole, L. L. Mack, and R. L. Hines, *J. Chem. Phys.* **49**, 2240 (1968).
72. M. Yamashita, J. B. Fenn, *J. Phys. Chem.* **88**, 4451 (1984).
73. J. B. Fenn, *Angew. Chem. Int. Ed.* **42**, 3871 (2003).
74. X. B. Wang, C. F. Ding, and L. S. Wang, *Phys. Rev. Lett.* **81**, 3351 (1998).
75. L. S. Wang, C. F. Ding, X. B. Wang, and J. B. Nicholas, *Phys. Rev. Lett.* **81**, 2667 (1998).
76. L. S. Wang, C. F. Ding, X. B. Wang, and S. E. Barlow, *Rev. Sci. Instrum.* **70**, 1957 (1999).
77. X. B. Wang, and L. S. Wang, *Nature* **400**, 245-248 (1999).
78. X. B. Wang, X. Yang, and L. S. Wang, *Int. Rev. Phys. Chem.* **21**, 473 (2002).
79. A. Henley, and H. Fielding, *Int. Rev. Phys. Chem.* **38**, 1 (2019).
80. T. R. Rizzo, J. A. Stearns, and O. V. Boyarkin, *Int. Rev. Phys. Chem.* **28**, 481 (2009).
81. A. B. Wolk, C. M. Leavitt, E. Garand, and M. A. Johnson, *Acc. Chem. Res.* **47**, 202 (2014).
82. E. Garand, *J. Phys. Chem. A* **122**, 6479 (2018).

BIBLIOGRAPHY

83. R. E. Smalley, L. Wharton, and D. H. Levy, *Acc. Chem. Res.* **10**, 139 (1977).
84. S. Goyal, D. L. Schutt, and G. Scoles, *Phys. Rev. Lett.* **69**, 933 (1992).
85. M. Y. Choi, G. E. Douberly, T. M. Falconer, W. K. Lewis, C. M. Lindsay, J. M. Merritt, P. L. Stiles, and R. E. Miller, *Int. Rev. Phys. Chem.* **25**, 15 (2006).
86. W. H. Robertson, J. A. Kelly, and M. A. Johnson, *Rev. Sci. Instrum.* **71**, 4431 (2000).
87. W. H. Robertson, and M. A. Johnson, *Annu. Rev. Phys. Chem.* **54**, 173 (2003).
88. D. Gerlich, *Adv. Chem. Phys.* **82**, 1 (1992).
89. D. Gerlich, and S. Horning, *Chem. Rev.* **92**, 1509 (1992).
90. D. Gerlich, *Phys. Scr.* **T59**, 256 (1995).
91. R. Wester, *J. Phys. B: At. Mol. Opt. Phys.* **42** 154001 (2009).
92. E. K. Campbell, M. Holz, D. Gerlich, and J. P. Maier, *Nature* **523**, 322 (2015).
93. G. L. Hou, X. B. Wang, and M. Valiev, *J. Am. Chem. Soc.* **139**, 11321 (2017).
94. G. L. Hou, N. Govind, S. S. Xantheas, and X. B. Wang, *J. Phys. Chem. A* **122**, 1209 (2018).
95. H. T. Liu, C. G. Ning, D. L. Huang, and L. S. Wang, *Angew. Chem. Int. Ed.* **53**, 2464 (2014).
96. D. L. Huang, G. Z. Zhu, and L. S. Wang, *J. Chem. Phys.* **142**, 091103 (2015).
97. G. Z. Zhu, Y. Liu, and L. S. Wang, *Phys. Rev. Lett.* **119**, 023002 (2017).
98. C. M. Choi, D. H. Choi, N. J. Kim, and J. Heo, *Int. J. Mass Spectrom.* **314**, 18 (2012).
99. H. Kang, G. Féraud, C. Dedonder-Lardeux, and C. Jouvet, *J. Phys. Chem. Lett.* **5**, 2760 (2014).
100. B. M. Marsh, J. M. Voss, and E. Garand, *J. Chem. Phys.* **143**, 204201 (2015).
101. S.-i. Ishiuchi, H. Wako, D. Kato, and M. Fujii, *J. Mol. Spectrosc.* **332**, 45 (2017).
102. D. W. Chandler, P. L. Houston, and D. H. Parker, *J. Chem. Phys.* **147**, 013601 (2017).
103. J. Solomon, *J. Chem. Phys.* **47**, 889–895 (1967).
104. J. J. Czyzewski, T. E. Madey, and J. T. Yates, *Phys. Rev. Lett.* **32**, 777 (1974).
105. M. H. M. Janssen, D. H. Parker, G. O. Sitz, S. Stolte, and D. W. Chandler, *J. Phys. Chem.* **95**, 8007 (1991).

BIBLIOGRAPHY

106. A. J. R. Heck, D. W. Neyer, R. N. Zare, and D. W. Chandler, *J. Phys. Chem.* **99**, 17700 (1995).
107. T. N. Kitsopoulos, M. A. Buntine, D. P. Baldwin, R. N. Zare, and D. W. Chandler, *Science* **260**, 1605 (1993).
108. H. A. Cruse and T. P. Softley, *J. Chem. Phys.* **122**, 124303 (2005).
109. B. W. Toulson, K. M. Kapnas, D. A. Fishman, and C. Murray, *Phys. Chem. Chem. Phys.* **19**, 14276 (2017).
110. S. J. Greaves, R. A. Rose, and A. J. Orr-Ewing, *Phys. Chem. Chem. Phys.* **12**, 9129 (2010).
111. R. Wester, *Phys. Chem. Chem. Phys.* **16**, 396 (2014).
112. H. Helm, N. Bjerre, M. J. Dyer, D. L. Huestis, and M. Saeed, *Phys. Rev. Lett.* **70**, 3221 (1993).
113. R. Mabbs, E. R. Grumbling, K. Pichugin, and A. Sanov, *Chem. Soc. Rev.* **38**, 2169 (2009).
114. X. P. Xing, X. B. Wang, and L. S. Wang, *Phys. Rev. Lett.* **101**, 083003 (2008).
115. C. G. Ning, P. D. Dau, and L. S. Wang, *Phys. Rev. Lett.* **105**, 263001 (2010).
116. D. L. Huang, P. D. Dau, H. T. Liu, and L. S. Wang, *J. Chem. Phys.* **140**, 224315 (2014).
117. H. T. Liu, C. G. Ning, D. L. Huang, P. D. Dau, and L. S. Wang, *Angew. Chem. Int. Ed.* **52**, 8976 (2013).
118. D. L. Huang, H. T. Liu, C. G. Ning, G. Z. Zhu, and L. S. Wang, *Chem. Sci.* **6**, 3129 (2015).
119. D. L. Huang, H. T. Liu, C. G. Ning, and L. S. Wang, *J. Chem. Phys.* **142**, 124309 (2015).
120. D. L. Huang, H. T. Liu, C. G. Ning, and L. S. Wang, *J. Phys. Chem. Lett.* **6**, 2153 (2015).
121. D. L. Huang, H. T. Liu, C. G. Ning, P. D. Dau, and L. S. Wang, *Chem. Phys.* **482**, 374 (2017).
122. G. Z. Zhu, C. H. Qian, and L. S. Wang, *J. Chem. Phys.* **149**, 164301 (2018).
123. J. Simons, *J. Phys. Chem. A* **112**, 6401 (2008).
124. R. N. Compton, and N. I. Hammer, *Advances in Gas-Phase Ion Chemistry*, edited by N. Adams and I. Babcock (Elsevier Science, New York) **4**, 257 (2001).

BIBLIOGRAPHY

125. K. D. Jordan, and F. Wang, *Annu. Rev. Phys. Chem.* **54**, 367 (2003).
126. K. Fosse, N. Michel, W. Nazarewicz, M. Płoszajczak, and Y. Jaganathen, *Phys. Rev. A* **91**, 012503 (2015).
127. C. G. Bailey, C. E. H. Dessent, M. A. Johnson, and K. H. Bowen, Jr., *J. Chem. Phys.* **104**, 6976 (1996).
128. G. L. Gutsev, and R. J. Bartlett, *J. Chem. Phys.* **105**, 8785 (1996).
129. R. N. Compton, J. H. S. Carman, C. Desfrancois, H. Abdoul-Carime, J. P. Schermann, J. H. Hendricks, S. A. Lyapustina, and K. H. Bowen, *J. Chem. Phys.* **105**, 3472 (1996).
130. T. Sommerfeld, *Phys. Chem. Chem. Phys.* **4**, 2511 (2002).
131. A. Kunin, and D. M. Neumark, *Phys. Chem. Chem. Phys.* **21**, 7239 (2019).
132. P.J. Sarre, *Mon. Not. R. Astron. Soc.* **313**, 14 (2000).
133. F. Güthe, M. Tulej, M. V. Pachkov, and J. P. Maier, *Astrophys. J.* **555**, 466 (2001).
134. E. Fermi, E. Teller, *Phys. Rev.* **72**, 399 (1947).
135. A. S. Wightman, *Phys. Rev.* **77**, 521 (1950).
136. K. Fox, and J. E. Turner, *J. Chem. Phys.* **45**, 1142 (1966).
137. O. H. Crawford, and A. Dalgarno, *Chem. Phys. Lett.* **1**, 23 (1967).
138. J.-M. Lévy-Leblond, *Phys. Rev.* **153**, 1 (1967)
139. W. B. Brown, R. E. Roberts, *J. Chem. Phys.* **46**, 2006 (1967).
140. J. E. Turner, *Am. J. Phys.* **45**, 758 (1977).
141. W. R. Garrett, *Chem. Phys. Lett.* **5**, 393 (1970)
142. W. R. Garrett, *Phys. Rev. A* **3**, 961 (1971)
143. O. H. Crawford, *Mol. Phys.* **20**, 585 (1971).
144. O. H. Crawford, and W. R. Garrett, *J. Chem. Phys.* **66**, 4968 (1977).
145. C. Desfrancois, H. Abdoul-Carime, N. Khelifa, and J.P. Schermann, *Phys. Rev. Lett.* **73**, 2436 (1994).
146. C. Desfrancois, H. Abdoul-Carime, and J.P. Scherman, *Int. J. Mod. Phys. B* **10**, 1339 (1996).

BIBLIOGRAPHY

147. J. Simons, and K. D. Jordan, *Chem. Rev.* **87**, 535 (1987).
148. L. Adamowicz, *J. Chem. Phys.* **91**, 7787 (1989)
149. R. Ramaekers, D. M. A. Smith, Y. Elkadi, and L. Adamowicz, *Chem. Phys. Lett.* **277**, 269 (1997)
150. M. Gutowski, P. Skurski, K. D. Jordan, and J. Simons, *Int. J. Quantum Chem.* **64**, 183 (1997).
151. M. Gutowski, and P. Skurski, *J. Phys. Chem. B* **101**, 9143 (1997).
152. M. Gutowski, K. D. Jordan, and P. Skurski, *J. Phys. Chem. A* **102**, 2624 (1998)
153. P. Skurski, M. Gutowski, and J. Simons, *Int. J. Quantum Chem.* **80**, 1024 (2000).
154. F. Wang, and K. D. Jordan, *J. Chem. Phys.* **114**, 10717 (2001)
155. T. Sommerfeld, *J. Phys. Chem. A* **108**, 9150 (2004).
156. T. Sommerfeld, *J. Phys. Chem. A* **112**, 11817 (2008).
157. Y. Zhang, P. M. Weber, and H. Jónsson, *J. Phys. Chem. Lett.* **7**, 2068 (2016)
158. T.-C. Jagau, K.B. Bravaya, and A.I. Krylov, *Ann. Rev. Phys. Chem.* **68**, 525 (2017)
159. H. Hao, J. Shee, S. Upadhyay, C. Ataca, K. Jordan, and B. M. Rubenstein. *J. Phys. Chem. Lett.* **9**, 6185 (2018).
160. R.F. Wallis, R. Herman, and H.W. Milnes, *J. Mol. Spectrosc.* **4**, 51 (1960).
161. O.H. Crawford, *Proc. Phys. Soc.* **91**, 279 (1967).
162. W.R. Garrett, *J. Chem. Phys.* **73**, 5721 (1980).
163. W.R. Garrett, *J. Chem. Phys.* **77**, 3666 (1982).
164. D. L. Huang, G. Z. Zhu, Y. Liu, and L. S. Wang, *J. Mol. Spectrosc.* **332**, 86 (2017).
165. S. F. Wong, and G. Schulz, *Phys. Rev. Lett.* **33**, 134 (1974).
166. A. H. Zimmerman, and J. I. Brauman, *J. Chem. Phys.* **66**, 5823 (1977).
167. R. L. Jackson, P. C. Hiberty, and J. I. Brauman, *J. Chem. Phys.* **74**, 3705 (1981).
168. R. D. Mead, K. R. Lykke, W. C. Lineberger, J. Marks, and J. I. Brauman, *J. Chem. Phys.* **81**, 4883 (1984).

BIBLIOGRAPHY

169. K. R. Lykke, R. D. Mead, and W. C. Lineberger, *Phys. Rev. Lett.* **52**, 2221 (1984)
170. K. R. Lykke, D. M. Neumark, T. Andersen, V. J. Trapa, and W. C. Lineberger, *J. Chem. Phys.* **87**, 6842 (1987).
171. K. Yokoyama, G. W. Leach, J. B. Kim, and W. C. Lineberger, *J. Chem. Phys.* **105**, 10696 (1996).
172. K. Yokoyama, G. W. Leach, J. B. Kim, and W. C. Lineberger, A. I. Boldyrev, and M. Gutowski, *J. Chem. Phys.* **105**, 10706 (1996).
173. J. A. D. Stockdale, F. J. Davis, R. N. Compton, and C. E. Klots, *J. Chem. Phys.* **60**, 4279 (1974).
174. T. Kondow, *J. Phys. Chem.* **91**, 1307 (1987)
175. N.I. Hammer, K. Diri, K.D. Jordan, C. Desfrancois, and R.N. Compton, *J. Chem. Phys.* **119**, 3650 (2003)
176. N. I. Hammer, R. N. Compton, L. Adamowicz, and S. Stepanian, *Phys. Rev. Lett.* **94**, 153004 (2005).
177. C. Desfrancois, V. Periquet, Y. Bouteiller, and J. P. Schermann, *J. Phys. Chem. A* **102**, 1274 (1998).
178. J. H. Hendricks, S. A. Lyapustina, H. L. de Clercq, J. T. Snodgrass, and K. H. Bowen, *J. Chem. Phys.* **104**, 7788 (1996).
179. J. H. Hendricks, S. A. Lyapustina, H. L. de Clercq, and K. H. Bowen, *J. Chem. Phys.* **108**, 8 (1998).
180. E. F. Belogolova, G. Liu, E. P. Doronina, S. M. Ciborowski, V. F. Sidorkin, and K. H. Bowen, *J. Phys. Chem. Lett.* **9**, 1284 (2018).
181. L. Suess, Y. Liu, R. Parthasarathy, and F.B. Dunning, *J. Chem. Phys.* **119**, 12890 (2003).
182. F. B. Dunning, and S. Buathong, *Int. Rev. Phys. Chem.* **37**, 287 (2018).
183. S. Y. Han, J. H. Kim, J. K. Song, and S. K. Kim, *J. Chem. Phys.* **109**, 9656 (1998)
184. S.-J. Xu, J. M. Nilles, and K. H. Bowen, *J. Chem. Phys.* **119**, 10696 (2003)

BIBLIOGRAPHY

185. A.M. Buytendyk, A.M. Buonaugurio, S.J. Xu, J.M. Nilles, K.H. Bowen, N. Kirnosov, and L. Adamowicz, *J. Chem. Phys.* **145**, 024301 (2016).
186. C. G. Bailey, C. E. Dessent, and M. A. Johnson, *J. Chem. Phys.* **104**, 6976 (1996)
187. M. A. Yandell, S. B. King, and D. M. Neumark, *J. Chem. Phys.* **140**, 184317 (2014).
188. A. B. Stephansen, S. B. King, Y. Yokoi, Y. Minoshima, W. L. Li, A. Kunin, T. Takayanagi, and D. M. Neumark, *J. Chem. Phys.* **143**, 104308 (2015).
189. R. S. Berry, *J. Chem. Phys.* **45**, 1228 (1966).
190. J. Simons, *J. Am. Chem. Soc.* **103**, 3971 (1981).
191. D. B. Dao, and R. Mabbs, *J. Chem. Phys.* **141**, 154304 (2014).
192. K. J. Mascaritolo, A. M. Gardner, and M. C. Heaven, *J. Chem. Phys.* **143**, 114311 (2015).
193. A. R. Dermer, M. L. Green, K. J. Mascaritolo, and M. C. Heaven, *J. Phys. Chem. A* **121**, 5645 (2017).
194. A. Ferron, P. Serra, and S. Kais, *J. Chem. Phys.* **120**, 8412 (2004).
195. W. R. Garrett, *J. Chem. Phys.* **136**, 054116 (2012).
196. K. D. Jordan, and J. F. Liebman, *Chem. Phys. Lett.* **62**, 143 (1979).
197. M. Gutowski, P. Skurski, X. Li, and L. S. Wang, *Phys. Rev. Lett.* **85**, 3145 (2000).
198. G. L. Gutsev, P. Jena, and R. J. Bartlett, *J. Chem. Phys.* **111**, 504 (1999).
199. I. Anusiewicz, P. Skurski, and J. Simons, *J. Phys. Chem. A* **106**, 10636 (2002).
200. T. Sommerfeld, K. M. Dreux, and R. Joshi, *J. Phys. Chem. A* **118**, 7320 (2014).
201. C. Desfrancois, N. Khelifa, J. P. Schermann, T. Kraft, M. W. Ruf, and H. Hotop, *Z. Phys. D* **27**, 365 (1993).
202. R. N. Compton, F. B. Dunning, and P. Nordlander, *Chem. Phys. Lett.* **253**, 8 (1996).
203. C. Desfrancois, V. Periquet, S. Carles, J. P. Schermann, and L. Adamowicz, *Chem. Phys.* **239**, 475 (1998)
204. C. Desfrancois, V. Periquet, S. A. Lyapustina, T. P. Lippa, D. W. Robinson, K. H. Bowen, H. Nonaka, and R. N. Compton, *J. Chem. Phys.* **111**, 4569 (1999).

BIBLIOGRAPHY

205. C. Desfrancois, Y. Bouteiller, J. P. Schermann, D. Radisic, S. T. Stokes, K. H. Bowen, N. I. Hammer, and R. N. Compton, *Phys. Rev. Lett.* **92**, 083003 (2004).
206. T. Sommerfeld, *J. Chem. Phys.* **121**, 4097 (2004).
207. L. M. Branscomb, and W. L. File, *Phys. Rev.* **93**, 651(D1) (1954).
208. L. M. Branscomb, and S. J. Smith, *Phys. Rev.* **98**, 1028 (1955).
209. P. P. Sorokin, and J. R. Lankard, *IBM J. Res. Develop.* **10**, 162 (1966).
210. F. P. Schafer, W. Schmidt, and S. Volze, *Appl. Phys. Lett.* **9**, 306 (1966).
211. W. C. Lineberger, and B. W. Woodward, *Phys. Rev. Lett.* **25**, 424 (1970).
212. O. Lakhmanskaya , M. Simpson , S. Murauer , V. Kokoouline, and R. Wester , *J. Chem. Phys.* **149**, 104302 (2018).
213. R. Otto, A. von Zastrow, T. Best, and R. Wester, *Phys. Chem. Chem. Phys.* **15**, 612 (2013).
214. T. A. Patterson, H. Hotop, A. Kasdan, D. W. Norcross, and W. C. Lineberger, *Phys. Rev. Lett.* **32**, 189 (1974).
215. S. E. Novick, P. L. Jones, T. J. Mulloney, and W. C. Lineberger, *J. Chem. Phys.* **70**, 2210 (1979).
216. P. L. Jones, R. D. Mead, B. E. Kohler, S. D. Rosner, and W. C. Lineberger, *J. Chem. Phys.* **73**, 4419 (1980).
217. D. M. Neumark, K. R. Lykke, T. Andersen, and W. C. Lineberger, *J. Chem. Phys.* **83**, 4364 (1985).
218. A. S. Mullin, K. K. Murray, C. P. Schulz, D. M. Szaflarski, and W. C. Lineberger, *Chem. Phys.* **166**, 207 (1992).
219. C. G. Bailey, D. J. Lavrich, D. Serxner, and M. A. Johnson, *J. Chem. Phys.* **105**, 1807 (1996).
220. J. Schiedt, and R. Weinkauff, *J. Chem. Phys.* **110**, 304 (1999).
221. I. Leon, Z. Yang, and L. S. Wang, *J. Chem. Phys.* **139**, 194306 (2013).
222. P. K. Acharya, Rick A. Kendall, and J. Simons, *J. Am. Chem. Soc.* **106**, 3402 (1984).

BIBLIOGRAPHY

223. P. D. Dau, Ph. D. dissertation (Brown University, January 2014).
224. D. L. Huang, Ph. D. dissertation (Brown University, May 2016).
225. V. Dribinski, A. Ossadtchi, V. A. Mandelshtam, and H. Reisler, *Rev. Sci. Instrum.* **73**, 2634 (2002).
226. G. A. Garcia, L. Nahon, and I. Powis, *Rev. Sci. Instrum.* **75**, 4989 (2004).
227. Y. Hashikawa, M. Murata, A. Wakamiya, and Y. Murata, *J. Am. Chem. Soc.* **138**, 4096 (2016).
228. J. Broggi, T. Terme, and P. Vanelle, *Angew. Chem. Int. Ed.* **53**, 384 (2014).
229. M. Mahesh, J. A. Murphy, F. LeStrat, and H. P. Wessel, Beilstein, *J. Org. Chem.* **5**, 1 (2009).
230. R. Mathur, and P. B. O'Connor, *Rev. Sci. Instrum.* **77**, 114101 (2006).
231. P. B. O'Connor, C. E. Costello, and W. E. Earle, *J. Am. Soc. Mass Spectrom.* **13**, 1370 (2002).
232. G. Z. Zhu and L. S. Wang, *J. Chem. Phys.* **143**, 221102 (2015)
233. J. Ferraris, D. O. Cowan, V. Walatka Jr, and J. H. Perlstein, *J. Am. Chem. Soc.* **95**, 948 (1973).
234. L. B. Coleman, M. J. Cohen, D. J. Sandman, F. G. Yamagishi, A. F. Garito, and A. J. Heeger, *Solid State Commun.* **12**, 1125 (1973).
235. F. H. Herbstein, and M. Kapon, *Crystallogr. Rev.* **14**, 3 (2008).
236. K. P. Goetz, D. Vermeulen, M. E. Payne, C. Kloc, L. E. McNeil, and O. D. Jurchescu, *J. Mater. Chem. C* **2**, 3065 (2014).
237. C. E. Klots, R. N. Compton, and V. F. Raaen, *J. Chem. Phys.* **60**, 1177 (1974).
238. R. N. Compton, and C. D. Cooper, *J. Chem. Phys.* **66**, 4325 (1977).
239. E. A. Brinkman, E. Gunther, and J. I. Brauman, *J. Chem. Phys.* **95**, 6185 (1991).
240. E. A. Brinkman, E. Gunther, O. Schafer, and J. I. Brauman, *J. Chem. Phys.* **100**, 1840 (1994).

BIBLIOGRAPHY

241. S. Panja, U. Kadhane, J. U. Andersen, A. I. S. Holm, P. Hvelplund, M.-B. S. Kirketerp, S. B. Nielsen, K. Stochkel, R. N. Compton, J. S. Forster, K. Kilsa, and M. B. Nielsen, *J. Chem. Phys.* **127**, 124301 (2007).
242. G. M. Roberts, J. Lecointre, D. A. Horke, and J. R. R. Verlet, *Phys. Chem. Chem. Phys.* **12**, 6226 (2010).
243. L. Ma, P. Hu, C. Kloc, H. Sun, M. E. Michel-Beyerle, and G. G. Gurzadyan, *Chem. Phys. Lett.* **609**, 11 (2014).
244. S. A. Pshenichnyuk, A. Modelli, E. F. Lazneva, and A. S. Komolov, *J. Phys. Chem. A* **118**, 6810 (2014).
245. V. G. Zakrzewski, O. Dolgounitcheva, and J. V. Ortiz, *J. Chem. Phys.* **105**, 5872 (1996).
246. E. Orti, R. Viruela, and P. M. Viruela, *J. Phys. Chem.* **100**, 6138 (1996).
247. P. Skurski and M. Gutowski, *J. Mol. Struct.* **531**, 339 (2000).
248. M. Sobczyk, P. Skurski, and J. Simons, *J. Phys. Chem. A* **107**, 7084 (2003).
249. B. Milian, R. Pou-Amerigo, R. Viruela, and E. Orti, *J. Mol. Struct.* **709**, 97 (2004).
250. B. Milian, R. Pou-Amerigo, R. Viruela, and E. Orti, *Chem. Phys. Lett.* **391**, 148 (2004).
251. H. Nakashima, Y. Honda, T. Shida, and H. Nakatsuji, *Mol. Phys.* **113**, 1728 (2015).
252. M. J. Frisch et al., gaussian 09, Revision C.01, Gaussian, Inc., Wallingford, CT, 2010.
253. H. T. Liu, D. L. Huang, Y. Liu, L. F. Cheung, P. D. Dau, C. G. Ning, and L. S. Wang, *J. Phys. Chem. Lett.* **6**, 637 (2015).
254. C. Blondel, *Phys. Scr.* **58**, 31 (1995).
255. G. Z. Zhu, Y. Hashikawa, Y. Liu, Q. F. Zhang, L. F. Cheung, Y. Murata, and L. S. Wang, *J. Phys. Chem. Lett.* **8**, 6220 (2017).
256. A. Hirsch, and B. Nuber, *Acc. Chem. Res.* **32**, 795 (1999).
257. O. Vostrowsky, and A. Hirsch, *Chem. Rev.* **106**, 5191 (2006).
258. W. Andreoni, F. Gygi, and M. Parrinello, *Chem. Phys. Lett.* **190**, 159 (1992).
259. T. Kaneko, Y. Li, S. Nishigaki, and R. Hatakeyama, *J. Am. Chem. Soc.* **130**, 2714 (2008).

BIBLIOGRAPHY

260. W. Andreoni, A. Curioni, K. Holczer, K. Prassides, M. Keshavarz-K, J. C. Hummelen, and F. Wudl, *J. Am. Chem. Soc.* **118**, 11335 (1996).
261. T. Pichler, M. Knupfer, M. S. Golden, S. Haffner, R. Friedlein, J. Fink, W. Andreoni, A. Curioni, M. Keshavarz-K, C. Bellavia-Lund, A. Sastre, J.-C. Hummelen, and F. Wudl, *Phys. Rev. Lett.* **78**, 4249 (1997).
262. W. Andreoni, *Annu. Rev. Phys. Chem.* **49**, 405 (1998).
263. A. Ren, J. Feng, X. Sun, W. Li, W. Tian, C. Sun, X. Zheng, and M. C. Zerner, *Int. J. Quantum Chem.* **78**, 422 (2000).
264. D. Erbahar, T. Susi, X. Rocquefelte, C. Bittencourt, M. Scardamaglia, P. Blaha, P. Guttman, G. Rotas, N. Tagmatarchis, X. Zhu, and A. P. Hitchcock, *Sci. Rep.* **6**, 35605 (2016).
265. C. Bellavia-Lund, M. Keshavarz-K., T. Collins, and F. Wudl, *J. Am. Chem. Soc.* **119**, 8101 (1997).
266. I. Lamparth, B. Nuber, G. Schick, A. Skiebe, T. Grosser, and A. Hirsch, *Angew. Chem. Int. Ed.* **35**, 2257 (1995).
267. J. C. Hummelen, B. Knight, J. Pavlovich, R. Gonzalez, and F. Wudl, *Science* **269**, 1554 (1995).
268. S. Haffner, T. Pichler, M. Knupfer, B. Umlauf, R. Friedlein, M. S. Golden, J. Fink, M. Keshavarz-K., C. Bellavia-Lund, A. Sastre, J. C. Hummelen, and F. Wudl, *Eur. Phys. J. B* **1**, 11 (1998).
269. M. R. C. Hunt, T. Pichler, L. Siller, P. A. Bruhwiler, M. S. Golden, N. Tagmatarchis, K. Prassides, and P. Rudolf, *Phys. Rev. B* **66**, 193404 (2002).
270. K. Schulte, L. Wang, P. J. Moriarty, K. Prassides, and N. Tagmatarchis, *N. J. Chem. Phys.* **126**, 184707 (2007).
271. Y. Deng, B. Gao, M. Deng, and Y. Luo, *J. Chem. Phys.* **140**, 124304 (2014).
272. H. Kuzmany, W. Plank, J. Winter, O. Dubay, N. Tagmatarchis, and K. Prassides, *Phys. Rev. B* **60**, 1005 (1999).

BIBLIOGRAPHY

273. W. Plank, T. Pichler, H. Kuzmany, O. Dubay, N. Tagmatarchis, and K. Prassides, *Eur. Phys. J. B* **17**, 33 (2000).
274. M. Krause, S. Baea-Fischmair, R. Pfeiffer, W. Plank, T. Pichler, H. Kuzmany, N. Tagmatarchis, and K. Prassides, *J. Phys. Chem. B* **105**, 11964 (2001).
275. J. Auerhammer, T. Kim, M. Knupfer, M. Golden, J. Fink, N. Tagmatarchis, and K. Prassides, *Solid State Commun.* **117**, 697 (2001).
276. A. Gruss, K. P. Dinse, A. Hirsch, B. Nuber, and U. Reuther, *J. Am. Chem. Soc.* **119**, 8728 (1997).
277. K. Hasharoni, C. Bellavia-Lund, M. Keshavarz-K, G. Srdanov, and F. Wudl, *J. Am. Chem. Soc.* **119**, 11128 (1997).
278. F. Simon, D. Arčon, N. Tagmatarchis, S. Garaj, L. Forro, and K. Prassides, *J. Phys. Chem. A* **103**, 6969 (1999).
279. M. J. Butcher et al., *Phys. Rev. Lett.* **83**, 3478 (1999).
280. M. Butcher et al. *Appl. Phys. Lett.* **75**, 1074 (1999).
281. F. H. Jones et al., *Phys. Rev. B* **59**, 9834 (1999).
282. C. Silien et al., *Surf. Sci.* **482**, 1 (2001).
283. J. Zhao et al., *Phys. Rev. Lett.* **95**, 045502 (2005).
284. C. Fang et al., *Phys. Lett. A* **374**, 4465 (2010).
285. S. A. Tawfik et al., *J. Chem. Phys.* **144**, 021101 (2016).
286. R. Kumashiro et al., *Appl. Phys. Lett.* **84**, 2154 (2004).
287. Y. Li et al., *J. Am. Chem. Soc.* **131**, 3412 (2009).
288. F. Hauke et al., *Chem. Comm.* 600 (2004).
289. G. Rotas, and N. Tagmatarchis, *Chem. Eur. J.* **22**, 1206 (2016).
290. G. Rotas et al., *Chem. Eur. J.* **22**, 15137 (2016).
291. L. S. Wang, and X. B. Wang, *J. Phys. Chem. A* **104**, 1978 (2000).
292. X. B. Wang et al., *J. Chem. Phys.* **128**, 114307 (2008).

BIBLIOGRAPHY

293. S. F. Parker et al., *Phys. Chem. Chem. Phys.* **13**, 7789 (2011).
294. N. Tagmatarchis et al., *Carbon* **44**, 1420 (2006).
295. X. B. Wang et al., *Phys. Rev. Lett.* **96**, 143002 (2006).
296. X. B. Wang et al., *J. Phys. Chem. C* **111**, 17684 (2007).
297. G. Z. Zhu, Y. Liu, Y. Hashikawa, Q. F. Zhang, Y. Murata, and L. S. Wang, *Chem. Sci.* **9**, 5666 (2018).
298. S. Guha, and K. Nakamoto, *Coor. Chem. Rev.* **249**, 1111 (2005).
299. N. J. Turro, J. Y. C. Chen, E. Sartori, M. Ruzzi, A. Marti, R. Lawler, S. Jockusch, J. Lopez-Gejo, K. Komatsu, and Y. Murata, *Acc. Chem. Res.* **43**, 335 (2010).
300. A. A. Popov, S. Yang, and L. Dunsch, *Chem. Rev.* **113**, 5989 (2013).
301. J. R. Heath, S. C. O'Brien, Q. Zhang, Y. Liu, R. F. Curl, H. W. Kroto, F. K. Tittel, and R. E. Smalley, *J. Am. Chem. Soc.* **107**, 7779 (1985).
302. T. Weiske, D. K. Bohme, J. Hrusak, W. Kratschmer, and H. Schwarz, *Angew. Chem. Int. Ed. Engl.* **30**, 884 (1991).
303. M. Saunders, H. A. Jimenez-Vazquez, R. J. Cross, and R. J. Poreda, *Science* **259**, 1428 (1993).
304. T. A. Murphy, Th. Pawlik, A. Weidinger, M. Hohne, R. Alcala, and J.-M. Spaeth, *Phys. Rev. Lett.* **77**, 1075 (1996).
305. T. Suetsuna, N. Dragoe, W. Harneit, A. Weidinger, H. Shimotani, S. Ito, H. Takagi, and K. Kitazawa, *Chem. Eur. J.* **8**, 5079 (2002).
306. L. S. Wang, J. M. Alford, Y. Chai, M. Diener, and R. E. Smalley, *Z. Phys. D* **26**, 297 (1993).
307. L. S. Wang, J. M. Alford, Y. Chai, M. Diener, J. Zhang, S. M. McClure, T. Guo, G. E. Scuseria, and R. E. Smalley, *Chem. Phys. Lett.* **207**, 354 (1993).
308. M. H. Levitt, *Phil. Trans. R. Soc. A.* **371**, 20120429 (2013).
309. Y. Rubin, *Chem. Eur. J.* **3**, 1009 (1997).
310. M. Murata, Y. Murata, and K. Komatsu, *Chem. Comm.* 6083 (2008).

BIBLIOGRAPHY

311. K. Komatsu, M. Murata, and Y. Murata, *Science* **307**, 238 (2005).
312. K. Kurotobi, and Y. Murata, *Science* **333**, 613 (2011).
313. A. Krachmalnicoff, M. H. Levitt, and R. J. Whitby, *Chem. Commun.* **50**, 13037 (2004).
314. A. Krachmalnicoff, R. Bounds, S. Mamone, S. Alom, M. Concistrè, B. Meier, K. Kouřil, M. E. Light, M. R. Johnson, S. Rols, A. J. Horsewill, A. Shugai, U. Nagel, T. Rõõm, M. Carravetta, M. H. Levitt, and R. J. Whitby, *Nat. Chem.* **8**, 953 (2016).
315. R. Zhang, M. Murata, T. Aharen, A. Wakamiya, T. Shimoaka, T. Hasegawa, and Y. Murata, *Nat. Chem.* **8**, 435 (2016).
316. R. Zhang, M. Murata, A. Wakamiya, T. Shimoaka, T. Hasegawa, and Y. Murata, *Sci. Adv.* **3**, e1602833 (2017).
317. C. N. Ramachandran, and N. Sathyamurthy, *Chem. Phys. Lett.* **410**, 348 (2005).
318. K. Yagi, and D. Watanabe, *Int. J. Quantum Chem.* **109**, 2080 (2009).
319. A. Varadwaj, and P. R. Varadwaj, *Chem. Eur. J.* **18**, 15345 (2012).
320. B. Ensing, F. Costanzo, and P. L. Silvestrelli, *J. Phys. Chem. A* **116**, 12184 (2012).
321. A. Galano, A. Pérez-González, L. del Olmo, M. Francisco-Marquez, and J. R. León-Carmona, *J. Mol. Model.* **20**, 1 (2012).
322. S. Aoyagi, N. Hoshino, T. Akutagawa, Y. Sado, R. Kitaura, H. Shinohara, K. Sugimoto, R. Zhang, and Y. Murata, *Chem. Commun.* **50**, 524 (2014).
323. B. Meier, S. Mamone, S. Concistre, J. Alonso-Valdesueiro, A. Krachmalnicoff, R. J. Whitby, and M. H. Levitt, *Nat. Commun.* **6**, 8112 (2015).
324. C. Beduz, M. Carravetta, J. Y.-C. Chen, M. Concistrè, M. Denning, M. Frunzi, A. J. Horsewill, O. G. Johannessen, R. Lawler, X. Lei, M. H. Levitt, Y. Li, S. Mamone, Y. Murata, U. Nagel, T. Nishida, J. Ollivier, S. Rols, T. Rõõm, R. Sarkar, N. J. Turro, and Y. Yanga, *Proc. Natl. Acad. Sci. U. S. A.* **109**, 12894 (2012).
325. S. Mamone, M. Concistrè, E. Carignani, B. Meier, A. Krachmalnicoff, O. G. Johannessen, X. Lei, Y. Li, M. Denning, and M. Carravetta, *J. Chem. Phys.* **140**, 194306 (2014).

BIBLIOGRAPHY

326. K. S. K. Goh, M. Jiménez-Ruiz, M. R. Johnson, S. Rols, J. Ollivier, M. S. Denning, S. Mamone, M. H. Levitt, X. Lei, Y. Li, N. J. Turro, Y. Murata, and A. J. Horsewill, *Phys. Chem. Chem. Phys.* **16**, 21330 (2014).
327. P. M. Felker, V. Vlcek, I. Hietanen, S. FitzGerald, D. Neuhauser, and Z. Bacic, *Phys. Chem. Chem. Phys.* **19**, 31274 (2017).
328. P. M. Felker, and Z. Bacic. *J. Chem. Phys.* **144**, 201101 (2016).
329. Z. Bacic, V. Vlcek, D. Neuhauser, P. M. Felker, *Faraday Discuss.* **212**, 547 (2018).
330. Y. Li, J. Y.-C. Chen, X. Lei, R. G. Lawler, Y. Murata, K. Komatsu, and N. J. Turro, *J. Phys. Chem. Lett.* **3**, 1165 (2012).
331. K. Min, A. B. Farimani, and N. R. Aluru, *App. Phys. Lett.* **103**, 263112 (2013).
332. Y. Gao, and B. Xu, *J. Phys. Chem. C* **119**, 20466 (2015).
333. C. Zhu, and X. Wang, *Sci. Rep.* **5**, 17932 (2015).
334. S. Kaneko, Y. Hashikawa, S. Fujii, Y. Murata, and M. Kiguchi, *ChemPhysChem* **18**, 1229 (2017).
335. E. E. Maroto, J. Mateos, M. Garcia-Borràs, S. Osuna, S. Filippone, M. Á. Herranz, Y. Murata, M. Solà, and N. Martín, *J. Am. Chem. Soc.* **137**, 1190 (2015).
336. J. U. Reveles, G. KC, T. Baruah, and R. R. Zope, *Chem. Phys. Lett.* **685**, 198 (2017).
337. T. Korona, and H. Dodziuk, *J. Chem. Theory Comput.* **7**, 1476 (2011).
338. C. I. Williams, and M. A. Whitehead, and L. Pang, *J. Phys. Chem.* **97**, 11652 (1993).
339. D. Bucher, *Chem. Phys. Lett.* **534**, 38 (2012).
340. A. B. Farimani, Y. Wu, and N. R. Aluru, *Phys. Chem. Chem. Phys.* **15**, 17993 (2013).
341. Y. Hashikawa, M. Murata, A. Wakamiya, and Y. Murata, *Angew. Chem. Int. Ed.* **55**, 13109 (2016).
342. Y. Hashikawa, M. Murata, A. Wakamiya, and Y. Murata, *J. Org. Chem.* **82**, 4465 (2017).
343. Y. Hashikawa, and Y. Murata, *J. Am. Chem. Soc.* **139**, 18468 (2017).

BIBLIOGRAPHY

344. C. G. Ning, B. Hajgato, Y. R. Huang, S. F. Zhang, K. Liu, Z. H. Luo, S. Knippenberg, J. K. Deng, and M. S. Deleuze, *Chem. Phys.* **343**, 19 (2008).
345. J. Stubbe, and W. A. van der Donk, *Chem. Rev.* **98**, 705 (1998).
346. A. L. Sobolewski, W. Domcke, C. Dedonder-Lardeux, and C. Jouvet, *Phys. Chem. Chem. Phys.* **4**, 1093 (2002).
347. S. J. Harris, D. Murdock, Y. Y. Zhang, T. A. A. Oliver, M. P. Grubb, A. J. Orr-Ewing, G. M. Greetham, I. P. Clark, M. Towrie, S. E. Bradforth, and M. N. R. Ashfold, *Phys. Chem. Chem. Phys.* **15**, 6567 (2013).
348. K. R. Yang, X. F. Xu, J. J. Zheng, and D. G. Truhlar, *Chem. Sci.* **5**, 4661 (2014).
349. C. M. Tseng, Y. T. Lee, and C. K. Ni, *J. Chem. Phys.* **121**, 2459 (2004).
350. M. G. D. Nix, A. L. Devine, B. Cronin, R. N. Dixon, and M. N. R. Ashfold, *J. Chem. Phys.* **125**, 133318 (2006).
351. C. M. Tseng, Y. T. Lee, M. F. Lin, C. K. Ni, S. Y. Liu, Y. P. Lee, Z. F. Xu, and M. C. Lin, *J. Phys. Chem. A* **111**, 9463 (2007).
352. A. Iqbal, L. J. Pegg, and V. G. Stavros, *J. Phys. Chem. A* **112**, 9531 (2008).
353. R. N. Dixon, T. A. A. Oliver, and M. N. R. Ashfold, *J. Chem. Phys.* **134**, 194303 (2011).
354. G. M. Roberts, A. S. Chatterley, J. D. Young, and V. G. Stavros, *J. Phys. Chem. Lett.* **3**, 348 (2012).
355. X. F. Xu, J. J. Zheng, K. R. Yang, and D. G. Truhlar, *J. Am. Chem. Soc.* **136**, 16378 (2014).
356. C. J. Xie, J. Y. Ma, X. L. Zhu, D. R. Yarkony, D. Q. Xie, and H. Guo, *J. Am. Chem. Soc.* **138**, 7828 (2016).
357. J. S. Lim, I. S. Lim, K. S. Lee, D. S. Ahn, Y. S. Lee, and S. K. Kim, *Angew. Chem. Int. Ed.* **45**, 6290 (2006).
358. I. S. Lim, J. S. Lim, Y. S. Lee, and S. K. Kim, *J. Chem. Phys.* **126**, 034306 (2007).
359. A. L. Devine, M. G. D. Nix, R. N. Dixon, and M. N. R. Ashfold, *J. Phys. Chem. A* **112**, 9563 (2008).

BIBLIOGRAPHY

360. T. S. Venkatesan, S. G. Ramesh, Z. Lan, and W. Domcke, *J. Chem. Phys.* **136**, 174312 (2012).
361. G.-S.-M. Lin, C. Xie, and D. Xie, *J. Phys. Chem. A* **121**, 8432 (2017).
362. R. A. Shandross, J. P. Longwell, and J. B. Howard, *Symp. (Int.) Combust. [Proc.]* **26**, 711 (1996).
363. J. Platz, O. J. Nielsen, T. J. Wallington, J. C. Ball, M. D. Hurley, A. M. Straccia, W. F. Schneider, and J. Sehested, *J. Phys. Chem. A* **102**, 7964 (1998).
364. H. Richter, and J. B. Howard, *Phys. Chem. Chem. Phys.* **4**, 2038 (2002).
365. P. Hemberger, G. da Silva, A. J. Trevitt, T. Gerber, and A. Bodi, *Phys. Chem. Chem. Phys.* **17**, 30076 (2015).
366. T. Jahnert, M. D. Hager, and U. S. Schubert, *J. Mater. Chem. A* **2**, 15234 (2014)
367. M. Araki, Y. Matsushita, and K. Tsukiyama, *Astron. J.* **150**, 113 (2015).
368. M. Araki, K. Niwayama, and K. Tsukiyama, *Astron. J.* **148**, 87 (2014)
369. J. H. Richardson, L. M. Stephenson, and J. I. Brauman, *J. Am. Chem. Soc.* **97**, 2967 (1975)
370. R. F. Gunion, M. K. Gilles, M. L. Polak, and W. C. Lineberger, *Int. J. Mass Spectrom. Ion Processes* **117**, 601 (1992).
371. J. B. Kim, T. I. Yacovitch, C. Hock, and D. M. Neumark, *Phys. Chem. Chem. Phys.* **13**, 17378 (2011).
372. J. Takahashi, T. Momose, and T. Shida, *Bull. Chem. Soc. Jpn.* **67**, 964 (1994).
373. J. G. Radziszewski, M. Gil, A. Gorski, J. Spanget-Larsen, J. Waluk, and B. J. Mróz, *J. Chem. Phys.* **115**, 9733 (2001).
374. C. W. Cheng, Y. P. Lee, and H. A. Witek, *J. Phys. Chem. A* **112**, 2648 (2008).
375. C. W. Cheng, H. Witek, and Y. P. Lee, *J. Chem. Phys.* **129**, 154307 (2008).
376. C. W. Cheng, Y. P. Lee, and H. A. Witek, *J. Phys. Chem. A* **112**, 11998 (2008).
377. D. M. Chipman, R. F. Liu, X. F. Zhou, and P. Pulay, *J. Chem. Phys.* **100**, 5023 (1994).
378. Y. Qin, and R. A. Wheeler, *J. Chem. Phys.* **102**, 1689 (1995).

BIBLIOGRAPHY

379. Y. Qin, and R. A. Wheeler, *J. Am. Chem. Soc.* **117**, 6083 (1995).
380. W. Xu, and A. Gao, *J. Phys. Chem. A* **110**, 997 (2006).
381. G. N. R. Tripathi, and R. H. Schuler, *J. Chem. Phys.* **81**, 113 (1984).
382. G. N. R. Tripathi, S. Qun, D. A. Armstrong, D. M. Chipman, and R. H. Schuler, *J. Phys. Chem.* **96**, 5344 (1992).
383. A. Mukherjee, M. L. McGlashen, and T. G. Spiro, *J. Phys. Chem.* **99**, 4912 (1995).
384. J. Spanget-Larsen, M. Gil, A. Gorski, D. M. Blake, J. Waluk, and J. G. Radziszewski, *J. Am. Chem. Soc.* **123**, 11253 (2001).
385. K. Shibuya, M. Nemoto, A. Yanagibori, M. Fukushima, and K. Obi, *Chem. Phys.* **121**, 237 (1988).
386. G. Z. Zhu, D. H. Huang, and L. S. Wang, *J. Chem. Phys.* **147**, 013910 (2017).
387. U. Fano, *Phys. Rev.* **124**, 1866 (1961).
388. H. Ibach, *Surf. Sci.* **299**, 116 (1994).
389. R. F. Egerton, *Rep. Prog. Phys.* **72**, 016502 (2009).
390. J. B. Kim, M. L. Weichman, T. I. Yacovitch, C. Shih, and D. M. Neumark, *J. Chem. Phys.* **139**, 104301 (2013).
391. K. Regeta, and M. Allan, *Phys. Rev. Lett.* **110**, 203201 (2013).
392. P. Hockett, M. Staniforth, K. L. Reid, and D. Townsend, *Phys. Rev. Lett.* **102**, 253002 (2009).
393. K. L. Reid, *Annu. Rev. Phys. Chem.* **54**, 397 (2003).
394. G. Z. Zhu, C. H. Qian, and L. S. Wang, *Angew. Chem. Int. Ed.* (2019). DOI: 10.1002/anie.201903444.
395. J. D. Watson, and F. H. C. Crick, *Nature* **171**, 964 (1953).
396. I. J. Kimsey, K. Petzold, B. Sathyamoorthy, Z. W. Stein, and H. M. Al-Hashimi, *Nature* **519**, 315 (2015).
397. C. Colominas, and F. J. Luque, M. Orozco, *J. Am. Chem. Soc.* **118**, 6811 (1996).

BIBLIOGRAPHY

398. Z. Yang, and M. T. Rodgers, *Phys. Chem. Chem. Phys.* **6**, 2749 (2004).
399. C. Yu, S. Peng, I. Akiyama, J. Lin, and P. R. LeBreton, *J. Am. Chem. Soc.* **100**, 2303 (1978).
400. E. Nir, I. Hünig, K. Kleinermanns, and M. S. de Vries, *Phys. Chem. Chem. Phys.* **5**, 4780 (2003).
401. K. Kosma, C. Schröter, E. Samoylova, I. V. Hertel, and T. Schultz, *J. Am. Chem. Soc.* **131**, 16939 (2009).
402. G. Bazsó, G. Tarczay, G. Fogarasi, and P. G. Szalay, *Phys. Chem. Chem. Phys.* **13**, 6799 (2011).
403. I. Reva, M. J. Nowak, L. Lapinski, and R. Fausto, *J. Chem. Phys.* **136**, 064511 (2012).
404. J. L. Alonso, V. Vaquero, I. Peña, J. C. López, S. Mata, and W. Caminati, *Angew. Chem. Int. Ed.* **52**, 2331 (2013).
405. Z. Chen et al., *J. Am. Chem. Soc.* **138**, 16596 (2016).
406. L. Jin, X. Song, Z. Cao, L. Luo, C. Zhao, J. Lu, and Q. Zhang, *J. Phys. Org. Chem.* **31**, e3831 (2018).
407. S.-C. Wei, J.-W. Ho, H.-C. Yen, H.-Q. Shi, L.-H. Cheng, C.-N. Weng, W.-K. Chou, C.-C. Chiu, and P.-Y. Cheng, *J. Phys. Chem. A* **122**, 9412 (2018).
408. S. A. Trygubenko, T. V. Bogdan, M. Rueda, M. Orozco, F. J. Luque, J. Šponer, P. Slavíček, and P. Hobza, *Phys. Chem. Chem. Phys.* **4**, 4192 (2002).
409. M. Dreyfus, O. Bensaude, G. Dodin, and J. E. Dubois, *J. Am. Chem. Soc.* **98**, 6338 (1976).
410. J. Schiedt, R. Weinkauff, D. M. Neumark, and E. W. Schlag, *Chem. Phys.* **239**, 511 (1998).
411. X. Li, K. H. Bowen, M. Haranczyk, R. A. Bachorz, K. Mazurkiewicz, J. Rak, and M. Gutowski, *J. Chem. Phys.* **127**, 174309 (2007).
412. M. Lesslie, J. T. Lawler, A. Dang, J. A. Korn, D. Bím, V. Steinmetz, P. Maître, F. Tureček, and V. Ryzhov, *ChemPhysChem* **18**, 1293 (2017).
413. J. M. Bakker, J.-Y. Salpin, and P. Maître, *Int. J. Mass Spectrom.* **283**, 214 (2009).

BIBLIOGRAPHY

414. M. Broquier, S. Soorkia, G. Pino, C. Dedonder-Lardeux, C. Jouvet, and G. Grégoire, *J. Phys. Chem. A* **121**, 6429 (2017).
415. Q. Luo, J. Li, Q. S. Li, S. Kim, S. E. Wheeler, Y. Xie, and H. F. Schaefer III, *Phys. Chem. Chem. Phys.* **7**, 861 (2005).
416. M.-V. Vázquez, A. Martínez, O. Dolgounitcheva, and J. V. Ortiz, *J. Phys. Chem. A* **110**, 11174 (2006).
417. B. F. Parsons, S. M. Sheehan, T. A. Yen, D. M. Neumark, N. Wehres, and R. Weinkauf, *Phys. Chem. Chem. Phys.* **9**, 3291 (2007).
418. B. Boudaïffa, P. Cloutier, D. Hunting, M. A. Huels, and L. Sanche, *Science* **287**, 1658 (2000).
419. S. Denifl, S. Ptasińska, M. Probst, J. Hrušák, P. Scheier, and T. D. Märk, *J. Phys. Chem. A* **108**, 6562 (2004).
420. W. Lu, and J. Liu, *Phys. Chem. Chem. Phys.* **18**, 32222 (2016).
421. I. Pugliesi, and K. Müller-Dethlefs, *J. Phys. Chem. A* **110**, 4657 (2006). See FC-LabII at <http://www.fclab2.net>.
422. PGOPHER, C. M. Western, University of Bristol, <http://pgopher.chm.bris.ac.uk>.

Abbreviations

BE	Binding energy
CCD	Charge-copuled device
cw	Continuous-wave
[Cy-H]⁻	Deprotonated cytosine anion
DBA	Dipole-bound anion
DBS	Dipole-bound state
DFT	Density functional theory
DNA	Deoxyribonucleic acid
EA	Electron affinity
ESI	Electrospray ionization
FC	Franck-Condon
FWHM	Full-width at half-maximum
HOMO	Highest occupied molecular orbital
KE	Kinetic energy
LUMO	Lowest unoccupied molecular orbital
MCA	Multiply-charged anion
MCP	Micro-channel plates
MP2	Møller-Plesset second-order perturbation theory
MS	Mass spectrometry
O.D.	Outer diameter
ODCB	o-dichlorobenzene
PAD	Photoelectron angular distribution
PDS	Photodetachment spectroscopy
PES	Photoelectron spectroscopy
QBA	Quadrupole-bound anion
QBS	Quadrupole-bound state
QID	Quadrupole ion guide
RET	Rydberg electron transfer
rf	Radio-frequency
SEVI	Slow photoelectron velocity-map imaging
TCNQ	Tetracyanoquinodimethane
TDAE	Tetrakis(dimethylamino)ethylene
TOF	Time-of-flight
UPS	Ultraviolet photoelectron spectroscopy
UV	Ultraviolet
VMI	Velocity-map imaging
XPS	X-ray photoelectron spectroscopy
ZEKE	Zero-electron kinetic energy